

Functional composites with damage control and repair

THÈSE N° 8296 (2018)

PRÉSENTÉE LE 19 JANVIER 2018

À LA FACULTÉ DES SCIENCES ET TECHNIQUES DE L'INGÉNIEUR
LABORATOIRE DE MISE EN OEUVRE DE COMPOSITES À HAUTE PERFORMANCE
PROGRAMME DOCTORAL EN SCIENCE ET GÉNIE DES MATÉRIAUX

ÉCOLE POLYTECHNIQUE FÉDÉRALE DE LAUSANNE

POUR L'OBTENTION DU GRADE DE DOCTEUR ÈS SCIENCES

PAR

Amaël Maximilien COHADES

acceptée sur proposition du jury:

Prof. H. Hofmann, président du jury
Prof. V. Michaud, directrice de thèse
Prof. N. R. Sottos, rapporteuse
Dr A. Gilliot, rapporteur
Prof. J. Botsis, rapporteur



ÉCOLE POLYTECHNIQUE
FÉDÉRALE DE LAUSANNE

Suisse
2018

*"Seul, on va plus vite.
Ensemble, on va plus loin."*

Proverbe Africain

A Barbara

A l'amitié

Acknowledgements

This thesis is the product of four years of research carried out at the Laboratory for Processing of Advanced Composites (LPAC) (former Laboratoire de Technologie des Composites et Polymères, LTC) at the École Polytechnique Fédérale de Lausanne (EPFL, Switzerland) and I am grateful for the opportunity I was given to explore such a fascinating field of research. This research was funded by the Swiss National Science Foundation (SNF 200020-150007-1), that is gratefully acknowledged. This work would not have been possible without the help, advice and support of many people who I would like to mention herein and express my gratitude.

First of all, my sincere acknowledgment goes to my thesis director, Prof. Véronique Michaud, for her constant help, support and freedom she gave me throughout this project, but also for the passion she transmitted me for such field from day one of my undergraduate studies. Also, I would like to thank her for the many opportunities she gave me to travel to conferences and the good memories that resulted. Acknowledgements are also going to Prof. Jan-Anders Månson, for giving me the opportunity to start this work in his lab. I would like also to thank Dr. Christopher Plummer, Dr. Pierre-Etienne Bourban and Dr. Yves Letterier for their help and fruitful discussion along the four years of project. Moreover, I express many thanks to my thesis jury members, Prof. Nancy R. Sottos, Prof. John Botsis, Dr. Anatole Gillot as well as the president of the jury Prof. Heinrich Hofmann for their time and inputs on this work.

Much of this research would not have been possible without the participation of other laboratories. I would like first to thank all my former colleagues from the Laboratory of Mechanical Metallurgy for their help and support, especially Raphaël Charvet and Cyril Dénéreaz for their help and accessibility of the machines. I would also like to acknowledge the COMATEC institute at HEIGH-VD and especially Prof. Jean-Pascal Reymondin for his help and accessibility to C-scan imaging. The use of nanofibres was made possible through the collaboration with the Department of Materials, Textiles and Chemical Engineering at Ghent University in Belgium and I would like to express my gratitude to Lode Daelemans for the fruitful work and great times in the laboratory. Many thanks also to the Interdisciplinary Centre for Electron Microscopy, especially to Grégoire Baroz and to the IMX workshop, especially to Pierre-André Despont, Yves Ruschetta and Werner Bronnimann for their endless technical help. A special thanks to Enrico Colla without whom "Rose" could not revive. The companies *Perstorp*, *Hexion* as well as *ZSK Technical Embroidery Systems* are also acknowledged for providing materials and materials manufacturing respectively. A warm thank you goes to all my students who contributed to this work: Ludovic Bescher, Alexandre Mordasini, Grégory Riesen, Aigoul Schreier, Nathan Hostettler, Tom Walet, Maxime Lagier, Malvina Pauchard, Jean-Baptiste Debrest and Charlie Ward.

The outcome of this thesis would not have been possible without all the former and actual colleagues/friends of LPAC/LTC. They provided an incredible work environment and I would like to thank them all for the advices, the help and the support they gave me. I would like to thank especially my self-healing mates Erica Manfredi for her incredible guidance in the early times of the project and Federica Sordo for the great times at conferences. A warm thank is then going to my office mates: Brennan for all the jokes, runs and travels; Florian for all the foolery we accomplished; Julien for all the great talks; Wouter for all the great souvenirs at conferences; Chloé and Anouk for your smiles. Thanks also to my PhD Italian mates Matteo and Damiano for all the great moments we shared during these four years. A special thank goes to Marina for the honour to lead the Sheriff task and Mathieu for leading this tough task with me. A warm thank also goes to all these members that became friends and with which I was able to share incredible moments.

I would like to thank all my friends who provided me constant support and with whom I can share incredible moments in the everyday life. Warm thanks also go to my family and especially to my Mum who supported me since ever and allowed me completing such an achievement. Finally, there are no sufficient words to thank Barbara; her love, help and support all these years made this work possible.

Abstract

Fibre-Reinforced Polymer (FRP) composite structures are subjected during service to low energy impacts or unexpected loads, leading to damage. Microcracks are generally first formed in the matrix and can reach up to several hundred microns in thickness. In many living systems, an initial self-sealing phase followed by self-healing of the original tissue leads to highly effective repair of minor damage events. A bio-inspired strategy for the efficient healing of microcracks in FRPs is hence to: (i) autonomously close cracks whose thickness is above a certain threshold to ensure better crack faces registry; (ii) use a healing matrix with structural properties close to that of a conventional FRP matrix, that is able to expand and fill the cracked regions repeatedly after multiple damage events. This strategy was investigated in the present work through (i) the use of Shape Memory Alloy wires (SMAs) as stitches in FRPs and (ii) a healing matrix based on thermoset-thermoplastic phase-separated blends. Blends composed of epoxy resin and different thermoplastics (PCL, PLA and PMMA) were evaluated for their potential as healing matrix, based on their room temperature toughness, stiffness and their capacity to heal when subjected to a moderate heating cycle. Three types of blend morphology resulted from polymerisation-induced phase separation during cure, depending on the thermoplastic content, including an interconnected particulate epoxy phase and a co-continuous thermoplastic phase at high thermoplastic contents. An optimal composition was found for epoxy-25vol%PCL blends. The PCL phase expands by 14% in volume upon melting at 150 °C, therefore enabling filling of small cracks. When further integrated to FRPs (with an adapted vacuum infusion moulding process), this healing matrix led to composites with similar stiffness and strength to that of pure epoxy composites, but also to full recovery of compression after impact strength for low damage extent (impacts of 8.5 J). To provide healing for larger damage extent, NiTiCu SMA wires, with a diameter of 150µm, were stitched in the dry fabric before processing. After damage and upon heating at 150 °C, SMA stitches, that have been stretched and partly debonded upon crack propagation, efficiently closed the cracks. This procedure demonstrated the capacity of the wires to close 200 µm thick cracks in the FRPs and led to fully heal impact damage events up to 17 J, corresponding to the main concern of maintenance activities in the composite industry (e.g. tools dropped from 1-2 m height). Finally, as an alternative to blends, PCL electrospun nanofibrous veils were interleaved into fabrics, infused with epoxy and cured to reach a microstructure combining both phase-separated domains as well as intact nanofibre regions. Interlaminar crack propagation demonstrated up to 48% toughness increase as compared to reference specimens. However, healing was prevented due to reduced flow of PCL in the fine channels resulting from phase separation, showing the limitation of this approach as compared to the use of blends and stitches. Phase-separated epoxy-PCL composites (with or without stitched SMA wires), considering their manufacturing feasibility through conventional industrial processes, their acceptable mechanical properties and their ability to fully heal low-velocity impact damage, demonstrated their relevance for composite structures that are subjected to moderate loads and not easily accessible to repair.

Keywords

Self-healing materials; Polycaprolactone; Phase separation; Fibre-reinforced polymers; Nanofibres; Fracture behaviour; Shape memory alloys; Crack closure; Mechanical properties; Vacuum infusion

Résumé

Les composites polymères renforcés de fibres (PRF) peuvent être soumis, lors de leur utilisation, à des impacts de faibles énergies ou des charges inattendues, endommageant le matériau. Des microfissures se forment dans le polymère entre les plis de renforts, qui peuvent atteindre plusieurs centaines de microns d'épaisseur. Afin d'éviter leur propagation qui peut conduire à une rupture catastrophique, une stratégie bio-inspirée pour réparer ces microfissures peut être formulée ainsi : (1) fermeture autonome des microfissures pour limiter leurs épaisseurs; (2) utilisation d'une matrice, structurellement équivalente aux matrices conventionnelles, qui peut se dilater jusqu'à un certain seuil pour remplir les fissures et les recoller. Cette stratégie a été déployée par (1) l'utilisation de fils d'alliage à mémoire de forme (AMF) comme couture dans les PRF et (2) une matrice de réparation basée sur une combinaison de polymères thermodurcissables et thermoplastiques obtenue par séparation de phase lors de la polymérisation. Des mélanges composés de résine Epoxy et de thermoplastiques (PCL, PLA, PMMA) ont été évalués comme matrices potentielles, en comparant la ténacité et la rigidité des mélanges à température ambiante ainsi que sur leurs capacités de réparation lors d'un traitement thermique. Pour les hautes teneurs en thermoplastique (>20% en volume), la morphologie du mélange se compose de particules interconnectées d'Epoxy entourées par une phase semi-continue de thermoplastique. Le mélange Epoxy-PCL contenant 25vol% de PCL s'est révélé un bon candidat pour l'auto-réparation, en termes de propriétés mécaniques. De plus, le PCL se dilate d'environ 14% en volume à 150°C, et coule dans les microfissures. Des PRF avec les mélanges Epoxy-PCL ont ensuite été fabriqués par injection de résine sous vide à haute température ; leurs résistances mécaniques sont similaires à celle des systèmes non-modifiés et recouvrent totalement leur résistance à la compression après impact à énergie modérée (8.5 Joules). Cette étude s'est ensuite intéressée à la réparation d'endommagements de plus grandes ampleurs ; pour cela, des fils d'AMF NiTiCu, de diamètre 150 µm, ont été cousus dans le renfort fibreux. Lors d'un endommagement, ces fils se déforment et déchaussent partiellement de la matrice ; chauffés, ils peuvent retrouver leur longueur initiale, ce qui permet de fermer la fissure. La fermeture de fissures d'environ 200 µm ainsi que l'accroissement de la ténacité d'environ trois fois a permis la réparation d'impacts jusqu'à 17 Joules, ce qui résout l'une des préoccupations majeures des activités de maintenance dans l'industrie du composite, telles que des chutes d'outils. Finalement, comme alternative aux mélanges Epoxy-PCL, des voiles de nanofibres de PCL ont été entrelacés dans les PRF, puis chauffés à des températures proches de celle de fusion du PCL pour obtenir une matrice tenace et réparable avec une microstructure combinant des domaines à séparation de phase et des régions de nanofibres intactes. La ténacité de ces systèmes a été augmentée jusqu'à 48% par rapport à des échantillons sans nanofibres. La réparation des fissures n'a cependant pu se faire du fait de l'écoulement limité du PCL visqueux dans la microstructure fine de particules d'Epoxy. Les PRF à matrice Epoxy-PCL (cousus ou non avec des fils AMF) forment cependant de bons candidats pour des structures composites exposées à des charges modérées mais difficiles d'accès pour la maintenance.

Mots-clés

Matériaux auto-réparant ; Polycaprolactone ; Séparation de phase ; Matériaux composites polymères renforcés de fibres ; Nanofibres ; Comportement à la rupture ; Alliages à mémoire de forme ; Propriétés mécaniques ; Infusion sous vide

Contents

Acknowledgements	i
Abstract	iii
Keywords	iii
Résumé	v
Mots-clés	v
List of Figures	xi
List of Tables	xxiii
List of Abbreviations	xxv
Chapter 1 Introduction and objectives	1
1.1 Motivation.....	1
1.2 Scope statement	2
1.3 Thesis Methodology and outline.....	4
Chapter 2 State of the art	5
2.1 Failure mechanisms and damage in FRPs	5
2.2 FRPs characterisation and healing efficiency assessment.....	9
2.2.1 Usual tests for FRPs characterisation and healing efficiency assessment	9
2.2.2 Interfacial shear strength determination.....	12
2.3 Traditional repair methods	17
2.4 Intrinsic self-healing	18
2.4.1 Healing of polymer interfaces before the self-healing concept.....	19
2.4.2 Self-healing through reversible covalent bonding	20
2.4.3 Self-healing through chain re-entanglement.....	21
2.4.4 Self-healing through non-covalent bonding	29
2.4.5 Integration to FRPs.....	30
2.5 Extrinsic self-healing.....	34
2.5.1 Vascular system	35
2.5.2 Microcapsule systems.....	36

Contents

2.6	Damage control in FRPs	40
2.6.1	Actuation system: Shape Memory Alloy (SMA) wires	40
2.6.2	Toughening	46
2.7	Conclusion	53
Chapter 3	Materials and Methods	55
3.1	Materials	55
3.1.1	Epoxy resins	55
3.1.2	Thermoplastics	55
3.1.3	Shape Memory Alloy (SMA) wires	55
3.1.4	E-glass fabric	55
3.1.5	Nanofibres	56
3.2	Specimens preparation	56
3.2.1	Preparation of the blends	56
3.2.2	SMA stitching procedure	57
3.2.3	Vacuum Assisted Resin Infusion Moulding (VARIM)	57
3.3	Characterisation methods	59
3.3.1	Morphological Characterisation	59
3.3.2	Thermomechanical characterisation	60
3.3.3	Interfacial characterisation	60
3.3.4	Tensile tests	63
3.3.5	Tapered Double Cantilever Beam (TDCB) tests	63
3.3.6	Flexural tests	64
3.3.7	Mode I Double Cantilever Beam (DCB) testing	64
3.3.8	Impact testing	65
3.3.9	C-scans	65
3.3.10	Damage recovery through optical analysis	66
3.3.11	Compression After Impact (CAI)	66
Chapter 4	Epoxy-thermoplastic blends	67
4.1	Assessment of potential epoxy-thermoplastic systems	67
4.1.1	Low molecular weight PCL	71
4.1.2	High molecular weight PCL	75
4.1.3	PLA	79
4.1.4	PMMA	83
4.1.5	Conclusion	86

Contents

4.2	Thermal mending in immiscible epoxy-PCL blends.....	88
4.2.1	Microstructural development in the blends.....	88
4.2.2	Thermal transitions in the cured blends.....	93
4.2.3	Mechanical properties.....	94
4.2.4	Conclusion.....	99
Chapter 5	E-glass epoxy-PCL blends.....	101
5.1	Thermal mending in E-glass reinforced epoxy-PCL blends.....	101
5.1.1	Microstructural development in the blends.....	101
5.1.2	Thermomechanical properties.....	103
5.1.3	Interfacial Shear Strength determination.....	104
5.1.4	Mode I Double Cantilever Beam Testing.....	105
5.1.5	Conclusion.....	109
5.2	Damage recovery after impact in E-glass reinforced epoxy-PCL blends.....	111
5.2.1	Impact testing.....	111
5.2.2	C-scans.....	114
5.2.3	Morphological characterisation.....	116
5.2.4	Compression After Impact (CAI).....	118
5.2.5	Healing efficiency comparison.....	119
5.2.6	Conclusion.....	120
Chapter 6	Stitched SMA wires for enhanced damage recovery of self-healing FRPs.....	121
6.1	Stitching design formulation.....	122
6.1.1	SMA wire characterisation.....	122
6.1.2	Interfacial behaviour of the SMA.....	123
6.2	Mode I Double Cantilever Beam Testing of SMA stitched composites.....	127
6.2.1	Fracture behaviour of composites containing stitched SMA wires.....	127
6.2.2	Crack closure and stiffness recovery.....	128
6.3	Impact damage of SMA stitched composites.....	132
6.3.1	Preliminary study.....	132
6.3.2	Impact testing.....	132
6.3.3	Impact damage recovery through optical analysis.....	134
6.3.4	Impact damage recovery through C-scan analysis.....	136
6.4	Conclusion.....	138
Chapter 7	Alternative methods for PCL introduction to FRPs.....	141
7.1	PCL microparticles introduction to FRPs.....	141

Contents

7.1.1	PCL microparticles production	141
7.1.2	Fracture properties in the virgin state	143
7.1.3	Fracture properties in the healed state	144
7.1.4	Conclusion.....	145
7.2	PCL nanofibre enhanced E-glass/epoxy composites	146
7.2.1	Phase separation in unreinforced epoxy-PCL nanofibre blends	147
7.2.2	Fracture properties of epoxy-PCL nanofibre composites	149
7.2.3	Healing efficiency assessment of epoxy-PCL nanofibre composites	152
7.2.4	Effect of nanofibre induced shrinkage on the bleeding mechanism	154
7.2.5	Size effect of the particle microstructure on the bleeding mechanism	155
7.2.6	Conclusion.....	157
Chapter 8	Cost modelling and industrial viability	159
8.1	Materials	160
8.2	Production line	160
8.3	Results	163
8.4	Conclusion and Industrial viability	164
Chapter 9	Conclusions	167
9.1	Outlook.....	171
Bibliography	173
Curriculum Vitae	189

List of Figures

Figure 1.1: Conceptual illustration of damage tolerance in self-healing composites [5].	2
Figure 1.2: Schematic drawing of the smart system aimed in the present study. An FRP containing (i) a healing matrix consisting of a thermoset-thermoplastic blend, (ii) stitched SMA wires to close cracks and (iii) thermoplastic nanofibres to be combined with the healing matrix in order to provide toughening. Inspired from [6].	3
Figure 1.3: Flow chart of the thesis.	4
Figure 2.1: Overview of ply-level failure modes [34].	6
Figure 2.2: Three general modes of fracture [50].	6
Figure 2.3: Comparison of fracture toughness for the three modes for G40-800/R6376 graphite-epoxy laminates [50].	6
Figure 2.4: Damage modes in polymer composites induced by indentation, impact, corrosive environments, ballistic punctures, surface scratching or fatigue loading [4].	7
Figure 2.5: The characteristic damage state of (A) $[0_n/90_m]_s$ laminate having symmetric microcracks and (B) $[90_m/0_n]_s$ laminate having antisymmetric microcracks [57].	8
Figure 2.6: Specimen geometries for mode I testing: a) TDCB [62], b) WTDCB [63], c) CT [64] and d) DCB [65].	10
Figure 2.7: A schematic shape of R-curve under large-scale fibre bridging [66].	11
Figure 2.8: (a) "Microbond" pull-out geometry [85]; (b) Equivalent concentric cylinder model for the embedded fibre zone of a single-fibre pull-out specimen [86].	13
Figure 2.9: Embedded fibre geometry for stress transfer determination [90].	14
Figure 2.10: Optical image of the indented fibre obtained by interrupting the test at increasing loads, showing the gradual fibre debonding [98].	15
Figure 2.11: Model systems considered for the measure of interfacial shear strength: (a) elasto-plastic indentation by a cone of fibre embedded in a cylinder of elastic matrix; (b) elastic indentation of a fibre in a matrix cylinder by a rigid flat punch; (c) elasto-plastic indentation by a cone of a body having the mechanical properties of bulk glass [96].	16
Figure 2.12: Extraction of a reduced indentation curve from a load/displacement curve: (a) indentation curve; (b) indentation of a bulk E-glass; (c) reduced indentation curve [96].	16
Figure 2.13: Schematic of typical repair schemes for an FRP: (a) simplistic external patch; (b) tapered scarf; (c) stepped-in repair [16].	17
Figure 2.14: Three main schemes for intrinsic self-healing: (1) Reversible bonding; (2) Chain re-entanglement; (3) Non-covalent healing [4].	18
Figure 2.15: Schematic diagram showing two random-coil chains on opposite crack surfaces during the five stages of healing: (a) rearrangement, (b) surface approach, (c) wetting, (d) diffusion to a distance χ , and diffusion to an equilibrium distance χ_∞ and randomization. Only one chain is shown for clarity. The dashed line represents the original crack plane [105].	20
Figure 2.16: Mending efficiency obtained by fracture toughness testing of compact tension test specimens [119].	21

Figure 2.17: Schematic illustration of the overall mechanism of thermal mending [7].	22
Figure 2.18: SEM images showing the bulk morphologies of fully cured epoxy-PCL(various wt%) blends of different compositions: (a) Epoxy-PCL(4.3), (b) Epoxy-PCL(11.5), (c) Epoxy-PCL(15.5), (d) Epoxy-PCL(27.0); (e) Epoxy-PCL(34.9) [7].	22
Figure 2.19: (a) Schematic illustration of DEB indicating its origin in differential thermal expansion between PCL and epoxy; (b) Visualisation of the fracture healing process demonstrating the DEB mechanism [7].	23
Figure 2.20: Chemical structure of DGEBA, PCL and DDS.	24
Figure 2.21: Nucleation and growth mechanism of Epoxy-PCL(9wt%) blends cured at 150 °C [135].	24
Figure 2.22: Spinodal decomposition mechanism of Epoxy-PCL(15wt%) blends cured at 150 °C [135].	24
Figure 2.23: Phase diagram of the conversion (P) vs weight fraction of PCL (w_1) [136].	25
Figure 2.24: Onset of phase separation for (a) DGEBA-PCL _{50,000} and (b) DGEBA-PCL _{5,000} blends at different isothermal cure temperature (T_{cure}) [142].	27
Figure 2.25: Optical microscopy images captured during the curing at 180 °C at the indicated time for 25 wt% PCL _{5,000} blends [142].	27
Figure 2.26: Transmission optical microscopy images of the EMAA particle embedded in epoxy resins (A) prior to post-curing at 150 °C and (B) after 5 min at 150 °C [178].	30
Figure 2.27: Schematic of the healing agent delivery mechanism utilised by the mendable epoxy resins containing EMAA particles [178].	30
Figure 2.28: Experimental interlaminar fracture toughness and short-beam-shear strength of modified carbon-epoxy prepreg with EMAA layers and comparison with theoretical constrained-layer fracture models [188].	33
Figure 2.29: Schematic representations of the 3D stitched network (a) before healing and (b) after healing in the carbon fibre-epoxy laminate [192].	34
Figure 2.30: Schematic representation of the self-healing delivery mechanism for the stitched laminate [192].	34
Figure 2.31: Approaches to extrinsic self-healing: (a) capsule-based systems where the healing agent is stored into capsules (blue is the resin and red the curing agent) until the crack ruptures these capsules which allows delivery of the healing agent into the crack plane; (b) vascular networks where the healing agent is stored into tubes or hollow fibres (blue resin and red curing agent) until the crack ruptures these tubes which allows delivery of the healing agent into the crack plane [4].	35
Figure 2.32: Life-cycle of a self-healing microvascular fibre-composite. Pristine woven composite laminate showing stacked textile reinforcement with dual-channel (red/blue), liquid filled vascular network. Delamination damage ruptures the internal vasculature leading to release of reactive liquid healing agents from fractured micro-channel orifices. Molecular diffusion and polymerisation (purple) of the healing agents leads to restoration of structural integrity over multiple healing cycles [202].	36
Figure 2.33: (left) The autonomic microcapsules healing concept. A microencapsulated healing agent is embedded in a structural composite matrix containing a catalyst capable of polymerising the healing agent. (a) Cracks form in the matrix wherever damage occurs; (b) the crack ruptures	

the microcapsules, releasing the healing agent into the crack plane through capillary action; (c) the healing agent contacts the catalyst, triggering polymerisation that bonds the crack faces closed. (right) SEM image showing rupture of the microcapsule inside the material fracture plane [203]..... 36

Figure 2.34: Typical DCB load-displacement curve for virgin and healed reference woven (8H satin weave E-glass/epoxy) specimens: A) crack propagation starts in the virgin specimen ahead the pre-crack (stick-slip behaviour); B) loading completed, mixture of DCPD/Grubbs is injected into the delamination, unloading and healing period in which the delamination is healed; C) crack propagation starts in the healed specimen (no stick-slip); D) crack has propagated till the extremity of the healed region; E) further loading creates a new virgin crack ahead of that propagated in the healed region [65]. 38

Figure 2.35: Performance map for self-healing materials. The data are organized according to the type of self-healing with shaded regions on the basis of data in the literature (plotted as discrete points). Each approach has demonstrated healing for different damage volume regimes. Intrinsic systems are relegated to small damage and can potentially heal at the molecular scale. Vascular systems have healed much larger damage volumes and can potentially extend the upper limit for self-healing systems. Capsule-based systems span the gap between intrinsic and vascular approaches [4]. 40

Figure 2.36: (Left) Actuation energy density diagram indicating typical ranges of actuation stress, actuation strain, and the actuation energy densities (dotted lines) of different active materials that exhibit direct coupling. (Right) Actuation frequency diagram comparing the actuation frequency ranges of different active materials that exhibit direct coupling [223]. 41

Figure 2.37: Stress-strain-temperature data exhibiting the shape memory effect for a typical NiTi SMA [223]. 42

Figure 2.38: Crack toughening mechanisms in rubber-filled modified polymers: (1) shear band formation near rubber particles; (2) fracture of rubber particles after cavitation; (3) stretching, (4) debonding and (5) tearing of rubber particles; (6) transparticle fracture; (7) debonding of hard particles; (8) crack deflection by hard particles; (9) voided/cavitated rubber particles; (10) crazing; (11) plastic zone at craze tip; (12) diffuse shear yielding; (13) shear band/craze interaction [55]. 47

Figure 2.39: Schematic representations of the process zone in front of the crack tip: (a) usual case where the process zone size is of the same order as the inter-particle size; (b) detrimental case because the process zone encompasses a large number of particles in front of the crack tip [245]. .. 48

Figure 2.40: Schematic illustration of the basic setup for electrospinning. The insets show a drawing of the electrified Taylor cone and a typical SEM image of the nonwoven mat of poly(vinyl pyrrolidone) nanofibres deposited on the collector [260]. 49

Figure 2.41: Schematic illustration of the delamination path in a nanofibre interleaved laminate under Mode I and Mode II loading conditions [11]. 51

Figure 2.42: SEM images of composite fracture surface (a) un-toughened and (b) toughened by 5 wt% PSF nanofibrous membranes [270]..... 52

Figure 3.1: SEM micrograph of a typical nanofibre veil obtained through electrospinning. 56

Figure 3.2: Illustration of (a) the stitching process on the stacked preform and (b) the dry preform after stitching..... 57

Figure 3.3: Schematic top view of the VARIM layout to produce DCB specimens (a) without stitched SMA wires and (b) with stitched SMA wires. The drawings include the fibre preform

(grey), the flow medium (grey mesh), the release film (blue), the inlet and outlet lines. Note that the release film lies on the eighth ply, but is shown at the top for clarity. The geometry of DCB specimens is also showed. In (b), SMA stitched lines are represented in dashed brown lines and were not lying on the entire plate height in order to produce control specimens. Dimensions are in mm. Adapted from [216]. 58

Figure 3.4: Schematic top view of the VARIM layout to produce impact specimens (a) without stitched SMA wires and (b) with stitched SMA wires. In (a), the drawing includes the fibre preform (grey), the flow medium (grey mesh), the inlet and outlet lines. In (b), the drawing includes the fibre preform (grey) and the SMA stitched lines; for clarity the flow mesh was not represented but lies at the same place as in (a). Dimensions are in mm. 58

Figure 3.5: Schematics of the used geometries for pull-out testing and the corresponding embedded lengths for (a) straight and (b) loop specimens. 61

Figure 3.6: Indentation test on an epoxy composite specimen: (a) Determination of the reduced curve from the initial indentation curve and that in a soda lime glass, fitted with Eq. (2.12) for the linear part and Eq. (2.13) for the non-linear part. Unloading portions of the tests are not shown for clarity; (b) corresponding indentation imprint on the fibre. 62

Figure 3.7: Contact angle measurement procedure. 62

Figure 3.8: Typical loading and unloading cycles for a DCB test (free of SMA wires) in the virgin state and in the healed. 65

Figure 4.1: PCL volume expansion in the liquid state, as a function of temperature. 69

Figure 4.2: Estimate of conversions corresponding to spinodal curves for five thermoplastics: (i) PCL similar to Luo *et al.* [7] ($M_n \approx 45,000$ g/mol); (ii) PCL low molecular weight ($M_n \approx 10,000$ g/mol); (iii) PCL high molecular weight ($M_n \approx 80,000$ g/mol); (iv) PMMA and (v) PLA; as a function of the thermoplastic volume fraction for $\chi=0.12$ according to the *Flory-Huggins* equation. 71

Figure 4.3: Blend morphology as a function of PCL ($M_n \approx 10,000$ g/mol) volume fraction (*Epoxy-PCL(various vol%)*). (a) Optical microscopy images; (b) Scanning electron microscopy images (fracture surfaces from tensile tests). 72

Figure 4.4: DSC heating scans for the different epoxy-PCL ($M_n \approx 10,000$ g/mol) blends after cure. 73

Figure 4.5: E' determined by DMA as a function of the PCL ($M_n \approx 10,000$ g/mol) volume fraction at room temperature and the healing temperature (150 °C). 73

Figure 4.6: (a) Maximum stress, (b) Young's Modulus and (c) strain to failure as a function of the PCL ($M_n \approx 10,000$ g/mol) volume fraction. 74

Figure 4.7: K_{IC} as a function of the PCL ($M_n \approx 10,000$ g/mol) volume fraction. 75

Figure 4.8: Blend morphology as a function of PCL ($M_n \approx 80,000$ g/mol) volume fraction (*Epoxy-PCL(various vol%)*). (a) Optical microscopy images; (b) Scanning electron microscopy images (fracture surfaces from tensile tests). 76

Figure 4.9: DSC heating scans for the different epoxy-PCL ($M_n \approx 80,000$ g/mol) blends after cure. 76

Figure 4.10: E' determined by DMA as a function of the PCL ($M_n \approx 80,000$ g/mol) volume fraction at room temperature and the healing temperature (150 °C). 77

Figure 4.11: (a) Maximum stress, (b) Young's Modulus and (c) strain to failure as a function of the PCL ($M_n \approx 80,000$ g/mol) volume fraction. 77

Figure 4.12: K_{IC} as a function of the PCL ($M_n \approx 80,000$ g/mol) volume fraction. 79

Figure 4.13: Schematic of the phase-separated structure containing epoxy-interconnected particles with a surrounding PCL matrix. When a crack propagates through the structure, different modes of failure arise and are detailed in the right close up look. The PCL plastic zone size to illustrate its premature rupture is also shown, but underestimated for the sake of the drawing.	79
Figure 4.14: Blend morphology as a function of PLA volume fraction (<i>Epoxy-PLA(various vol%)</i>). (a) Optical microscopy images; (b) Scanning electron microscopy images (fracture surfaces from tensile tests).....	80
Figure 4.15: DSC heating scans for the different epoxy-PLA blends after cure.	81
Figure 4.16: E' determined by DMA as a function of the PLA volume fraction at room temperature and the healing temperature (160 °C).	81
Figure 4.17: (a) Maximum stress, (b) Young's Modulus and (c) strain to failure as a function of the PLA volume fraction.	82
Figure 4.18: K_{IC} as a function of the PLA volume fraction.	83
Figure 4.19: Blend morphology as a function of PMMA volume fraction (<i>Epoxy-PMMA(various vol%)</i>). (a) Optical microscopy images; (b) Scanning electron microscopy images (fracture surfaces from tensile tests).	84
Figure 4.20: DSC heating scans for the different epoxy-PMMA blends after cure.	84
Figure 4.21: E' determined by DMA as a function of the PMMA volume fraction at room temperature and the healing temperature (150 °C).	85
Figure 4.22: (a) Maximum stress, (b) Young's Modulus and (c) strain to failure as a function of the PMMA volume fraction.	85
Figure 4.23: K_{IC} as a function of the PMMA volume fraction.	86
Figure 4.24: Maximum stress for the different epoxy-thermoplastic blends highlighted as best for thermal mending, along with the corresponding healing efficiency measured by means of TDCB tests. Pure epoxy and epoxy-PCL blends similar to Luo <i>et al.</i> [7] are also shown. For epoxy-PCL blends, the PCL molecular weight is provided to differentiate the blends.	87
Figure 4.25: Evolution of the microstructure of <i>Epoxy-PCL(21.3)</i> as a function of cure time at a nominal temperature of 180 °C.	89
Figure 4.26: Isothermal DSC heat flow curves at 180 °C for the different blends. The dashed circles indicate the times corresponding to the onset of phase separation.	89
Figure 4.27: Time for phase separation determined from DSC heat flow curves (cf. Figure 4.26) and times to reach the cloud-point determined by optical microscopy as a function of the PCL volume fraction at a nominal temperature of 180 °C.	89
Figure 4.28: Estimates of conversions corresponding to spinodal and binodal curves as a function of the PCL volume fraction for $\chi = 0.12$ according to the <i>Flory-Huggins</i> equation (see section 2.4.3.1), along with experimental data points for the conversion at onset of phase separation.	90
Figure 4.29: Morphology at different compositions for: (a) <i>Epon™ 828 EL (Momentive)</i> resin; (b) <i>DGEBA (Sigma)</i> resin.	91
Figure 4.30: Average epoxy particle diameter in microtomed sections as a function of the PCL volume fraction.	91

Figure 4.31: SEM image of <i>Epoxy-PCL(19.5)</i> at the interface between the coarse co-continuous domains visible in the corresponding optical micrograph in Figure 4.29.	92
Figure 4.32: FTIR spectra in the carbonyl stretch band (wavenumbers 1680-1780 cm^{-1}) from selected regions of (a) <i>Epoxy-PCL(25.0)</i> and (b) <i>Epoxy-PCL(17.7)</i> blends. Spectra for the pure epoxy and pure PCL are also shown for comparison.	93
Figure 4.33: DSC heating (a) and cooling (b) scans for the different blends after cure.	93
Figure 4.34: Crystallinity degree of the PCL phase within phase-separated blends after 3 h curing, as a function of the PCL volume fraction. Pure PCL as received and with 3h curing are also shown for comparison.	94
Figure 4.35: DMA results: (a) transition temperatures as a function of the PCL volume fraction. (b) E' as a function of the PCL volume fraction at room temperature and the healing temperature (150 °C), along with upper and lower bound predictions for E' as indicated.	95
Figure 4.36: (a) Maximum stress, (b) strain-to-failure and (c) Young's Modulus as a function of the PCL volume fraction.	96
Figure 4.37: SEM image of the tensile fracture surfaces for (a) <i>Epoxy-PCL(13.1)</i> ; (b) <i>Epoxy-PCL(17.7)</i> and (c) <i>Epoxy-PCL(25.0)</i>	96
Figure 4.38: K_{IC} as a function of the PCL volume fraction.	97
Figure 4.39: Reflected light optical microscopy of (a) a crack after testing and (b) the same crack after healing at 150 °C for 30 minutes.	98
Figure 4.40: Healing efficiency as a function of the PCL volume fraction for an applied stress of 50 kPa during healing.	98
Figure 4.41: Multiple healing assessment for <i>Epoxy-PCL(25.0)</i> and <i>Epoxy-PCL(26.9)</i>	98
Figure 5.1: Evolution of the microstructure of <i>PCL(25)</i> in presence of glass fibres as a function of cure time at a nominal temperature of 180 °C.	102
Figure 5.2: Transverse cut of the three assessed systems: (a) <i>Plain</i> ; (b) <i>PCL(25)</i> ; (c) <i>PCL(37)</i> . A schematic of the structure is drawn on the right of each image.	103
Figure 5.3: DSC heating scans for the different specimens after cure.	103
Figure 5.4: E' and $\text{Tan } \delta$ as a function of temperature for the three assessed specimens: <i>Plain</i> , <i>PCL(25)</i> and <i>PCL(37)</i>	104
Figure 5.5: Interfacial shear strength for the three assessed systems.	105
Figure 5.6: Interlaminar fracture toughness, G_{IC} , as a function of the PCL volume fraction in the matrix.	106
Figure 5.7: Multiple healing assessment in terms of stiffness based calculation for <i>PCL(25)</i> and <i>PCL(37)</i>	106
Figure 5.8: Multiple healing assessment in terms of interlaminar fracture toughness based calculation for <i>PCL(25)</i> and <i>PCL(37)</i>	107
Figure 5.9: (a) R-curve behaviour for unmodified (<i>Plain</i>) and modified (<i>PCL(25)</i> and <i>PCL(37)</i>) FRPs, as well as modified FRPs after thermal mending at 150 °C for 30 minutes (<i>PCL(25) healed</i> and <i>PCL(37) healed</i>); (b) Crack thickness as a function of the crack length during healing of a <i>PCL(25)</i> specimen, superimposed with its R-curve behaviour in the healed state.	108

Figure 5.10: SEM image of a DCB fracture surface for (a) <i>PCL(25)</i> specimen after a virgin cycle; (b) <i>PCL(25)</i> after one healing cycle and (c) <i>PCL(37)</i> after three healing cycles.	109
Figure 5.11: Impact force and energy as a function of time for three different impact energies, for (a) <i>Plain</i> system and (b) <i>PCL(25)</i> system.	112
Figure 5.12: Dissipated energy during impact as a function of the impact energy, for <i>Plain</i> as well as <i>PCL(25)</i> systems.	113
Figure 5.13: Impact force as a function of the deflection response for <i>Plain</i> and <i>PCL(25)</i> systems as well as three impact energies: 34, 17 and 8.5 J.	113
Figure 5.14: Front face optical image of <i>PCL(25)</i> specimens after impact (<i>Damaged</i>) and after a thermal mending cycle of 30 minutes at 150 °C (<i>Healed</i>) for three impact energies: 34, 17 and 8.5 J.	114
Figure 5.15: Damage area measured by C-scan analysis as a function of the impact energy, for <i>Plain</i> as well as <i>PCL(25)</i> systems.	115
Figure 5.16: C-scan images of <i>PCL(25)</i> specimens after impact (<i>Damaged</i>) and after a thermal mending cycle of 30 minutes at 150 °C (<i>Healed</i>) for three impact energies: 34, 17 and 8.5 J.	115
Figure 5.17: Transverse cut optical microscopy mapping of <i>PCL(25)</i> system impacted at energies of 8.5, 17 and 34 J.	116
Figure 5.18: Crack thickness distribution corresponding to the optical microscopy mapping of Figure 5.17.	117
Figure 5.19: PCL expansion thickness on the free surfaces of a heated element with varying area to volume ratio for epoxy-PCL(25) blends as <i>Pure resin</i> or in the <i>Composite</i> (with $V_f=50\%$). The top scale links the area to volume ratio to the example of a cubic element with varying volume.	117
Figure 5.20: Compressive residual strength as a function of the impact energy for <i>Plain</i> , <i>PCL(25)</i> in the damaged state and <i>PCL(25)</i> in the healed state.	118
Figure 5.21: Back face optical image of CAI specimens from the <i>PCL(25)</i> system impacted at 8.5 J (a) not healed and (b) healed.	119
Figure 5.22: Healing efficiency as a function of the impact energy, for three characterisation techniques: (i) damage area determined by C-scan; (ii) compression after impact tests; (iii) crack thickness distribution by optical microscopy observations.	119
Figure 6.1: Illustration of the proposed healing system and its process to efficiently close and heal cracks.	122
Figure 6.2: DSC heating and cooling scans for NiTiCu SMA wire. Martensite and Austenite characteristic temperatures are also indicated in the graph.	122
Figure 6.3: (a) SEM image of a fractured pull-out specimen prepared from <i>Epoxy-PCL</i> ; (b) SEM image of a pull-out specimen prepared from <i>Epoxy-PCL</i> in which the wire has been removed and the morphology provides an indication of the stress distribution in the loop geometry (a region of compressive deformation is circled in green and a region of tensile deformation is circled in red); (c) SEM image from the top surface of a pull-out specimen prepared from <i>Epoxy-PCL</i> showing matrix material drawn out of the specimen by the wire during testing.	124
Figure 6.4: Typical force-displacement curves during a pull-out test. (a) Straight and loops geometries in pure <i>Epoxy</i> ; (b) Straight and loops geometries in <i>Epoxy-PCL</i> blends. The embedded length was 3 mm for every represented curve.	124

List of Figures

Figure 6.5: Apparent IFSS as a function of the interfacial shear strength for different matrices and (a) straight SMA wires; (b) SMA loops. 125

Figure 6.6: Intrinsic IFSS for (a) straight specimens; (b) loop specimens..... 126

Figure 6.7: Apparent IFSS for straight and loop specimens and the corresponding geometrical IFSS as a function of the embedded length for *Epoxy* specimens..... 126

Figure 6.8: (a) SEM image of the cross-section of a polished specimen of an *Epoxy-PCL* blend containing glass fibre reinforcement; the pink areas indicate the presence of Si (determined by EDX analysis) and hence the location of the glass fibres. (b) Optical microscopy image of a polished specimen containing glass fibre reinforcement, *Epoxy* resin and an SMA wire inserted with the loop geometry (the dashed line indicates the trajectory of the wire). 127

Figure 6.9: (a) Typical loading-unloading curve from a DCB test on *GF-Epoxy* in the presence of SMA wires; (b) Typical R-curves from DCB tests on *GF-Epoxy* and *GF-Epoxy-PCL* in the presence of SMA wires; (c) *GF-Epoxy* DCB specimen after crack propagation over a distance of 4 cm showing breakage of the SMA wires. 128

Figure 6.10: (a) Optical micrographs of the crack in a *GF-Epoxy* DCB specimen: (top) after damage; (bottom) after damage and healing at 150 °C for 30 minutes. Separation of the crack faces as a function of crack length in *GF-Epoxy-PCL* after damage (in black) and after damage and healing (in red) for (b) specimens stitched with SMA wires, whose positions are indicated by the dashed lines, and (c) specimens without stitched SMA wires. The original data for the separation of the crack faces, also shown in the figure, were fitted using a standard Boltzmann procedure with a 95% confidence band..... 129

Figure 6.11: (a) Optical micrographs of the crack in a *GF-Epoxy-PCL* DCB specimen: (top) after damage; (bottom) after damage and healing at 150 °C for 30 minutes. Separation of the crack faces as a function of crack length in *GF-Epoxy-PCL* after damage (in black) and after damage and healing (in red) for (b) specimens stitched with SMA wires, whose positions are indicated by the dashed lines, and (c) specimens without stitched SMA wires. The original data for the separation of the crack faces, also shown in the figure, were fitted using a standard Boltzmann procedure with a 95% confidence band..... 130

Figure 6.12: (a) Optical micrograph of an interply crack in a *GF-Epoxy-PCL* DCB specimen: after crack propagation (top); after crack propagation followed by healing at 150 °C for 30 minutes (bottom). Separation of the crack faces as a function of crack length in *GF-Epoxy-PCL* specimens after crack propagation (black) and after crack propagation and healing (red) in: (b) specimens stitched with SMA wires (the dashed lines indicate the position of the SMA wires); (c) specimens without SMA wires. The results in (b) and (c) are for specimens subjected to three successive damage and healed cycles. During healing, the specimens were clamped at the loading points. The original data for the separation of the crack faces, also shown in the figure, were fitted using a standard Boltzmann procedure with a 95% confidence band. 131

Figure 6.13: Loading and unloading cycles for DCB specimens in the virgin and healed states: (a) *GF-Epoxy-PCL* stitched with SMA wires, (b) *GF-Epoxy-PCL* without SMA wires. The cycles shown for healed specimens were obtained after three successive damage and healing cycles. 131

Figure 6.14: Binarized optical images of impacted specimens made of epoxy-DETA resin, at impact energies of (a) 34, (b) 17 and (c) 8.5 J. Images are shown before (*virgin*) and after (*heat treated*) a thermal mending cycle of 30 minutes at 150 °C. 132

Figure 6.15: Impact force and energy as a function of time for three different impact energies, for (a) *GF-Epoxy* specimens and (b) *GF-Epoxy-PCL* specimens. 133

Figure 6.16: Back face optical image of *GF-Epoxy* specimens impacted at 34 J energy: (a) impact on an SMA stitched line and (b) impact in between two SMA stitched lines. 134

Figure 6.17: Binarized optical image of impacted *GF-Epoxy* specimens, at nominal impact energies of (a) 34, (b) 17 and (c) 8.5 J. Images are shown before (*virgin*) and after (*heat treated*) a thermal mending cycle of 30 minutes at 150 °C. 135

Figure 6.18: Front face optical image of impacted *GF-Epoxy-PCL* specimens, at impact energies of (a) 34, (b) 17 and (c) 8.5 J. Images are shown before (*virgin*) and after (*heat treated*) a thermal mending cycle of 30 minutes at 150 °C. 135

Figure 6.19: Damage area measured by C-scan analysis as a function of the impact energy, for *GF-Epoxy-PCL* (named *Plain SMA*) and *GF-Epoxy* (named *PCL SMA*) SMA stitched FRPs, and compared to the ones for *Plain* and *PCL(25)* FRPs without SMA wires determined in section 5.2. 136

Figure 6.20: C-scan images of *GF-Epoxy-PCL* FRP specimens containing SMA wires after impact (*Damaged*) and after impact followed by a thermal mending cycle of 30 minutes at 150 °C (*Healed*) for impact energies of 34, 17 and 8.5 J. 137

Figure 6.21: Comparison of damage area recovery in composites containing stitched SMA wires (*GF-Epoxy-SMA stitched*, *GF-Epoxy-PCL-SMA stitched*) and composites without SMA wires (*GF-Epoxy-PCL-no SMA*, from section 5.2), for three different impact energies. 138

Figure 7.1: Optical microscopy of PCL microparticles prepared by an oil-in-water solvent evaporation technique after sieving in the range 125-250 µm. 142

Figure 7.2: Heat flow curves for: (i) PCL pellets, as manufactured, (ii) PCL microparticles after oil-in-water solvent evaporation (PCL microparticles), (iii) PCL microparticles after oil-in-water solvent evaporation tuned with octanol (PCL microparticles (octanol)). 143

Figure 7.3: Interlaminar fracture toughness for specimens tested in Mode I, as a function of the local capsule weight fraction. 143

Figure 7.4: Typical DCB curves showing the loading/unloading cycles of virgin and healed composite specimens, typical specimen modified with PCL particles 30 wt%. 144

Figure 7.5: SEM image of the crack face of a specimen containing 30 wt% PCL particles over the ply matrix. Prior to imaging, the specimen has been tested, healed and re-tested. 145

Figure 7.6: DSC heating scans for the different blends after cure. PCL volumetric ratio is shown in brackets and the curing temperatures are also indicated. 147

Figure 7.7: Micrographic map of PCL nanofibres (20 vol%) in epoxy resin cured at 60 °C for 24h and post-cured for 15h at 80 °C. Close up on the right showing the transition between two phase-separated morphologies. 148

Figure 7.8: PCL nanofibres (20 vol%) in epoxy resin cured at 60 °C for 24h and post-cured at 80 °C for 15h. (a) Overall surface; (b) close up showing the complex phase-separated morphology; (c) close up showing large epoxy particles in PCL matrix and (d) close up showing smaller epoxy particles in PCL matrix. 148

Figure 7.9: Interlaminar fracture toughness for the different assessed composites. See Table 7.2 for details on specimens naming. 150

Figure 7.10: Virgin fracture surface of a nanofibre enhanced composite sample cured at room temperature (i.e. *GF-Epoxy-NF-RT*). 150

Figure 7.11: Virgin fracture surface of a nanofibre enhanced composite specimen cured at 60 °C (i.e. *GF-Epoxy-NF-60*). (a) low magnification image showing three distinct regions; (b) close up of the domain-like morphology; (c) close up of the morphology consisting of epoxy matrix with PCL particles and (d) close up of the morphology consisting of epoxy particles with a surrounding PCL matrix..... 151

Figure 7.12: Virgin fracture surface of a nanofibre enhanced composite specimen cured at 80 °C (i.e. *GF-Epoxy-NF-80*). Close up on the right to show the domain-like morphology. 152

Figure 7.13: Typical DCB curves showing the loading/unloading cycles of virgin and healed composite specimen, example of a *GF-Epoxy-NF-60* specimen. 152

Figure 7.14: Healed fracture surface of a nanofibre enhanced composite specimen cured at 60 °C (i.e. *GF-Epoxy-NF-60*) showing the morphology consisting of epoxy particles with a surrounding PCL matrix. 153

Figure 7.15: (a) Polished cross-section optical micrograph of a nanofibre enhanced composite specimen cured at 60 °C (i.e. *GF-Epoxy-NF-60*) showing phase separation on the entire specimen thickness and away from the crack path (shown at the bottom). (b) Close up of the same specimen..... 154

Figure 7.16: Healed fracture surface of a nanofibre enhanced composite specimen cured at 60 °C with 60 gsm nanofibres in between each fabric layer (i.e. *GF-Epoxy-NF60-60*) showing the morphology consisting of epoxy particles with a surrounding matrix..... 154

Figure 7.17: Corresponding healed fracture surface of the nanofibre enhanced composite specimen cured at 60 °C (i.e. *GF-Epoxy-NF-60*) shown previously in Figure 7.11. 154

Figure 7.18: Nanofibrous veils (a) before and (b) after heating at 60 °C for 1h. (c) Corresponding cycle in DMA tension test. 155

Figure 7.19: Comparison of sample strain as a function of temperature for epoxy-PCL nanofibre blends and the corresponding pure epoxy (*Pure epoxy RIM 135* and *Epoxy RIM 135/PCL*) with samples processed in section 4.2 (*Pure epoxy Epon 828* and *Epoxy Epon 828/PCL*). Slope of the pseudo linear plateau between the two arrows for each specimen is also showed..... 156

Figure 7.20: PCL flow time, calculated with Eq. (7.1), through a porous medium of 2.5 mm thickness as a function of the media particle diameter and for two different PCL viscosities. Arrows show two specific cases: (i) systems studied in the present section and (ii) systems studied throughout Chapter 4 to Chapter 6. 157

Figure 8.1: Reference part with 2.5 mm thickness. 160

Figure 8.2: Plant diagram for production of 12,500 parts per year. (1) Ultrasonic cutting machine; (2) Buffer; (3) Waste buffer; (4) IR oven; (5) Preforming press; (6) Buffer; (7) RTM press with thermoset injection machine; (8) Buffer; (9) Post-cure oven; (10) Trimming cell; (11) shipping. Arrows indicate the flow of production. [328] 161

Figure 8.3: Production cost per part as a function of the number of parts produced per year: for *Scenarios 1 to 4*. *Scenarios 3 and 4* are also shown for stitching only on 30% of the part surface (named part SMA)..... 163

Figure 8.4: Cost per part for a production rate of 10,000 and 100,000 parts per year. For *Scenario 4* where only 30% of the part surface is stitched with SMA wires (i.e. *Scenario 4 part SMA*)..... 164

Figure 8.5: (a) schematic of the embroidery principle, both threads are SMAs in the present case; (b) dry E-glass preform after embroidery. 165

List of Figures

Figure 9.1: Performance map for self-healing materials. The data are organized according to the type of self-healing with shaded regions on the basis of data in the literature (plotted as discrete points). Each approach has demonstrated healing for different damage volume regimes. Intrinsic systems are relegated to small damage and can potentially heal at the molecular scale. Vascular systems have healed much larger damage volumes and can potentially extend the upper limit for self-healing systems. Capsule-based systems span the gap between intrinsic and vascular approaches. The use of epoxy-PCL blends in combination to stitched SMA wires in FRPs has the ability to cover the entire range of damage events that can be healed with most of the existing healing systems. Adapted from [4]. 169

Figure 9.2: Interlaminar fracture toughness as a function of the corresponding healing efficiency in Mode I DCB testing (after thermal treatment at 150 °C for 30 minutes) for all the epoxy-PCL combination systems studied in the present work and integrated to FRPs (E-glass woven fabric). The two red regions show the healing efficiency for the corresponding system at the base of the arrow after impact loading of 8.5 or 17 J. The region shown for each system represents the standard deviation. Epoxy/E-glass woven fabric baseline is also shown as a threshold for design requirements, obviously the healing efficiency of this system is null. 171

List of Tables

Table 2.1: Some typical properties of binary Ni-Ti shape-memory alloys [226].	43
Table 3.1: Materials properties for IFSS determination.	61
Table 4.1: Intrinsic properties of epoxy and PCL ($M_n \approx 42,500\text{-}45,000$ g/mol).	68
Table 4.2: Specimen designations and the corresponding mass ratios of epoxy resin to PCL ($M_n \approx 10,000$ g/mol), and the overall PCL weight and volume fractions after addition of the DDS.	72
Table 4.3: Specimen designations and the corresponding mass ratios of epoxy resin to PCL ($M_n \approx 80,000$ g/mol), and the overall PCL weight and volume fractions after addition of the DDS.	75
Table 4.4: Specimen designations and the corresponding mass ratios of epoxy resin to PLA, and the overall PLA weight and volume fractions after addition of the DDS.	80
Table 4.5: Specimen designations and the corresponding mass ratios of epoxy resin to PMMA, and the overall PMMA weight and volume fractions after addition of the DDS.	83
Table 4.6: Specimen designations and the corresponding mass ratios of epoxy resin to PCL, and the overall PCL weight and volume fractions after addition of the DDS.	88
Table 5.1: Specimen designations and the corresponding mass ratios of epoxy resin to PCL, and the overall PCL volume fractions after addition of the DDS. Fibre volume fraction obtained after composite production is also given.	101
Table 6.1: NiTiCu wire characteristic transition temperatures determined by DSC.	123
Table 6.2: Maximum load (F_{\max}) and dissipated energy (E_{diss}) during impact at three nominal energies (34, 17 and 8.5 J) for <i>GF-Epoxy</i> and <i>GF-Epoxy-PCL</i> specimens.	134
Table 7.1: Mode I interlaminar fracture toughness values of specimens containing 0, 15, 30 wt% PCL microparticles over the local ply matrix. Relative fibre volume fractions are also indicated.	144
Table 7.2: Specimen designations, composition, curing conditions and the corresponding fibre volume fraction obtained after composite production as well as nanofibre (NF) volume fraction with respect to the matrix.	147
Table 8.1: Material costs and weights according to the defined geometry (Figure 8.1). For scenarios with 30% of SMA, the cost of SMAs is simply multiplied by 30%.	160
Table 8.2: Price, power and surface for each machine of the three different units defined in Figure 8.2. These parameters are also defined for additional machines to produce parts for <i>Scenarios 2-3-4</i> . Cycle time needed for each unit is also given.	162
Table 8.3: Various fixed parameters for the overall cost calculation.	162

List of Abbreviations

Abbreviation	Description
ABS	Acrylonitrile butadiene styrene
A_f	Austenite finish temperature
A_s	Austenite start temperature
BAPP	Bis[4-(4-aminophenoxy)phenyl]propane
CAI	Compression After Impact
CT	Compact tension
DA	Diels-Alder
DCB	Double Cantilever Beam
DCM	Dichloromethane
DCPD	Dicyclopentadiene
DDS	4,4'-diaminodiphenyl sulfone
DEB	Differential Expansive Bleeding
DETA	Diethylenetriamine
DGEBA	Diglycidyl ether bisphenol A
DMA	Dynamic Mechanical Analysis
DSC	Differential Scanning Calorimetry
E	Young's Modulus
E'	Storage Modulus
EMA	Ethylene maleic copolymer
EMAA	Polyethylene-co-methacrylic acid
EVA	Ethylene vinyl acetate
$f^{damaged}$	Property in the damaged state
f^{healed}	Property in the healed state
f^{virgin}	Property in the virgin state
FPZ	Fracture Process Zone
FRP	Fibre-reinforced Polymer
FTIR	Fourier Transform Infrared Spectroscopy
G_{IC}	Strain energy release rate or interlaminar fracture toughness
IFSS	Interfacial Shear Strength
K_{IC}	Fracture toughness
MCDEA	4,4'-methylenebis(3-chloro-2,6-diethylaniline)
MF	Melamine-Formaldehyde
M_f	Martensite finish temperature
M_n	Number average molar mass
MOCA	4,4'-methylenebis(2-chloroaniline)
M_s	Martensite start temperature
M_w	Mass average molar mass
n	Packing parameter
P	Curing conversion
PA6	Polyamide 6
PAI	Polyamide-imide
PAN	Polyacrilonytrile
PBAE, PBE	Poly(bisphenol A-co-epichlorohydrin)
P_c	Peak load
PCL	Poly(ϵ -caprolactone)

List of Abbreviations

P_d	Load at debonding
PDGEBA	Poly(bisphenol-A-co-epichlorohydrin)
PDGEBA	Poly(bisphenol-A-co-epichlorohydrin)
PE	Polyethylene
PEGMA	Polyethylene-co-glycidyl methacrylate
PEI	Polyetherimide
PEK	Polyetherketone
PES	Poly(ether sulfone)
PI	Polyimide
PLA	Poly(lactic acid)
PMMA	Poly(methyl methacrylate)
PP	Polypropylene
PPE	Poly(2,6-dimethyl-1,4-phenylene ether)
PS	Polystyrene
PSF, PSU	Polysulfone
PU	Polyurethane
PVA	Polyvinyl alcohol
PVB	Polyvinyl butyral
PVC	Polyvinyl chloride
PVDF	Poly(vinylidene fluoride)
ROMP	Ring-Opening Metathesis Polymerisation
RTM	Resin Transfer Moulding
SALLS	Small Angle Laser Light Scattering
SDS	Sodium Dodecyl Sulphate
SEM	Scanning Electron Microscopy
SENB	Single Edge Notched Bend
SMA	Shape Memory Alloy
T_c	Crystallisation temperature
TDCB	Tapered Double Cantilever Beam
TETA	Triethyltetramine
T_g	Glass transition temperature
T_m	Melting temperature
TPU	Thermoplastic polyurethane
TTT	time-temperature-transformation
UF	Urea-Formaldehyde
UTM	Universal Testing Machine
V_f	Fibre volume fraction
WTDCB	Width Tapered Double Cantilever Beam
η	Healing efficiency
λ	Fatigue life extension
ν	Poisson's ratio
τ_a	Apparent interfacial shear strength
τ_i	Intrinsic interfacial shear strength
τ_s	Interfacial shear strength

Chapter 1 Introduction and objectives

1.1 Motivation

The current structural product market needs high strength materials with low weight to reach high efficiency and limit energy consumption in transport and other industrial applications. In that scope, composite materials are increasingly used for many different applications such as aerospace, car manufacturing or sport equipment. Composite materials are by definition engineering or natural materials made from two or more constituents, each with different physical and chemical properties. In this field, Fibre-Reinforced Polymers (FRPs) dominate and are made of a matrix, a rather weak material used as protection and to transfer loads; and a reinforcement, a strong material that in general cannot be used separately due to its brittleness, and is often under the form of thin fibres. While fibre-reinforced thermosets usually display a very good strength to weight ratio, their mechanical properties are almost always anisotropic due to the orientation of the fibres. In particular, as several layers are superimposed, weaknesses are generated at the inter-layer interface, which creates, during out-of-plane loading, damage events such as delaminations and different forms of microcracking. These relatively small damage events need to be addressed in order to prevent their propagation and catastrophic failure of the structure.

Further integration of fibre-reinforced thermoset polymers into the current structural market requires three main steps: (i) development of industrial and cost-effective manufacturing processes; (ii) maintenance and repair during service; (iii) recyclability at the end of life. Delamination and microcracking in these FRPs is a main reason for which maintenance and repair during service would be needed, in particular when using thermoset matrices. As an example, low velocity impact damage is of main concern in aircrafts where damage events can be attributed to operational or maintenance activities (such as tool drops) and tend to decrease strength, durability and stability of the structure [1]. Considerable research efforts have been recently carried out in trying to limit propagation of cracks formed by these damage events during service and to provide autonomic repair if needed.

One way of limiting damage growth in FRPs is to provide toughening. This can be achieved through either modification of the matrix or reinforcement by micro- and nano-particles, or through the incorporation of a macroscopic arrangement (usually thermoplastic nanofibrous veils, rubber layers or stitches) in between or through the layers of a reinforcement fabric.

The difficulty to provide maintenance and repair of FRPs when damage is present, due to limited detection and accessibility, has motivated the creation of “smart” composite materials. These smart materials integrate new functionalities having the ability to detect damage, react to it and repair it if needed. Through these new functionalities, the material may be able to react to its service environment, enabling new possible applications; however, the influence of these functionalities on the part behaviour during process, preparation and service needs to be quantified and compared to unmodified ones. Detecting damage can be achieved through the insertion of sensors (piezoelectric materials and/or optical fibres) into the part, which may be able to determine the position and the extent of damage created [2]. Reacting to damage can be achieved through the insertion of actuators into the part. These actuators can be for example Shape Memory Alloys (SMA), which have the ability to reconstitute some energy dissipated in the part during the damaging process [3]. Finally, repairing damage in a “smart way” is currently achieved through the insertion of self-healing systems into the part. These self-healing systems are inspired from biological systems, such as skin, which reacts to and repairs small damage extents. This new field has recently attracted much attention. Two main categories of systems can be defined [4]: (i) intrinsic self-healing systems are able to heal a crack through interactions (physical or chemical) at the molecular level; (ii) extrinsic self-healing systems on

the other hand, need pre-embedded healing agents (such as microcapsules or tubes) which can fill the crack and rejoin its faces. In order to fully address this issue, a bio-inspired strategy for the efficient healing of microcracks in FRPs before they can propagate further and potentially cause catastrophic failure of the structure, would hence be to: (i) detect damage; (ii) autonomously close cracks whose thickness is above a certain threshold in order to ensure adequate proximity of the crack faces to be healed; (iii) make use of a healing matrix component that is able to expand, up to a certain threshold, and fill the cracked regions multiple times.

The development of past and present materials is most often based on preventing the occurrence of damage and thus consists in over-engineering the design requirements. However, nature has the inverse philosophy where damage is considered as unavoidable, healing mechanisms being active to compensate the occurrence of damage. The concept of self-healing is based on a similar philosophy and aims to shift the design concept of materials from damage prevention to damage management. This approach is illustrated in Figure 1.1 for the case of composite materials having a defined initial property that decreases with the damage amount. For conventional composite materials (the blue curve of Figure 1.1), the damage prevention design philosophy assigns initial properties that are most often over-engineered and thus well above the design limit value. When damage occurs, which amount increases, the property drops rapidly to zero and renders the composite part unusable. Oppositely, self-healing composites (the red curve of Figure 1.1) may be designed closer to a limit value, as they have the capacity to extend their life-time thanks to a built-in capacity to heal cracks. The challenge in developing self-healing composites (and self-healing materials in general) lies however in achieving a part that is above the design limit value defined by the application.

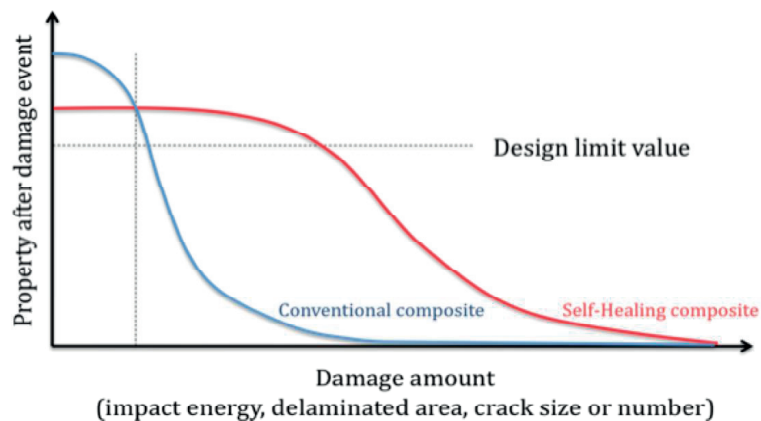


Figure 1.1: Conceptual illustration of damage tolerance in self-healing composites [5].

1.2 Scope statement

The present work aims to develop smart FRPs, containing a fibre volume fraction of 50%, with added functionalities, which can provide damage healing, while retaining properties close to those of conventionally used composite systems. In particular, three main topics are addressed to reach this goal:

- (i) **Repair:** Development of an intrinsic self-healing system that is compatible with FRP processing and property requirements;
- (ii) **Actuation:** Introduction of active stitches in FRPs with aim to close cracks after damage and improve the crack healing mechanism;
- (iii) **Initial damage prevention:** Ideally, combination of the self-healing ability with toughening of the FRP to ensure limited initial damage extent in service.

In addition, manufacturing the functionalised FRPs needs to be performed with industrially relevant processes in order to ease the path towards potential applications. Figure 1.2 schematically illustrates such a smart system containing (i)

a healing matrix consisting of a thermoset-thermoplastic blend, (ii) stitched SMA wires to close cracks and (iii) thermoplastic nanofibres to be combined with the healing matrix in order to provide toughening.

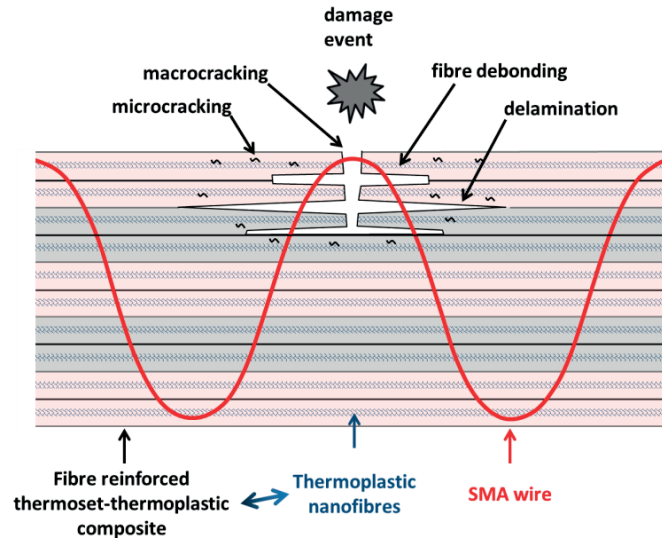


Figure 1.2: Schematic drawing of the smart system aimed in the present study. An FRP containing (i) a healing matrix consisting of a thermoset-thermoplastic blend, (ii) stitched SMA wires to close cracks and (iii) thermoplastic nanofibres to be combined with the healing matrix in order to provide toughening. Inspired from [6].

Luo *et al.* [7] have pioneered the use of immiscible thermoset-thermoplastic blends to provide efficient matrix **repair**. These blends have the ability to compete with conventional epoxy systems as they consist, thanks to a phase separation mechanism, of interconnected thermoset particles with a surrounding semicrystalline thermoplastic matrix. Crack healing is then provided through a thermal treatment, which allows re-establishment of thermoplastic entanglements across the crack faces. These systems have so far been studied for crack healing purposes only for one thermoset-thermoplastic combination and with limited properties characterisation. In addition, these have never been, to the author's best knowledge, integrated to FRPs. While the healing phenomenon in such blends can provide volume expansion of the thermoplastic followed by melt flow into the damage volume before crack healing through thermoplastic re-entanglement, this process is efficient only for crack thicknesses of some tens of microns. In order to achieve healing over a larger range of damage volume, the crack faces should ideally be first brought back closer before the healing process can take place.

For example, large wound healing is treated in biological systems with the use of stitches to reduce the distance between the edges. **Actuation** of strained SMA wires can thus be well-suited to autonomously close cracks in FRPs, to ensure closer contact between the faces to heal. SMAs exhibit a martensitic transformation, which can recover the shape of a strained wire and exert large recovery stresses up to 800 MPa [3]. This strategy was demonstrated to improve the crack healing efficiency in several matrix formulations if the wire is constrained at both ends [8], [9] and further modelled as stitches in FRPs to show promise to close delamination at interfaces [10]. However, practical implications for inserting SMA wires as stitches in FRPs and the resulting improvement in damage healing have not been explored so far in the available literature.

Even though developing systems in FRPs that can efficiently heal large damage sizes is of high interest, the opposite strategy consisting in **initial damage prevention** would provide many benefits in real applications. One strategy to limit the growth of damage in FRPs consists in the use of thermoplastic nanofibres placed in between the layers of the reinforcing fibres. These nanofibres, made of the same thermoplastic as used by Luo *et al.* [7] in thermoset-thermoplastic blends for healing purposes, have demonstrated much interest in FRPs for toughness improvement [11]–[13]. These could be thus used to combine damage prevention with healing if needed.

This work assesses for the first time the use of thermoset-thermoplastic blends combined with stitched SMA wires to provide crack healing in FRPs over a large range of damage sizes, as well as the insertion of the healing agent as nanofibres to additionally provide toughening to the system, while keeping the process and materials selection close to realistic application cases.

1.3 Thesis Methodology and outline

The thesis methodology is presented in Figure 1.3. The first phase consists in reviewing the existing literature on healing systems, SMA properties and toughening mechanisms as well as reviewing the testing protocols needed to characterise intrinsic material properties as well as to quantify the crack healing capability (Chapter 2). This allows the definition of the materials to use as well as methods to characterise the different functionalities of the aimed smart system (Chapter 3). The experimental work starts with an extension of Luo *et al.* [7] study to other epoxy-thermoplastic systems with aim of improved mechanical and healing properties (Chapter 4.1). The optimum healing matrix is then deeper analysed over a large composition range with the aim to analyse the properties and healing mechanisms (Chapter 4.2). This optimum epoxy-thermoplastic blend is then used as a matrix in FRPs and the resulting composite intrinsic and healing properties assessed (Chapter 5). The damage volume reduction functionality is addressed by first stitching SMA wires to the FRPs and secondly combining it with the previously chosen healing matrix to assess the improvement in damage healing efficiency (Chapter 6). Damage prevention is at last addressed through the use of thermoplastic microparticles and nanofibres in FRPs that can provide toughness improvement while keeping the healing functionality (Chapter 7). Through every step in the development (Chapter 3 to Chapter 7), the properties of each individual components (such as phase separation morphology, thermal transitions (i.e. T_g , T_m , T_c) and viscosity) are first assessed in order to best process the material before characterising it in terms of mechanical, fracture and healing properties, with support of microscopy investigations. Since such FRPs are developed while keeping in mind their industrial relevance, cost modelling of a production line is also addressed to evaluate their promise for potential applications (Chapter 8). Finally, overall conclusions as well as outlook of the present research are provided in Chapter 9.

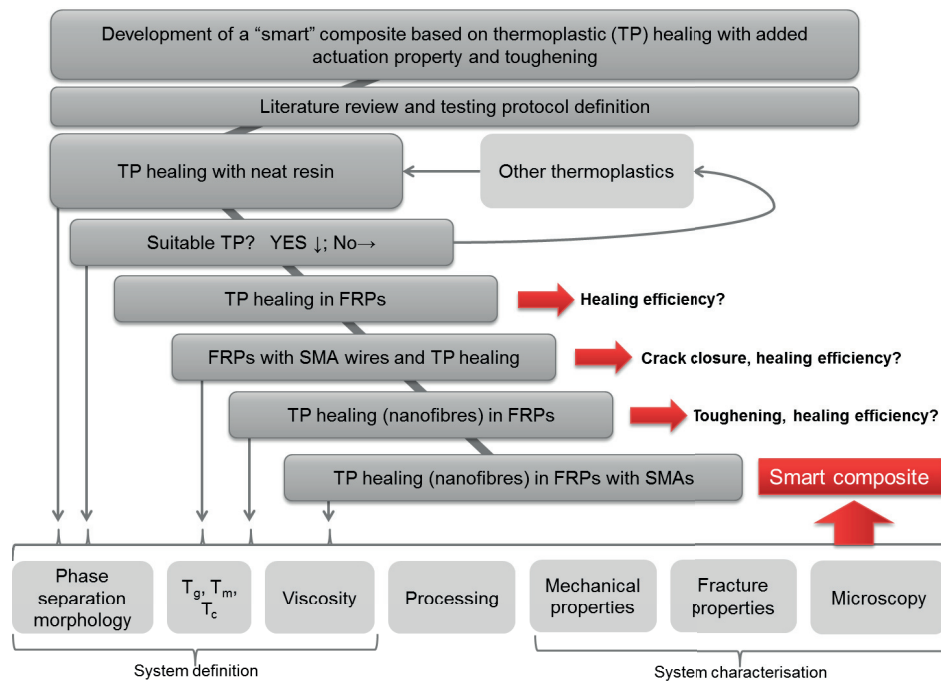


Figure 1.3: Flow chart of the thesis.

Chapter 2 State of the art

Aiming to study Fibre-Reinforced Polymers (FRPs) with damage control and repair, the basic background on fracture mechanics in FRPs is first reviewed (section 2.1) to discuss where and how damage can be controlled and healed. These FRPs, once modified, have to be characterised as well as the efficiency of their repair methods (called healing efficiency); these methods are reviewed in section 2.2.

In section 2.3, traditional repair methods of polymer composites are explored and allow understanding the difficulty to repair these materials and therefore the need to develop healing systems. Healing systems started to be highly studied since the 21st century and several articles now review this field [4], [14]–[33] for polymers and polymer composites. These healing systems can be classified into two major categories [24]: (i) intrinsic self-healing systems are those able to heal a crack through interactions (physical or chemical) at the molecular level; (ii) extrinsic self-healing systems on the other hand, need pre-embedded healing agents which can fill the crack and rebound its faces upon damage. An overview of the existing literature in these two categories is given in sections 2.4 and 2.5. The concept of self-healing is also sometimes divided into non-autonomic self-healing (which requires an external trigger such as heat or light) and autonomic self-healing (which does not require any external trigger) [19].

However, healing systems are often efficient for limited damage volumes. Reduction of large damage volumes is thus of high interest to improve the efficiency of the repair methods. This is here considered using Shape Memory Alloy (SMA) wires stitched through the composite reinforcement. A detailed overview of the existing literature and integration of SMAs into FRPs is given in section 2.6.1.

Healing systems are defined to function once damage has already occurred. However, another research area, predating by a large amount the healing approach, is to control and prevent the damage creation into the material. This is here considered through the use of additional materials, which have the ability to provide toughening. A detailed overview of the existing literature in polymers and polymer composites toughening is thus finally given in section 2.6.2.

2.1 Failure mechanisms and damage in FRPs

Due to their heterogeneous nature, composite materials can lead to a multiplicity of failure modes depending on the intrinsic properties of the reinforcement and the matrix, but also on the interaction between these phases and thus their interfacial and interlaminar properties. The present work focuses on composites with long fibres and thermoset matrices, thus failure mechanisms and damage growth are presented for this type of composites. Failure modes in FRPs can be divided into three categories: delamination (which occurs when a gap is formed between two plies of the laminate and is also denoted as interlaminar fracture), intralaminar and translaminar fracture (Figure 2.1) [34].

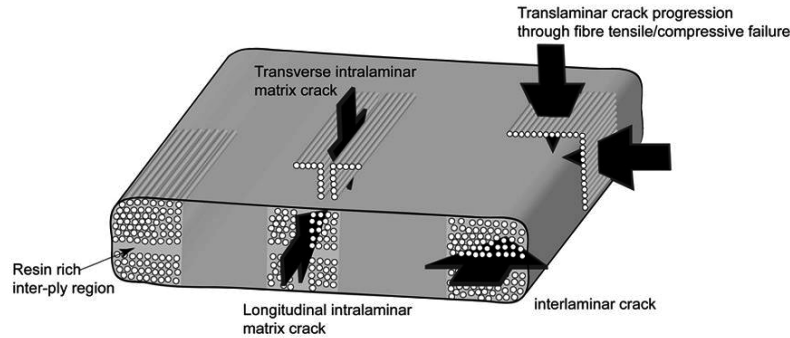


Figure 2.1: Overview of ply-level failure modes [34].

Delamination, or interlaminar cracking/fracture, has been under extensive investigation to standardise procedures for Mode I [35] and Mode II [36] (or mixed Mode III [37]) fracture toughness determination; detailed reviews of the available characterisation methods have been published by several authors [34], [38]–[41]. The three general modes of fracture are depicted in Figure 2.2 and typical values for a carbon-epoxy laminate in each mode are given in Figure 2.3. Delamination is a function of the composite interlaminar properties, i.e. interfacial effects between the matrix and the fibres, matrix effects and effects of fibre constraints [42]. Interfacial effects were demonstrated [43]–[45] to play an important role on interlaminar properties as a weaker interface leads to poorer interlaminar properties. Concerning matrix effects, the matrix strength is known to increase the interlaminar shear strength of the overall composite [46], [47], provided that the interface strength is high enough. The manufacturing process also has a significant effect because the void content of the matrix and the fibre residual stresses influence interlaminar properties [42]. Finally, concerning the fibres only, the ply stacking sequence can influence the interlaminar properties as demonstrated by Mandell *et al.* [48], and the ply thickness also has a strong influence [49]. Choosing the right reinforcement-matrix system in order to reach the highest interlaminar properties is therefore of high importance.

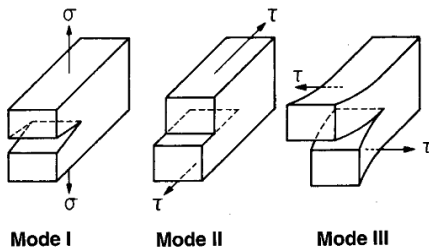


Figure 2.2: Three general modes of fracture [50].

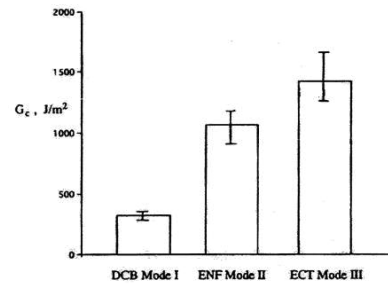


Figure 2.3: Comparison of fracture toughness for the three modes for G40-800/R6376 graphite-epoxy laminates [50].

Intralaminar fracture is also caused by matrix cracking, either longitudinally or transversely to the fibre direction (Figure 2.1). Fracture toughness values for this mode of failure are generally comparable to those observed for interlaminar failure [51], [52].

Translaminar fracture corresponds to fibre rupture within the composite. This type of failure mode appears mostly when loading is in the fibre direction, and is therefore dependent on fibre properties. The matrix also plays a role in energy transfer after fibre failure in this fracture mode, however, as the interest here is in polymer matrices, this load transfer can be neglected and the rule of mixture is in general sufficient for mechanical properties prediction in the fibre direction (dealing with ceramic or metal matrices does not lead to the same conclusion, as well

summarized in the extensive review by W. A. Curtin [53]). Even if fibre breakage appears in other loading types, matrix cracking appears first and is therefore of greater interest for the present work as described further below.

The three failure modes discussed above are a consequence of several damage modes (dependent on the type of loading conditions applied), which are presented in Figure 2.4 [4].

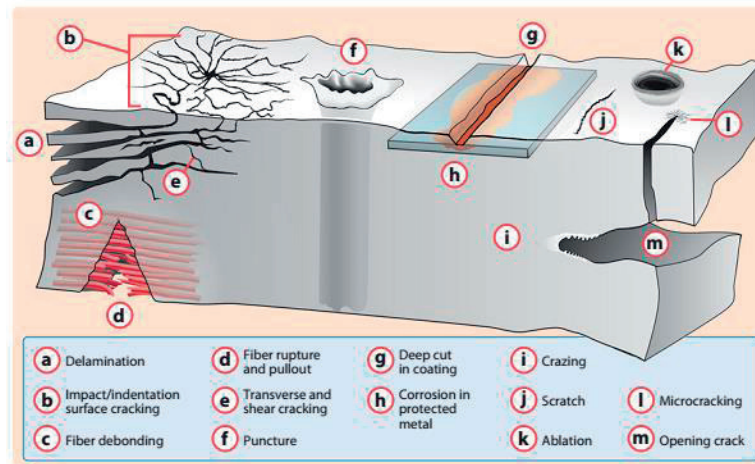


Figure 2.4: Damage modes in polymer composites induced by indentation, impact, corrosive environments, ballistic punctures, surface scratching or fatigue loading [4].

When a polymer composite is subjected to any type of loading or variation in temperature, the first form of damage to appear is usually matrix microcracks. These microcracks usually form in plies that are oriented off-axis to the loading directions, but they can appear in any ply. The first consequence of microcracks on a composite part is the degradation of its thermo-mechanical properties leading to variations in modulus, Poisson's ratio as well as thermal conductivity coefficient. The nucleation of worse forms of damage can be a second consequence of matrix microcracks, which is translated into delamination, intralaminar fracture, fibre breaks (translaminar fracture) or even creation of pathways for intrusion of corrosive liquids [54]. During load application, matrix cracking thus appears first and is commonly named as the first-ply failure. As loading continues, nucleation of cracks in other off-axis plies appears until crack saturation is reached, which is referred to as the characteristic damage state. During the development of this damage state, matrix crack connections between the different plies are formed through the resin rich regions and correspond to the growth of delamination. As reviewed by Garg and Mai [55], the other elements responsible for delamination development are: (i) free edges, notches, ply terminations, cut-outs and other geometric discontinuities which initiate from regions containing high interlaminar stresses; (ii) external sources such as incomplete curing during manufacture or when foreign particles are introduced into the system.

Improving the design of commercial composite parts therefore goes with understanding which are the crucial parameters influencing this first mode of failure in FRPs. For example, in $[0/90]_s$ cross-ply laminates, these parameters include [54], [56]:

- *Ply thickness*: in $[0/90]_s$ laminates with thick 90° plies under uniaxial tension, microcracks can be formed as instantaneous fracture events and propagate over the entire cross-sectional area. For lower thicknesses, these cracks are observed on free edges and propagate along the width of the laminate. For even lower thicknesses, microcracks can be suppressed and the laminate fails before microcracking initiation.
- *Stacking sequence*: in two laminates with different stacking sequences, the crack density as well as the characteristic damage state may differ. For example, in $[90_m/0_n]_s$ laminates, microcracks tend to form earlier during loading, however $[0_n/90_m]_s$ laminates appear to develop more microcracks at saturation. Also, the final

characteristic damage state is different in both laminates: in $[0_n/90_m]_s$ laminates, microcracks are symmetric when developing under loading, while in $[90_m/0_n]_s$ laminates, microcracks tend to be staggered, rather than aligned with other groups because of the different stress state in this laminate (this behaviour along with a schematic illustration of the two stacking sequences are depicted in Figure 2.5). This stress state induces a net bending moment in $[90_m/0_n]_s$ laminates promoting Mode I delamination, which is not the case in $[0_n/90_m]_s$ [57]. Finally, similar stress effects can be noticed for microcracking in $[0/+θ/-θ]_s$ laminates but require 3D stress analysis [54], which will not be detailed in the present work.

- *Loading and environmental effects:* Uniaxial tension is often taken as an ideal case while assessing FRPs damage development. However, microcracks can also form under other loading conditions such as: (i) bending where similar results as in tension are observed or biaxial loading which can be considered as two superimposed uniaxial tests (one $[90_m/0_n]_s$ laminate and one $[0_n/90_m]_s$ laminate, where microcracks can be of the two types shown in Figure 2.5); (ii) fatigue loading where propagation of microcracks does not depend on the 90° ply thickness as for static loading; (iii) or even non-uniform stress state if inclusions or holes are present in the laminate. This last state is far more complicated and usually neglected when the amount of holes is low in the laminate, however, this can be used as a strategy to arrest crack propagation in composites (see section 2.6.2). Finally, environmental effects can influence microcracking, as for example shrinkage during thermal variation where biaxial loading may be induced.
- *Intrinsic properties of the composite:* as already stated above, delamination, and therefore microcracking is also influenced by the intrinsic properties of the FRPs and in particular by interfacial effects between the matrix and the fibres, matrix effects and effects of fibre constraints.

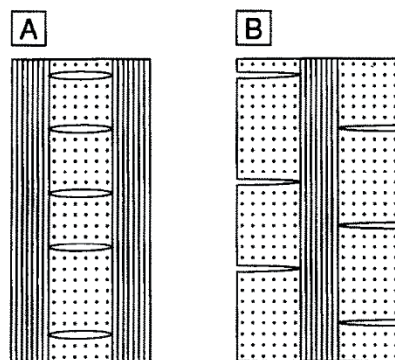


Figure 2.5: The characteristic damage state of (A) $[0_n/90_m]_s$ laminate having symmetric microcracks and (B) $[90_m/0_n]_s$ laminate having antisymmetric microcracks [57].

Relatively minor changes in thermo-mechanical properties of the FRP can easily lead to microcracking and potential higher damage level which may reduce the structural ability of this kind of materials for practical applications. Therefore, considerable efforts have been made to first understand, then predict, but also to detect and finally repair damage in FRPs. Damage predictions can be carried out through several theoretical models, from the basic rule of mixture, through shear-lag analysis with global or local load sharing models [53], until 3D modelling of complex structures [58]. These theoretical models also need parameters, which are found experimentally, such as Mode I and Mode II fracture toughness but also thermal properties (see section 2.2.1.1). An exhaustive definition of tests performed in the aerospace industry is given in [59]. If damage occurs in the part, detection is then required and can be performed through several non-destructive evaluation methods, such as radiographic, ultrasonic, optical or acoustical techniques [59]. Once damage is detected, the part can be finally repaired, but tests to characterise the repair must be performed (see section 2.2). If the damage extent is high and visible from the side of the part, it can be repaired by manual intervention (see section 2.3). However, when the damage extent is low and barely visible (i.e.

microcracks), it is far more complicated with composite materials to repair it as not necessarily detectable and accessible. This complicated problem has been extensively studied over the last decade and is the concept of self-healing detailed in sections 2.4 and 2.5.

2.2 FRPs characterisation and healing efficiency assessment

2.2.1 Usual tests for FRPs characterisation and healing efficiency assessment

The previous section highlighted that a number of different damage types can coexist in an FRP depending on the loading case (Figure 2.4). Damage repair (through manual intervention or more interestingly autonomously) can provide recovery to the degraded function(s) of the part that was (were) followed by any type of damage. To quantify this recovery, the repair/healing efficiency concept was introduced. Multiple definitions have been introduced to this concept, however by convenience, we define it by the ratio of changes in material properties as [4]:

$$\eta = \frac{f^{healed} - f^{damaged}}{f^{virgin} - f^{damaged}} \quad (2.1)$$

where f is the property of interest.

To complete this equation and calculate the healing efficiency of any damage, the following steps must be followed [56]:

1. Choice of material property to assess and therefore choice of a suitable test;
2. Measurement of the chosen property for the virgin material (f^{virgin}) (this step introduces damage in the material and therefore a loss in the property);
3. Measurement of the property in the damage state ($f^{damaged}$);
4. Healing of the material under specific conditions: time, temperature, humidity, etc...;
5. Measurement of the property as in step 2, but in the healed state (f^{healed}).

However, caution must be taken when calculating healing efficiency, for two reasons:

- $f^{damaged}$, the property in the damage state is often set to zero. This setting is true when measuring fracture properties in Mode I where the fracture resistance, after testing, is null. However, for other fracture modes and loading conditions, the property in the damage state is not null and thus needs to be measured (see section 2.2.1.1);
- f^{virgin} , the property in the virgin state, can be that of the neat material (without healing system) or that of the modified material (with healing system). Indeed, the healing system usually influences the initial material properties (as seen with Figure 1.1) and depending on which virgin property is used, the healing efficiency can be completely different. Thus considering the two cases is of high importance.

Different tests are considered in the next section to assess healing in either neat resin systems or FRPs. The different tests and corresponding healing assessment are reviewed following the classification made by Blaszik *et al.* [4]: recovery of quasi-static fracture, fatigue, impact and indentation properties as well as recovery of barrier properties. Notice that for further details on quantifying healing efficiency of thermoset polymers, the reader is referred to the review of Tsangouri *et al.* [60]. Notice also that virgin state characterisation of those FRPs provides their initial intrinsic properties.

2.2.1.1 Quasi-static fracture

Quasi-static fracture experiments are the most common ones found when crack healing needs to be assessed as it allows controlled and predictable crack propagation with limited damage volumes. As discussed, three modes of fracture can be found and differ in the type of property measured:

Mode I Mode I is the most common type of fracture test. The principle is to provide a notch to a specimen, which allows the crack to propagate in a controlled manner under tensile loading. The acquired data are the force versus the crack opening displacement and allow extracting the peak load (P_c), the fracture toughness (K_{IC}) and the strain energy release rate (G_{IC}). G_{IC} is also named as interlaminar fracture toughness, work of fracture or fracture energy. K_{IC} and G_{IC} are defined with the following equations:

$$K_{IC} = \sqrt{EG_{IC}} \qquad G_{IC} = \frac{3P_c \delta}{2ba} \qquad (2.2)$$

where E is the Young's modulus, δ the load displacement point (determined through the compliance calculation of the specimen), b the specimen width and a the delamination length. Notice that the equation on the left is valid in plane strain conditions, whereas in plane stress, the Poisson's ratio needs to be taken into account. Several specimen geometries can be used for Mode I testing (see Figure 2.6 along with the references to each image for representative studies): the double cantilever beam (DCB) is the most common due to its simple geometry; width tapered double cantilever beam (WTDCB) and tapered double cantilever beam (TDCB) were developed to assess interlaminar delamination in composite matrices and are nowadays widely used tests for healing efficiency assessment [60] as precise measurements of the crack length are not needed for the characterisation of the fracture toughness of linear elastic specimens [61], [62] (notice that WTDCB allows a control on stick slip crack growth [21]); compact tension (CT) which causes a large crack separation.

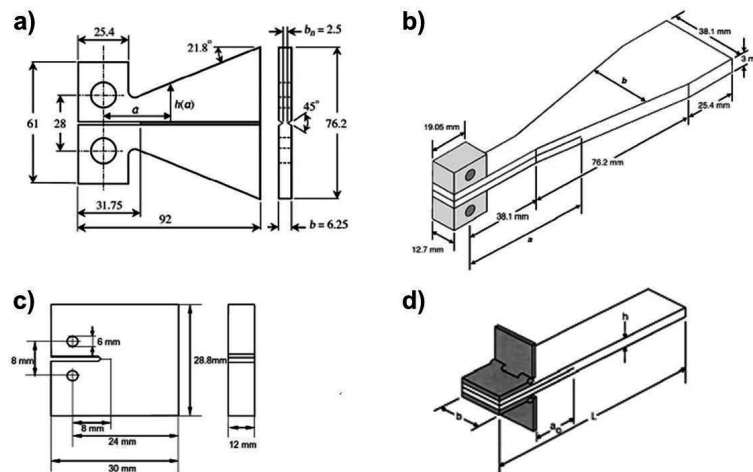


Figure 2.6: Specimen geometries for mode I testing: a) TDCB [62], b) WTDCB [63], c) CT [64] and d) DCB [65].

From Eq. (2.2), interlaminar fracture toughness is determined as a function of the crack length. Usually, toughness increases as a function of the crack length, and is described (commonly for Mode I DCB testing) by the concept of resistance curves (R-curves) represented schematically in Figure 2.7. The reason of this increase in crack propagation resistance can differ depending on the assessed material. For ductile solids, the plastic zone ahead of the crack tip is the main reason, whereas in FRPs, it is fibre bridging between two crack faces that makes toughness to increase with the crack length [66]. Stating the problem of crack propagation pairs with the concept of process zone (or fracture process zone, FPZ), which defines the two positions in a crack [67]: (i) the crack tip and (ii) the notch root at the beginning of the crack. R-curves are explained by the development of this process zone. When the process zone is in development (meaning that the crack tip is propagating), it is characterised by an increase in toughness, i.e. a rising R-curve. Then two scenarios can take place [67]: (i) the R-curve reaches a plateau because crack propagation reaches steady state conditions and in this case, the process zone is small and the fracture problem can be analysed by conventional fracture mechanics seen above; (ii) the R-curve continues to rise because the process zone is larger, and

in this case fracture, and especially the rise of the R-curve, needs to be modelled. This modelling problem was well assessed by Nairn [67] but is beyond the scope of the present research. It is however important to notice that several external parameters also influence this behaviour and therefore the modelling of delamination fracture in the case of laminated composites. These parameters, listed by Tay [50] are as follows: crack jumping, fibre bridging, interaction between matrix cracks and delamination, the effect of stacking sequence, residual thermal stresses, friction and contact, and dynamic fracture characterisation. In particular, the effect of residual stresses were highly assessed by Nairn [68]–[70], and are usually resulting from material manufacturing.

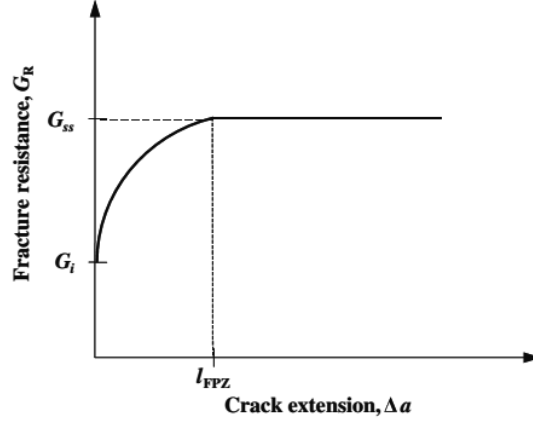


Figure 2.7: A schematic shape of R-curve under large-scale fibre bridging [66].

In Mode I fracture testing, healing efficiencies in terms of fracture toughness or strain energy release rate are given as:

$$\eta = \frac{K_{IC}^{healed}}{K_{IC}^{virgin}} = \sqrt{\eta_G} \qquad \eta_G = \frac{G_{IC}^{healed}}{G_{IC}^{virgin}} \qquad (2.3)$$

since K_{IC} and G_{IC} in the damaged state are zero. Moreover, the interest of using TDCB or WTDCB is that the specimen compliance changes linearly with the crack length [61], [62]. In this case, the fracture toughness healing efficiency is defined by the recovery in fracture load (P_C) as:

$$\eta = \frac{P_C^{healed}}{P_C^{virgin}} \qquad (2.4)$$

Mode II Crack growth in Mode II can be assessed by flexural testing in either 3-point or 4-point bending. Simple beam geometry with a notch is only required for this test called end-notched flexure (ENF). In this case, due to the geometry of the test, there exists some residual flexural strength in the sample and the healing efficiency must be assessed as presented in Eq. (2.1). Similar properties as the ones for Mode I tests are obtained, but its interest is the crack propagation through shear forces.

Mode III Crack growth in this mode (tearing) is achieved through trouser test specimens (rectangular specimens cut in the middle defining two legs) where the two specimen legs are gripped and loaded in tension [71]. The tear strength is then defined as two times the average force over the specimen thickness. As for Mode I, healing efficiencies can be assessed without taking into account the property in the damaged state.

Fracture testing is highly used to characterise healing in literature. However, because a precrack is needed to measure fracture toughness and strain energy release rate, it is possible to obtain healing efficiencies over 100% as this precrack is usually not re-formed in the healed state. Care must therefore be taken when experimental work shows

over 100% recovery in a property (even if it is possible depending on the property and healing system assessed, if the healing phase is tougher than that it replaces for example).

2.2.1.2 Fatigue

Fatigue testing is another common mode of failure in structural materials; characterising repair systems in fatigue loading conditions is thus of high interest as it is representative of many cases in real life structures. The testing principle is the same as for static testing, except that the applied stress is varied at a defined amplitude and frequency. In fatigue loading for healing systems, the fatigue life extension (λ) is the parameter of interest and can be defined as [4]:

$$\lambda = \frac{N^{healed} - N^{control}}{N^{control}} \quad (2.5)$$

where N^{healed} and $N^{control}$ are respectively the number of cycles to failure for the healed specimen and the specimen without any healing system.

2.2.1.3 Impact and compression after impact (CAI)

Impact testing is another test, which is highly representative of industrial applications and was standardised for FRPs [72]. Low velocity impact damage is of main concern in aircrafts where damage events can be attributed to operational or maintenance activities and tend to decrease strength, durability and stability of the structure [1]. It is a test where massive damage volumes from several failure modes are observed, which was reviewed in [73], [74]. Quantification of damage through impact is performed with the use of drop towers where a defined mass is dropped on the specimen and the impact force as well as absorbed energy can be measured. Healing efficiency can be quantified through this test in terms of recovery of impact force and absorbed energy, however the obtained values were demonstrated to be only indicative [75]–[77]. A more common way to measure healing efficiency is to measure the recovery in impact damage area by means of optical observations or C-scan [75]–[77]. Healing assessment in terms of strength recovery after impact damage can also be performed through the Compression After Impact (CAI) test (i.e. measuring the recovery of compressive strength after impact) [78], which was also standardised for FRPs [79]. Notice that Eq. (2.1) should be used to quantify healing efficiency in these cases as only partial damage is made on the specimen.

2.2.1.4 Barrier properties

Composites are often designed to prevent fluid or gas diffusion between two elements, but when a crack crosses the thickness of the FRP, it will degrade its barrier properties. Some healing systems have the ability to seal damage; sealing efficiency in that case can be either visually observed (as for impact testing) or measured through permeation measurements [80]. In this second case, the amount of gas or liquid that passes through the damage is measured before and after healing.

Coating applications are also of use for barrier and corrosion resistance. Self-healing systems were developed for these applications but are out of the scope of the present work [81].

2.2.2 Interfacial shear strength determination

Characterisation of the fibre-matrix interface (i.e. through interfacial shear strength (IFSS) determination) is also of interest here as modifying the matrix of FRPs with healing systems can highly modify its adhesion with the reinforcement, therefore leading to debonding effects upon mechanical loading. Several micromechanical tests can be performed; they were well described and reviewed by Zhandarov and Mäder [82]. These tests can be classified into two groups: (i) those where external load is directly applied to the fibre (single-fibre pull-out test, which is the most used in literature, microbond test, three-fibre test, push-out and push-in test); (ii) those where external load is applied only to the matrix (fragmentation tests and Broutman test). The output of these tests is a load-displacement curve, where a parameter (IFSS or τ_i) characterising the quality of interfacial bonding is obtained:

$$\tau_s = \frac{F_{max}}{2\pi r_f l_e} \quad (2.6)$$

where F_{max} is the force required to debond the fibre, r_f is the fibre radius and l_e the embedded length.

Two tests need particular attention and are developed hereafter: the pull-out and push-in tests. The major difference between these two tests being that the pull-out test considers the intrinsic interfacial shear strength between a single fibre and its surrounding matrix, whereas the push-in test has the ability to take into account the surrounding fibre environment. Even though these tests should provide similar values of IFSS, this is not the case due to their different nature and data reduction scheme. An interesting round-robin programme on fibre-matrix interfacial test methods is provided in [83].

2.2.2.1 Pull-out test

To measure interfacial properties between a fibre (or wire) and a matrix, the pull-out test or the microbond test are commonly used [84]. These tests consider a fibre embedded in a matrix; the fibre is pulled-out while a holder retains the matrix. Several geometries exist to perform this test, with the fibre going across the whole sample (microbond test) or embedded at one end; here, an open-end specimen with top holding is considered (Figure 2.8).

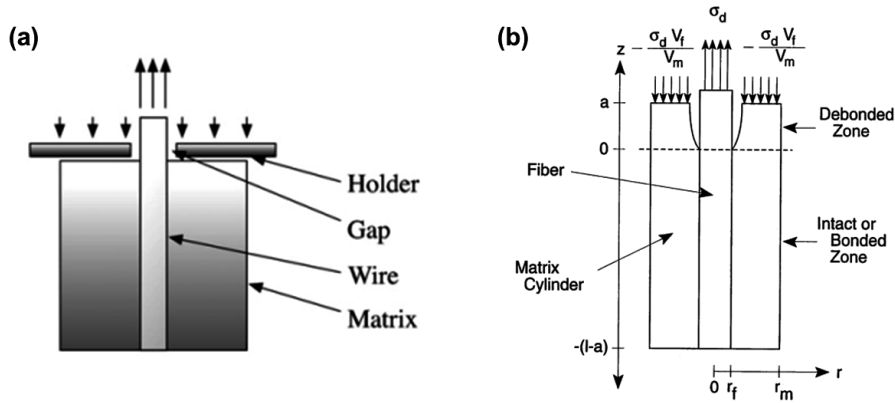


Figure 2.8: (a) “Microbond” pull-out geometry [85]; (b) Equivalent concentric cylinder model for the embedded fibre zone of a single-fibre pull-out specimen [86].

The output of the test is a measure of the external force to pull-out the fibre as a function of the fibre displacement. When a peak force is observed, the fibre debonds from the matrix and the value is used in Eq. (2.6) to determine the average interfacial shear strength (IFSS, named also apparent IFSS, τ_a). The average IFSS as defined by Eq. (2.6) however assumes a uniform shear stress state along the embedded fibre length, which is in reality not the case. Several stress transfer models have been developed to accurately determine IFSS through different shear-lag parameters, for example Greszczuk [87], Nairn [88], [89] and Mendels [90]–[92] can be cited; for more details, a review of other models is given in [93]. Here the model of Mendels is of interest and its geometry considering the embedded fibre for the axisymmetric two-dimensional stress transfer determination is shown in Figure 2.9. It considers a $2a$ fibre diameter, with Young’s modulus E_f and length $2t$, embedded in a $2b^*$ diameter matrix specimen, whose Young’s modulus is E_m and Poisson’s ratio ν_m . The applied stress σ_0 is entirely transferred to the composite section at $z = \pm t$, where z stands for the axial axis.

The hypotheses in this model for stress transfer over a cylinder are [90]:

- Perfectly elastic and isotropic matrix and fibre;
- Perfect bonding between matrix and fibre;

- Constant stress through a radial section of fibre, and integral stress transfer from matrix to fibre by shear at the interface;
- Axial derivative of the axial stress in matrix is graded in the radial direction by a function of $1/r$;
- Elastic properties define the matrix bounds a and b to stress transfer phenomenon, where a is the fibre radius and b satisfies to $(b-a)E_m = aE_f$ if the sample radius b^* is greater than b , else $b = b^*$; E_m and E_f being the matrix and fibre Young's modulus respectively. Notice that the physical meaning of b^* was not clearly established and a more accurate solution for this problem is $(b^2 - a^2)E_m = a^2E_f$ [84].

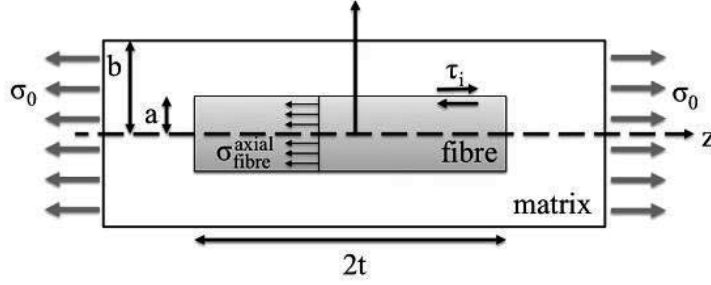


Figure 2.9: Embedded fibre geometry for stress transfer determination [90].

Considering this geometry and using force equilibrium, the interface shear stress τ_i is given by (the complete derivation of this equation is given in [92]):

$$\tau_i = \frac{F\alpha \cosh(\alpha(z-t))}{2\pi a \sinh(2\alpha t)}$$

where

$$\alpha = \left[\kappa \frac{a^2 E_f + (b^2 - a^2) E_m}{a E_f (1 + \nu_m)} \right]^{1/2} \quad (2.7)$$

with

$$\kappa = \frac{12(2(b-a) + \xi(b-a)^2)}{a \left\{ 24a(b^2 - a^2) - 16(b^3 - a^3) - 3\xi(a^2 - b^2)^2 + 6b(2 + \xi b) \left[2b^2 \ln\left(\frac{a}{b}\right) - (b^2 - a^2) \right] \right\}}$$

and

$$\xi = \frac{-E_m}{aE_f}$$

where F is the external load applied to the fibre.

However, Eq. (2.7) does not take into account internal stresses that are built from the resin cure shrinkage and the difference in thermal expansion coefficients of both components. Considering the simple case of elastic thermal stresses, the far field shrinkage can be written as $(\alpha_m - \alpha_f)\Delta T$ where α_m and α_f are the coefficient of thermal expansion of respectively the matrix and fibre, and ΔT is an effective temperature difference usually defined as the difference between either the matrix glass transition temperature, T_g , or the cure temperature and the ambient temperature. Notice that this field is symmetric and that this simple case is valid only below the matrix T_g . The interface shear stress, τ_i , taking into account internal stresses of the fibre-matrix system can therefore be stated as:

$$\tau_i = \frac{F\alpha \cosh(\alpha(z-t))}{2\pi a \sinh(2\alpha t)} - K \frac{\sinh(\alpha z)}{\cosh(\alpha t)}$$

where

(2.8)

$$K = \frac{1}{2} a\alpha E_f (\alpha_m - \alpha_f) \Delta T$$

The increase of τ_i resulting from the introduction of the internal stress term K can be relatively significant and therefore care must be taken while defining the parameter ΔT . On top of the analysis given above for the pull-out test, or “microbond” test, it is important to remember that experimental parameters of the test are also of main importance. A detailed procedure, as well as details on the effect of the embedment area, the initial tension on the fibre or the loading rate are given in [94]. For representative values of fibre-resin IFSS, the reader is referred to [83], [94].

2.2.2.2 Push-in test

The fibre push-in test has for principle to indent (either with micro- or nano-indenter machines) a fibre inside a well-polished composite surface having embedded fibres perpendicular to the observation plane. The advantage of this test is that it takes into account, due to its nature, the surrounding fibre environment, therefore being representative of what is encountered in real composites. With the neighbouring fibres, complicated analysis to take into account residual stresses as seen in the previous section is thus not needed. The only analysis needed goes through a simple shear-lag model adapted with a parameter n for taking fibre packing into account. The interfacial shear strength of a push-in test can be written as [95]–[97]:

$$\tau_s = \frac{nF_{deb}}{2\pi r_f^2} \quad (2.9)$$

where

$$n^2 = \frac{2E_m}{E_f(1 + \nu_m) \ln\left(\frac{2\pi}{\sqrt{3}V_f}\right)} \quad (2.10)$$

with F_{deb} being the decohesion force, r the fibre radius, E_f and E_m the Young’s moduli of the fibre and matrix respectively, ν_m the Poisson’s ratio of the matrix and V_f the local fibre volume fraction.

Measuring IFSS by means of the fibre push-in test therefore requires the determination of the debonding load and the parameter n of Eq. (2.10). However, discontinuities in the load-displacement curves are generally due to fibre splitting and not to debonding of the fibres. Determination of the debonding load can be made by performing tests at increasing load levels and detecting visually when the fibre is debonding (Figure 2.10).

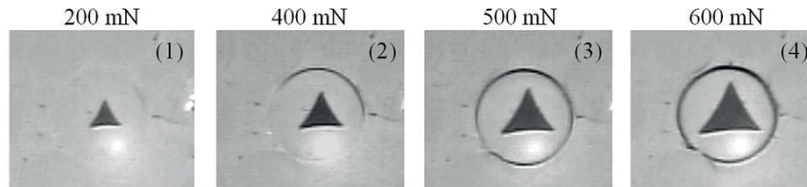


Figure 2.10: Optical image of the indented fibre obtained by interrupting the test at increasing loads, showing the gradual fibre debonding [98].

The increasing load steps technique requires a significant amount of tests and most importantly the definition of an inaccurate threshold for fibre debonding as seen with Figure 2.10 (usually it is defined that if 2/3 of the fibre

perimeter is debonded, the debonding load is reached). From these difficulties arose the development of a data reduction scheme for determining the load at debonding directly from the load-displacement curve. This approach, developed by Kharrat *et al.* [95] assumes the displacement, u , during an indentation test (using a Vickers' indenter) as the sum of two independent contributions, see Figure 2.11 [96]:

- (i) The displacement u_{ep} due to the elasto-plastic indentation of the fibre surface by the indenter. It was proposed to determine this component from the indentation behaviour in a bulk material having the same composition as the fibre;
- (ii) The displacement u_0 of the fibre surface due to the compression of the fibre into the matrix and the deflexion of the matrix.

The extraction of u_0 provides useful information on the interfacial behaviour when related to an equivalent stress $\sigma_0 = P/\pi a^2$ (directly given from the initial indentation curve). An example of such reduced curve is given in Figure 2.12, where fitting of the indentation in bulk was necessary and made through the following empirical relations:

- Loading: $u_{ep} = KP^m$ where $K, m = cst$
- Unloading: $u_{ep} = \alpha + \beta P + \gamma P^2$ where $\alpha, \beta, \gamma = cst$

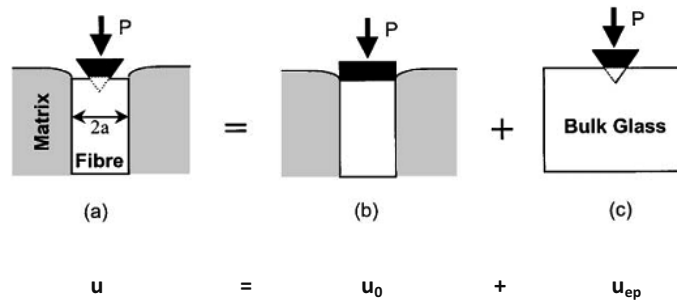


Figure 2.11: Model systems considered for the measure of interfacial shear strength: (a) elasto-plastic indentation by a cone of fibre embedded in a cylinder of elastic matrix; (b) elastic indentation of a fibre in a matrix cylinder by a rigid flat punch; (c) elasto-plastic indentation by a cone of a body having the mechanical properties of bulk glass [96].

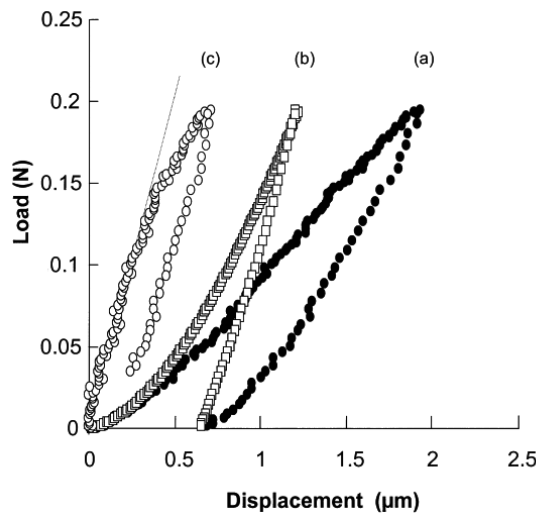


Figure 2.12: Extraction of a reduced indentation curve from a load/displacement curve: (a) indentation curve; (b) indentation of a bulk E-glass; (c) reduced indentation curve [96].

Given that the stress on the fibre is $\sigma_0 = P/\pi a^2$ and far away it equals 0, the linear displacement of the fibre surface as a function of the applied load is given by:

$$u = \frac{P}{n\pi r_f E_f} \quad (2.11)$$

Therefore, by simply determining the slope of the initial linear part of the reduced indentation curve, the parameter n can be deduced. As stated by Kharrat *et al.* [95], the debonding load is then given when the reduced load curve deviates from linearity. This method demonstrated coherent values for known systems, as shown in [98], [99]. However, determining the deviation of the linear part from the reduced curve can be relatively imprecise, even if a criterion is defined. Zidi *et al.* [96] therefore extended the work to model the entire reduced curve and determine the load at debonding from the non-linear loading part of the reduced load-displacement curve, given the following equations:

$$u_0 = \frac{\sigma_0}{nE_f} \quad \text{when } \sigma_0 \leq \sigma_d \quad (2.12)$$

$$u_0 = \frac{1}{2nE_f} \left(\frac{\sigma_0^2}{\sigma_d} + \sigma_d \right) \quad \text{when } \sigma_0 > \sigma_d \quad (2.13)$$

Using these two equations and a least square fitting on the entire loading curve, the debonding strength σ_d and therefore the interfacial shear strength can be determined. Notice that as compared to the method of Kharrat *et al.* [95], this method removes the imprecisions in the determination of the onset of debonding.

When developing a new healing system, the characterisation of healing efficiency in terms of mechanical, barrier or corrosion properties are of high interest. However, the intrinsic behaviour of every system constituent (the healing system, the matrix and the reinforcement) needs also to be addressed. This can go through several other tests that will be developed throughout the present report if needed. For other techniques evaluation, characterisation and monitoring in self-healing materials, the reader is also referred to the review of Bekas *et al.* [33].

2.3 Traditional repair methods

The previous section underlined the different types of damage that can be present in a composite part. For low damage extent (i.e. microcracks), repair methods are almost inexistent as the damage is barely visible and not easily accessible. However, for more extensive damage, repair methods were developed [16], [100], [101], which can be of three types: (i) application of external patches where the thickness of the laminate is increased (Figure 2.13 (a)), (ii) tapered scarf where an area around the hole or the scarf is sanded to expose a section of each ply in the laminate (Figure 2.13 (b)), (iii) stepped-in repair where the laminate is sanded down to expose flat bands of each layer and producing a stepped finish (Figure 2.13 (c)) [16], [100].

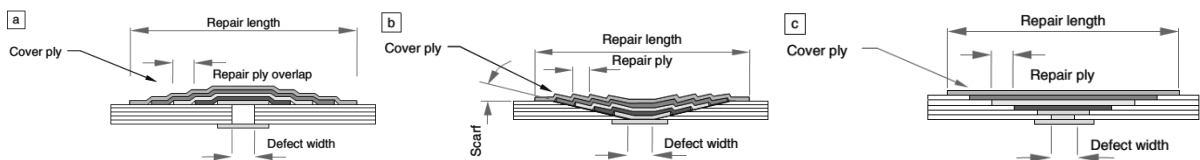


Figure 2.13: Schematic of typical repair schemes for an FRP: (a) simplistic external patch; (b) tapered scarf; (c) stepped-in repair [16].

When structural integrity of the fibre reinforcement is not attained and only the resin contains some visible damage, two additional repair methods can be mentioned [23]: welding which joins or fuses two faces of the cracked material

(further detailed in section 2.4.1 when discussing healing of polymers) and in-situ curing of new resin which is similar to reinforcement patching, but uses only the resin.

These repair methods are appropriate for large and visible damage extent. However, for smaller damage, not directly accessible, two strategies can be followed: either holes can be drilled in the part to access the damage and repair it with either of the three methods seen in Figure 2.13; or, if safety limits are not reached, the damage can be left as it is until higher damage extend is reached in order to avoid risking to further reduce the part integrity. For safety critical applications, there is thus reticence from designers to use FRPs as no damage growth can be tolerated.

Slightly more than a decade ago, the concept of self-healing appeared to counter this low damage level drawback in FRPs where the matrix only should be repaired and has been extensively studied and reviewed [4], [14]–[32]. The literature in this field is presented hereafter as a function of two categories of self-healing systems: intrinsic (section 2.4) and extrinsic (section 2.5) systems.

2.4 Intrinsic self-healing

Intrinsic self-healing systems are based on the performance of the polymer matrix; they have the ability to repair a crack through reversible bonding of the matrix and under certain stimulations (usually heat). These self-healing systems have been demonstrated through three main strategies at the molecular level [4] (Figure 2.14): (i) reversible bonding which is based on the reversibility of specific chemical reactions; (ii) chain re-entanglement which utilises mobility through a thermal trigger spanning the crack surfaces; (iii) noncovalent healing which relies on hydrogen bonding and ionic clustering and where reversibility in polymer cross-linking is observed. The intrinsic healing systems are often defined as mendable polymers as many of the developed systems heal damage events under an external trigger (usually heat) [102]. The present section is organised as follows: the first part (section 2.4.1), constituting the oldest way of healing, is the repair of two interfaces and was extensively studied in the 80's as it is in fact similar to welding. Then, three parts (sections 2.4.2 to 2.4.4) follow the structure given in Figure 2.14. Finally, integration of these intrinsic systems into FRPs is explored (section 2.4.5).

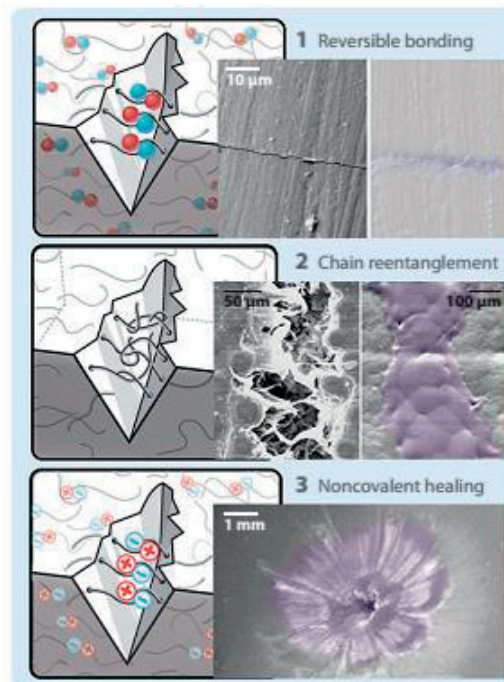


Figure 2.14: Three main schemes for intrinsic self-healing: (1) Reversible bonding; (2) Chain re-entanglement; (3) Non-covalent healing [4].

2.4.1 Healing of polymer interfaces before the self-healing concept

People are facing the problem of cracking in polymers since their discovery. In that scope, joint strength between two surfaces was quantified following three concepts [103]: polymer-polymer interdiffusion, jointing by flow of molten material and adhesion between rough surfaces; the first two being of interest for crack healing. Two interfaces that need to be re-joined can be two thermoplastics (same material or not), two thermosets (this case is detailed through reworkable matrices in section 2.4.2) or a combination of the two. Notice that to perform joining, the temperature of the process needs to be above the T_g or the T_m of the material considered.

Early studies in the field of polymer healing were performed by Jud and Kausch [103], [104] where primary application of their research was butt-welds. They assessed crack-healing in PMMA specimens of different molecular weights and degrees of copolymerisation slightly above T_g where diffusional interpenetration of chain segments takes place. Main conclusions were that: (i) the strength (calculated through fracture toughness with CT tests) of the interface formed during crack healing can fully recover that of the virgin specimen and is a function of the temperature and the time of healing; (ii) when the temperature of healing is higher than the glass transition temperature (T_g), physical links are formed across interfaces through interdiffusion, (iii) the strain energy release rate (G_{IC}) and the fracture toughness (K_{IC}) of the new joint are directly proportional to the interpenetration time t as:

$$G_{IC} \propto t^{1/2} \qquad K_{IC} \propto t^{1/4} \qquad (2.14)$$

In parallel, Wool and O'Connor [105] published a theory on thermal crack healing in polymers, which explains the results produced by Jud and Kausch [103], [104]. Indeed, they determined five stages in which healing develops (Figure 2.15):

- (i) **surface rearrangement:** affects the diffusion initiation function and topological features of the interface;
- (ii) **surface approach:** controls the mode of healing, line mode (uniform healing at all points of the interface) or point mode (healing at the crack tip only), or mixed;
- (iii) **wetting:** depends on the process time and surface roughness;
- (iv) **diffusion:** modelled by a reptation model from de Gennes [106] where the polymer chain is confined in a tube to model its movements;
- (v) **randomization:** equilibrium (or not) of the chains conformation near surfaces and determines if there is complete loss of memory in the cracked interface.

Notice that mechanical properties of the interface are developed during the wetting and the diffusion stage. Wool and O'Connor [105] also derived some simple relationships (similar to the ones of Eq. (2.14)) that link stress, strain, strain energy release rate and fracture toughness of the new joint to the interpenetration time and to the polymer molecular weight.

Similar results can be found in other work under isothermal healing [107], [108] or non-isothermal healing [109] and an extensive review on the basics of polymer-polymer interfaces is provided in [110]. In particular, crack healing in PS and HTPB (an elastomer) was studied and similar recovery properties as above after thermal healing of the crack were observed; they also depended on the healing time.

On thermoset polymer-polymer interfaces, a study performed by Raghavan and Wool [111] assessed crack healing, welding and joining of a vinyl-ester thermoset resin through CT tests. After the repair process, they obtained recovery in G_{IC} of 1.7%, 13.5% and 22% for respectively crack-healing (annealing of specimen for 24h above T_g), welding (insertion of a Kapton film in the crack and annealing for 24h above T_g) and joining (application of a Super glue gel). This study shows the difficulty of crack healing in conventional thermoset resins.

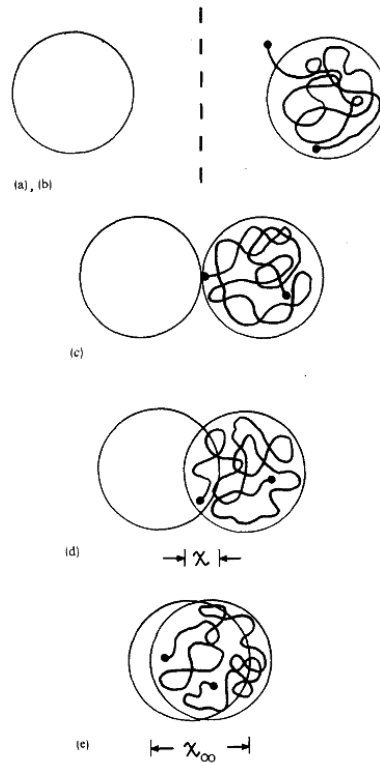


Figure 2.15: Schematic diagram showing two random-coil chains on opposite crack surfaces during the five stages of healing: (a) rearrangement, (b) surface approach, (c) wetting, (d) diffusion to a distance χ , and diffusion to an equilibrium distance χ_{∞} and randomization. Only one chain is shown for clarity. The dashed line represents the original crack plane [105].

2.4.2 Self-healing through reversible covalent bonding

Through the increasing use of thermoset matrices with or without fibre reinforcements for several applications (structural parts or electronic parts), the difficulty to recycle or repair these covalent bonded systems has raised much research.

The first field of research focused on how to cleave the chemical bonds of thermoset systems in order to repair or remove them from the part; these systems are called reworkable thermoset systems. Sastri and Tesoro [112], [113] introduced covalently bonded disulphide groups within an epoxy network which provided reversible crosslinks that can be activated upon thermal heating while keeping relatively high mechanical properties of the system (Young's modulus in the range of 20-200 MPa). These systems further demonstrated recovery of tensile strength in excess of 90% after a thermal treatment at 80 °C for 2h [114]. Also, Yang *et al.* [115] synthesised a series of epoxies with primary, secondary and tertiary ester linkages where the tertiary linkages have the ability to break down at 220 °C, therefore enabling to rework the matrix at reasonable temperatures while keeping its original mechanical properties below the T_g . Similar work allowed further understanding of these matrices in terms of mechanical properties [116], chemical formulation and thermal properties [117], or even in terms of crosslink density threshold to allow breakdown of the entire structure [118].

A step further was to develop polymeric systems in which covalent bonds can be cleaved upon heating, but also in which the same bonds are reformed upon cooling as in thermoplastic welding, with mechanical properties close to those of commercial epoxies and unsaturated polyesters. The most widely used reaction for these re-mendable systems is based on the Diels-Alder (DA) reaction where highly cross-linked polymeric materials with multi-furan and multi-maleimide are synthesised. At temperatures above 120 °C, 30% of monomer linkages disconnect and then

reconnect upon cooling to restore the fracture part properties and to anneal visual observation of the fracture surfaces thanks to the transparency of these polymers. The first work performed in this field by Chen *et al.* [119] followed this DA reaction and showed recovery of 57% in fracture load and of 41% in fracture toughness, through CT tests and after thermal mending at 120 °C (Figure 2.16). The authors also showed only 20% of loss in the load to failure between the second and third healing cycle, showing the ability of these systems to work several times. However, these premature systems have a low temperature resistance, which limits their applications [120]. Improved systems were provided by Tian *et al.* [121] where furan-maleimide linkages were functionalised to the base epoxy, providing better thermal resistance to the DA reaction systems, while keeping thermal mending at reasonable temperatures (120 °C). The chemistry and the wide variety of the different existing DA reaction systems was reviewed by Liu and Chuo [25] and Bergman and Wudl [15]. These thermally re-mendable systems led to a first patent in sport equipment (golf ball) [122], which was complemented by another patent on the DA reaction itself two years later [123].

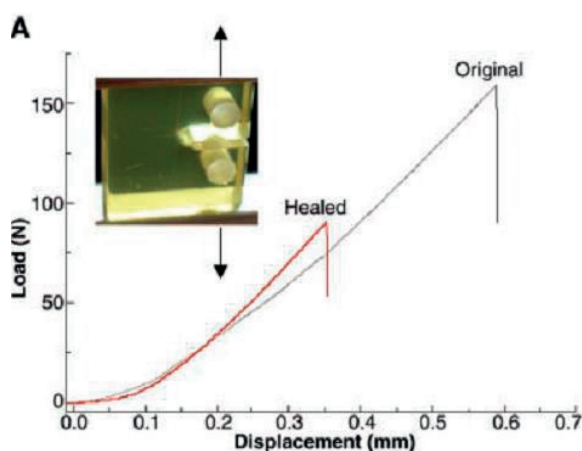


Figure 2.16: Mending efficiency obtained by fracture toughness testing of compact tension test specimens [119].

2.4.3 Self-healing through chain re-entanglement

Self-healing through reversible covalent bonding demonstrated efficient crack healing; however, it implies completely new formulations of resin systems, which can delay its introduction into composite manufacturing. A self-healing system using conventional resin systems can thus be of better use for the industrial field. In that scope, the self-healing concept in thermoset materials can also be achieved by dispersing a thermoplastic polymer, which can melt upon heating and achieve crack healing. The first study in this field is a set of two papers by Hayes *et al.* [64], [124] where a solid-state epoxy resin was created by dissolving a thermoplastic (polybisphenol-A-co-epichlorohydrin) into *Epikote 828* epoxy resin (a conventional diglycidyl ether bisphenol A (DGEBA) resin). Upon curing, the thermoplastic remained dissolved into the thermoset. After damage was created, healing could be achieved through heating at 130 °C where the thermoplastic diffused through the thermoset allowing chain bridging and re-entanglement of the crack faces. Results showed recovery in load to failure of these blend samples up to 70% with CT tests, and a recovery in Charpy impact energy of 50%.

Another similar idea comes from older studies on the subject of brittle thermosets (mainly epoxy resins) toughened by thermoplastic additives. Using thermoplastics has the advantage to provide toughening without affecting thermal-mechanical properties [125] as opposed to rubber toughening (rubber and thermoplastic toughening are discussed in section 2.6.2.1). Toughening of thermoset matrices by thermoplastic additives (in an amount between 2-50 wt%) is usually achieved thanks to a phase separation process where the initial thermoset-thermoplastic blend is homogeneous and the resulting blend can contain particles, co-continuous phases or phase-inverted morphologies. The achieved morphologies depend on the thermoset/thermoplastic ratio, the cure temperature and the diffusion

rate between the phases [125]. During this phase separation, nucleation and growth, or spinodal decomposition or a mixed mode may occur, which can lead to the different morphologies stated above. Healing behaviour of these blends is then achieved through chain re-entanglement (by thermal activation) of the thermoplastic additive and is a function of the type of phases obtained through the phase separation process.

Crack healing based on this phase separation concept was demonstrated by Luo *et al.* [7]. They aimed to create a biphasic structure with a major load bearing phase (the brick) and a healing phase (the mortar) having the ability to restore structural integrity after a damage event. The concept of brick and mortar morphology for thermal mending applications is illustrated in Figure 2.17 and was applied to epoxy(DGEBA)-poly(ϵ -caprolactone) (epoxy-PCL) systems cured with 4,4'-diaminodiphenyl sulfone (DDS).

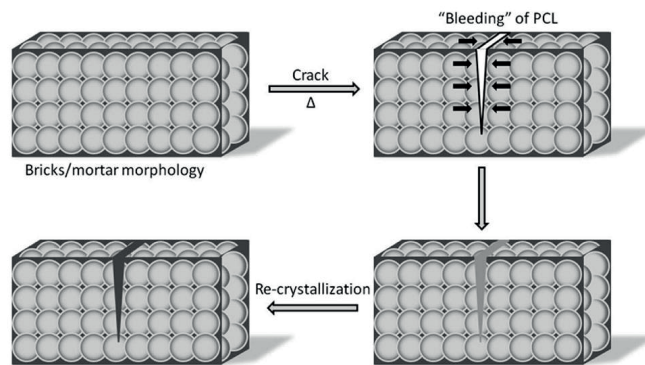


Figure 2.17: Schematic illustration of the overall mechanism of thermal mending [7].

Phase separation in thermoset-thermoplastic blends is a function of the components composition and the authors showed a range of morphologies when the PCL content in epoxy-DDS was varied from 4.3 wt% to 34.9 wt% (Figure 2.18). At low PCL content (4.3 wt%), the matrix phase was formed by epoxy with randomly dispersed PCL particles. When increasing the PCL content to 11.5 wt%, the morphology of the blend became highly complex with secondary and tertiary phase separation; however by further increasing the PCL content (15.5 wt%), the epoxy phase became the discrete phase where the brick and mortar morphology was obtained. The epoxy particulate phase appeared to be less interconnected with finer particles and observed when the PCL content was further increased (27 and 34.9 wt% PCL). From these different morphologies, that with the lower PCL content but showing brick and mortar morphology appeared to be the most promising one for thermal mending applications without affecting the material load bearing capacity thanks to the interconnected epoxy particles network.

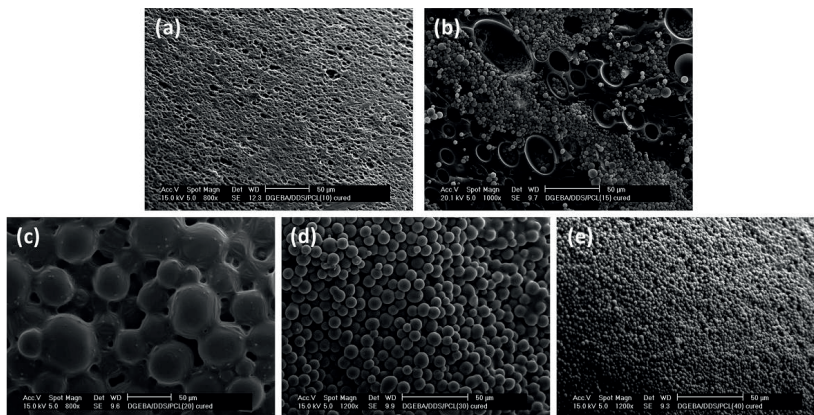


Figure 2.18: SEM images showing the bulk morphologies of fully cured epoxy-PCL(various wt%) blends of different compositions: (a) Epoxy-PCL(4.3), (b) Epoxy-PCL(11.5), (c) Epoxy-PCL(15.5), (d) Epoxy-PCL(27.0); (e) Epoxy-PCL(34.9) [7].

Healing efficiency (or thermal mending efficiency) was assessed in the same study by three-point bending, where a thermal treatment at 190 °C for 8 minutes was applied after damage. The authors showed full recovery in strain energy to failure and peak load for the blend with 15.5 wt% PCL. This healing performance was explained by a “differential expansive bleeding” (DEB) phenomenon of PCL during heat treatment. Indeed, PCL had the ability to wet the crack faces completely because it expanded at least 10% more than epoxy, enabling crack closure. This expansive bleeding behaviour as well as SEM images demonstrating crack healing are shown in Figure 2.19.

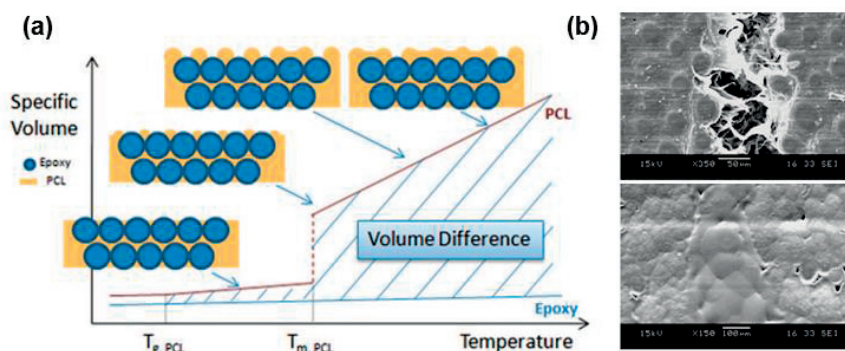


Figure 2.19: (a) Schematic illustration of DEB indicating its origin in differential thermal expansion between PCL and epoxy; (b) Visualisation of the fracture healing process demonstrating the DEB mechanism [7].

Luo *et al.* then used these blends to assess their ability to bond aluminium and steel [126]. Thanks to the flow of molten PCL upon heating, blends containing 15.5 wt% of PCL were observed to directly compete with existing reversible adhesives as they showed pull-off strength values in the range of 1-10 MPa, and this over 3 bonding cycles. They also extended their study with PCL by mixing linear and cross-linked network of PCL for shape memory self-healing coatings [127]–[129]. Shape memory through the use of PCL in thermosetting resin has been further demonstrated to visually close tension induced cracks, but no further studies are known up to date [130].

Considering the goal of the present thesis, the study of Luo *et al.* [7] on epoxy-PCL systems constitutes a reference work for achieving the introduction of epoxy-PCL systems into FRPs. Some other studies integrating PCL into FRPs were performed [131], [132] and are presented in section 2.4.5.2. Epoxy-PCL blends demonstrated thermal mending capabilities when a phase separation process takes place during material curing. The field of phase separation was well studied for epoxy-PCL blends and is detailed in the following subsection. Other epoxy-thermoplastic blends have been observed to show phase separation and are also reviewed as they may open a door for other healing systems.

2.4.3.1 Polymerisation-induced phase separation

Polymerisation-induced phase separation is the mechanism by which epoxy-PCL blends formed a morphology enabling healing. The miscibility of anhydride-cured epoxy with PCL of various low molecular weights was assessed experimentally in the 70's by Noshay and Robeson [133]. They found that, above a critical PCL molecular weight (3,000-5,000 g/mol), a two-phase structure was created, which was attributed to the reaction of PCL end groups with the anhydride curing agent. Williams *et al.* [134] reviewed this process in thermosetting polymers and showed that phase diagrams can be drawn to predict this process. In two successive studies, Chen and Chang [135], [136] applied this theory to epoxy(DGEBA)-PCL($M_n \approx 80,000$ g/mol) blends with DDS curing agent to predict if and when phase separation occurs (see Figure 2.20 for chemical formulae of these three components). PCL is miscible with some, but not all amine-cured epoxy resins. Hydroxyl groups in the amine-cured epoxy are responsible of this miscibility as they are capable of hydrogen bonding to PCL ester groups. This miscibility behaviour is one of the governing parameter for the phase separation process (i.e. immiscibility is necessary for phase separation).

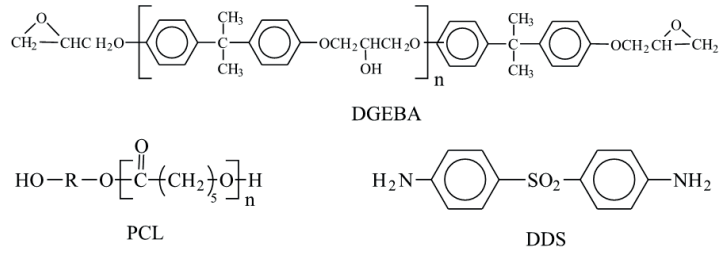


Figure 2.20: Chemical structure of DGEBA, PCL and DDS.

Chen and Chang [135], [136] studied three epoxy-PCL blend compositions cured at 150 °C: 9, 12 and 15 wt% of PCL. At 9 wt% PCL, PCL was segregated from the matrix by a nucleation and growth mechanism (see Figure 2.21). However, at 12 and 15 wt%, a complicated second phase separation was involved (see Figure 2.22 with schematic of the process on the left) [135]. From **A to C** of Figure 2.22 schematic, spinodal decomposition of the epoxy occurred and led to small epoxy particles in the matrix. From **C to E** epoxy particles grew further, connected to each other and led to the epoxy-rich macrophase domains with irregular shape. At the same time, small epoxy particles appeared in the PCL rich phase while small PCL particles appeared in the epoxy-rich phase (see point **E**). In **F**, phase inversion finally occurred and an epoxy microphase with even smaller particles appeared.

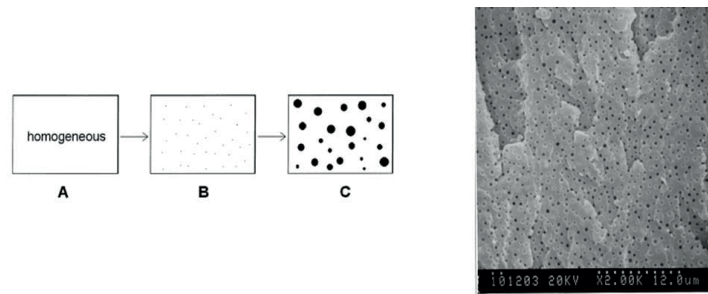


Figure 2.21: Nucleation and growth mechanism of Epoxy-PCL(9wt%) blends cured at 150 °C [135].

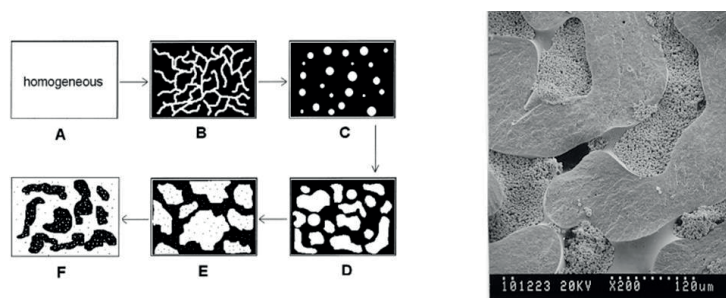


Figure 2.22: Spinodal decomposition mechanism of Epoxy-PCL(15wt%) blends cured at 150 °C [135].

To further understand the phase separation mechanisms, phase diagrams of the thermoset curing conversion (P) versus the thermoplastic weight fraction in the blend can be modelled using classical *Flory-Huggins theory* [134]. Indeed, the spinodal curve can be determined by [134]:

$$\frac{\varphi_{PCL}}{n_{epoxy}(P)} + \frac{1-\varphi_{PCL}}{n_{PCL}} = 2\chi\varphi_{PCL}(1-\varphi_{PCL}) \quad (2.15)$$

where p is the degree of epoxy conversion, ϕ_{PCL} the volume fraction of PCL, $n_{PCL} = V_{PCL}/V_r$ and V_{PCL} and V_r are the molar volumes for the PCL and the PCL monomer respectively, $n_{epoxy} = V_{epoxy}/V_r$ where V_{epoxy} is a number average molar volume estimated from the number average degree of polymerisation assuming a four-functional hardener, and χ is an independent interaction parameter to account for the effect of the increase in molar mass on miscibility.

The coexistence of the PCL and epoxy phase is characterised by the binodal curve, which is determined by [134]:

$$\Delta\mu_{epoxy}^{\alpha} = RTn_{epoxy}(p) \left\{ \frac{1}{n_{epoxy}(p)} \ln(1 - \phi_{PCL}^{\alpha}) + \left(\frac{1}{n_{epoxy}(p)} - \frac{1}{n_{PCL}} \right) \phi_{PCL}^{\alpha} + \chi(1 - \phi_{PCL}^{\alpha})^2 \right\} \quad (2.16)$$

$$\Delta\mu_{PCL}^{\alpha} = RTn_{PCL} \left\{ \frac{1}{n_{PCL}} \ln(\phi_{PCL}^{\alpha}) - \left(\frac{1}{n_{epoxy}(p)} - \frac{1}{n_{PCL}} \right) (1 - \phi_{PCL}^{\alpha}) + \chi\phi_{PCL}^{\alpha 2} \right\}$$

Chen and Chang [136] modelled the phase diagram of the epoxy curing conversion versus the PCL weight fraction for the same materials as in [135], see Figure 2.23, to understand the morphologies obtained in Figure 2.21 and Figure 2.22. The critical point of the phase diagram is located where the spinodal (dashed) and binodal (continuous) curves are cotangent; it defines if phase separation will start from the epoxy or PCL rich phase, thus leading to different morphologies in the cured state. The morphology observed in Figure 2.21 with low PCL concentration (9 wt%) is thus explained by a nucleation and growth mechanism of PCL on the left of the critical point. At higher PCL concentration (15 wt%, Figure 2.22), the process is more complicated but can be again explained by the phase diagram of Figure 2.23. First, when the epoxy conversion reaches **Point A**, above the spinodal and binodal curves, phase separation initiates by spinodal decomposition where the structure is formed of small epoxy droplets. Phases then grow and coalesce with each other to form larger particles following the binodal curve **B**→**C**. When the particles concentration exceeds a critical level, a new phase separation occurs via nucleation and growth (**D**→**E**). The epoxy microphase growth then continues until **Point F** and a similar nucleation and growth mechanism is observed through **Points F-G-H** except that smaller particles are formed as the epoxy conversion is higher. The solubility of the epoxy-rich phase gets worse as the conversion increases and a microphase of PCL is created (phase inversion) via a nucleation and growth mechanism.

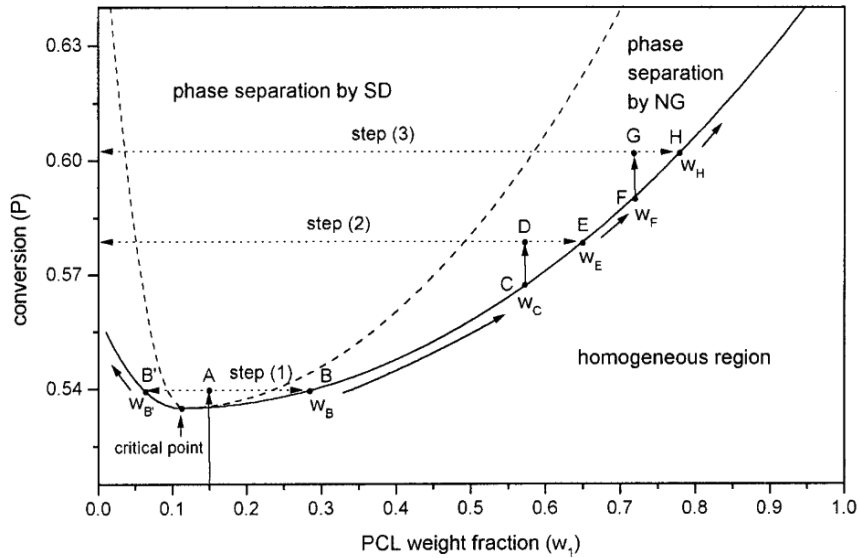


Figure 2.23: Phase diagram of the conversion (P) vs weight fraction of PCL (w_1) [136].

The brick and mortar morphology highlighted by Luo *et al.* [7] for healing applications is thus found only when spinodal decomposition happens; the construction and use of such phase diagram is therefore of high interest to design systems with this morphology.

Meanwhile, three studies [137]–[139] assessed miscibility and crystallisation kinetics of epoxy-PCL blends by Differential Scanning Calorimetry (DSC) and Fourier Transform Infrared Spectroscopy (FTIR) analyses, all with DGEBA epoxy resin and DDS or MCDEA (4,4'-methylenebis(3-chloro-2,6-diethylaniline)) curing agents as well as different PCL molecular weights ($M_w \approx 17,600$ g/mol [137] and 94,000 g/mol [138], [139]). In these three studies, the same conclusions arose: PCL and epoxy were completely miscible in the uncured state while two distinct phases existed in the cured state (either before or after the critical point of Figure 2.23). The immiscibility in the cured state was concluded from the single melting temperature shown by DSC analysis, which did not change when modifying the PCL content and by the constant rate of PCL crystallisation when the PCL content decreased.

The epoxy-PCL immiscibility in the cured state was not observed in all studies. Ni and Zheng [140] studied thermosetting blends of epoxy (DGEBA) and various PCL ($M_n \approx 80,000$ g/mol) contents cured with 4,4'-methylenebis(2-chloroaniline) (MOCA). From DSC analysis, epoxy and PCL were miscible in the cured state over the entire composition range and the T_g followed the *Gordon-Taylor* equation (notice that this equation is also valid for the blends studied in [137]–[139] in the uncured state):

$$T_g = \frac{W_1 T_{g1} + kW_2 T_{g2}}{W_1 + kW_2} \quad (2.17)$$

where k is an adjustable parameter related to the degree of curvature of the T_g -composition curve (see [140] for details) and W is the composition of the thermoplastic/thermoset phases. The miscibility in these MOCA cured blends was explained (through FTIR measurements) by the intermolecular specific interactions (hydrogen bonding), which were much stronger as compared to DDS-crosslinked epoxy-PCL blends. The origin of phase separation in epoxy-PCL blends cured with DDS was further explained by the presence of intramolecular interactions between sulfonyl and hydroxyl groups. The same author related similar miscibility behaviour over the entire composition range in epoxy-PCL blends cured with 2,2-Bis[4-(4-aminophenoxy)phenyl]propane (BAPP) [141].

Vanden Poel *et al.* [142] studied the reaction-induced phase separation of epoxy (DGEBA)-PCL ($M_w \approx 5,000$ and 50,000 g/mol) and DDS curing agent. By performing small angle laser light scattering (SALLS), the onset of phase separation as a function of the cure time/temperature and the PCL content could be obtained, and phase diagrams were built (Figure 2.24). By increasing cure temperature, the phase separation was therefore triggered earlier due to an increased reaction rate; the kinetics of this process were also increased; SEM images demonstrated a coarser microstructure. They also observed the phase separation process by optical imaging at different cure times (Figure 2.25), and a similar spinodal decomposition with secondary phase separation by nucleation and growth as that schematically represented in Figure 2.22 was observed.

By mixing PCL in epoxy, the viscosity of the resulting blend (a critical factor for fibre-reinforced composite processing) is expected to increase. Barone *et al.* [143] studied the miscibility of epoxy (DEGBF)-PCL ($M_w \approx 80,000$ g/mol) and DETDA curing agent in the uncured state. As in previous studies, they showed complete miscibility over the entire composition range. Moreover, they measured the viscosity of these uncured blends as a function of the PCL content and time. Because the blends were miscible over the entire composition range, their viscosity was observed to increase linearly with the PCL content following a logarithmic rule of mixture.

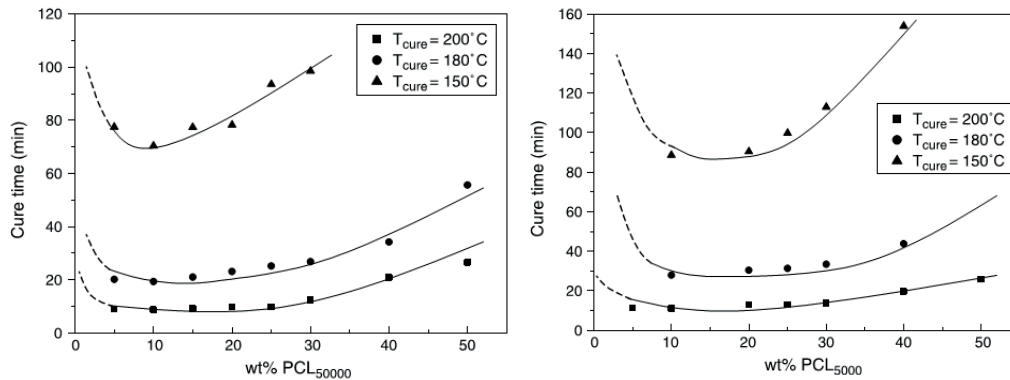


Figure 2.24: Onset of phase separation for (a) DGEBA-PCL_{50,000} and (b) DGEBA-PCL_{5,000} blends at different isothermal cure temperature (T_{cure}) [142].

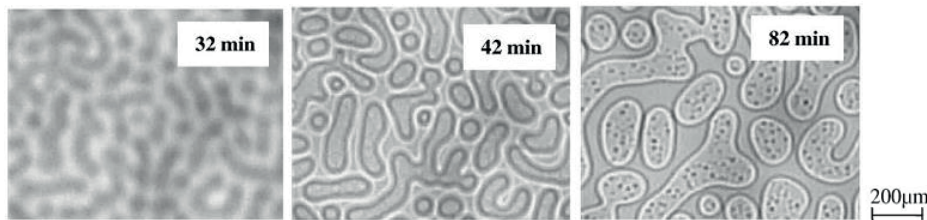


Figure 2.25: Optical microscopy images captured during the curing at 180 °C at the indicated time for 25 wt% PCL_{5,000} blends [142].

Critical factors leading to a reaction-induced phase separation mechanism in epoxy-PCL blends are therefore: the type of curing agent, the PCL molecular weight, the cure temperature and cure time. The range of morphologies observed for different PCL content may obviously alter the blend mechanical properties in addition to the sole variation in component concentration. Siddhamalli [144] assessed mechanical properties (tensile and 3-point bending) of phase-separated blends prepared by mixing DDS cured epoxy resin with two different PCL ($M_w \approx 4,000$ and $40,000$ g/mol) and 0, 10, 20 and 30 wt% of PCL in the blends. Their results showed improvements in tensile elongation and decrease in flexural strength with the increase in PCL content. However, the elastic modulus and the tensile strength showed an optimum of PCL concentration between 20 and 30 wt% for the low molecular weight PCL and between 10 and 20 wt% for the high molecular weight PCL. While with the high molecular weight PCL, the epoxy particulate phase-separated morphology demonstrated lower strength (45%) than the reference epoxy specimen, the blends with the same morphology but the lower molecular weight PCL demonstrated slightly higher strength (3%) than the reference epoxy. Also, a 3.4 times fracture energy improvement was observed in blends of PCL and a cationically polymerised cycloaliphatic epoxy resin as compared to reference epoxy specimens [145], but no further characterisation was given. These studies suggest that the mechanical properties may vary significantly for a given overall composition, depending on the relative stiffness and strength of the continuous and discrete phases, and the mechanisms of energy dissipation during crack propagation.

Other epoxy-thermoplastic systems display the two-phase morphology observed with PCL and a non-exhaustive set of examples are given below. For more examples the reader is referred to the following reviews [134], [146]. Thermoset-thermoplastic phase separation was observed for example by Zhang *et al.* [147], in blends made of epoxy and PVA, PMMA, PSF, PEI or PI. To the critical factors leading to phase separation cited above, an additional one was demonstrated in this study as the T_g of the thermoplastic: the higher the T_g , the broader the composition range where a complex morphology with secondary and tertiary phase separation existed. In blends made of epoxy (DGEBA)-PES (poly(ether sulfone)) and an amine curing agent, the epoxy phase-separated globular morphology was also observed [148]–[150]. Phase diagrams similar to Figure 2.23 were drawn as well as time-temperature-transformation (TTT) diagrams where phase separation was explained through a five stage transformation [148]: (i) onset of phase

separation; (ii) gelation; (iii) fixation of the dimension of phase-separated structure; (iv) end of phase separation and (v) vitrification. Another study [125] on epoxy-PES blends showed nucleation and growth of PES particles (i.e. the PES concentration was low in the blend (5 wt%)) in presence of a fibre reinforcement. Interface morphology of this blend with single glass and carbon fibre was studied and led to a main conclusion: the heating rate during cure induced a significant influence on the fibre-matrix interface morphology as a higher heating rate led to accumulation of PES particles close to the fibres in both glass and carbon reinforcements. No mechanical characterisation of the interface was performed, but higher interface strength can be expected with higher heating rate during cure.

Interface studies were also conducted in epoxies modified by PMMA (poly(methyl methacrylate)) or PS (polystyrene) and reinforced by glass fibres [151], [152]. The concentration of PMMA (or PS) being low (less than 5 wt%), particles of PMMA (or PS) were formed by phase separation and segregated at the fibre-matrix interface, preventing crack propagation. This particle aggregation behaviour in fibre-reinforced epoxy-thermoplastic (low weight content) systems was also observed (by SEM) with the use of polysulfone (PSU) [153], a high T_g thermoplastic, and demonstrated a 60% fracture toughness (K_{IC}) improvement [154]. Phase separation of PSU with epoxy was also studied in [155], [156], but no mechanical characterisation could be found to date. Oppositely, it has been demonstrated that with epoxy-PEI (polyetherimide, another high T_g thermoplastic) blends as a matrix in fibre-reinforced composites with high thermoplastic concentration [157], the resulting morphology consisted in epoxy particles with a surrounded PEI matrix. However, due to preferential wetting of the fibres by the epoxy, these were surrounded by a thin epoxy layer. Epoxy-PEI phase-separated blends have been extensively studied in [158]–[161]. Another study of this epoxy-thermoplastic system reinforced by glass fibres [162] showed good adhesion (SEM observation) between the fibre and the matrix, providing good expectations for an application to structural composite materials. This good adhesion resulted most probably from the epoxy-glass interface thanks to the observed wetting behaviour.

Blends made of epoxy and PMMA were also highly studied for their phase separation behaviour upon polymerisation. As for PCL, the type of epoxy curing agent was observed as determinant in the miscibility behaviour of this thermoset-thermoplastic system [163]. Indeed, DDS and MDA curing agents led to phase-separated blends whereas the use of MCDEA led to a uniform structure, indicating full miscibility of PMMA and epoxy in the cured state. For phase-separated systems, at low PMMA contents, the morphology consisted of PMMA particles embedded into an epoxy matrix, until a threshold (the critical point) was reached where a complex phase-separated morphology was observed. These two types of morphologies were also studied for their capacity to improve toughness [164] and flexural properties [165] of neat epoxies (this will be further discussed in section 2.6.2.1). At higher PMMA content, phase inversion also occurred and led to epoxy spheres embedded in a PMMA matrix [166], [167]. However, as compared to PCL systems, epoxy particles were in this case not interconnected and not spherical. Rastegar *et al.* [168] demonstrated that mechanical property improvements could be achieved with very low PMMA content (2.5 wt%) and the co-continuous phase-separated morphology if a mix of curing agents is used. Indeed, partially using a curing agent that did not induce phase separation could lower the thresholds of phase separation morphologies. Interface properties between the different phases were moreover improved.

PS was also used to create the brick and mortar morphology where spinodal decomposition and epoxy particles formation was observed [169], [170]. In that case [169], optimal blend compositions (10 wt%) showed improvements (as compared to neat epoxy systems) in fracture energy, G_{IC} , from 175 J/m² for the neat brittle epoxy to 810 J/m² for the modified system.

PPE (poly(2,6-dimethyl-1,4-phenylene ether)) also exhibits this two-phase morphology when dissolved in epoxy and then cured. PPE is a high T_g thermoplastic used for some structural applications, however its processing route is difficult due to its high viscosity and therefore its dissolution into epoxy is of high interest. By SALLS measurement, Ishii and Ryan [171] demonstrated the spinodal decomposition of epoxy-PPE systems and defined a four stage process: (i) reaction prior to phase separation; (ii) early stage of spinodal decomposition; (iii) late stage of spinodal decomposition and (iv) refractive index variation and apparent phase dissolution. Globular epoxy morphology was

similar to epoxy-PCL systems and this brick and mortar type material was observed to provide toughness improvements as compared to neat epoxy systems [172].

2.4.4 Self-healing through non-covalent bonding

The third class of intrinsic self-healing systems comprises systems where healing occurs through reversibility of non-covalent bonds. Two classes can be identified: systems with ionomeric copolymers and systems with supramolecular materials.

Ionomeric copolymers contain ionic segments having the ability to form clusters that act as reversible cross-links. These clusters can then be triggered by UV radiation or temperature multiple times thanks to the reversibility of the system. The principal ionomeric copolymer studied in healing systems is polyethylene-co-methacrylic acid (EMAA). Kalista *et al.* [173], [174] performed projectile and peel testing of commercial EMAA copolymers *Nucrel*[®] 925 and 920 from *Dupont*. They showed by peel tests that the maximum load was reached when the two peel faces were placed in contact for short times around the melting temperature of EMAA, which hints towards their potential properties for ballistic puncture repair. This was confirmed by projectile testing with a bullet at a measured speed and energy of 197 m/s and 9.9 Joules, respectively. The bullet energy was transferred to the resin through friction, allowing a local temperature of 98 °C which was slightly above the melting temperature of EMAA. The hole obtained after puncture was completely closed and the authors defined a three-stage process for explaining the healing mechanism: (i) elastic recovery of the surface which brought back the hole faces almost in contact (ii) interdiffusion and sealing (iii) strength generation thanks to further interdiffusion, crystallisation and polymer chains long term relaxation. Similar ballistic impact recovery was observed by Varley and van der Zwaag [175], [176] with another commercially available ionic copolymer: *Surlyn 8940* from *Dupont*.

Meure *et al.* [177] further integrated EMAA into DGEBA epoxy and cured it first at 50 °C with a TETA (triethyltetramine) curing agent. DGEBA and TETA were adsorbed by EMAA thanks to hydrogen bonding and ionic bonding respectively. Then, during post-cure at 150 °C, covalent bonding was formed between DGEBA and EMAA in addition to the reversible hydrogen and ionic bonds. The fully cured system thus experienced strong adhesion between the different chemicals (that are immiscible in the cured state, similar to the systems of Luo *et al.* [7]) while some weak links allowed the healing properties. This concept was demonstrated by mechanical characterisation when integrating 15 vol% EMAA particles (250-425 µm diameter) into the DGEBA-TETA system [178]. They first measured the effect of these particles on the initial resin properties and showed that the load to failure obtained in TDCB and SENB (Single Edge Notched Bend) tests was increased by respectively 10 and 25% when EMAA particles were inserted into the resin system. They assessed healing by damaging the specimens with a first test (either TDCB or SENB) and by retesting it after a healing cycle of 30 minutes at 150 °C. This led to recovery in fracture strength of 81% and 85% for SENB and TDCB respectively. These healing properties were attributed to a differential expansive bleeding mechanism like the one defined in [7] as the thermal expansion coefficient of EMAA is around 7 times higher than that of epoxy. In addition to this mechanism, optical microscopy images (Figure 2.26) showed the formation of small bubbles within EMAA particles during post-curing at 150 °C due to volatile products formed by the reaction of EMAA with epoxy. Therefore, during healing, the EMAA clusters started to melt; due to their high thermal expansion coefficient and the expansion of the bubbles, EMAA was forced into the crack plane and thus brought in contact the two crack faces. A schematic of this process is depicted in Figure 2.27.

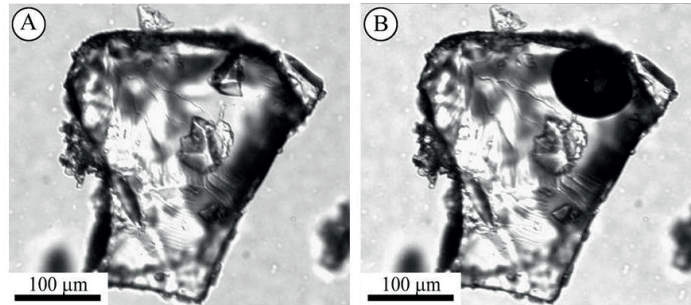


Figure 2.26: Transmission optical microscopy images of the EMAA particle embedded in epoxy resins (A) prior to post-curing at 150 °C and (B) after 5 min at 150 °C [178].

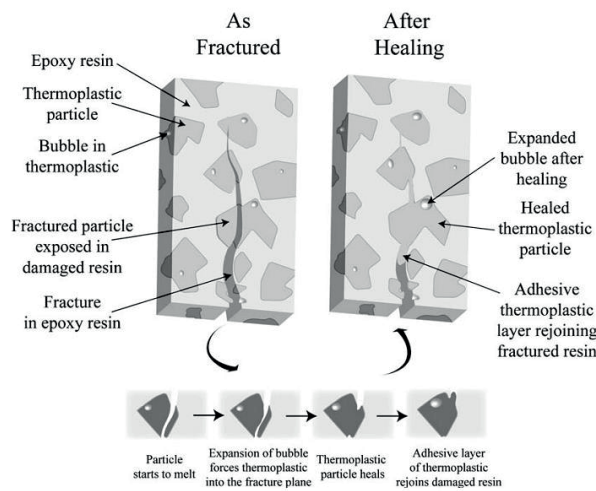


Figure 2.27: Schematic of the healing agent delivery mechanism utilised by the mendable epoxy resins containing EMAA particles [178].

The same cluster principle as for the ionomeric copolymer EMAA has been applied for solid-state healing of epoxy, with an amine curing agent and with dissolved poly(bisphenol-A-co-epichlorohydrin) (PDGEBA), polyvinyl chloride (PVC), polyvinyl alcohol (PVA), polyethylene (PE) and polypropylene (PP) [179] as well as with low molecular weight polybisphenol A-co-epichlorohydrin thermoplastics [180]. The healing process in these systems was also activated by a thermal trigger.

In order to avoid a thermal trigger, systems based on non-covalent interactions have been developed [20], but resulted in low mechanical properties and are thus of lower interest for the present work. To overcome this issue while keeping the healing process at room temperature (even if helped if the temperature is increased), hybrid systems combining covalent and non-covalent bonds were developed [181]–[183]. Especially, Sordo *et al.* [182] have successfully demonstrated that by combining bifunctional and tetrafunctional epoxy resins, the resulting resin has the ability to fully recover (after 24h healing at room temperature) tensile properties after a cut.

2.4.5 Integration to FRPs

Resin based intrinsic self-healing systems showed appropriate recovery of mechanical properties after a damage event. However, their integration into FRPs leads to a more complicated problem as the fibre reinforcement can influence the healing system behaviour and also its process ability (key parameters of self-healing integration to FRPs are given in section 2.5.2 for extrinsic self-healing systems which induce the same, but more, parameters). Studies, which integrated the three types of intrinsic self-healing systems to FRPs, are given below.

2.4.5.1 Matrix based reversible bonding systems

Park *et al.* [184] proved the efficiency of remendable matrices based on the DA reaction once inserted into an FRP. They processed a carbon fibre composite with this matrix by a pressure holding process in an autoclave and achieved a fibre volume fraction of 40%. They assessed damage healing efficiency through 3-point bending tests and showed recovery in strain energies of 92.3%, 94.2% and 94.3% after the 1st, 2nd and respectively the 3rd thermal treatment at 150 °C through resistive heating; however this healing temperature was higher than the glass transition of the matrix and no quantification of the properties in the damage state were performed. Notice that hardness of these systems was also assessed and showed values similar as a traditional DGEBA epoxy resin (*EPON 862*) used in the aerospace industry.

Even though the processing route of Park *et al.* [184] allowed the production of FRPs with fast curing healing resin systems, many conventional composite manufacturing processes are nowadays based on resin infusion. To solve this problem, Ghezzi *et al.* [185] developed an adapted RTM (Resin Transfer Moulding) technique to infuse a carbon fibre reinforcement with the same resin system as described in Chen *et al.* study [119]. Their resin injection system had the ability to mix the resin just before the resin entry in the mould, to accommodate its fast reaction kinetics. Even if the resin was not degassed before injection, a void content less than 1.2% was achieved. However, no damage healing characterisation was performed in this study. Heo and Sadano [186] achieved the production of short-beam-shear specimens with similar systems as Ghezzi *et al.* [185] by vacuum assisted transfer moulding. Short beam strength healing efficiencies of 85% and 73% for respectively the first and second healing cycle were demonstrated while keeping intrinsic mechanical properties of the laminates in the range of conventional carbon-epoxy systems.

A recent study [76] successfully processed, by vacuum assisted resin infusion moulding, glass fibre-reinforced composites based on disulphide-containing organic-inorganic thermoset matrices and achieved fibre volume fractions of about 50%. By inducing damage followed by a thermal treatment at 85 °C for 16h (with an applied pressure up to 20 bars), the authors demonstrated full recovery of interlaminar fracture toughness and recovery of 8 Joules impact damage in excess of 80%. As with other intrinsic healing systems that do not expand upon heating (unlike thermoset-thermoplastic blends [7] or systems using EMAA [177]), the authors here suggested to use pressure to bring the crack faces into contact before the healing process can start. It is of course disputable whether the application of pressure is technologically relevant to provide crack healing; however, as mentioned in [76], small de-mounted composite parts can be of interest for such systems. Applying pressure to bring the crack faces into contact before healing is further discussed in section 2.5 with extrinsic healing systems.

2.4.5.2 Matrix based chain re-entanglement systems

Some authors integrated similar matrix based chain re-entanglement systems to FRPs for toughening purposes (see section 2.6.2.1). However, using these blends into FRPs for healing purposes is almost inexistent to date. Lim and Pickering [187] used a blend of epoxy and PBE (poly(bisphenol A-co-epichlorohydrin)) into a carbon fibre fabric processed by hand lay-up. No characterisation of healing into this material was performed (even though the authors stated its healing properties); however they demonstrated an increase of 5% and 17% in modulus and strength respectively as compared to the fabric with pure epoxy. Another study using PCL under the form of particles and integrated into a PU (polyurethane) fibre based epoxy resin system was performed by Li *et al.* [131]. The PU reinforcing fibres were shape memory fibres that were well characterised in a previous study by the same authors [132]. PCL ($M_n \approx 45,000$ g/mol) was mixed with an epoxy resin at room temperature in order to keep the PCL particles extrinsically in the system. Healing characterisation was performed by TDCB testing with a healing cycle of 15 minutes at 80 °C to allow PU fibres and PCL particles performing shape and interface recovery respectively. This healing process triggered by temperature was a two-stage process: first the PU shape memory fibres closed the crack; second the PCL healing agent wetted and healed the crack. Recovery in load to failure in excess of 90% after TDCB testing was observed for several healing cycles, showing the efficiency and repeatability of this healing system.

2.4.5.3 Matrix based non-covalent bonding systems

EMAA was integrated into FRPs under the form of particles [188], [189], layers [190] or stitches [102], [191]–[193] to form localised clusters and provide healing once heated (as depicted in Figure 2.27). Pingkarawat *et al.* [188] inserted EMAA particles into an FRP made of the DGEBA-TETA system and a plain weave carbon fabric. The composite was processed by hand lay-up with 10 wt% particles spread on the fabric. A similar procedure was used to process specimens with various thermoplastics: PEGMA (polyethylene-co-glycidyl methacrylate), EVA (ethylene vinyl acetate) and ABS (acrylonitrile butadiene styrene). Notice that PEGMA is also a reactive thermoplastic, which has the ability, as EMAA, to expand during healing. They quantified healing through Mode I DCB testing by damaging first the specimens and then performing a healing cycle of 30 minutes at 150 °C. Interlaminar fracture toughness, G_{IC} , was improved by 63%, 25%, 260% and 0% for EMAA, PEGMA, EVA and ABS respectively as compared to neat epoxy composites. After healing, recovery in G_{IC} was of 156%, 57%, 103% and 0% for EMAA, PEGMA, EVA and ABS respectively. Healing through EMAA modification was therefore confirmed by this expansive bleeding mechanism, whereas for PEGMA, even if the same mechanism occurred, the interface strength with the epoxy matrix seemed lower from SEM imaging. EVA also showed good adhesion with the epoxy, which was translated in good healing properties even if no clustering mechanism was formed (EVA has the lowest viscosity and was therefore able to easily flow into the crack). Finally, ABS showed no improvement as this thermoplastic has a high viscosity at the healing temperature and could not flow into the crack.

Wang *et al.* [190] studied the effect of EMAA patches covering 23% of the interlayer of a carbon-epoxy prepreg composite. Covering part of the composite surface was made in order to limit the loss in composite structural integrity when integrating such healing agent at the crack plane [194]. They assessed interlaminar fracture toughness by Mode I DCB testing and interlaminar shear strength by short-beam-shear testing (SBS), before and after healing at 150 °C for 30 minutes. As expected from the tough but low shear strength EMAA, interlaminar fracture toughness and interlaminar shear strength of the pristine specimens were respectively increased and decreased by 106% and 33%. Also, healing efficiencies were observed to be 88% and 36% for DCB and SBS tests respectively. Healing efficiency for DCB was lower as compared to the study of Pingkarawat *et al.* [188] and was explained by the lower ability of the EMAA to cover the crack plane during healing (here estimated as 25%). The authors also provided theoretical predictions of interlaminar fracture toughness before and after healing as well as predictions of short-beam-shear strength, all in function of the healing agent areal coverage. These were based on the constrained-layer fracture model developed by Wang [195], [196]. In particular, fracture energy can be expressed in terms of the elastic-plastic properties of the constrained layer as:

$$G_c = t_h \int_0^{\varepsilon_f} \sigma d\varepsilon \quad (2.18)$$

where t and ε_f are the thickness and the failure strength of the constrained layer. If the area of the healing material is A_h , the total interlaminar fracture energy of the composite containing the healing agent is given by a rule of mixture based equation, which can be written as:

$$G_c = A_h G_{c,healing} + (1 - A_h) G_{c,laminate} \quad (2.19)$$

After healing, the interlaminar fracture energy is that of the healing agent (i.e. $G_{c,healing}$). However, the relative area of the healing agent after repair, A_h^* , is generally larger than the initial area. The interlaminar fracture energy after healing must thus be written as:

$$G_c = A_h^* G_{c,healing} \quad (2.20)$$

Finally, short-beam-shear strength can be estimated for the modified composite in a similar way as for interlaminar fracture energy as:

$$\tau_{SBS} = A_h \tau_{EMAA} + (1 - A_h) \tau_{epoxy} \quad (2.21)$$

where τ_{epoxy} and τ_{EMAA} denote the shear strengths of the epoxy and EMAA respectively. The agreement between these three equations and the experimental data of Wang *et al.* [190] is demonstrated in Figure 2.28.

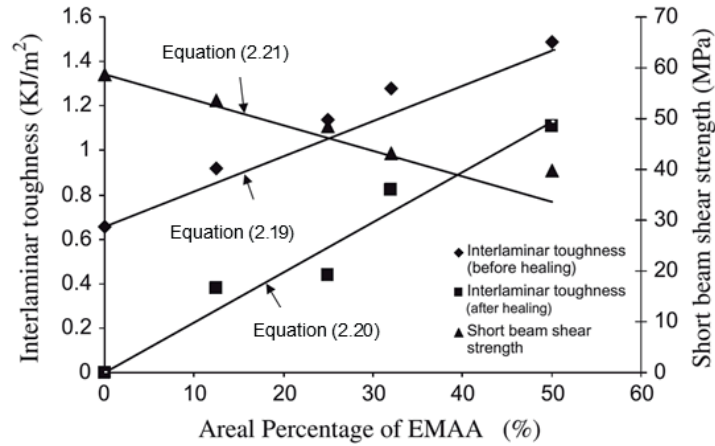


Figure 2.28: Experimental interlaminar fracture toughness and short-beam-shear strength of modified carbon-epoxy prepreg with EMAA layers and comparison with theoretical constrained-layer fracture models [188].

Finally, EMAA was incorporated into FRPs as stitches. Meure *et al.* [193] extended their previous work to carbon fibre reinforcements made by hand lay-up with an epoxy (DGEBA) resin. They produced two different EMAA stitches (50 to 75 and 100 to 150 μm diameter) by continuous fibre extrusion and inserted them into the carbon reinforcement with two different configurations (two or four interleaves). They performed Mode I DCB testing, before and after healing at 150 $^{\circ}\text{C}$ for 30 minutes, and compared these results with those of specimens modified by EMAA particles. The areal weight of particles on each ply was 33 g/m^2 and the one with the highest stitch content (4 interleaves of 100 to 150 μm diameter) was 27 g/m^2 on each ply. Recoveries in failure energy, G_{IC} and peak load (again after thermal treatment at 150 $^{\circ}\text{C}$ for 30 minutes) were respectively of 221, 185 and 121% for the particle specimens whereas of 137, 45 and 119% for the stitched specimens. Notice that G_{IC} recovery showed a maximum of 156% when 2 interleaves of 100 to 150 μm diameter were used. The authors also performed repeated healing tests and showed a constant recovery in peak and failure energy over 10 healing cycles. However, G_{IC} recovery decreased over these repeated cycles and this was explained by a gradual increase of carbon fibre breakage. Notice that damage recovery by EMAA was confirmed in this study by visual observations of damaged and healed fracture surfaces, which were previously stained with potassium; images overlay provided insights of EMAA morphology and its flow into the crack during the healing treatment.

EMAA stitching of composite laminates was further assessed in [102], [191], [192], [197]. In particular, the stitch size and density inside the composites were varied and showed improvements in interlaminar fracture toughness (from 35 to 650%) as well as multiple cycle crack healing capabilities (from 50 to 250%). Even though the presence of stitches reduced tensile and compressive strength up to 50%, this loss was deemed acceptable considering the great improvements in other properties. The high healing efficiencies could be achieved only through an appropriate design of the stitching network providing sufficient EMAA flow into the crack plane (see Figure 2.29). Indeed, EMAA stitches were inserted through the thickness of the prepreg, but EMAA filaments were also inserted within the prepreg ply to interconnect the stitch bends. The healing mechanism was then similar to that for particles or patches: upon heating, EMAA flowed into the crack plane thanks to the pressure driven mechanism, then two EMAA stitches were bridged thanks to the interconnected fibre network supplying the healing agent (see Figure 2.30).

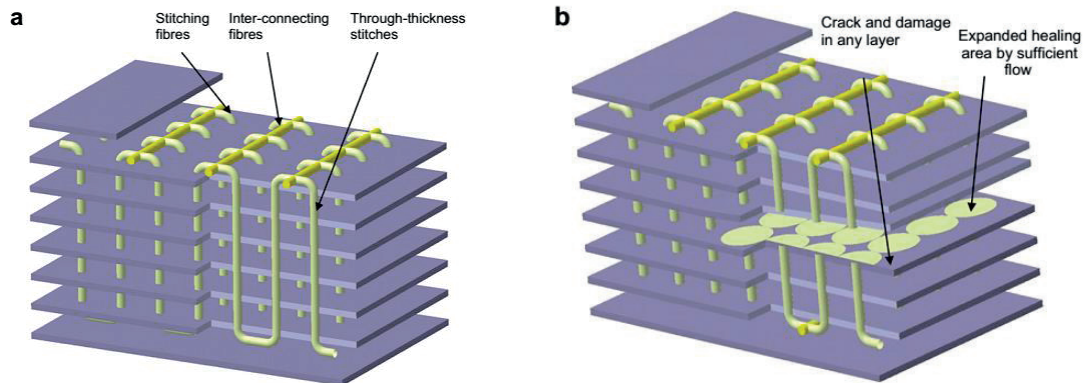


Figure 2.29: Schematic representations of the 3D stitched network (a) before healing and (b) after healing in the carbon fibre-epoxy laminate [192].

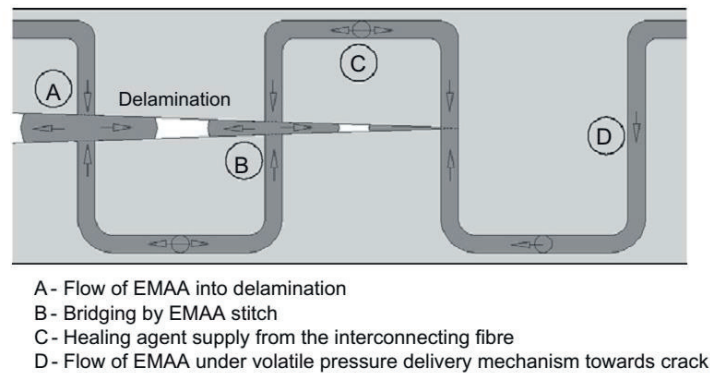


Figure 2.30: Schematic representation of the self-healing delivery mechanism for the stitched laminate [192].

Yang *et al.* [191] applied this stitching 3D network to carbon fibre-epoxy composite T-joints in the stiffener web and flange directions. Experimental work on the T-joint pulled by the stiffener direction showed that fracture work (representative to toughness) of the joint increased by 20% without reducing stiffness and strength, whereas stiffness, ultimate tensile load and absorbed energy were restored by more than 50%. This incomplete restoration was explained by the impossibility of the mendable thermoplastic to infiltrate every damage site due to the low stitch density used. EMAA stitches could therefore be an appropriate and efficient healing mechanism to be used in FRPs as it is cheap, effective and easily processed thanks to conventional stitching production methods.

Hybrid supramolecular systems were also used as a matrix in glass fibre-reinforced polymer composites. Sordo and Michaud [198] demonstrated that composites with 50% volume fraction could be successfully processed by conventional manufacturing techniques, and provided recovery (after healing at room temperature) of the flexural strength and bending stiffness respectively of 65% and 72% [198] as well as recovery in impact force and dissipated energy of respectively 55% and 76% [75]. Even though these systems have shown high healing and damping properties, the low stiffness of the obtained composites limit them to semi-structural applications.

2.5 Extrinsic self-healing

In extrinsic self-healing systems, the healing agent is inserted extrinsically (embedded or encapsulated) in the resin. When a crack propagates, it ruptures a container with the healing agent, which is released into the crack plane, flows thanks to capillary forces or under an externally applied pressure and heals the crack. Two types of containers are studied in this field: healant loaded microcapsules and healant loaded tubular pipes (Figure 2.31).

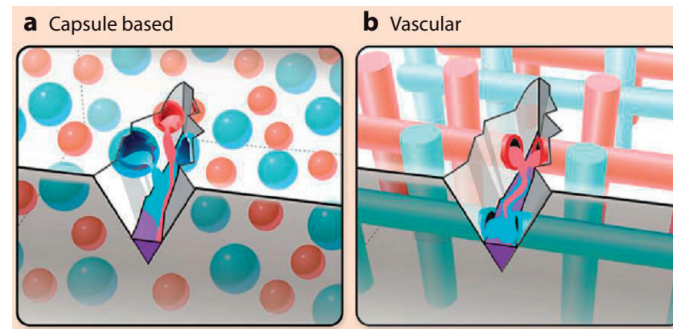


Figure 2.31: Approaches to extrinsic self-healing: (a) capsule-based systems where the healing agent is stored into capsules (blue is the resin and red the curing agent) until the crack ruptures these capsules which allows delivery of the healing agent into the crack plane; (b) vascular networks where the healing agent is stored into tubes or hollow fibres (blue resin and red curing agent) until the crack ruptures these tubes which allows delivery of the healing agent into the crack plane [4].

2.5.1 Vascular system

The field of extrinsic self-healing systems in FRP was pioneered by the University of Illinois at Urbana-Champaign (USA) where they developed a fibre-reinforced polymer with hollow fibres containing a healing agent [199]. These fibres were placed at regular intervals into the FRP; when a crack propagated into the FRP, these hollow fibres broke and released the healing agent (see Figure 2.31 (b)). The repair efficiency of this system was assessed through SEM imaging where migration of the healing agent inside the crack could be identified.

These systems demonstrated high amount of recovery with impact induced damage. Williams *et al.* [200] observed, in a carbon fibre-reinforced polymer with a resin filled hollow glass fibre system distributed at specific interfaces, a compressive strength recovery of 84%. While this value has been measured for impacts at 2.2 Joules energy (i.e. generating small matrix cracks), this system was not able to efficiently heal larger impact damage and the importance of optimising the location, the viscosity and the amount of resin necessary to fill the damage volume was highlighted. Norris *et al.* [201] demonstrated that the above-mentioned optimisations enabled this system to fully recover compressive strength after impacts up to 20 Joules. Even though vascularised systems demonstrated the ability to fully heal large damage extents, using such multifunctional systems in real life structures remains difficult due to their inability to (i) provide multiple healing to a single damage and (ii) heal low levels of damage that do not rupture a vasculature. The multiple healing issues were improved through 3D microvascular networks delivering the healing agent, made by inserting a fugitive template which is removed after composite processing. This improvement was inspired by biological systems where networks of blood allow recovery of injuries. Figure 2.32 depicts an application of these systems to FRPs [202]. The 3D network contains two different types of channel where resin and hardener are flowing. Once a crack propagates at the inter-layer, the channels are broken releasing these two components that will mix and cure, repairing the crack. This concept allows multiple healing to occur as both channels in the network keep their healing agent as liquid. Through Mode I DCB testing, healing efficiencies of more than 100% were demonstrated over 3 cycles.

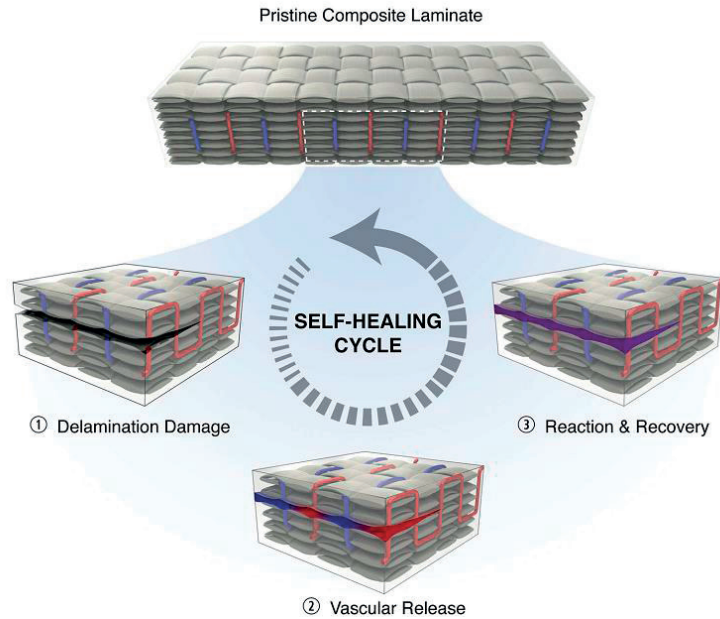


Figure 2.32: Life-cycle of a self-healing microvascular fibre-composite. Pristine woven composite laminate showing stacked textile reinforcement with dual-channel (red/blue), liquid filled vascular network. Delamination damage ruptures the internal vasculature leading to release of reactive liquid healing agents from fractured micro-channel orifices. Molecular diffusion and polymerisation (purple) of the healing agents leads to restoration of structural integrity over multiple healing cycles [202].

2.5.2 Microcapsule systems

University of Illinois at Urbana-Champaign (USA) also pioneered in 2001 the microcapsule healing concept, explained through Figure 2.33 (left) [203]. Their concept consists in inserting microcapsules containing a liquid healing agent into a matrix containing a catalyst. When a crack forms into the matrix, it ruptures the capsule (Figure 2.33 (right)), delivering the healing agent into the crack plane where curing can occur thanks to the embedded catalyst. The efficiency of this system was assessed by Mode I TDCB testing in neat epoxy resin and 75% recovery in fracture load was demonstrated.

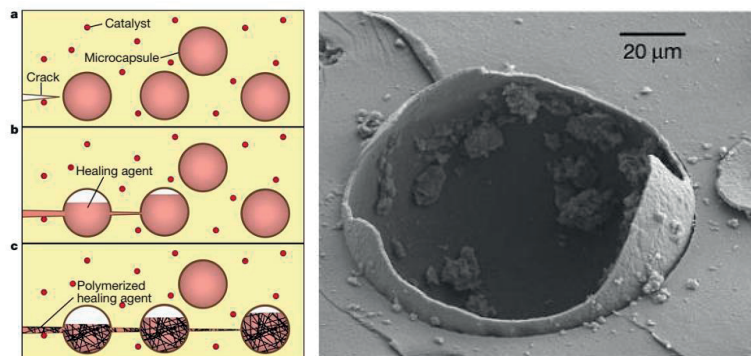


Figure 2.33: (left) The autonomic microcapsules healing concept. A microencapsulated healing agent is embedded in a structural composite matrix containing a catalyst capable of polymerising the healing agent. (a) Cracks form in the matrix wherever damage occurs; (b) the crack ruptures the microcapsules, releasing the healing agent into the crack plane through capillary action; (c) the healing agent contacts the catalyst, triggering polymerisation that bonds the crack faces closed. (right) SEM image showing rupture of the microcapsule inside the material fracture plane [203].

Within this microcapsule based self-healing concept, four different schemes used to incorporate the healing capsules can be highlighted:

- **Capsule-catalyst system:** the healing agent is a liquid encapsulated component and the catalyst is a dispersed phase. The best known example is the dicyclopentadiene (DCPD)/Grubb's first generation catalyst system (White *et al.* [203]). The healing phenomenon taking place in this system is based on the ring-opening metathesis polymerisation (ROMP) of DCPD catalysed by the Grubb's component. This last is usually encapsulated in a shell of wax to prevent its deactivation if in contact with the other components in the system. Several encapsulation techniques and materials have been proposed for the liquid; however they are almost all based on the same principle: either urea-formaldehyde (UF), melamine-formaldehyde (MF), melamine-urea-formaldehyde, polyurethane (PU) or acrylates are used to create a polymer shell wall at the interface of droplets (the liquid agent to be encapsulated) in an oil-in-water (o/w) emulsion.
- **Multicapsule:** both the healing agent and the catalyst are encapsulated [204]–[206]. The healing agent encapsulation is similar to that above, whereas methods to encapsulate the catalyst vary.
- **Latent functionality:** a solvent/resin blend is encapsulated as the two other schemes and reacts through diffusion into the host matrix and activation of latent functionalities [207]–[210].
- **Phase separation:** One of the two components is phase-separated within the matrix, whereas the other may be encapsulated or dispersed into the matrix [211], [212].

The microcapsule healing system of White *et al.* [203] was integrated to FRPs, both for glass and carbon reinforcements [63], [65], [78], [80]. Healing of delamination damage was first assessed through DCB testing of woven E-glass/epoxy composites (a plain and satin woven reinforcement) [65]. Two types of specimens were manufactured by hand lay-up: reference specimens (without any healing agent) and self-activated specimens (the catalyst was embedded into the resin of the composite). The reference specimens were first tested, and at the highest displacement point of the curve, the already mixed DCPD-catalyst was manually injected thanks to a syringe. The specimen was left at rest for 48h and then retested. For the self-activated specimens, the same procedure was used except that only the DCDP healing agent (uncatalysed) was manually injected at the highest displacement point. A typical load-displacement curve for the reference specimen is given in Figure 2.34. During crack propagation of the virgin cycle, the crack advance was a mix between a ductile and brittle unstable failure, characteristic of the so-called "stick-slip" behaviour, whereas in healed specimens the crack growth was stable. Interlaminar fracture toughness, G_{IC} , was measured for specimens before (virgin specimens) and after (healed specimens) healing. In virgin specimens, G_{IC} increased with the crack length until a plateau was reached (nearly 1.5 and 2 times the initiation for satin and plain respectively). This increase in delamination resistance was explained, as expected from section 2.2.1, by: (i) fibre bridging between the plies (ii) development of the damage zone around the crack tip and (iii) crack path tortuosity. In healed specimens, the energy release rate was constant with the crack length and was explained by the absence of fibre bridging. Interlaminar fracture toughness recovery was quantified through Eq. (2.3) and reached only about 20% for the self-activated specimens whereas for reference specimens it reached up to 80%. The lack of healing in self-activated specimens was explained by interfacial failure during virgin testing which allowed only little amount of the catalyst to be exposed on the fracture plane, thus preventing polymerisation of the healing agent. This study was a first demonstration of damage delamination healing with the components used in the microcapsule self-healing concept but not encapsulated, before assessing the ultimate self-healing of encapsulated components.

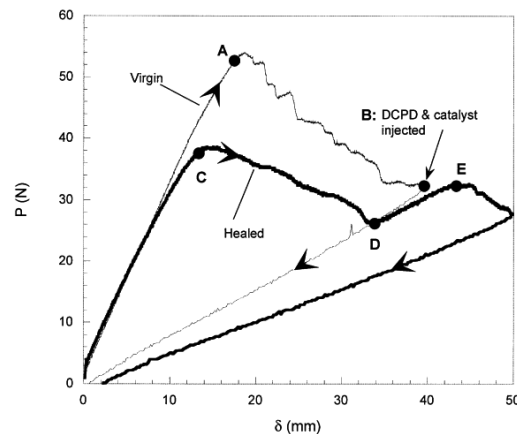


Figure 2.34: Typical DCB load-displacement curve for virgin and healed reference woven (8H satin weave E-glass/epoxy) specimens: A) crack propagation starts in the virgin specimen ahead the pre-crack (stick-slip behaviour); B) loading completed, mixture of DCPD/Grubbs is injected into the delamination, unloading and healing period in which the delamination is healed; C) crack propagation starts in the healed specimen (no stick-slip); D) crack has propagated till the extremity of the healed region; E) further loading creates a new virgin crack ahead of that propagated in the healed region [65].

Kessler *et al.* thus extended this work [63] to the ultimate self-healing system where the encapsulated DCPD healing agent and the encapsulated Grubb's catalyst were embedded into the reinforcement (plain weave). Healing properties of such system were assessed by Mode I WTDCB tests, which allowed a constant energy release rate with the crack length advancement. For comparison, reference specimens and self-activated specimens as for the previous study [65] were tested with this geometry as well as a fourth specimen type which was the self-healing specimen but heated at 80 °C during healing. Results showed higher healing efficiencies as compared to the previous study for the reference (99%) and self-activated specimens (73%). These higher efficiencies were simply due to the fact that specimens were clamped during healing in order to reduce the crack thickness and improve healing efficiency. Self-healing specimens demonstrated healing efficiencies of 38% whereas this value increased to 66% when the temperature during healing was increased to 80 °C. The increase in temperature demonstrated two beneficial effects: higher rate of polymerisation of the healing agent and higher degree of curing for both components. Again, reducing the crack gap manually during the healing cycle is disputable. However, crack opening in Mode I, even though creating a large crack thickness range, induces large damage volumes, which might not be representative of the microcracks found in real-life structure. Clamping of such specimens during healing can thus be relevant as long as the measured healing efficiency can be linked to the healed crack thickness.

The DCPD-Grubb's catalyst system contains several limitations. The Grubb's catalyst, if not encapsulated, has poor dispersion properties within the matrix and tends to cluster, which prevents the efficient DCPD activation on the entire crack surface (i.e. efficient healing) [63], [65]. Also, it has been found to be deactivated by the epoxy curing agent during curing of the host matrix. The cumbersome wax encapsulation technique of the catalyst has been developed to counter these problems of clustering and deactivation [213]. More limitations of this system are found in its cost, toxicity and low temperature resistance. Other systems were developed to remove these inherent limitations, in particular catalyst systems based on metal triflate [214] (which also demonstrated interest when integrated in FRPs [215]) or the solvent based healing systems (systems based on latent functionalities [207]–[210]).

Solvent based healing systems were studied in neat resins by [207]–[210] and further integrated into FRPs by Manfredi *et al.* [216]. They showed that glass fibre-reinforced epoxy plates, containing the capsule-based healing system and fibre volume fractions of approximately 50 vol%, could be processed through Vacuum Assisted Resin Infusion Moulding, a reproducible and industrially relevant manufacturing route. Particularly, the healing capsules were introduced in the composite via manual dispersion on one ply of the fabric preform prior to processing, as explored in a previous study [217]. The introduction of 15 wt% of capsules within the "local" matrix of the central ply

resulted in decreased interlaminar fracture toughness in Mode I and Mode II (approximately 25-30%) as compared to reference composites, but did not significantly affect the peak load. Second tests after healing revealed that composites could not be healed due to two interdependent causes: (i) the lack of thick resin layers on the fracture surface, resulting from interfacial debonding (observed as the main fracture mechanism occurring during crack propagation), (ii) the poor swelling of the matrix in the presence of EPA when embedded into a fibrous reinforcement, revealing a decrease of 80-95% compared to the neat resin. It has been concluded that a solvent capsule-based healing system is only suitable for repairing neat resins (as demonstrated in [207]–[210]) or fractures that occurred within the matrix rather than at the matrix-fibre interface, after static damage in FRPs.

Solvent based microcapsules have also been used to heal cracks in thermoset-thermoplastic phase-separated systems [211], [212], which avoided the need to leave residual functionalities into the resin reducing initial mechanical properties. Based on the same phase separation mechanism as seen through section 2.4.3, Jones *et al.* [212] blended poly(bisphenol A-co-epichlorohydrin) (PBAE) thermoplastic with a conventional epoxy resin (*EPON 828*) and cured with DDS to achieve the co-continuous complex morphology. Upon damage, capsules were ruptured, released the solvent into the crack plane and dissolved locally the thermoplastic, which redistributed in the damage region. This healing concept demonstrated, through TDCB tests, recovery in fracture toughness up to around 60% with in addition an initial K_{IC} value tripled as compared to neat epoxy systems. Toughness increase is further developed for similar systems in section 2.6.2 below.

Overall, extrinsic systems, under the form of capsules, have been successfully integrated to FRPs, but demonstrated limited healing and resulted in a loss of mechanical properties both when assessing interlaminar crack opening [65], [216] and impact induced damage [78], [218]. As compared to vascular systems, one of the main limitations is that capsules only store a limited amount of healing agent and are thus not able to provide healing for large damage extents. These studies however highlighted the complexity found with such an application to FRPs. In particular, key parameters to extend the capsule based healing systems to FRPs are:

- **Damage mode:** As seen in section 2.1, several damage modes, more complicated than in neat resins, are found in FRPs. Therefore, the healing system has to heal other type of damage events and even if its efficiency was proven for neat resins, it could not be the case for FRPs.
- **Rheological properties of the matrix:** Industrially, FRPs are manufactured by liquid composite moulding processes, which imply that the resin should flow through the reinforcement. This behaviour is characterised by the permeability that measures the ease of a liquid to flow through a porous medium. For intrinsic systems, the resin viscosity is usually higher and therefore flow is limited (this can be for example solved by a resin modifier such as Heloxy which can decrease the resin viscosity, but might interfere with the healing system). For extrinsic systems such as microcapsules, the viscosity of the resin is highly increased and aggregation of the particles might limit the flow of liquid through the reinforcement if microcapsules are inserted into the resin prior to infusion. One solution to this problem, which does not change the resin permeability (and can even increase it), is to functionalise the reinforcement prior to infusion and was demonstrated by Manfredi *et al.* [217].
- **Reinforcement architecture:** In the case of extrinsic healing system integration to FRPs, the architecture of the reinforcement is of high importance. Indeed, woven reinforcements were used in many healing studies, rather than unidirectional ones, because resin rich areas are found between crossing warp and fill yarns where the capsules can be naturally stored without affecting the intrinsic waviness of the fibre reinforcement [219].
- **Manufacturing:** Experimental studies usually rely on a hand lay-up manufacturing technique to process FRPs. The problem with this process is the low fibre volume content achieved (usually 30%) as well as the high void content of the final part. Therefore, one has to be careful when assessing healing in FRPs because wrong properties could be measured due to improper manufacturing techniques. Cure and post-cure temperature/schedule are also important. Indeed, for microcapsule healing systems, the temperature needs to be properly set to avoid damaging the microcapsules, whereas in latent functionality systems, proper cure

schedules need to be defined in order to achieve the right amount of latent functionality. Pressure applied to the composite during the process is also relevant so as to preserve the healing reservoirs [216].

- **Microcapsule size, distribution and shape:** The microcapsules used for self-healing studies in FRPs were usually of 200 μm in diameter, which is around 20 times larger than single glass or carbon fibres. Thickness of the stacks of plies is therefore increased, which results in a decrease of the fibre volume content and of virgin interlaminar fracture toughness. As these microcapsules may have a toughening effect (by crack arrest), a compromise can be found to keep similar interlaminar properties as FRPs without self-healing agents. Another route would be to vary the aspect ratio of the spherical particles in order to keep the same volume of liquid healing agent, while keeping the same FRP thickness.

The two main categories of self-healing systems (i.e. intrinsic and extrinsic) overall showed both drawbacks and advantages in terms of mechanical integrity as well as their efficiency in healing cracks. Blaiszik *et al.* [4] provided an interesting comparison between the different systems studied. Figure 2.35 shows crack healing efficiency as a function of the damage volume imparted to the specimen during test. Dividing healing systems into three categories (i.e. intrinsic, vascular extrinsic and capsule based extrinsic) showed that these are efficient for different damage volumes, thus highlighting one of their main limitation restricting them to be further integrated into structural components such as FRPs. Indeed, through the review of FRP damage mechanisms in section 2.1, microcracks formation impart damage volumes covering the range 0.01-100 mm^3 , thus none of the existing self-healing systems developed can cover the full range of what real-life structures experience.

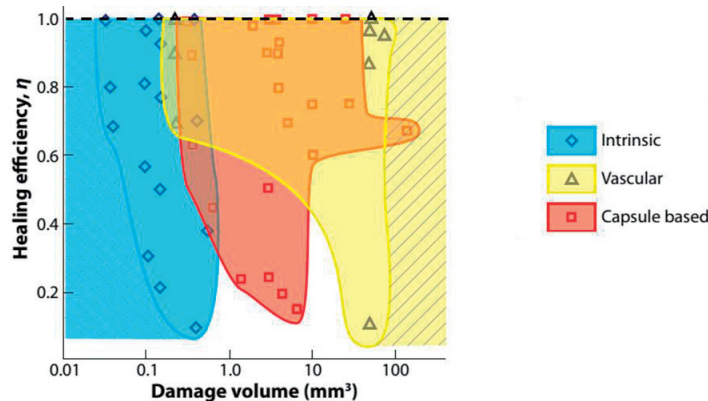


Figure 2.35: Performance map for self-healing materials. The data are organized according to the type of self-healing with shaded regions on the basis of data in the literature (plotted as discrete points). Each approach has demonstrated healing for different damage volume regimes. Intrinsic systems are relegated to small damage and can potentially heal at the molecular scale. Vascular systems have healed much larger damage volumes and can potentially extend the upper limit for self-healing systems. Capsule-based systems span the gap between intrinsic and vascular approaches [4].

2.6 Damage control in FRPs

Some self-healing systems were successfully inserted into FRPs, however many demonstrated limited healing due to incomplete crack filling (see Figure 2.35) by the healing agent as well as losses in mechanical properties as compared to unmodified systems. The present work aims to address these two issues by (i) the insertion of Shape Memory Alloy (SMA) wires to close cracks, and (ii) the use of an added phase (particles or nanofibres) to provide toughening but which can be used also as the healing agent. A review of these two fields is provided below.

2.6.1 Actuation system: Shape Memory Alloy (SMA) wires

Kirkby [6] and Neuser [210] showed that there is a threshold crack gap below which the healing system is inefficient. A crack filling factor was thus defined as the volume of available healing agent divided by the healed total crack volume, which corresponds to the amount of healing agent needed to fill a crack of known volume. Kirkby [6] showed that a fill

factor of at least unity is needed to provide maximum healing performances. In order to repair damage, intuitively, the two faces of a crack need to be as close as possible in order to bond them together. However, once a crack is opened, without any actuation, the two crack faces will never be brought back together. Some healing systems seen previously (like PCL and its differential expansive bleeding phenomenon [7]) allow a better crack filling, but if the crack opening is above a certain threshold, this mechanism does not reach the required fill factor. Even if White *et al.* [220] demonstrated the restoration (65% healing efficiency through CAI testing) of large damage volumes (35 mm in diameter) through vascular systems, closing or reducing the crack opening before the activation of the self-healing mechanism is of high interest in order to improve properties recovery. One solution was explored for neat resin specimens in [8], [9], [210], [221], [222]. The principle relies on the use of SMA wires, which cross the crack path, and once activated, have the ability to reduce or even close the crack gap. Indeed, SMAs present a behaviour called shape memory effect. In one phase, the material can be deformed (at low temperature) and in the other one (at high temperature), the shape before deformation is recovered. If a pre-strained SMA wire is constrained at both ends and subsequently heated, it has the ability to provide compressive stresses of several hundred MPa [3]. Brief theoretical considerations are given on SMAs before discussing the existing literature of SMAs integration to composites for damping properties improvement and to self-healing resins for crack healing improvement.

2.6.1.1 Working principle of SMAs [223]

Active materials are materials exhibiting actuation and sensing capabilities. A sensing material has the ability to convert a mechanical signal into a non-mechanical output as for example piezoelectric materials where the output is a voltage. Oppositely, an actuating material has the ability to convert a non-mechanical input (electrical power or heat) into a mechanical output. The interest of active materials relies in their response (thermal or mechanical for example) that is one or two orders of magnitude more than conventional material behaviour. Active materials can be divided into two groups: those exhibiting direct coupling and those exhibiting indirect coupling. Materials exhibiting direct coupling are for example piezo-ceramics and piezoelectric polymers (where coupling is between a mechanical and an electric field), magnetostrictive ceramics (where coupling is between a mechanical and a magnetic field), shape memory alloys or polymers (where coupling is between a thermal and a mechanical field). Materials exhibiting indirect coupling are for example electro-rheological fluids or magneto-rheological fluids (where a variation in the electric or magnetic field induces a variation in fluid viscosity which indirectly couples with a mechanical behaviour). Active materials exhibiting direct coupling are characterised by two main parameters: the material actuation frequency and the actuation energy density (available work output per unit volume). The design approach requires both of these parameters to be as high as possible. Figure 2.36 compares these two characteristics for different active materials and shows the interest of SMAs. Thanks to their high actuation energy density, SMAs have been used in many applications in fields such as aerospace, automotive or biomedical [224], [225].

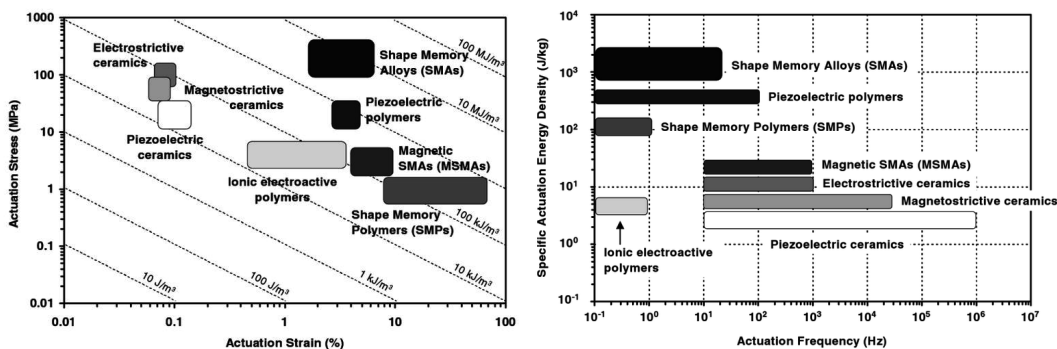


Figure 2.36: (Left) Actuation energy density diagram indicating typical ranges of actuation stress, actuation strain, and the actuation energy densities (dotted lines) of different active materials that exhibit direct coupling. (Right) Actuation frequency diagram comparing the actuation frequency ranges of different active materials that exhibit direct coupling [223].

The working principle of SMAs is based on the reversible phase transformation from one crystallographic phase (called austenite (A)) to another one (called martensite (M)) or vice versa. Austenite, existing at high temperature, is

generally cubic, whereas martensite, existing at low temperature, can be tetragonal, orthorhombic or monoclinic. This transformation, from one structure to another (well known as martensitic transformation), occurs by shear lattice distortion (movement of atoms) and induces a strain called the lattice invariant strain. When the SMA is heated and subsequently cooled down, it passes through several states, which are described in Figure 2.37 for the example of NiTi SMAs. The global process is known as shape memory effect and is as follows [223]:

- **A:** At elevated temperature, the material is in the crystallographic parent phase, austenite;
- **A→B:** Upon cooling and without any applied load, a forward transformation transforms the crystal structure from austenite to martensite. During this phase change, many martensitic variants result (up to 24 for the NiTi system) and their arrangement occurs in such a way that the average macroscopic shape changes can be neglected. After this transformation, the martensite is called twinned martensite. The formation of this phase starts at the martensite start temperature (M_s) and is completed at the martensite finish temperature (M_f). These temperatures are characteristic of the considered system;
- **B:** At low temperature and without any mechanical load, the material is in the product phase, called twinned martensite;
- **B→C:** If mechanical load is applied at this stage, detwinning of the martensite can occur and reorient a number of variants. This process induces macroscopic shape changes, which are kept when the load is released. Also, it starts at a minimum stress (σ_s) and is completed at the detwinning finish stress (σ_f);
- **C:** At low temperature and under a certain level of mechanical load, the martensite is in the detwinned state;
- **C→D:** The load is removed and no macroscopical shape change occurs;
- **D:** At low temperature and without any mechanical load, the martensite is in the detwinned state;
- **D→E→F→A:** Upon heating and without any mechanical load, the reverse transformation initiates at the austenite start temperature (A_s) (point E) and ends at the austenite finish temperature (A_f) (point F). After A_f , the austenite parent phase is regained, and if no excessive load was applied during detwinning, the original material shape is regained at point A.

This cycle can be repeated many times (with various hysteresis levels depending on the system) and is called one-way shape memory effect. Notice that some SMAs can be trained to remember a specific low temperature martensitic phase, which is different from the high temperature austenitic phase. This effect, where shape variation is achieved with the need only of temperature, is called two-way shape memory effect.

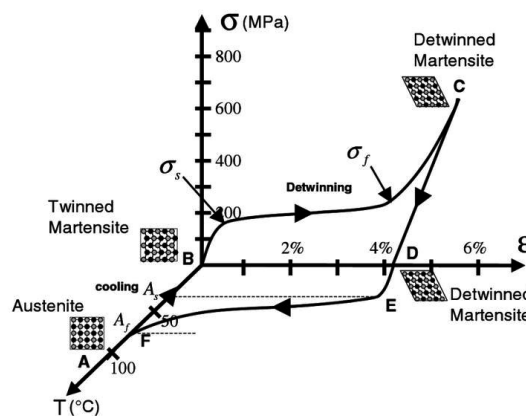


Figure 2.37: Stress-strain-temperature data exhibiting the shape memory effect for a typical NiTi SMA [223].

The shape memory effect can provide various features that may be utilised in engineering applications [226]: sensing (sensitivity to thermal stress or electric field stimuli), switch or control capacity (critical value to trigger the effect); actuation (possibility of very large displacement and high forces for actuation); adaptation (thanks to phase

transformation); memory and recovery (reversibility and repeatability of the transformation); energy storage and conversion (possibility of thermal-mechanical, electrical-mechanical energy conversions); damping (thanks to characteristic microstructures and phase transitions).

All of these features can be seen through some typical property values of NiTi systems in Table 2.1 [226].

Table 2.1: Some typical properties of binary Ni-Ti shape-memory alloys [226].

Melting point	~ 1573 K
Density	6.4–6.5 g cm ⁻³
Transformation temperatures	173–390 K
Transformation enthalpy	1.46–1.88 kJ mol ⁻¹
Transformation hysteresis	20–50
Recoverable strain	
one-way-effect	< 8%
two-way-effect	< 5%
Recovery stress	< 500 MPa
Damping capacity, Q^{-1}	~ 10 ⁻²
Ultimate tensile strength	800–1100 MPa
Yield strength	
Parent phase	200–800 MPa
Martensite	70–200 MPa
Young's modulus	
Parent phase	50–90 GPa
Martensite	10–35 GPa
Shear modulus	
Parent phase	15–20 GPa
Martensite	3.5–5 GPa
Thermal expansion coefficient	
Parent phase	10.0–11.0 × 10 ⁻⁶ K ⁻¹
Martensite	5.8–8.6 × 10 ⁻⁶ K ⁻¹
Thermal conductivity	
Parent phase	0.18 W cm ⁻¹ K ⁻¹
Martensite	0.086 W cm ⁻¹ K ⁻¹
Electrical resistivity	
Parent phase	70–110 μΩ cm
Martensite	40–70 μΩ cm
Magnetic susceptibility	
Parent phase	2.7–3.0 × 10 ⁻⁶ e.m.u. g ⁻¹
Martensite	1.9–2.1 × 10 ⁻⁶ e.m.u. g ⁻¹

NiTi systems have been the most widely used SMAs due to their high recovery properties, mechanical properties, corrosion resistance or even their biocompatibility (see Table 2.1). However, it has to be noticed that many other systems have been studied. In particular, alloying this system with copper is of interest as it reduces the hysteresis response of the SMA, even if it reduces also its transformation strain. SMAs integration to composites was mainly performed with NiTi systems; the reader is referred to the review of Wei [226] for other system properties.

2.6.1.2 Integration of SMAs to FRPs and self-healing polymers

The use of SMA wires into FRP structures was first studied by Rogers *et al.* [227], [228]. By embedding NiTi SMA wires into a carbon-epoxy prepreg parallel to the reinforcement layers, they demonstrated that upon heating, the Young's modulus of the structure as well as the yield strength increased by a factor 4 and 10 respectively. They further showed that the natural frequency of these systems could be tuned by heating the SMAs, which allowed tailoring vibration properties of the FRPs. Since then, SMAs into composites were highly studied for impact damage resistance and suppression, as reviewed in [225], [229].

Considerable research efforts have been made at LTC (EPFL) with two principle directions: (i) the insertion of SMAs to FRPs for improving damping and vibrational properties [3], [230]–[232] and (ii) the insertion of SMAs into self-healing polymers for crack closure and healing efficiency improvement [6], [8], [9], [221]. In direction (i), SMA wires were inserted parallel to the reinforcement layers of the FRPs, this strategy was also highly studied for damage resistance and suppression in composites (the interested reader is referred to refs. [225], [229]). In field (ii) the target was to insert SMA wires perpendicular to the crack direction. Crack closure in FRPs would thus require inserting the SMAs perpendicular to the reinforcement layers (through stitching), which was not yet experimentally validated, to the author's knowledge, in self-healing FRPs. However, crack closure through the use of SMAs was studied in self-healing resins with two studies of particular interest:

1. Kirkby [6], [9] showed that the addition of pre-strained SMA wires into an epoxy resin containing the microcapsules of DCPD-Grubb's healing system, improved the healed peak fracture load during TDCB testing by a factor up to 1.6. This improvement was explained by two reasons: (i) the pre-strained SMAs, upon heat activation, allowed crack closure and therefore reduced the crack volume; (ii) heating of the healing agent during its polymerisation increased the degree of cure. Notice that Kirkby [6] stitched SMA wires into FRPs to provide crack closure and improve the healing process, however, the beneficial effect of SMA wires could not be concluded and further experiments were needed.
2. Neuser [8], [210] showed that the addition of SMAs into an epoxy resin where solvent microcapsules based healing systems were added, improved, upon heating of the SMAs, the healing efficiency up to 78% (as compared to 24% without SMAs). He also pointed out the need to anchor the SMAs away from the crack path, and to take advantage of interface debonding to spread the deformation field in the SMA wires.

These research papers provide understandings of the critical parameters for integrating SMAs to FRPs and especially the care that must be taken when the integration is aimed for self-healing applications.

Position of the SMAs into the system In order to efficiently close a crack, one SMA (or more) should cross it perpendicularly. However, damage to be closed can be oriented in the three dimensions of the reinforcement, which includes cumbersome integration. An efficient way for closing every crack arrangement would be to insert SMAs through the thickness of the reinforcement as a continuous stitch. Such stitches are commonly named as translaminar reinforcements; a detailed review of these materials and their behaviour as compared to conventional FRPs is given by Dickinson [233]. A translaminar fibre-reinforced composite is defined as a composite with up to 5 vol% of fibre reinforcement oriented in the through-thickness direction. Inserting this kind of reinforcement considerably disturbs the behaviour of the FRP, however it has been observed to provide several advantages including: improving the CAI response, increasing interlaminar fracture toughness in Mode I and II, restricting impact damage and edge delamination. The cost to these improved properties is the decrease in in-plane properties. Inserting these translaminar reinforcements to an FRP are of course accessible, but time consuming on a lab scale. On an industrial scale, this can be achieved through conventional stitching machines for FRPs with minor changes as SMA wires down to 0.2 mm in diameter can be produced [3]. Lau *et al.* [234] manufactured by RTM a ten layers E-glass epoxy woven composite stitched by NiTi SMA wires of 0.22 mm diameter. Through impact tests, they demonstrated that SMA stitches decreased the delamination energy and the number of translaminar cracks, and also increased the tensile modulus as well as the damping ratio of the composites as compared to unstitched systems. These property variations were reinforced when increasing the volume fraction of SMA wires. Vachon *et al.* [235] manufactured similar SMA stitched FRPs and observed a 7% decrease in the impact delamination area which was translated in a 1% increase of the CAI response as compared to unmodified systems. Considering that with SMA wires placed in between the laminate layers, the delaminated area can be reduced up to 58% [236] (for other studies in this field, the interested reader is again referred to refs. [225], [229]), stitching SMA wires into FRPs did not induce the expected energy absorption effect. Finally, Bor *et al.* [10] modelled FRPs with SMA wires as translaminar stitches with the aim to determine if the SMAs can provide crack closure after heat treatment. From their model simulation, it was concluded that SMA wires can compress delamination interfaces when a heat treatment is applied on the composite part. However, they also concluded that this crack closure behaviour may be obtained with other wire materials as the heat treatment applied in their simulation was above the matrix T_g which softened the system and allowed such compressive stresses. Applying heat treatments above the matrix T_g needs careful composite design as structural integrity of the system might be lost. Nevertheless, this study showed promise to close delamination cracks when SMA wires are integrated as stitches into FRPs.

Cure schedule of the system Balta *et al.* [230] showed that 3% of pre-strain of the NiTiCu SMA wire provides the highest recovery stress upon activation. Pre-straining the wire might be of interest upon activation, but it renders the processing conditions complicated. Indeed, in order to provide the highest load transfer during strain recovery of the wire, the activation temperature of the SMA must stay below the T_g of the matrix. However, composite processing implies peak post-cure temperatures above the T_g and therefore above the wire activation

temperature. If pre-strained, the wire may therefore recover its initial strain already upon curing, preventing its use when needed. This problem is also present for two-way shape memory alloys. The use of frames [221], [230], [232] or of some preliminary treatments of the wires [237] (to raise A_s) was demonstrated as an efficient way to prevent early strain recovery, however this does not necessarily scale-up well towards industrial manufacturing techniques. Increasing the interfacial shear strength was also demonstrated as possible [221], but this can lead to problems of load dissipation during damage (see next point). Inserting the SMA wires as stitches could solve this problem as the resulting 3D network and its adhesion to the matrix (without raising it too much) may prevent strain recovery upon heating. A last solution is to perform curing below A_s ; load transfer as well as wire strain recovery may not be obtained in this case due to poor matrix properties but can be solved by a post-curing treatment [221]. Notice however that if SMAs are used for crack closure, no pre-straining may in general be required as the crack opening will strain the wire, thus preventing cure schedule complications.

SMA-matrix adhesion Providing the highest recovery of SMAs upon heating into the FRP goes through load transfer from the SMA to the surrounding matrix, and therefore the adhesion between these two is of high importance. For crack closure, the adhesion level should be high enough to avoid wire debonding during recovery, but should not be too high to avoid permanent plastic deformation and failure of the wire, which prevents efficient strain recovery. Upon crack opening, the wire should therefore debond partially, to provide enough wire length to be strained to the appropriate level, but should also be able not to debond later upon activation in order to provide crack closure. Neuser [8] introduced wire knots, which allowed a controlled debond length through anchoring, and uniform strain over a significant length of wire to close the crack efficiently upon activation. This technique, not suitable for industrial purposes, however indicates what could happen with translaminar stitched wires as the top and bottom bends of the stitch may act as knots. Controlling the adhesion level goes through the control of the wire surface properties and especially the wire roughness. Several techniques are available to vary the adhesion level like chemical treatments [238] or various polishing (sand blasting) [239], presence of oxide layers [230], wire twisting [240] and the martensite twinning amount [241]. The adhesion level can also be increased by curing the system above the wire A_s level [242], which induces thermal shrinkage of the austenite phase, and subsequent thermal expansion of the martensitic phase upon cooling, therefore creating compressive stresses of the wire. Characterisation of the adhesion between the wire and the surrounding matrix is of interest and interfacial shear-strength characterisation methods were reviewed in section 2.2.2.

Pre-strain level Pre-straining the wire before embedding it into the polymer is of interest to provide highest recovery capacity. For example, the highest recovery force arises when the NiTiCu wire is strained to 3%, but the pre-strain should be adapted depending of its application purpose. Indeed, for large damage volumes, the required pre-strain may reach more likely 0% (preventing processing complications) whereas it would be closer to 3% for small damage volumes.

Activation type The method to heat up the SMA to reach the austenitic transformation temperature is also of importance. Indeed, heating can be performed using an oven, however this depends on the part size and only local heating can be desired. Local heating requires external insulation of the part, which leads to further design complications. The other possibility is by Joule heating thanks to the high electrical resistivity of the wires, however this also requires electrical insulation if carbon fibres are present in the system. The type of wire activation therefore depends on the system of interest.

The use of SMAs in FRPs is therefore of high interest as it may allow damage prevention, damage reduction as well as crack healing performances improvement. However, care must be taken on several points and characterisation still remains to be performed, especially to quantify crack closure and to find an efficient and industrially scalable technique for their integration to FRPs. Also, these are in competition with shape-memory polymers, which are gaining interest for self-healing applications [127]–[129], [132] because they offer low weight as compared to the dense SMAs, but have lower actuation properties (see Figure 2.36).

2.6.2 Toughening

Thermoset matrices, and in particular epoxy resins, are highly used in the composite field for laminates manufacturing but suffer from their brittle behaviour, which limits strain of the FRP as well as energy absorption ability and their low toughness values. Toughness is defined, in the context of fracture mechanics, as the total energy required for failure, which is, in experimental terms, the total (and only total) area under the stress-strain curve. Lack of toughness is related to the growth of damage, and especially delamination, in FRPs. Improving the energy absorption ability by chemical modifications or toughening agents has been an attractive field of research for many years; toughening mechanisms were well reviewed in [55], [243], [244]. Unnikrishnan [243] classified 3 different ways for toughness modification of epoxy resins: (i) elastomer modification, (ii) particulate modification and (iii) thermoplastic modification. However, to these three categories, a fourth one needs to be added and is toughening through the use of a nanophase. This last field has recently attracted interest as it can provide large improvements in interlaminar properties thanks to the high surface area provided by nano-scale materials. The present section considers first toughening by agents on a micro-scale, which is of interest in phase-separated systems that demonstrated also crack healing capabilities, whereas toughening by agents on a nano-scale is considered in a second paragraph, which is of interest through the use of thermoplastic nanofibres that may provide both healing and toughening.

2.6.2.1 Micro-scale toughening

The 3 different methods for toughness modification of epoxy resins described in [243] can be described by mechanisms taking place on a micro-scale:

Elastomer modification This category (commonly named rubber toughening) is the most studied and is achieved through the process of phase separation already discussed in section 2.4.3.1. Toughness modification is usually achieved in that case when the epoxy stays as the continuous phase whereas the elastomer nucleates and forms particles. The highest level of toughening was found for a particle concentration of 10% in volume of the matrix (preventing phase inversion where particle toughening mechanism could not be efficient) [243]. Although it has been shown that particles down to 0.01 μm can be obtained, the micro-scale level is a requirement for efficient toughening (notice that high surface area of the nano-sized particles is not taken into account in this statement). For some elastomer modification strategies, particles were inserted into the host matrix and kept their shape upon polymerisation (i.e. no phase separation mechanism took place).

Particulate modification This category consists in inserting particulate fillers such as silica, which has the advantage over elastomeric particles to enhance the modulus of the host matrix. However the level of toughening for particles such as silica is lower as compared to elastomeric particles.

Thermoplastic modification Similarly to rubber toughening, thermoplastic toughening is achieved through phase separation as discussed in section 2.4.3.1. As compared to rubber toughening, this modification induces a lower level of toughening.

Mechanical characterisation, and especially toughness increase for the modified systems, was quantified by many studies for many systems in the three different categories, and the level of increase could reach several hundred percent. For details on the many possible systems, the reader is referred to the review of Hayes and Seferis [18].

The optimal path for toughening thermoset resins is therefore through the creation of a multiphase structure where particles are dispersed into the host matrix. Several mechanisms have been proposed to explain how particles toughen a hosting phase. These different mechanisms were divided by Unnikrishnan into five categories (for rubber or thermoplastic particles) and are induced by the wide variety of failure mechanisms found in particle modified thermosets, as depicted in Figure 2.38 for rubber-filled modified polymers:

Particle deformation The faces of a propagating crack are held together by the particles and the toughness of such system is controlled by the energy required to rupture the particles.

Multiple crazing A craze can be defined as a small crack where fibrils of the polymer are drawn across. It has been demonstrated that crazes frequently initiate from the elastomeric particles and terminate when encountering another particle. This mechanism stabilizes the crazes and prevents them to grow into large cracks, therefore increasing the amount of energy that can be absorbed by the system and at the same time the toughness.

Shear yielding The presence of elastomeric particles induces stress concentrations in the system. These stress concentrations serve as nucleation sites for shear deformation under the form of shear bands, and thus plastic shear yielding is enhanced as compared to unmodified resins. This was observed to be the main source of energy absorption in a resin system modified by particles, and therefore responsible for toughness improvement.

Cavitation-shear yielding Shear deformation of the matrix also induces cavitation of the elastomeric particles. Both cavitation and shear yielding occur during the early stage of load application. Cavitation of the elastomeric particles is assumed to be responsible of matrix shear yielding and therefore an increased plastic zone development at the crack tip.

Crack pinning When a crack tip propagates and encounters a particle, it is temporarily pinned at that point. The crack front between the particles is then bowed out as the load increases, resulting in a toughness increase. This mechanism is however present only for particles strong enough to pin the crack (i.e. hard filler particles).

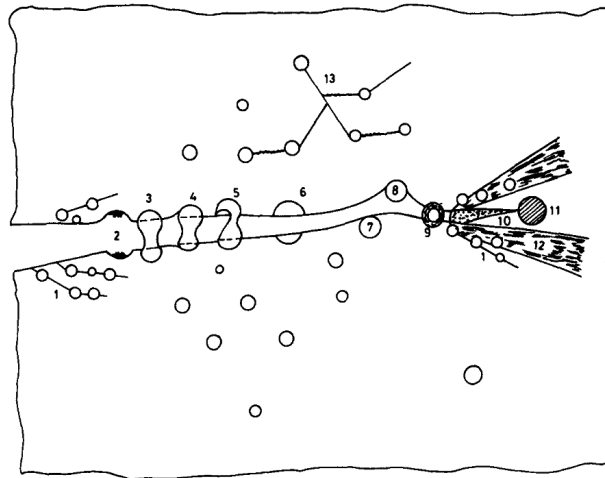


Figure 2.38: Crack toughening mechanisms in rubber-filled modified polymers: (1) shear band formation near rubber particles; (2) fracture of rubber particles after cavitation; (3) stretching, (4) debonding and (5) tearing of rubber particles; (6) transparticle fracture; (7) debonding of hard particles; (8) crack deflection by hard particles; (9) voided/cavitated rubber particles; (10) crazing; (11) plastic zone at craze tip; (12) diffuse shear yielding; (13) shear band/craze interaction [55].

Elastomeric or thermoplastic particles modification can achieve high level of toughness improvement, however often at the expense of other properties. In rubber modified epoxies for example [55], if impact strength, fracture energy and toughness are increased, a decrease is observed in the Young's modulus and the yield strength, and in many cases in the T_g . In addition, the schematic drawing of Figure 2.38 shows a small plastic zone size at the crack tip, which may not be the case in all systems. Smith *et al.* [245] examined the processes of damage initiation, development and fracture in silica-filled epoxy resin. In particular, they observed that the process zone size ahead of the crack tip can be detrimental to the fracture toughness of the modified resin. Figure 2.39 shows a schematic of two process zone sizes in particulate modified resins. It has been demonstrated [245] that in the case of a process zone in the same size order as the inter-particle size, there is no change in fracture toughness (Figure 2.39 (a)) whereas when the process zone

size is larger, there is a decrease in fracture toughness due to the formation of small cracks ahead of the main crack (Figure 2.39 (b)). This behaviour must thus be considered when modifying polymeric matrices with second phases.

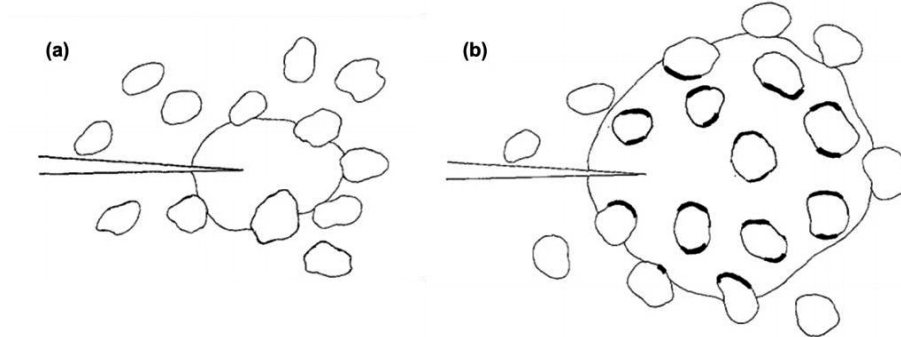


Figure 2.39: Schematic representations of the process zone in front of the crack tip: (a) usual case where the process zone size is of the same order as the inter-particle size; (b) detrimental case because the process zone encompasses a large number of particles in front of the crack tip [245].

2.6.2.2 Nano-scale toughening

Much attention has been devoted recently to the field of nanomaterials to provide toughness improvement to the FRPs; the main advantage of these nanomaterials being their extremely high surface area to volume ratio. This fact was identified as a potential solution (better than microparticles) to the lack of matrix plastic deformation and low interlaminar shear strength of FRPs. Three different approaches have been employed to insert a toughening nanophase into an FRP: (i) modification of the matrix, (ii) modification of the reinforcement and (iii) incorporation of a macroscopic arrangement of a nanometre-dimensional material [246].

Modification of the matrix

It is the most common approach in literature. Studies made in this field include for example the use of silica nanoparticles [247], graphite and nanoTiO₂ [248], organoclay [249], nano-scale Montmorillonite particles [250], carbon nanotubes [244], [251] or graphite nanoplatelets [252]. They consist all in mixing the nanophase with the matrix before the FRP infusion. Even if this approach resulted in fracture toughness improvements (and other properties depending on the nanophase, like electrical properties improvement for carbon nanotubes), two main issues concerning specimens processing were highlighted: (i) the increase in resin viscosity even with a low amount of nanoparticles, (ii) particles filtration by the reinforcement as nanoparticles tend to agglomerate due to their high surface area, leading to an uneven distribution of the particles within the reinforcement. In addition to the processing limitations, several health issues have to be considered when nanoparticles are used because harmful to the operator with their submicron size. This category is similar to the insertion of microparticles into FRPs discussed above.

Modification of the reinforcement

This second field has been motivated by processing time issues, and consists in changing the surface of the reinforcement. Studies mainly focus on the growth of carbon nanotubes onto the surface of micro-scale reinforcing fibres [253]–[256]. It is similar to the technique of Blaiszik *et al.* [257] where functionalisation of the reinforcement fibres by the healing microcapsules was performed.

Macroscopic arrangement incorporation

Studies made in this third field consist in inserting a third phase in between two layers of a reinforcement fabric before impregnation and cure of the FRP. Only a third continuous phase is considered here, but functionalisation of the fabric seen through the studies of Manfredi *et al.* [216], [217] with healing microcapsules could be inserted in this category. The third continuous phase considered is a thermoplastic nanofibre veil (or mat) with fibres oriented randomly and ranging from the micrometre scale down to the nanometre scale. These ultra-fine fibres have three main properties: a very high surface to volume ratio (which is suitable for applications requiring high degree of physical contact), a defect free structure at the molecular level (which allows reaching the maximal theoretical strength of the spun material), and at the difference of nanoparticles,

nanofibres can be handled more easily and no health issues must be considered. These increased properties induce high potential applications in fields such as: structures with high stiffness and mechanical strength thanks to a higher bond strength of nanofibres; protective clothing thanks to light weight and highly breathable nanofibre membranes; tissue engineering thanks to the high surface area available in nanofibres to host various proteins; or various electronic devices that require a material capable to host different electrolytes or nano-sized materials [258], [259]. The field of thermoplastic nanofibres and their integration to FRPs is further reviewed below as of interest for the present work.

The production process of thermoplastic nanofibres is electrospinning, a technology that uses an electrical charge to draw very fine continuous fibres from a liquid thanks to a needle (Figure 2.40). The basic set-up for electrospinning nanofibres includes three leading components: a high voltage supply, a spinneret (a metallic needle) and a collector plate (a grounded conductor). The spinneret is directly connected to a syringe, which contains a solution with the dissolved polymer to spin. A high voltage (between 1 and 30 kV) is then applied in the system and the droplet that stays at the extremity of the needle becomes highly electrified. This electrified droplet experiences two major types of forces: (i) the electrostatic repulsions between the charged surfaces and (ii) the columbic forces exerted by the external electric field. Under these electrostatic forces, the droplet is distorted into a conical object (the Taylor cone). Above a threshold electric field, the electrostatic forces inside the drop can overcome surface tension of the polymer solution, which ejects a liquid jet from the extremity of the spinneret. This liquid jet is then collected on a collector plate (or various medium) where the nanofibre takes its final solid shape. Because the liquid jet is continuously elongated as it leaves the spinneret nozzle, the diameter of the produced fibre can be controlled and reduced from micro- to nano-sizes [260].

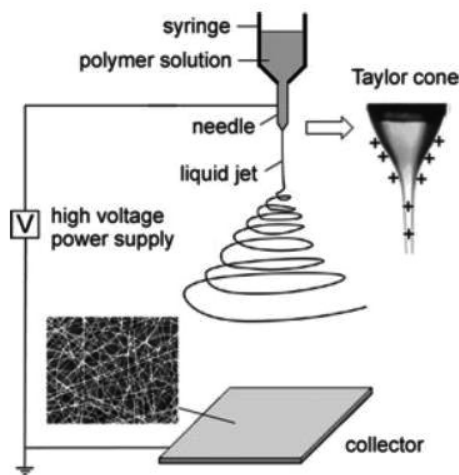


Figure 2.40: Schematic illustration of the basic setup for electrospinning. The insets show a drawing of the electrified Taylor cone and a typical SEM image of the nonwoven mat of poly(vinyl pyrrolidone) nanofibres deposited on the collector [260].

The electrospinning process allows producing highly porous mat materials, with a large surface area and a minimum weight. It has been shown that hundreds of polymers can be electrospun [258], [260], but in theory many more polymers can be electrospun. This implies that several polymer properties can be exploited commercially. For example most known polymers used for electrospinning nanofibres are [258], [260]: Poly-benzimidazole and polyamide for their high modulus and fracture toughness; Poly(vinylidene fluoride) (PVDF) for its electroactivity, mechanical strength, flexibility, easy conformability, good processability, piezo-pyro-ferroelectricity and flammability properties; poly(ϵ -caprolactone), polyvinyl alcohol, poly lactic acid and poly(glycolide) for their biological properties and potential medical applications as wound dressing; polyaniline and polyethylene oxide with carbon black for their electrical properties; polycarbonate for its flammability and mechanical properties; Poly[2-methoxy-5-(2-ethylhexyloxy)-1,4-phenylene-vinylene] for its electroluminescence behaviour.

The basic electrospinning set-up uses a single needle to produce continuous nanofibres. However, this technique has a very low productivity (<300 mg/h per needle) and the use of several needles is complex and leads to high clogging probability due to some interactions between the needles [261]. Zussman and Yarin [261] developed needleless electrospinning, which allows increasing the production rate of nanofibres (by nearly 12 times) due to several polymer jets/filaments on a flat surface.

To enhance interlaminar fracture toughness of FRPs by nanofibre veils, two different approaches were explored: inserting the membranes in between the composite laminate layers or electrospinning directly the nanofibres onto each laminate layer.

Indirect electrospinning placed on fabrics The first scientific approach (as a patent was written by Dzenis [262] in 2001) was former studied by Liu *et al.* [263] where they related the influence of three electrospun nanofibre veils (made of PA6, EPO and TPU polymers) on the mechanical properties of a glass-epoxy laminate (with one nanofibre membrane in between each ply). After processing the FRP by hand lay-up with a cure temperature of 120 °C, nanofibre membrane thicknesses ranged from 0.02 to 1.2 mm and nanofibre diameters from 150 to 1200 nm, they measured an increase of the flexural strength, shear strength, and flexural modulus of the composite by 10%. This relatively low property increase was explained by a poor matrix-nanofibre adhesion (a poor impregnation of the resin into the nanofibre membrane) quantified by SEM. Sangwook *et al.* [264] followed the same approach with nanofibre veils of polycarbonate. This membrane had a thickness of 0.001 mm and a nanofibre diameter of 350 nm. By performing uniaxial tension loading, they found that the stress level at the first-ply-failure, delamination and ultimate failure have increased by 8.4%, 8.1% and 9.8% respectively with the addition of the veils. Therefore, the addition of this interlayer can decrease and maybe suppress microcracking and delamination damage thanks to an interlaminar stress concentration decrease. Harmer *et al.* [265] studied the influence of Nylon 6,6 nanofibre mats on the interlaminar fracture toughness, G_{IC} , of a carbon-epoxy laminate made by wet lay-up with a cure at room temperature. The electrospun nanofibre veils were 70-100 μm thick and their areal density was 8-12 g/m^2 . Even if they observed by SEM a poor adhesion between the epoxy matrix and the nanofibre mats, an increase of 255-322% in interlaminar fracture toughness was demonstrated in the specimens modified by nanofibre membranes. This toughening was explained by the high energy absorption of bridged thermoplastic fibres and the creation of a plastic zone near the crack tip.

More recently, several studies assessed interlaminar toughening of fibre-reinforced composites with nanofibre veils of Nylon 6,6 or PCL. Saghafi *et al.* [266] inserted nanofibres of Nylon 6,6 and PCL (of diameters 150 and 270 nm respectively) in the mid-plane of unidirectional glass-epoxy laminates manufactured by hand lay-up and cured at 150 °C in an autoclave. Fracture tests on Nylon 6,6 enhanced FRPs did not show any improvement of Mode I delamination properties whereas in Mode II, 68% improvement in resistance to crack propagation was demonstrated thanks to the nanofibre structure. Tests on PCL modified composites showed 25% improvement in fracture properties for both modes. However, this improvement was not the result of the nanofibre structure as during cure, PCL melted and dissolved into epoxy, providing a phase-separated morphology that was seen in section 2.6.2.1 as ideal for toughening purposes (i.e. epoxy matrix with PCL particles). van der Heijden *et al.* [267] also processed (by vacuum assisted resin transfer moulding (VARTM)) glass-epoxy composites modified by nanofibres of PCL (400 nm diameter), but cured at room temperature and post-cured at 80 °C, therefore preventing the PCL to melt. For nanofibres with an areal density of 20 g/m^2 per applied layer, an improvement of almost 100% in interlaminar fracture toughness was demonstrated and explained by the inherent toughness and ductility of PCL but also by a good adhesion between the different components. Three successive studies by the same authors [11]–[13] on glass-epoxy composites modified by nanofibres of PCL or PA6 (different nanofibre diameters) showed that (i) the main toughening mechanism is provided through microcracks bridging by the nanofibres both in Mode I and Mode II loading conditions (see Figure 2.41) [11], (ii) nanofibres can decrease the rate of delamination by one order of magnitude under fatigue conditions [12] and (iii) random orientation of the nanofibres lead to the highest increase in Mode II fracture toughness (up to 2 folds) as compared to nanofibres oriented parallel or transversely to the crack growth [13]. Finally, Beckermann and Pickering [268] inserted five electrospun polymer nanofibre mats in autoclave cured (120 °C) carbon-epoxy composites: PA66,

PVB, PCL, PES and PAI. Interlaminar fracture toughness in Mode I and II was increased at best with PA66 mats by 156% and 69% respectively thanks to its good compatibility with the carbon-epoxy system. PVB also increased interlaminar fracture toughness in both modes, which was demonstrated, as for PA66, by ductile failure on the fracture surface. For PES and PAI, a decrease of toughness was explained by a brittle system failure observed on the fracture surface. PCL, as in the case of [266], showed medium increase in toughness (20%) due to its melting during composite processing. This last fact, as compared to [11]–[13], [267] where large toughness improvements with PCL nanofibres have been demonstrated, thus shows the importance of the nanofibre structure to provide toughening and microcrack bridging by the nanofibres.

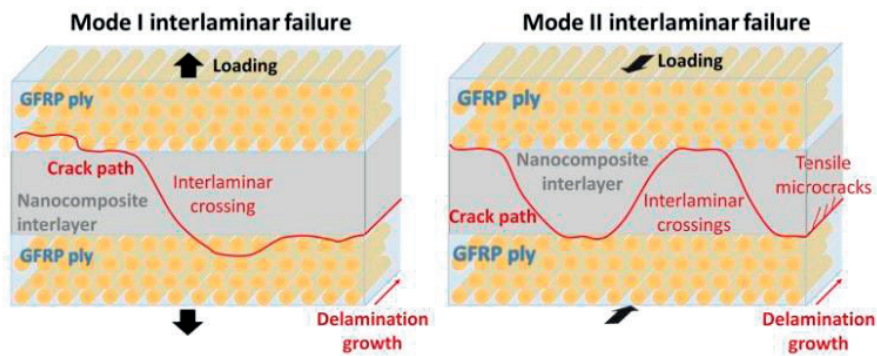


Figure 2.41: Schematic illustration of the delamination path in a nanofibre interleaved laminate under Mode I and Mode II loading conditions [11].

Direct electrospinning onto fabrics The second approach appeared later and was first reported by Kelkar *et al.* [269] in their study where they assessed the influence of electrospun Tetra Ethyl Orthosilicate (TEOS) nanofibres on the interlaminar properties of glass fibre composite laminates. The nanofibres were directly deposited onto woven glass reinforcements and the composite laminate was then processed by heated VARTM. Modified short-beam-shear and short-beam-shear tests showed an improvement of more than 20% in delamination resistance for the nano-enhanced composite as compared to the traditional two-phase composite.

Li *et al.* [270], in the first study that relates a control of nanofibre content and diameter, directly electrospun polysulfone (PSF) nanofibres (in the diameter range of 150-300 nm) onto a carbon epoxy prepreg. They also compared their results with cast PSF films of 30 μm thickness and showed that the G_{IC} of PSF nanofibre toughened composites with 1, 2 and 3 wt% of nanofibres was 158%, 261% and 281% higher than the un-toughened composites, respectively, and 132%, 150% and 140% higher than the PSF casted films toughened composites with the same content of PSF. Fracture surfaces of the nanofibre enhanced composites observed by SEM revealed a phase-separated morphology showing PSF particles whereas for un-toughened composites, the fracture surfaces were flat (Figure 2.42). The increase in interlaminar fracture toughness for toughened composites was thus explained by the PSF phase-separated particles, which restrained crack propagation and thus increased the energy to propagate it. The use of PSF films did also translate into a phase-separated microstructure, and thus explained the increase in interlaminar fracture toughness found with those specimens as well. The higher toughness improvements found with nanofibre enhanced composites was further explained by aligned PSF particles after phase separation along the fibre reinforcement.

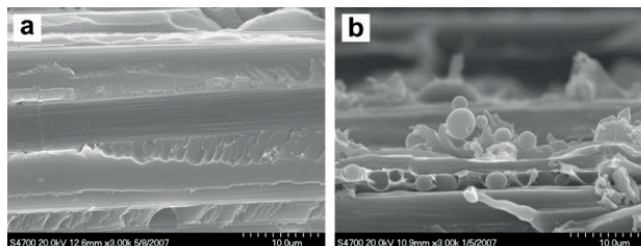


Figure 2.42: SEM images of composite fracture surface (a) un-toughened and (b) toughened by 5 wt% PSF nanofibrous membranes [270].

Magniez *et al.* [271] adopted the same kind of approach but with poly (vinylidene fluoride) (PVDF) nanofibres and films in carbon prepreg epoxy laminates (cured at 150 °C). They inserted these different films between the 4th and 5th ply in the composite laminate and tested interlaminar fracture toughness in Mode I and Mode II. They observed a decrease of Mode I interlaminar fracture toughness for both cases (around 20% for the fibres directly electrospun and more than 80% for the PVDF films), whereas in Mode II they related an increase of more than 50% for the electrospun PVDF nanofibres and a decrease of more than 50% for the films. These differences were explained by the polymorphic structure of PVDF after electrospinning, which could be better controlled and could thus improve the epoxy plastic deformation. In a second study, Magniez *et al.* [272] directly electrospun phenoxy nanofibres on carbon prepreg epoxy laminates (cured then at 150 °C). SEM observations revealed an inverse phase separation between phenoxy and epoxy, leading to globules of epoxy (see section 2.4.3.1). This morphology induced improvements in Mode I and Mode II interlaminar fracture toughness of respectively 150% and 30% and was explained by failure micromechanisms around the epoxy globules such as cavitation, voiding and localised shear yielding.

VanderVennet *et al.* [273] used Polyacrylonitrile (PAN) nanofibres for reinforcing a 12 plies carbon-epoxy laminate. They aimed to show the difference between direct electrospinning of nanofibres on the fabric and the lay-up of a nanofibre membrane previously electrospun using a nanomat transfer film. All the parts were processed by hand lay-up with a cure at room temperature. Interlaminar fracture toughness of the tested specimens decreased respectively by 54.5% and 26.9% when nanofibres were deposited with a nanomat or directly electrospun. These poor results were explained by a lack of control in the manufacturing parameters. They then performed the same tests with carbon-epoxy prepregs and showed an 18.9% increase in interlaminar fracture toughness when the nanofibres were directly electrospun on the fabric and thus where manufacturing was better controlled.

Zhang *et al.* [274] assessed the increase in interlaminar fracture toughness of carbon-epoxy laminates (processed by hand lay-up with a cure temperature of 175 °C) modified by polyetherketone cardo (PEK-C) nanofibres directly electrospun on the fabric. They used a single 0.4 wt% of nanofibres, and varied the nanofibre diameter: 450, 750 and 950 nm. With these parameters, they demonstrated an interlaminar fracture toughness increase of 65% (450 nm), 51% (750 nm) and 60% (950 nm) as compared to reference specimens without affecting the in-plane properties of the laminates for low nanofibre diameters (450 nm). They then used a nanofibre diameter of 950 nm and varied the weight of nanofibres by 0.22 wt%, 0.44 wt% and 0.65 wt% and showed respectively an increase in interlaminar fracture toughness of 31%, 40% and 81%. The increase in nanofibre wt% induced a slight decrease of in-plane properties. Following this study and due to the misunderstanding of the toughening mechanism that occurred when nanofibres were inserted into a composite laminate, the same authors [275] assessed the phase behaviour of PCL, PVDF and PAN nanofibre interlayers into the same composite laminates. They used a single 0.2 wt% of nanofibres on the fabric, and varied the nanofibre diameter by 450, 750 and 950 nm. With these parameters, an increase in interlaminar fracture toughness with PCL nanofibres but not with PAN and PVDF nanofibres was demonstrated. The PCL nanofibre modified composite laminates showed an increase in interlaminar fracture toughness of 55%, 92% and 87%, respectively for nanofibre diameter of 103 nm, 125 nm and 210 nm. This enhancement was explained by phase separation between the matrix and the nanofibres during polymerisation (see section 2.4.3.1), effective to improve the resistance to crack propagation within the composite matrix (see section 2.6.2.1).

To date, three articles combining nanofibres toughening and self-healing can be reported. The first one is a study made by Zhang *et al.* [276] aiming to reinforce epoxy-PCL blends with carbon nanofibres. The blend of epoxy-PCL (90-10 wt%) exhibited, as seen in section 2.4.3.1, a phase separation morphology consisting of an epoxy-rich macrophase with PCL particles and a PCL rich macrophase with epoxy particles. By inserting the carbon nanofibres (100 nm diameter) into the polymer blend, flexural strength and tensile strength were improved by 221% and 270% respectively as compared to the unreinforced blend. These specimens, after healing at 175 °C for 10 minutes exhibited recovery of flexural load between 60% and 80%. The second article by Wu and Yarin [277] reports the production of co-electrospun DCPD/PAN nanofibres, leading to a shell of PAN with liquid DCPD inside and therefore a similar system than the pioneered system of White *et al.* [203] with the microcapsules. However, no mechanical testing was performed. Finally, Zanjani *et al.* [278] produced tri-axial electrospun fibres where epoxy resin and its hardener were encapsulated. When used as interlayer in FRPs, tensile and flexural modulus could be recovered after damage thanks to the flow and polymerisation of the healing agent within the crack.

2.7 Conclusion

The state-of-the-art research presented throughout the present chapter provides insights for the study of the smart composites aimed in the present work. Damage growth being the main concern in the development of such materials, failure mechanisms in FRPs as well as their characterisation methods were first reviewed. Representative studies on the different systems available to provide crack healing in polymeric matrices were then reviewed. While extrinsic self-healing systems were highly characterised when integrated to FRPs, this was less the case for intrinsic self-healing systems and links between these two large fields were made to inspire one another in the development of composite laminates having the ability to repair microcracks. The major highlight while reviewing this field is that an ideal system for the efficient healing of microcracks in FRPs before they can propagate further and potentially cause catastrophic failure of the structure, would need to: (i) autonomously close cracks whose thickness is above a certain threshold in order to minimise the healing volume; (ii) make use of a healing matrix component that is able to expand up to a certain threshold and fill the cracked regions multiple times. The field of SMAs was then reviewed with highlights on their integration to FRPs. While most of the research integrated SMAs into composites for damage suppression, no one, to the author's knowledge, experimentally investigated the shape memory effect of such materials to autonomously close cracks in FRPs. The combination of an intrinsic healing system as proposed by Luo *et al.* [7] (phase separation of epoxy and PCL) with the use of stitched SMA wires is thus believed to achieve the ideal system for the efficient healing of microcracks in FRPs aforementioned. Finally, the field of damage prevention through the use of thermoplastic second phases (particles or nanofibres) has been reviewed and provided insights for the combined toughening and healing effects with the system targeted in the present work. However, a compromise may need to be found between the brick and mortar structure created by Luo *et al.* [7] (phase separation of epoxy with a continuous PCL phase) for crack healing applications and the phase separation of Zhang *et al.* [275] (phase separation of PCL with a continuous epoxy phase) by nanofibre insertion for toughening applications. Chapter 3 to Chapter 7 below present the experimental methods and work performed during the present study aiming to the development of such smart composites combining repair, actuation and prevention of microcracks damage.

Chapter 3 Materials and Methods

This chapter describes the main materials and methods used throughout the present study. It is divided into three parts: materials, specimens preparation and characterisation methods. In the materials part, the use of epoxy resins and thermoplastics for specific chapters is highlighted for clarity. Furthermore, several blend compositions and composite systems have been explored and will rather be described at the beginning of each relevant chapter. During the discussion of the different specimens within this chapter, two major categories are considered: blend specimens (consisting of epoxy-thermoplastic blends, without any glass fibres) and composite specimens (consisting of fibre-reinforced epoxy-thermoplastic composites).

3.1 Materials

3.1.1 Epoxy resins

Three resin systems have been used throughout the present work:

- In Chapter 4 to Chapter 7, *Epon™ 828EL (Momentive)*, a widely available diglycidyl ether bisphenol A (DGEBA) resin with a molar mass of 340.41 g/mol and a molar mass per epoxide group of 185-192 g/eq was cured with 4,4'-diaminodiphenyl sulfone (4,4' DDS 98%, *ABCR*, molar mass = 248.3 g/mol, 2:1 molar ratio with respect to the epoxy). Unless otherwise mentioned, this resin is named as epoxy in the rest of the present report.
- In Chapter 4, for comparison, DGEBA (*Sigma Aldrich*) with the same molar mass but a reduced molar mass per epoxide group (172-176 g/eq, as in reference [7]) was also used and cured with DDS.
- In Chapter 7 (section 7.2), *Epikote™ MGS® RIM 135* from *Hexion*, another commercial DGEBA resin with a molar mass per epoxide group of 166-185 g/eq was cured with *RIMH 137* in a 100:30 weight ratio.

3.1.2 Thermoplastics

The above-mentioned DGEBA resins have been blended with different thermoplastics:

- Chapter 4 to section 7.1: PCL, $M_n \approx 45,000$ g/mol, *Sigma Aldrich*;
- Chapter 5 and Chapter 6: PCL, $M_n \approx 49,000$ g/mol, *Capa™ 6500* from *Perstorp*;
- Section 4.1: PCL, $M_n \approx 10,000$ g/mol, *Sigma Aldrich*;
- Section 4.1 and 7.2: PCL, $M_n \approx 80,000$ g/mol, *Sigma Aldrich*;
- Section 4.1: PLA, $M_n \approx 125,000$ g/mol, *Ingeo* grade 2003D from *Natureworks LLC*;
- Section 4.1: PMMA, $M_n \approx 150,000$ g/mol, *Evonik Industries AG*.

3.1.3 Shape Memory Alloy (SMA) wires

The SMA wires used were made of a martensitic NiTiCu alloy with relative composition 44.86/45.08/10.06 and a diameter of 150 μm (*Furukawa Techno Material*). Thermal and mechanical properties of these wires have been determined in [6].

3.1.4 E-glass fabric

For composite production, the glass fibre reinforcement was a woven twill 2x2 E-glass fabric, with a nominal areal weight of 390 g/m², 6 end/cm for warp fibres and 6.7 picks/cm for weft fibres, fibre diameter of 9 μm , yarn thickness of 0.45 mm, warp tex of 68x5 and weft tex of 272, from *Suter-Kunststoffe AG*.

3.1.5 Nanofibres

Nanofibrous veils of PCL ($M_n \approx 80,000$ g/mol, *Sigma Aldrich*) of around 30 g/m^2 (gsm) were produced by electrospinning following similar procedures as in [11]–[13]. Formic acid (98%–100%) and acetic acid (98%), all purchased from *Sigma Aldrich* were used as solvent for the electrospinning process [279]. Nanofibrous membranes of homogeneous thickness were produced on an in-house developed multinozzle electrospinning setup using 8 nozzles (internal diameter of 1.024 mm). To produce the nanofibres, 14 wt% PCL was dissolved in a 1/1 volumetric ratio of formic acid/acetic acid solution. This solution was fed through the nozzles at a rate of 1.5 ml/h per nozzle. The tip-to-collector distance was 30 cm. With a voltage set at 35 kV, nanofibres were spun on a moving conveyer belt (aluminium foil). These parameters allowed spinning veils of around 30 g/m^2 (gsm) with a diameter of 345 ± 150 nm. A typical SEM micrograph of such veil is depicted in Figure 3.1.

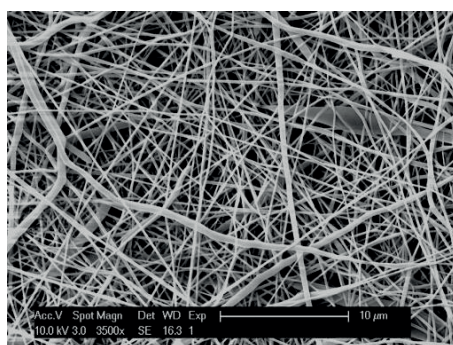


Figure 3.1: SEM micrograph of a typical nanofibre veil obtained through electrospinning.

3.2 Specimens preparation

3.2.1 Preparation of the blends

Blends of PCL (various molecular weights) and epoxy (DGEBA) were prepared with various compositions following a similar procedure to that of Luo *et al.* [7]. The liquid epoxy and the PCL pellets were first melt-mixed in glass jars at 120°C by mechanical stirring at 100 rpm for 1 h with a three-blade propeller (*Caframo*, Canada, 1", 5/16" bore). After 1 h, the temperature was increased to 140°C , the stirring rate was increased to 400 rpm, and DDS (in powder form) was slowly added to the mixture. When the mixture became transparent, it was degassed at 120°C for 20 min. The degassed blend was then used for two purposes:

- **Neat blends:** these were cast immediately into hot silicone moulds (*Elastosil M4670*) and cured at 180°C for 3h.
- **Fibre-reinforced composites:** the blends were infused in the E-glass reinforcement through Vacuum Assisted Resin Infusion Moulding (VARIM) and further cured at 180°C for 3h (see section 3.2.3).

Notice that to produce blends of PLA and PMMA with epoxy, the same procedure was followed except for initial melt-mixing which occurred at 170°C before decreasing the temperature to 140°C to add the DDS hardener.

Four types of model samples made of nanofibres and epoxy resin (*RIM 135*) with two different compositions (20 or 25 vol% of PCL nanofibres with respect to epoxy resin) and two curing conditions to obtain phase-separated microstructures (60°C or 80°C curing for 24h followed by a post-cure at 80°C for 15h) were produced. Nanofibre veil rectangles of $12.5 \times 35 \text{ mm}^2$ were cut and disposed in the right concentration into silicon moulds (*Elastosil M4670*) of the same dimensions. The epoxy resin (mixed with the hardener and degassed for 20 minutes) was then poured in between each nanofibre layer before letting the samples to cure.

Fibre-reinforced composites with nanofibrous veils have also been produced by the VARIM process. In this case, epoxy resin (*RIM 135*) was mixed, degassed and infused at room temperature before curing the composites at room temperature, 60 or 80 °C for 24h and post-curing at 80 °C for 15h (see section 3.2.3).

3.2.2 SMA stitching procedure

The glass fibre stack was stitched with SMA wires using a commercial *Singer* (model 632G) sewing machine, using a jean needle. Notice that SMA wires were pre-cleaned with acetone before any further processing. Lines spaced each by 4 mm were drawn on the fabric to ease alignment during the stitching process (Figure 3.2 (a)) and a target distance between two needle knots of 4 mm was set via the speed and wire tension on the machine. This stitching pattern resulted in 700 SMAs/m². The reproducibility achieved through such a semi-automatic process is depicted in Figure 3.2 (b) and the mean achieved values between two stitched lines and two needle knots were respectively of 4.49 ± 0.75 mm and 3.94 ± 0.78 mm.

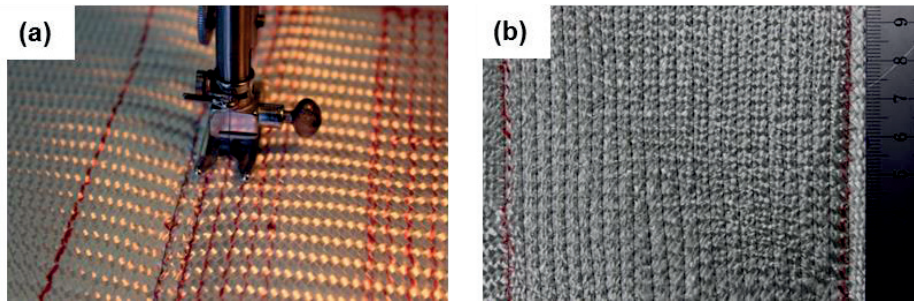


Figure 3.2: Illustration of (a) the stitching process on the stacked preform and (b) the dry preform after stitching.

3.2.3 Vacuum Assisted Resin Infusion Moulding (VARIM)

FRPs with either pure epoxy or epoxy-PCL ($M_n \approx 45,000$ g/mol and $M_n \approx 49,000$ g/mol) blends in different compositions (which are further detailed at the beginning of the relevant chapters) were produced. The different composite plates were processed by VARIM and all contained 16 layers of fibre reinforcement with a sequence of $[(+45/-45)/(0/90)_2/(+45/-45)]_4$. This stacking sequence was used to test a 45° interface through DCB tests (see section 3.3.7), but keeping similar stress and strain intensities as the stacking sequence $[(+45/-45)/(0/90)]_{4s}$ required in the ASTM standard for impact testing [72] (see section 3.3.8). A target fibre volume fraction (V_f) of 50 vol% and a final plate thickness of 5 mm were sought for each composite. Two types of layout have been used for respectively Mode I double cantilever beam (DCB) test (stitched and unstitched with SMA wires) and for impact test specimens (stitched and unstitched with SMA wires).

For DCB specimens, the preforms (cut in 210 x 180 mm rectangles) to be infused were prepared following the layout as depicted in Figure 3.3 (a) for composites unstitched with SMA wires and in Figure 3.3 (b) for composites stitched with SMA wires. A release film (*Cytec*, 15 µm, non-perforated) was placed between the two central plies to form the crack, which was the starting point for the delamination in Mode I (DCB) specimens. This design has already been determined in a previous study [216] as optimum for the VARIM process considering that the film is resin proof and therefore confines the flow of resin.

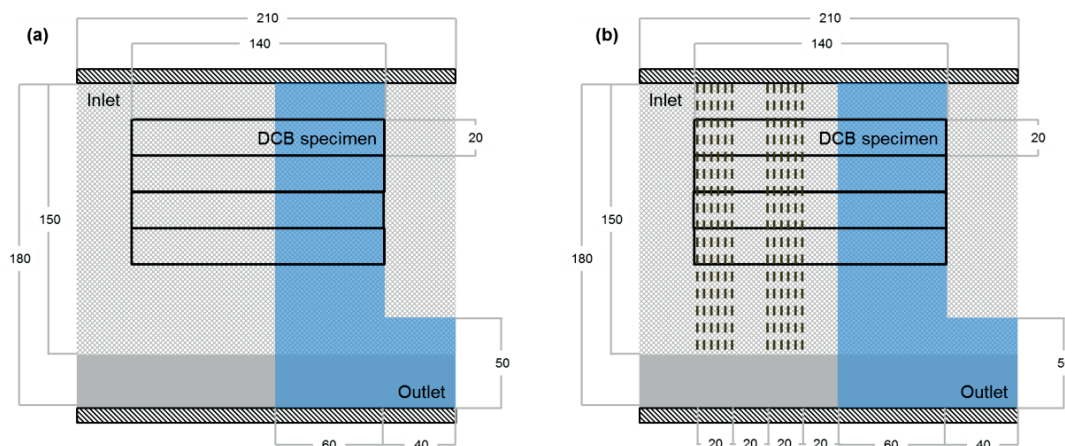


Figure 3.3: Schematic top view of the VARIM layout to produce DCB specimens (a) without stitched SMA wires and (b) with stitched SMA wires. The drawings include the fibre preform (grey), the flow medium (grey mesh), the release film (blue), the inlet and outlet lines. Note that the release film lies on the eighth ply, but is shown at the top for clarity. The geometry of DCB specimens is also showed. In (b), SMA stitched lines are represented in dashed brown lines and were not lying on the entire plate height in order to produce control specimens. Dimensions are in mm. Adapted from [216].

For impact specimens, the preforms (cut in 350 x 250 mm rectangles) to be infused were prepared following the layout as depicted in Figure 3.4 (a) for composites unstitched with SMA wires and in Figure 3.4 (b) for composites stitched with SMA wires. Notice that in order to use specimens unstitched with SMA wires for compression after impact (CAI) in addition to impact tests, these were of larger dimensions than specimens stitched with SMA wires, which were only used for impact tests. In order to ease resin infusion, the inlet was placed at the middle of the infusion design and the flow medium both at the top and bottom of the reinforcement.

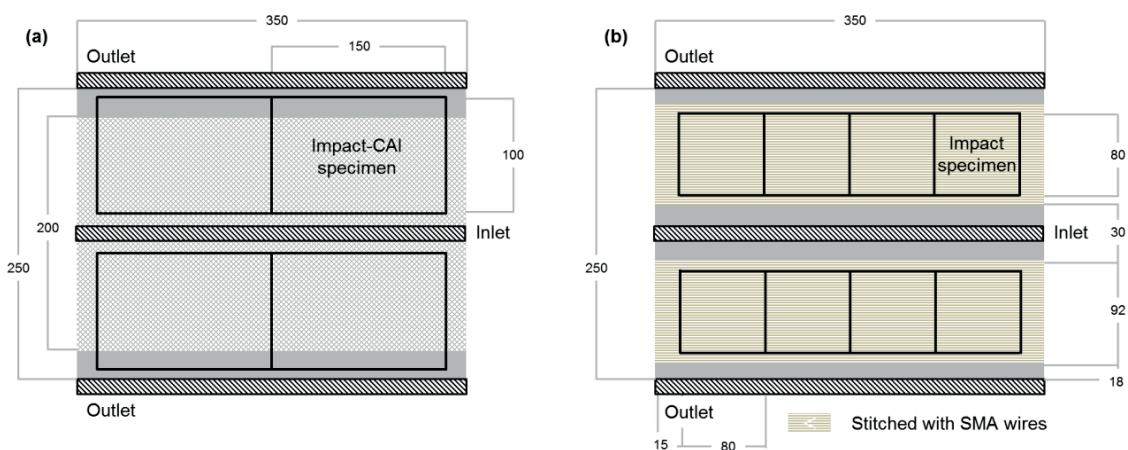


Figure 3.4: Schematic top view of the VARIM layout to produce impact specimens (a) without stitched SMA wires and (b) with stitched SMA wires. In (a), the drawing includes the fibre preform (grey), the flow medium (grey mesh), the inlet and outlet lines. In (b), the drawing includes the fibre preform (grey) and the SMA stitched lines; for clarity the flow mesh was not represented but lies at the same place as in (a). Dimensions are in mm.

Notice that for specimens stitched with SMA wires, the stitched preforms were placed, before any bagging, at 150 °C for 30 minutes in order to (i) remove any internal stresses due to the sewing process and (ii) ensure that the SMA wires were in a fully twinned martensitic state and hence maximise the shape memory effect.

The epoxy-PCL blends were, after preparation (see section 3.2.1), infused into the different preform layouts (see Figure 3.3 and Figure 3.4) in an oven set to 140 °C, which ensured a viscosity below 1 Pa·s for the blends containing

the highest PCL content (determined by a plate rheometer AR 2000 from *TA Instrument*). The plates then underwent a curing treatment at 180 °C for 3h. Specimens were cut out of the plates (following the dimensions shown in Figure 3.3 and Figure 3.4) using a *Maïco* saw equipped with a diamond blade. For each specimen, the weight was recorded, the thickness measured in 3 points, averaged and the fibre volume fraction calculated.

To produce composites with nanofibres for Mode I DCB specimens, the same infusion layout as shown in Figure 3.3 (a) was used. PCL nanofibre veils with dimensions 140x100 mm² were cut and weighed before being placed in between each dry reinforcement layer using a template to ensure their exact positioning. A part of the plate without nanofibres was used to provide reference (non-modified) specimens. Infusion was then performed with the epoxy resin (*RIM 135*, degassed for 20 minutes before infusion) at room temperature (to avoid any PCL melting and diffusion) before placing the composite plate to cure at the desired temperature (room temperature, 60 or 80 °C) for 24h. Each composite plate underwent a post-curing treatment for 15h at 80 °C. Preparation of DCB specimens followed the same procedure as described above except that the stacking sequence was [(+45/-45)/(0/90)]_{4s}.

3.3 Characterisation methods

3.3.1 Morphological Characterisation

3.3.1.1 For epoxy-thermoplastic blend specimens

In situ observations of the morphology during cure were made on drops of the as-prepared epoxy-PCL blends inserted between two glass cover-slides immediately after degassing (for some specimens, few glass fibres were also inserted), using a transmission optical microscope (*Olympus BX-60*) equipped with a hot-stage held at 180 °C (*Linkam THMS600/Linkam TMS92*). The specimen was placed directly onto the hot-stage and images were taken every 20 seconds in order to determine the time for the onset of phase separation. For every epoxy-thermoplastic blends, drops of the as-prepared blends inserted between two glass cover-slides immediately after degassing, were observed after curing to determine the phase separation morphology using a transmission optical microscope (*Olympus BH-2*). Transmission optical microscopy (*Olympus BH-2*) of roughly 10 µm thick microtomed sections (*Reichert-Jung Ultracut E/Diatome* diamond knife) was used in order to estimate the mean diameters of the epoxy particulate inclusions (50 measurements per image) within epoxy-PCL blends.

Scanning electron microscopy (SEM, *Philips XLF-30 FEG*) was used on 10 nm gold coated fractured (tensile tests) epoxy-thermoplastic blends in order to determine the rupture behaviour. For epoxy-PCL blends, specimens were also fractured in liquid nitrogen, treated with chloroform (*Sigma Aldrich*) in order to etch away the PCL, and then 10 nm gold-coated.

The composition of the phases in selected epoxy-PCL blends was also assessed using Fourier transform infrared (FTIR) microscopy (*Perkin Elmer Spotlight 200 FTIR Imaging System*) of polished sections (embedded in *Epofix* Resin and then polished until 1 µm size diamond disc polishing).

3.3.1.2 For composite specimens

Transverse cuts of some cured composite specimen were embedded in *Epofix* Resin, polished until 1 µm size diamond disc polishing, and observed with a reflexion optical microscope (*Olympus BH-2*). Fracture surfaces of DCB specimens, coated with 10 nm of gold, were also observed by scanning electron microscopy (SEM, *Philips XLF-30 FEG*). Transverse cuts of selected impact specimens at impact location were embedded in *Epofix* Resin, then polished until 1 µm size diamond disc polishing, and observed with a reflexion optical microscopy (*Olympus BX61*) having an automated plate displacement. A map of the impact damage was built and the crack size distribution measured with *AnalySIS pro* software.

Note that for every composite process, a small droplet of the epoxy-PCL blend was placed in between two glass cover-slides in order to control by optical microscopy (*Olympus BX-60*) the obtained phase-separated morphology.

3.3.2 Thermomechanical characterisation

3.3.2.1 Differential scanning calorimetry (DSC)

Thermal transitions of the matrix materials were determined by means of DSC experiments. 5-10 mg specimens (raw materials of section 3.1 as well as blends and composites), were subjected to DSC (*TA Q100, TA Instruments*) heating scans from -90 to 300 °C at 10 °C/min followed by cooling to 0 °C at the same rate. For *in situ* investigations of the cure rates in epoxy-PCL ($M_n \approx 45,000$ g/mol) blends, 10-15 mg specimens taken from the blends immediately after degassing were maintained at 180 °C for 3 hours.

3.3.2.2 Dynamic Mechanical analysis (DMA)

For the DMA measurements (*TA Q800, TA Instruments*) 35×12.5×2 mm³ strips were cut from the cast epoxy-thermoplastic specimens (the dimensions were reproduced by grinding to a precision of ± 0.05 mm) and 35×12.5 mm² rectangles were cut from the cured composite specimens. Tests were performed at 1 Hz in single-cantilever mode, with a displacement amplitude of 15 µm and assuming a Poisson's ratio, ν , of 0.4 in calculating the storage modulus, E' , from the bending stiffness. The temperature was ramped from -150 to 300 °C at 6 °C/min. Transition temperatures were defined as the temperatures corresponding to the peaks in $\tan \delta$; each material was tested in triplicate.

For specimens with nanofibres, two types of measurements have been carried out on the DMA in tensile mode: (i) thermal expansion of (modified) resin specimens (35×12.5 mm²), by ramping the temperature from 30 to 160 °C at 1 °C/min while applying a static force of 0.05 N and measuring the elongation of the specimens; (ii) dimensional change of the nanofibrous veils (20×10 mm² rectangles) close to the PCL melting temperature by measuring the contraction/elongation of the specimens at an isothermal temperature of 60 °C.

3.3.3 Interfacial characterisation

3.3.3.1 Pull-out tests

Interfacial shear strength (IFSS) between the SMA wire and epoxy-PCL ($M_n \approx 45,000$ g/mol) blends as well as epoxy-PCL ($M_n \approx 45,000$ g/mol) composites was assessed by means of pull-out tests and compared with reference specimens (epoxy without and with reinforcement). Pull-out specimens consisted of SMA wires embedded (1 to 5 mm embedded length) into a resin (or composite) block. Two geometries were assessed: straight wires and looped wires to simulate stitches in composites (see Figure 3.5). For specimens without fibres, the mixture was cast into hot silicon moulds (*Elastosil M4670*) with SMA wires previously inserted. For the composite specimens, the VARIM process was performed with various amounts of fibre reinforcement layers (3, 6, 9 and 16 layers of 0/90 orientations ensuring different specimen thicknesses for pull-out testing, but keeping a targeted 50 vol% of fibre reinforcement). SMA wires were previously inserted into the reinforcement and then passed through the vacuum bag of the system (and through a drilled infusion plate, with holes filled with silicon). As the vacuum bag had to be perforated to ensure clean wires outside of the specimens, a second vacuum bag was used to provide full vacuum to the entire system. Notice that SMA wires were pre-cleaned with acetone and pre-heated before resin casting or infusion in order to remove any strain history. The specimens were tested on a Universal Testing Machine (UTM, *Walter & Bai AG*) equipped with a 50 N load cell. The wire was held at one end and pulled at a constant crosshead speed of 1 mm/min while the block of resin was kept in place thanks to a steel holder with a 0.4 mm gap. The gauge length was set to 15 mm. The thickness of every specimen was recorded before the test to determine the wire embedded length (for loop specimens, the diameter was recorded). Notice also that specimens were subjected to a heating cycle of 150 °C during 30 minutes before testing to anneal any strain history that could have appeared during processing and demoulding.

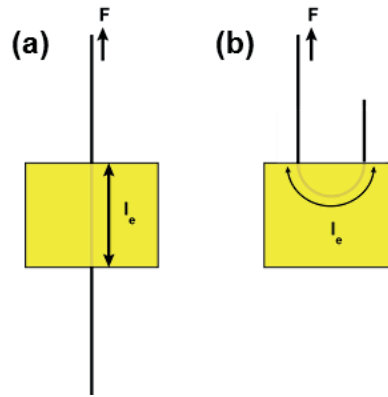


Figure 3.5: Schematics of the used geometries for pull-out testing and the corresponding embedded lengths for (a) straight and (b) loop specimens.

On each force-displacement curve, the peak force (corresponding to the force at debonding) was recorded in order to determine IFSS. Apparent IFSS, τ_a , following Eq. (2.6) was first determined as a function of the embedded length. Then, intrinsic IFSS was determined following Mendels model [92] seen in Eq. (2.7). Notice that internal stresses were also considered through Eq. (2.8).

For the loop geometry, the same procedures were applied, except that embedded lengths were determined as the perimeters of a circle with varying diameter.

For epoxy-PCL ($M_n \approx 45,000$ g/mol) blends, the wire was replaced back after test, heated to 150 °C during 30 minutes and retested again. Healing efficiency during this test was then determined through Eq. (2.1). Notice that a low constant force was found after debonding, which corresponds to the friction of the wire once debonded. This value was defined as the IFSS in the damaged state, used for healing efficiency determination.

Several intrinsic material properties are needed during IFSS calculation. These are summarized in Table 3.1 and based on Chapter 4 for resin properties and on [210] for SMA properties.

Table 3.1: Materials properties for IFSS determination.

Material	E [GPa]	ν	α [$^{\circ}\text{C}^{-1}$]
Epoxy	2.69	0.3	$4.5 \cdot 10^{-5}$
Epoxy-PCL	1.46	0.34	$9.22 \cdot 10^{-5}$
SMA	19	0.33	$9.22 \cdot 10^{-5}$

3.3.3.2 Push-in tests

Interfacial shear strength between glass fibres and epoxy-PCL ($M_n \approx 45,000$ g/mol) blends (or epoxy resin) on the previously polished cured composite specimens was determined by means of nanoindentation tests (Nanoindentation Tester *NHT²*, *Anton Paar*) with a Berkovich diamond indenter ($\alpha = 65.3^{\circ} \pm 0.3$) at fibre locations. Loading and unloading rates were set to 200 mN/min with a pause of 15 s whereas the maximum load was set to 100 mN. This maximum load was sufficient to ensure entire debonding of the largest fibres (determined through increasing load step tests). At least 50 measurements were performed per system. The data reduction scheme for interfacial shear strength determination followed the procedure developed by Kharrat *et al.* [95] and Zidi *et al.* [96] assuming that the displacement during the indentation test, u , is the sum of two independent contributions: (i) the displacement u_{ep} due to the elasto-plastic indentation of the fibre surface by the indenter (this component is determined from the indentation behaviour in a bulk material having the same composition as the fibre, i.e. glass lamellae (*Assistent*) made of soda lime glass in the present work); (ii) the displacement u_o of the fibre surface due to the fibre compression into

the matrix and the matrix deflexion. Interfacial shear strength between the fibre and the matrix is therefore found from the curve of indentation stress versus $u_0 = u - u_{ep}$, which can be fitted with Eqs. (2.12) and (2.13).

Knowing the radius of the indented fibre, r_f , the load P_0 at each displacement u_0 and E_f , n can be determined from Eq. (2.12). By using then Eq. (2.13), σ_d and therefore the load at debonding, P_d , can be determined and used to finally calculate the interfacial shear strength (similar to Eq. (2.9)):

$$\tau_s = \frac{nP_d}{2\pi r_f^2} \quad (3.1)$$

An example of this approach (specific of the present work) is provided in Figure 3.6 (a) where Eqs. (2.12) and (2.13) demonstrated appropriate fitting of this system. Only the indentation loading portion is considered here, which is sufficient in the interfacial shear strength determination (further details on the unloading portion fitting are provided in [96]). Notice that the load at debonding (P_d) can also be defined as: the deviation between the linear and non-linear part of the reduced curve (but its determination was here performed through Eq. (2.13)). Figure 3.6 (b) shows the corresponding indented fibre image (taken through optical microscopy) where the black circle around the fibre is characteristic of its debonding.

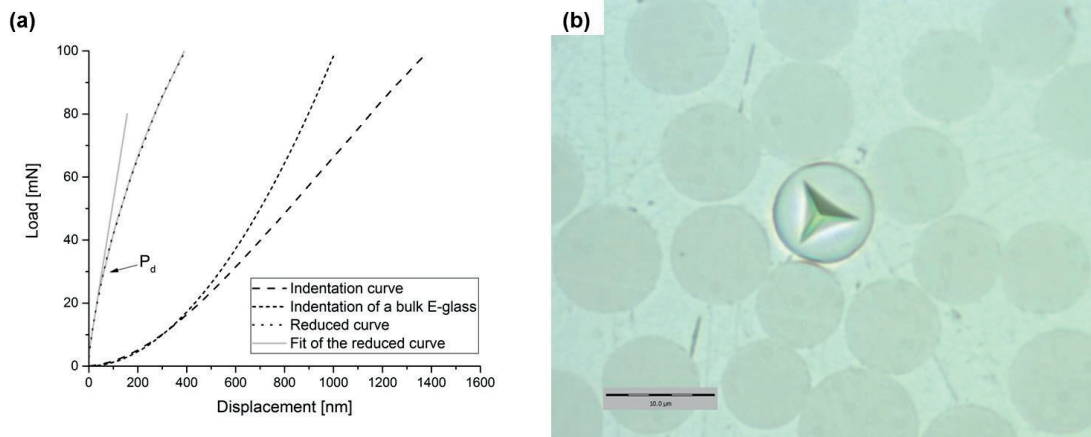


Figure 3.6: Indentation test on an epoxy composite specimen: (a) Determination of the reduced curve from the initial indentation curve and that in a soda lime glass, fitted with Eq. (2.12) for the linear part and Eq. (2.13) for the non-linear part. Unloading portions of the tests are not shown for clarity; (b) corresponding indentation imprint on the fibre.

3.3.3.3 Contact angles measurement

Small droplets of the used matrices were deposited on cleaned SMA wires with the help of a syringe tip and then cured for 3h at 180 °C. The cured droplets were then observed under a transmission optical microscope (*Olympus BH-2*) and their diameter, l , thickness, x_2 , as well as the wire radius, x_1 , measured (Figure 3.7). Contact angles were then determined from these measured quantities and the method of Carroll [280].

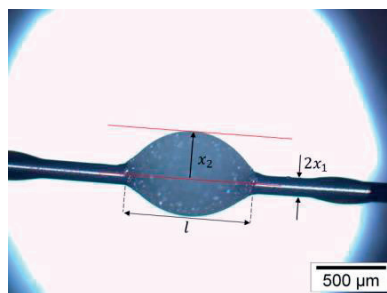


Figure 3.7: Contact angle measurement procedure.

3.3.4 Tensile tests

Tensile tests on epoxy-thermoplastic blends were carried out following the ASTM standard D638, type V specimens [281] using the UTM equipped with a 10 kN load cell. The extensometer gage length was set to 10 mm and the crosshead speed was 1 mm/min. The ends of the specimens were polished in order to avoid slippage in the grips and at least five specimens were tested for each composition.

3.3.5 Tapered Double Cantilever Beam (TDCB) tests

Fracture toughness of the cured epoxy-thermoplastic blends was evaluated from long-groove TDCB specimens using the UTM, equipped with a 10 kN load cell. The TDCB test geometry is convenient because precise measurements of the crack length are not needed for the characterisation of the fracture toughness of linear elastic specimens [61], [62]; it is also currently widely used to quantify the healing efficiency of a variety of materials [60]. However, while TDCB testing is popular for the investigation of self-healing in microcapsule-based systems, its application to thermal mending systems is less frequently reported [178], [212].

The TDCB specimens were prepared using the geometry and three-step procedure described in [8]. (1) *Epon™ 828EL* mixed with diethylenetriamine (DETA, *Sigma Aldrich*) in the stoichiometric mass ratio 100:12 was cast into silicone moulds corresponding to the external dimensions of the TDCB specimens, with a silicone spacer placed along the centre of the mould in line with the moulded-in starter notch. The Epon/DETA mixture was left for 1 h at room temperature and then cured at 140 °C for 1 h. (2) The moulds were opened to remove the inner spacers, closed again and held at 160 °C for 20 min. (3) The degassed epoxy-thermoplastic blend of interest was then immediately cast into the space left by the spacer, the temperature raised to 180 °C, and the blend allowed to cure for 3 h, providing excellent adhesion with the surrounding cured epoxy. After cure, a sharp pre-crack was created by tapping a fresh razor blade into the starter notch. This procedure provided optimum use of relatively small amounts of the epoxy-PCL blends.

For the TDCB geometry specified, the plane strain critical stress intensity factor, K_{Ic} (see Eq. (2.2) for definition), for crack advance is given by:

$$K_{Ic} = \alpha \sqrt{\frac{E_{blend}}{E_{Epon}}} P_c \quad (3.2)$$

where P_c is the maximum load, $\alpha = 11.2 \cdot 10^{-3} \text{m}^{-3/2}$ [282] and the factor $\sqrt{E_{blend}/E_{Epon}}$, where E_{blend} is the Young's modulus of the blend insert and E_{Epon} is that of the remainder of the specimen, takes into account the locally modified stiffness in the vicinity of the crack tip [283]. The specimens were deformed in tension with a loading point displacement rate of 5 $\mu\text{m/s}$. Once the crack had propagated over 2/3 of the initial ligament length of the virgin specimens (virgin cycle), the load was released by reducing the displacement at a speed of 20 $\mu\text{m/s}$. The specimens were then healed by holding them at 150 °C for 30 min with a constant applied compressive load perpendicular to the crack faces of 0.39 kg (corresponding to about 50 kPa when normalized with respect to the crack area), then retested using the same procedure as for the virgin cycle (healed cycle). The healing efficiency was defined as the ratio of P_c measured during the healed and virgin cycles, following Eq. (2.1). Notice that fracture toughness in the damage state is here null and thus the healing efficiency equation is reduced to:

$$\eta = \frac{P_{c,healing}}{P_{c, virgin}} \quad (3.3)$$

3.3.6 Flexural tests

Three point bending tests, following the ASTM standard D790 [284], were performed on composite specimens at room temperature only, using 96×13 mm² coupons cut from the cured plates. Tests were performed using the UTM equipped with a 10 kN load cell. A span-to-depth ratio of 16:1 was used, corresponding to a span of 80 mm and a cross-head speed of 2 mm/min. At least 8 specimens were tested per system. Notice that 2 specimens were cut larger in order to reach a span-to-depth ratio of 32:1 and confirm the validity of the results.

3.3.7 Mode I Double Cantilever Beam (DCB) testing

The fracture behaviour of the composites (stitched and unstitched with SMA wires) was assessed in Mode I Double Cantilever Beam (DCB) following the ASTM standard D5528 [35] and using the UTM, equipped with a 10 kN load cell. For load introduction, aluminium blocks were glued on each side of the specimens using *Spabond* resin cured with *Spabond* adhesive non-pigmented hardener purchased from *Gurit* (5 minutes curing at room temperature). Each specimen underwent four loading-unloading cycles (in addition to the pre-cracking procedure), the first one corresponded to the test of the *virgin* specimen, whereas the three others applied to the *healed* specimens each after a thermal mending cycle of 30 minutes at 150 °C, i.e. the healing ability was tested three consecutive times. In each cycle, loading was performed until displacement reached 30 mm (for SMA stitched specimens, loading was performed until crack length reached 24 mm) before unloading at the same speed of 4 mm/min until the load reached zero. At least 7 specimens (3 for SMA stitched composites) were tested for each batch. During thermal mending, the specimens were unloaded, and placed in the oven either without any clamping (for SMA stitched specimens) or with the crack faces imposed to be in contact at the location of the loading blocks (both for stitched and unstitched specimens, with a force of 90 N). In order to determine the crack thickness distribution before and after the thermal mending cycle, specimens were positioned to show their side under an optical microscope (*Olympus BX-60*), and several images taken and assembled to reconstruct the entire crack. The crack was then isolated through image analysis (*Matlab* software) and the crack thickness distribution determined as a function of the crack length.

A typical load-displacement curve with the loading-unloading cycles of the *virgin* and *healed* specimens (for a composite free of SMA wires) is depicted in Figure 3.8. Healing efficiency was first estimated by comparing the slope during loading of the *healed* specimen ($slope_{load,healed}$, after thermal mending) to the slope during loading ($slope_{load, virgin}$, 100% efficiency) and unloading ($slope_{unload, virgin}$, 0% efficiency) of the *virgin* specimen. The efficiency was therefore defined, in this stiffness based calculation, as:

$$\eta = \frac{slope_{load,healed} - slope_{unload, virgin}}{slope_{load, virgin} - slope_{unload, virgin}} \quad (3.4)$$

In addition, interlaminar fracture toughness, G_{IC} (see Eq. (2.2) for definition), was calculated based on crack length measurements (Modified Beam Theory) [35] and therefore a second way of characterising healing efficiency was defined as (again interlaminar fracture toughness in the damaged state is null):

$$\eta = \frac{G_{IC, healed}}{G_{IC, virgin}} \quad (3.5)$$

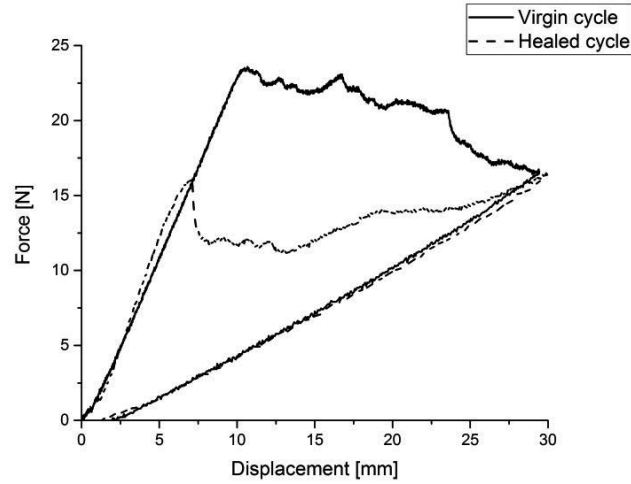


Figure 3.8: Typical loading and unloading cycles for a DCB test (free of SMA wires) in the virgin state and in the healed.

3.3.8 Impact testing

The low-velocity impact behaviour of the produced composite specimens (stitched and unstitched with SMA wires) was assessed following ASTM 7136 [72] with a *Rosand* impact testing machine. The load imparted by the 5.5 kg impactor was recorded by a 60 kN *Kistler* load cell, allowing the impact velocity, impactor displacement and energy absorbed to be determined as a function of time. The velocities before and after impact were also measured using light gates placed just above the specimens, allowing a direct estimate of the energy dissipated within the specimens. The impact energy, E , imparted to the specimen prior to drop was determined following the ASTM standard [72]:

$$E = C_E h \quad (3.6)$$

with C_E the specified ratio of impact energy to specimen thickness, 6.7 J/mm, and h the nominal thickness of the specimen. In order to observe different damage areas, three nominal energies have been tested: E , $E/2$ and $E/4$ which corresponded to energies of around 34, 17 and 8.5 J and inbound velocities of 3.0, 2.2 and 1.5 m/s. Notice that because healing is the main concern of this study and in order to maintain a constant level of initial damage in the different materials, the impact energies were adjusted (based on ASTM 7136 [72]) to take into account variations in the thickness of individual specimens. Hence, the nominal impact energies referred to in the discussion corresponded to true fracture energies of 33.2 ± 1.1 J; 16.6 ± 0.6 J; 8.29 ± 0.3 J. At least 4 specimens were tested for each impact energy and system.

3.3.9 C-scans

The damage areas of the composite specimens (stitched and unstitched with SMA wires) were quantified by means of C-scan tests (at the HEIG-VD in the COMATEC institute). Each specimen (protected with a Teflon tape on the sides to prevent water penetration) was placed in a water bath and scanned with a 2.5 MHz piezoelectric transducer at steps of 0.2 mm. 2D-maps of the specimen (squares of 50×50 mm²) were generated, analysed with *TomoView* software to show the variation in the attenuation of the transmitted sound wave when damage was present. Damage was defined to correspond to regions where 80% of the sound wave was attenuated. To quantify healing, an initial C-scan was taken after impact, followed by a healing treatment at 150 °C for 30 minutes and a second C-scan. Healing efficiency was calculated as follows:

$$\eta = 1 - \frac{A_{healed}}{A_{virgin}} \quad (3.7)$$

with A_{healed} and A_{virgin} the damage area in the virgin and healed state respectively. At least 3 specimens were scanned for each energy, condition and system.

In order to further use the specimens that were not stitched with SMA wires for CAI tests, these were placed after C-scan at 40 °C for 1h in order to dry potential infiltrated water. DMA measurements in single-cantilever mode (TA Q800, *TA Instruments*) of the specimens as produced, and compared to specimens placed in water for 30 minutes, then dried for 1h at 40 °C showed similar storage modulus over a temperature range of 0 °C to 200 °C, thus demonstrating that C-scanning followed by a drying procedure did not affect mechanical properties of the specimens.

3.3.10 Damage recovery through optical analysis

Pictures of composite specimens before and after impact as well as before and after the thermal mending cycle (30 minutes at 150 °C) were taken with a *Canon D600* camera and then binarized with *Matlab* software. Pictures before impacts were used as baseline to isolate the impact. The ratio between the area of damage before and after thermal mending was defined as the efficiency of impact damage recovery (similar to Eq. (3.7)).

3.3.11 Compression After Impact (CAI)

The ultimate compressive residual strength, F_{CAI} , of the impacted specimens (composites unstitched with SMA wires) was assessed following the ASTM standard D7137 [79] with a 600 kN *Schenk* universal testing machine. At least 3 specimens were tested for each energy, condition and system. Compressive properties of undamaged specimens were also tested as reference. Healing efficiency was defined following Eq. (2.1) as:

$$\eta = \frac{F_{CAI, healed} - F_{CAI, impacted}}{F_{CAI, virgin} - F_{CAI, impacted}} \quad (3.8)$$

with respectively $F_{CAI, virgin}$, $F_{CAI, impacted}$ and $F_{CAI, healed}$, the compressive residual strength of the specimens before (*virgin*) and after impact (*impacted*), and after healing (*healed*) at 150 °C for 30 minutes.

Chapter 4 Epoxy-thermoplastic blends

In the present chapter, phase separation, mechanical properties and the crack healing capacity of immiscible thermoplastic blends with a commercial DDS-cured epoxy are investigated, based on previous studies [7], [135], using a relatively mild healing temperature. Because the ultimate aim is to use such blends as a matrix for healing fibre-reinforced composites, it was considered important to choose a reference epoxy formulation and cure conditions leading to an optimum combination of toughness and stiffness. Using such blends as a matrix in fibre-reinforced polymer composites is believed to: (i) provide autonomous healing functionality (thanks to thermoplastic expansion within the cracks) that is absent in many intrinsically self-healing systems; (ii) provide similar stiffness and toughness as conventional epoxy formulations; (iii) allow the use of a relatively low healing temperature so that the overall mechanical integrity of the system is maintained during the healing cycle. The influence of the thermoplastic nature, content and phase morphology on the mechanical performance of the epoxy was assessed through static and dynamic tests on un-notched specimens, and static fracture tests using the tapered double cantilever beam (TDCB) geometry. TDCB specimens were then used to investigate the healing capacity of the blends after thermal mending at 150 °C for 30 min. Section 4.1 first screens various thermoplastics to be blended with epoxy while section 4.2 presents a deeper study on the most appropriate thermoplastic to be further integrated in FRPs.

4.1 Assessment of potential epoxy-thermoplastic systems

Luo *et al.* [7] pioneered the work on epoxy-thermoplastic blends for crack healing applications, as reviewed in section 2.4.3. A biphasic structure was shown to be most effective, with a major load bearing phase (the brick, epoxy) and a healing phase (the mortar, PCL) having the ability to restore structural integrity of the initial material.

The epoxy-PCL ($M_n \approx 42,500$ g/mol) blends studied by Luo *et al.* [7] could thus be applied as the matrix in FRPs. However, similar brick and mortar morphology obtained through phase separation can be reached with many other thermoplastics (see section 2.4.3.1), which could be relevant to composite processing, and possibly more adapted. Various epoxy-thermoplastic blends are compared in this section. In particular, stiffness, strength and fracture toughness as well as recovery in fracture toughness (i.e. healing assessment) are measured to provide an appropriate comparison. The healing temperature is set to 150 °C max (as opposed to 190 °C in Luo *et al.* [7] study) in order to stay far away from epoxy glass transition temperature (200 °C in Luo *et al.* [7] study) so as not to strongly affect the structural integrity of the produced blends.

Since a large library of thermoplastics is available, the best candidates are first screened based on expected requirements, deduced from the main intrinsic properties of epoxy and PCL (see Table 4.1) determined in [7] and from preliminary experiments (see the experimental procedures detailed in Chapter 3) on the miscibility of blends in the uncured melt state. Regarding mechanical properties, knowing that the Elastic modulus (taken from DMA data in [7]) of epoxy and PCL ($M_n \approx 42,500$ g/mol) are respectively of 3 and 0.5 GPa, the chosen thermoplastic should have a minimum modulus of 0.5 GPa. Strength of the blends is critical in structural integrity of the produced specimens. Strength of epoxy and PCL was here measured (following the procedures detailed in Chapter 3) as 79 and 16 MPa respectively. Notice that the PCL molecular weight used was slightly higher ($M_n \approx 45,000$ g/mol as opposed to $M_n \approx 42,500$ g/mol) than that of Luo *et al.* [7] due to manufacturer constraints. Strain of the thermoplastic should be higher than 5% in order to be above the epoxy one but no further specific requirements are needed. Directly linked to mechanical properties, the thermoplastic T_g should be above room temperature (i.e. above 60 °C) to remain far from the rubbery state and preserve some structural integrity of the blend. As these blends are targeted for a use as matrices in FRPs, their viscosity in the uncured state should remain low enough to target realistic flow kinetics during

infusion, ideally below 1 Pa·s. In addition, the thermoplastic should also be able to provide appropriate healing properties. This goes through the ability of the thermoplastic to flow and expand within the crack. In particular, the thermoplastic should have a melting temperature below the healing temperature and have a viscosity allowing its flow within the crack. For the present case, the thermoplastic melting temperature should be below 130 °C, whereas it should also have a viscosity below 100 Pa·s at the healing temperature. Considering expansion during healing, the thermoplastic should be as close as possible to PCL, which allowed filling low damage extents, as determined by Luo *et al.* [7]. While the above-mentioned properties are generally determined experimentally, volume expansion of the thermoplastic can be calculated from Tait equation and the study of Rodgers [285] (for 56 polymers) as a function of the temperature, T :

$$V(P, T) = V(0, T)\{1 - C \ln[1 + P/B(T)]\} \quad (4.1)$$

where P is the environment pressure (here set to atmospheric pressure), C is a universal constant equal to 0.0894, and $V(0, T)$ and $B(T)$ respectively the zero pressure isotherm and the Tait parameter given by:

$$V(0, T) = V_0 \exp(\alpha T) \quad B(T) = B_0 \exp(-B_1 T) \quad (4.2)$$

with α the thermal expansion coefficient and V_0 , B_0 , B_1 parameters.

Tait equation in the case of PCL, based on the study of Rodgers [285], is used to describe volume expansion for PCL in Figure 4.1 (notice that below 55 °C, PCL is in the solid state where volume expansion is considered here as null). At the healing temperature, 150 °C, PCL therefore expands by 14%, which allows calculating its filling capacity for specific geometries (further details are given in Chapter 5 and Chapter 7). Considering these specifications, a semicrystalline thermoplastic will be preferred. However, notice that some amorphous thermoplastics also have the ability to phase separate with epoxy and can therefore be of interest (see section 2.4.3.1). Finally, the thermoplastic should also have free hydroxyl groups to bond well the epoxy and should be miscible with epoxy in the uncured (i.e. liquid) state.

Table 4.1: Intrinsic properties of epoxy and PCL ($M_n \approx 42,500-45,000$ g/mol).

Property	Epoxy	PCL
E [GPa]	2.7	0.5
σ [MPa]	79	16
ϵ [%]	4.6	382
T_g [°C]	200	-55
Viscosity [Pa·s]	1 (at 35 °C)	100 (at 120 °C)
T_m [°C]	-	55
Volume expansion [%]	-	14 at 150 °C

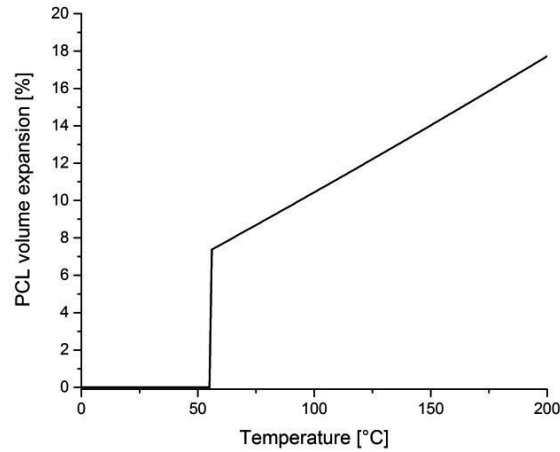


Figure 4.1: PCL volume expansion in the liquid state, as a function of temperature.

Based on the properties given in Table 4.1 and the studies presented in section 2.4.3.1, several thermoplastics can form suitable candidates as phase-separated blends for thermal mending applications. Notice that amorphous thermoplastics are also considered, even if the melting state with semicrystalline thermoplastics will be favoured. All general material properties were taken from [286].

- **PCL** with lower molecular weights (lower than that used by Luo *et al.* [7]) should first be mentioned to potentially increase the strength of the blend [144], while reducing its viscosity. For example, the PCL 4,000 g/mol used by Siddhamalli [144] was reported to show no decrease in tensile strength for the phase-separated epoxy particles morphology. Notice that the strength level of PCL depends on its degree of crystallinity.
- **PCL** with higher molecular weights (higher than that used by Luo *et al.* [7]) could provide higher overall strength and phase separation capability with epoxy [135], [136]. Notice that the strength level of PCL also depends on its degree of crystallinity.
- **Polybutylene succinate** (PBS) is a semicrystalline thermoplastic similar to PCL with the same T_g but a T_m of 115 °C and therefore an expected higher viscosity. It has been copolymerised with PCL and has demonstrated phase separation behaviour when blended with epoxy, which also improved fracture toughness [287]. Due to its low T_g , properties at room temperature are expected to be similar to those in Luo *et al.* [7] study while providing a higher blend viscosity.
- **Ethylene vinyl acetate** (EVA) was demonstrated as an effective healing agent when used as particles in FRPs [188], [189]. In addition, this thermoplastic copolymer was also used for phase separation in epoxy [288]. In the study of Pingkarawat *et al.* [188], it has a T_m of 97 °C, where its volume expansion is of 25% and has a viscosity close to 100 Pa·s at 150 °C, as required. As demonstrated by Siddhamali [288], tensile strength in blends of epoxy-EVA with the targeted co-continuous morphology is of 7 MPa, which thus does not compete with the blends studied by Luo *et al.* [7].
- **Polysulfone** (PSU) is immiscible in the cured state with epoxy and creates a co-continuous morphology for PSU contents over 25 wt% in the blend [155]. Moreover, for this content, Young's modulus, flexural strength as well as fracture toughness were observed to increase by respectively 12, 18 and 120% as compared to epoxy [156]. However, T_g of PSU is around 170 °C, which does not match the healing temperature requirement.

- **Poly(methyl methacrylate)** (PMMA) is a widely known thermoplastic with relatively elevated modulus (2.6 GPa) and strength (60 MPa). Even though it is amorphous, its T_g of around 100 °C can allow healing of crack interfaces at 150 °C. Also, it is known for its ability to phase separate and create the co-continuous morphology [163]–[168].
- **Polystyrene** (PS) was also used to create the brick and mortar morphology with epoxy [169], [170]. In that case [169], optimal blend compositions (10 wt%) showed improvements in fracture toughness from 0.73 MPa m^{1/2} for the neat brittle epoxy to 1.37 MPa m^{1/2} for the blend. T_g of PS is around 100 °C and when made as semicrystalline polymer (syndiotactic polystyrene) the melting temperature is around 270.3 °C. This last temperature is certainly too high for the present work, but its T_g can make it suitable.
- **Polyvinyl butyral** (PVB) is a commercial amorphous thermoplastic often used for toughening purposes through phase separation as it dissolves into epoxy in the uncured state [289]. This polymer has a T_g of 97 °C, a modulus of 2.3 GPa and a tensile strength of around 50 MPa. In addition, it was already studied for its healing purposes at room temperature as it has the ability to reform bounds below its T_g [290].
- **Poly(lactic acid)** (PLA) is a biodegradable semicrystalline thermoplastic with a T_g of 60 °C and a T_m of 150 °C. Its tensile strength reaches for many grades 50 MPa. It has never been used for phase separation in epoxy, but its free hydroxyl groups can allow this process.
- **Polyamide** (PA) can also suite the present work with phase separation. PA6 and PA11 have melting temperatures of respectively 220 °C and 150 °C whereas their tensile strengths are respectively of 75 and 18 MPa. Both have a glass transition temperature around 45 °C. The interest with this thermoplastic is that, when copolymerised with different grades, properties can be highly tuned. For example, *Elvamide*® 8063 from *DuPont*TM is a copolymer of PA6/66/610 and has a melting point of 158 °C and a tensile strength of 52 MPa. *Elvamide*® 8066 also from *DuPont*TM is another copolymer of PA6/66/610 and has a melting point of 115 °C and a tensile strength of 39 MPa. Notice however that the chemical structure of polyamides makes them difficult to be phase-separated with epoxy and their relatively high viscosity in the melt state makes them inappropriate for healing purposes.
- ABS, PEGMA and many other amorphous thermoplastics could be thought for the present purpose, but were directly discarded, as their intrinsic viscosity is too high to allow future processing of the blends inside FRPs.
- Thermoplastic elastomers could also be of interest regarding their thermal properties and tensile strength. However, due to their low modulus, these materials were directly discarded for the present work.

Many thermoplastics can be highlighted to provide higher mechanical performances as compared to the PCL of Luo *et al.* [7]. However, a compromise has to be made between the increase in strength and the variation in other properties of interest (viscosity, modulus, etc...). Considering the above-mentioned parameters, four thermoplastics have been earmarked as potential candidates to compare with the PCL used by Luo *et al.* [7]:

- (i) Low molecular weight PCL ($M_n \approx 10,000$ g/mol);
- (ii) High molecular weight PCL ($M_n \approx 80,000$ g/mol);
- (iii) PLA;
- (iv) PMMA.

Notice finally that thermal expansion coefficients for these four materials in the liquid state are of around 16-17, 8.5 and 7·10⁻⁵/°C for respectively PCL, PLA and PMMA [291]. Their volume expansion is therefore acceptable considering the requirements in Table 4.1.

The assessment of these thermoplastics to be blended with epoxy for thermal mending applications is based on different experimental techniques (detailed in Chapter 3): microscopy, DSC, DMA, Tensile and TDCB testing. However, composition of the blends must be first defined. From *Flory Huggins Theory* (see section 2.4.3.1) and studies of Chen and Chang [135], [136], phase diagrams of the epoxy-thermoplastic blends can be drawn (more details about the phase diagrams modelling are given in section 4.2.1.2). These phase diagrams (Figure 4.2) allow designing the different epoxy-thermoplastic blend compositions that are seen through sections 4.1.1 to 4.1.4. Indeed, compositions

must be varied as the phase diagram critical point changes with the type of thermoplastic and thus the composition to obtain the phase separation targeted for healing will vary. In particular, four compositions are targeted for each epoxy-thermoplastic system in order to reach (i) one time the morphology consisting of an epoxy matrix with thermoplastic inclusions, (ii) one time the complex morphology and (iii) two times the inverse phase-separated morphology consisting of epoxy particles with a surrounding thermoplastic matrix (this last morphology being targeted for thermal mending). In addition, properties of pure epoxy and pure thermoplastic are studied.

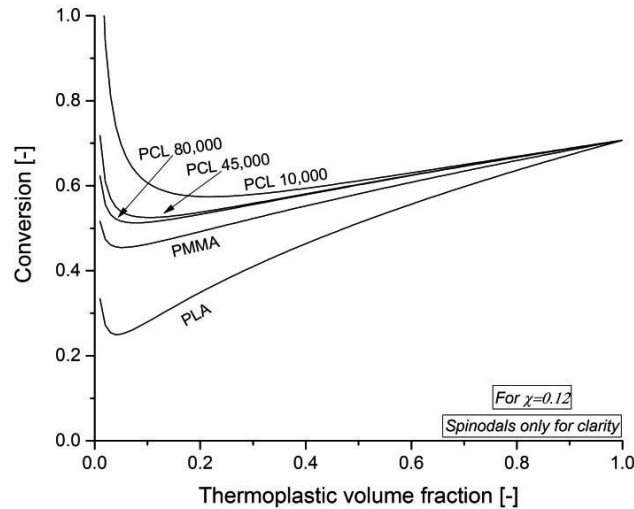


Figure 4.2: Estimate of conversions corresponding to spinodal curves for five thermoplastics: (i) PCL similar to Luo *et al.* [7] ($M_n \approx 45,000$ g/mol); (ii) PCL low molecular weight ($M_n \approx 10,000$ g/mol); (iii) PCL high molecular weight ($M_n \approx 80,000$ g/mol); (iv) PMMA and (v) PLA; as a function of the thermoplastic volume fraction for $\chi=0.12$ according to the Flory-Huggins equation.

4.1.1 Low molecular weight PCL

PCL with a low molecular weight ($M_n \approx 10,000$ g/mol) is first investigated. From the study of Siddhamalli [144], lowering the PCL molecular weight (4,000 g/mol in [144]) should not result in a decrease in tensile strength for the epoxy particulate morphology. Procedures to process and test the specimens are the same as detailed in Chapter 3, unless otherwise mentioned. Six different specimen compositions were produced including pure epoxy, pure PCL and varying the PCL content (Table 4.2). Similar types of morphologies as Luo *et al.* [7] were obtained and observed by optical microscopy and scanning electron microscopy (Figure 4.3): (i) at concentrations above 30.6 vol% PCL, the morphology consisted of a particulate epoxy phase and a co-continuous PCL phase, the epoxy particles decreased in diameter as the PCL concentration increased; (ii) at concentrations up to 17.7 vol% PCL, the morphology consisted of a continuous epoxy phase with PCL inclusions; (iii) at concentrations between 17.7 and 30.6 vol% PCL, a complex morphology was observed with relatively large co-continuous PCL and/or epoxy domains containing much smaller epoxy and PCL inclusions respectively. Notice that SEM pictures shown are the fracture surfaces obtained after tensile tests. Overall, the obtained morphologies were similar to Luo *et al.* [7]; however the compositions were tuned as from Figure 4.2, it is known that the critical point, which determines the different morphologies, appears at much higher PCL concentrations.

Epoxy-thermoplastic blends

Table 4.2: Specimen designations and the corresponding mass ratios of epoxy resin to PCL ($M_n \approx 10,000$ g/mol), and the overall PCL weight and volume fractions after addition of the DDS.

Specimen	epoxy to PCL	PCL weight fraction [%]	PCL volume fraction [%]
	$m_{\text{epoxy}}:m_{\text{PCL}}$	m_{PCL}	ϕ_{PCL}
Epoxy-PCL(0)	100:0	0	0
Epoxy-PCL(17.7)	80:20	15.5	17.7
Epoxy-PCL(26.9)	70:30	23.9	26.9
Epoxy-PCL(30.6)	66:34	27.4	30.6
Epoxy-PCL(34.5)	62:38	31.0	34.5
Epoxy-PCL(100)	0:100	100	100

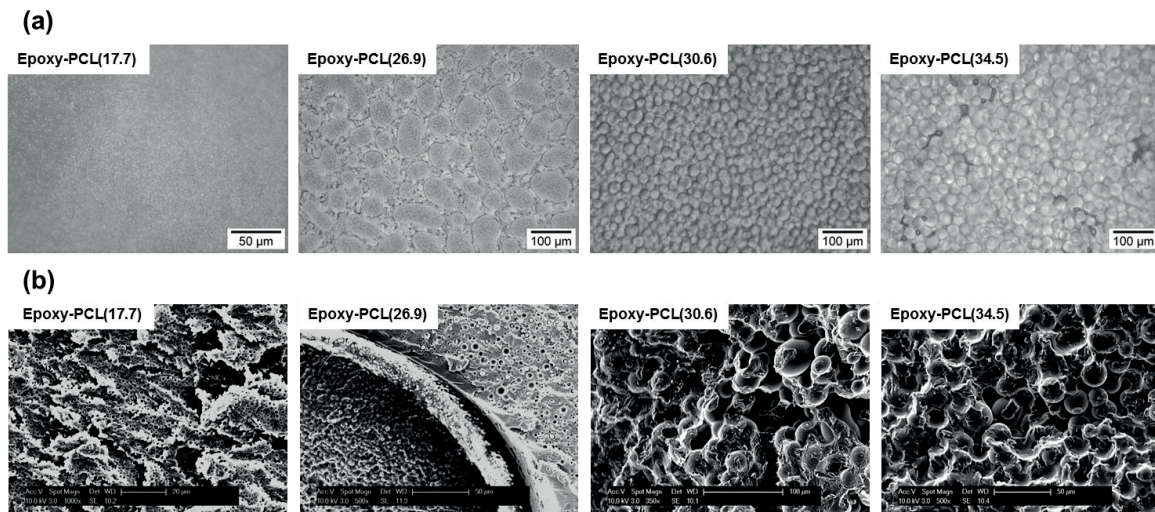


Figure 4.3: Blend morphology as a function of PCL ($M_n \approx 10,000$ g/mol) volume fraction (*Epoxy-PCL(various vol%)*). (a) Optical microscopy images; (b) Scanning electron microscopy images (fracture surfaces from tensile tests).

Figure 4.4 shows DSC heating scans for the different epoxy-PCL ($M_n \approx 10,000$ g/mol) blends after cure. Two characteristic transitions were observed for all the compositions. The endothermic peak at about 54 °C corresponded to melting of the PCL, whereas the small enthalpic peak and step-like increase in heat capacity at about 197 °C were associated with the glass transition of the epoxy. These transition temperatures were generally similar to those of the pure PCL and pure epoxy, indicating a high degree of phase purity and immiscibility between the two components. Notice that above a PCL concentration of 30% the epoxy glass transition is less well pronounced and appears slightly lowered, which was explained by the high PCL concentration that may have prevented full phase separation.

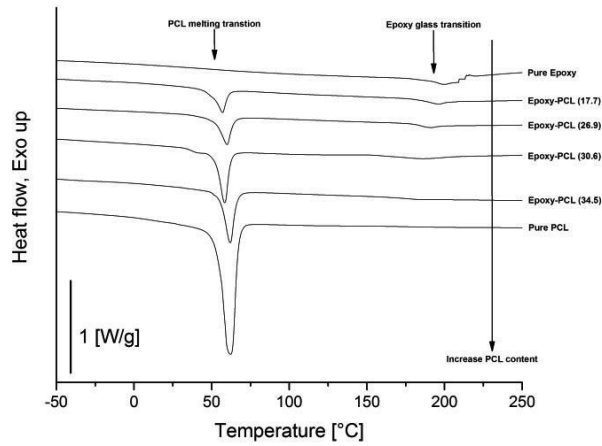


Figure 4.4: DSC heating scans for the different epoxy-PCL ($M_n \approx 10,000$ g/mol) blends after cure.

The storage modulus, E' , is shown as a function of the PCL ($M_n \approx 10,000$ g/mol) content in Figure 4.5 for two different temperatures: 25 °C (room temperature) and 150 °C (the targeted healing temperature). At room temperature, a decrease in E' from 2.5 to close to 1.3 GPa was observed as the PCL content increased from 0 to 30.6 vol%, corresponding to the establishment of the co-continuous morphology visible in Figure 4.3. At 150 °C, E' decreased from about 1.7 to about 0.003 GPa in the same composition range, reflecting the molten state of the PCL. At 150 °C, the blend therefore lost its dimensional stabilities, indicating poor contacts between the epoxy particles (Figure 4.3 (b)). This behaviour, as opposed to the blends of Luo *et al.* [7] where structural integrity was kept during the mending cycle, was explained by incomplete phase separation and thus some miscibility between the components as observed through DSC scans (Figure 4.4).

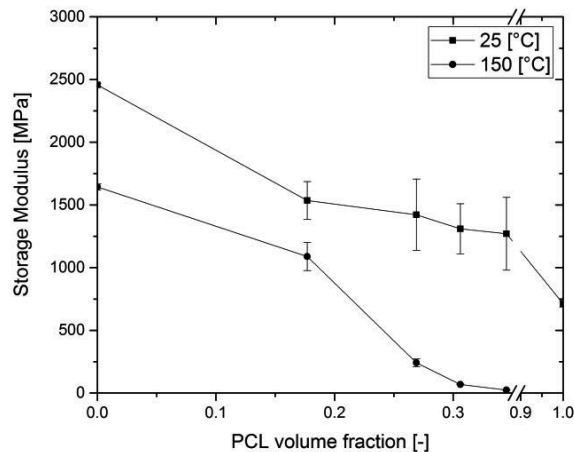


Figure 4.5: E' determined by DMA as a function of the PCL ($M_n \approx 10,000$ g/mol) volume fraction at room temperature and the healing temperature (150 °C).

The maximum stress observed during the tensile tests decreased approximately eleven fold when the PCL ($M_n \approx 10,000$ g/mol) content was 30.6% (Figure 4.6 (a)), almost reaching the yield stress, σ_y , of pure PCL. This low PCL yield stress as compared to the PCL studied by Siddhamalli [144] was explained by the curing cycle at 180 °C for 3h which

most probably ruptured polymer chains. Notice also that *Epoxy-PCL(34.5)* could not be tested as the specimens ruptured during demoulding reflecting an extremely low tensile strength. The corresponding Young's moduli, E (Figure 4.6 (b)), were consistent with the values of E' obtained by DMA (Figure 4.5). These mechanical property behaviours can also be explained from observation of the fracture surfaces (see Figure 4.3 (b)): at high PCL contents (*Epoxy-PCL(26.9)* and *Epoxy-PCL(30.6)*) cohesive failure of the PCL dominates due to its extremely low strength; in the limit of low PCL contents (*Epoxy-PCL(17.7)*), brittle failure of the epoxy dominated, implying the PCL particles not to promote matrix ductility; and at intermediate PCL contents (*Epoxy-PCL(26.9)*), failure of PCL interfaces again dominated due to its low intrinsic strength. More details on the different failure types are given in section 4.1.2 through Figure 4.13. The decrease in strain-to-failure (Figure 4.6 (c)) from about 4.5%, where the epoxy was the continuous phase, to only about 0.5% for *Epoxy-PCL(30.6)*, where the continuous phase was essentially PCL, was attributed to the low strain of the monolithic PCL explained again by the curing conditions.

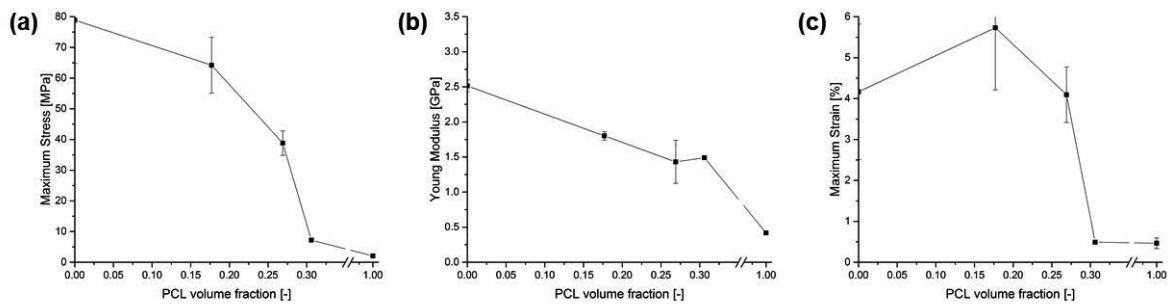


Figure 4.6: (a) Maximum stress, (b) Young's Modulus and (c) strain to failure as a function of the PCL ($M_n \approx 10,000$ g/mol) volume fraction.

Figure 4.7 shows fracture toughness, K_{IC} , from the TDCB tests as a function of the PCL ($M_n \approx 10,000$ g/mol) content. Consistent with the trends in the maximum stress and the strain-to-failure in the tensile tests, K_{IC} was generally observed to decrease on addition of PCL to the epoxy. Although addition of ductile thermoplastics, including PCL, to an epoxy matrix has frequently been reported to result in improved fracture resistance, in the present case, K_{IC} for the unmodified epoxy was already comparable with values obtained in many optimised rubber-modified systems, accounting for the apparent absence of any toughening effect on PCL addition [144], [243]. As with the strain-to-failure in the tensile tests, the extremely low K_{IC} at high PCL contents was attributed to cure conditions, which might have degraded the PCL. The relatively large scatter in K_{IC} among the individual specimens, as reflected by the error bars in Figure 4.7 was attributed to variations in the geometry of the specimen side-grooves [292], and is commonly reported for TDCB tests, as for example in [206], [293]. The use of an insert in combination with the TDCB geometry to measure the fracture properties of the blends (section 3.3.5) is also expected to lead to systematic errors in K_{IC} of up to 20% at high PCL contents owing to the reduced compliance of regions remote from the crack tip.

Even though low fracture toughness values were observed, healing (after a thermal cycle of 150 °C for 30 minutes) up to 86% and 67% for respectively *Epoxy-PCL(30.6)* and *Epoxy-PCL(34.5)* could be reached, which proved again the ability of PCL to wet and heal the crack faces. *Epoxy-PCL(30.6)* was highlighted as the best candidate for thermal mending applications with these blends.

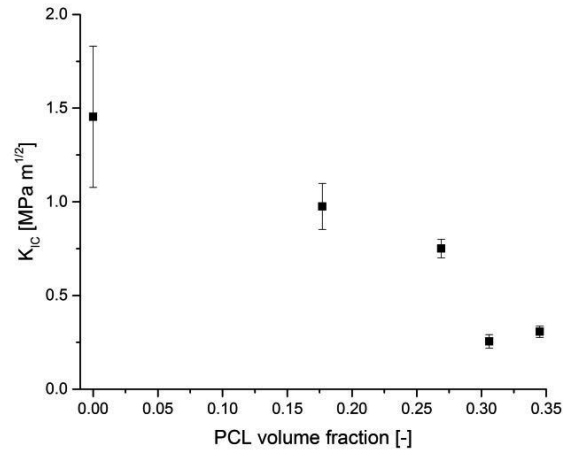


Figure 4.7: K_{IC} as a function of the PCL ($M_n \approx 10,000$ g/mol) volume fraction.

4.1.2 High molecular weight PCL

PCL with a high molecular weight ($M_n \approx 80,000$ g/mol) is believed to provide higher overall strength and it is also known for its phase separation capability with epoxy [135], [136]. Procedures to process and test the specimens are the same as detailed in Chapter 3, unless otherwise mentioned. Six different specimen compositions were produced including pure epoxy, pure PCL and varying the PCL content (Table 4.3). Similar types of morphologies as observed with previous blends were obtained and observed by optical microscopy and scanning electron microscopy (Figure 4.8): (i) at concentrations above 21.3 vol% PCL, the morphology consisted of a particulate epoxy phase and a co-continuous PCL phase, the epoxy particles decreased in diameter as the PCL concentration increased; (ii) at concentrations up to 8.7 vol% PCL, the morphology consisted of a continuous epoxy phase with PCL inclusions; (iii) at concentrations between 8.7 and 21.3 vol% PCL, a complex morphology was observed with relatively large co-continuous PCL and/or epoxy domains containing much smaller epoxy and PCL inclusions respectively. Notice that SEM pictures shown are the fracture surfaces obtained after tensile tests. Overall, the obtained morphologies were similar to the epoxy-PCL blends studied previously (see Luo *et al.* [7] study and section 4.1.1); however the compositions were tuned as from Figure 4.2 it is known that the critical point which determines the different morphologies appears at lower PCL concentrations as compared to lower molecular weight PCL.

Table 4.3: Specimen designations and the corresponding mass ratios of epoxy resin to PCL ($M_n \approx 80,000$ g/mol), and the overall PCL weight and volume fractions after addition of the DDS.

Specimen	epoxy to PCL	PCL weight fraction [%]	PCL volume fraction [%]
	$m_{\text{epoxy}}:m_{\text{PCL}}$	m_{PCL}	ϕ_{PCL}
Epoxy-PCL(0)	100:0	0	0
Epoxy- PCL(8.7)	90:10	7.5	8.7
Epoxy- PCL(17.7)	80:20	15.5	17.7
Epoxy- PCL(21.3)	76:24	18.8	21.3
Epoxy- PCL(23.2)	74:26	20.5	23.2
Epoxy- PCL(100)	0:100	100	100

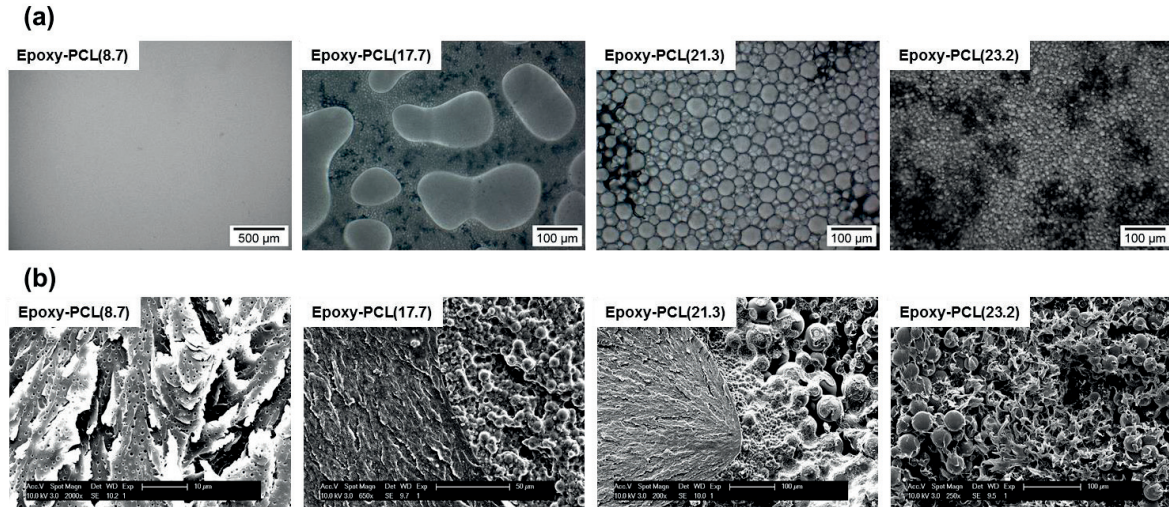


Figure 4.8: Blend morphology as a function of PCL ($M_n \approx 80,000$ g/mol) volume fraction (*Epoxy-PCL(various vol%)*). (a) Optical microscopy images; (b) Scanning electron microscopy images (fracture surfaces from tensile tests).

Figure 4.9 shows DSC heating scans for the different epoxy-PCL ($M_n \approx 80,000$ g/mol) blends after cure. Two characteristic transitions were observed for all the compositions. The endothermic peak at about 54 °C corresponded to melting of the PCL, whereas the small enthalpic peak and step-like increase in heat capacity at about 197 °C were associated with the glass transition of the epoxy. These transition temperatures were generally similar to those of the pure PCL and pure epoxy, indicating a high degree of phase purity and immiscibility between the two components.

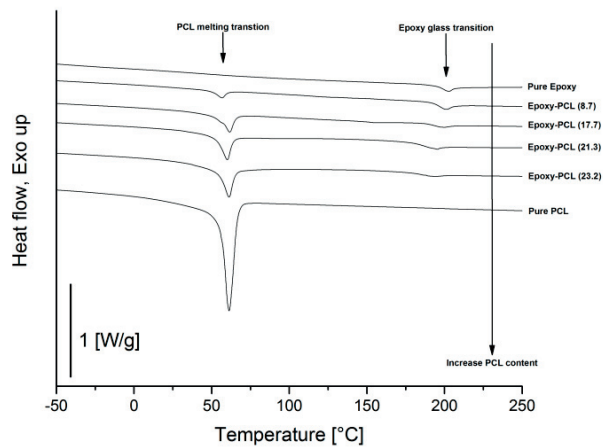


Figure 4.9: DSC heating scans for the different epoxy-PCL ($M_n \approx 80,000$ g/mol) blends after cure.

The storage modulus, E' , is shown as a function of the PCL ($M_n \approx 80,000$ g/mol) content in Figure 4.10 for two different temperatures: 25 °C (room temperature) and 150 °C (the targeted healing temperature). At room temperature, a decrease in E' from 2.6 to close to 1.6 GPa was observed as the PCL content increased from 0 to 21.3 vol%, corresponding to the establishment of the co-continuous morphology visible in Figure 4.8. At 150 °C, E' decreased from about 1.8 to about 0.003 GPa in the same composition range, reflecting the molten state of PCL. At 150 °C, the blend therefore lost its dimensional stabilities, indicating poor contacts between the epoxy particles (Figure 4.8 (b)).

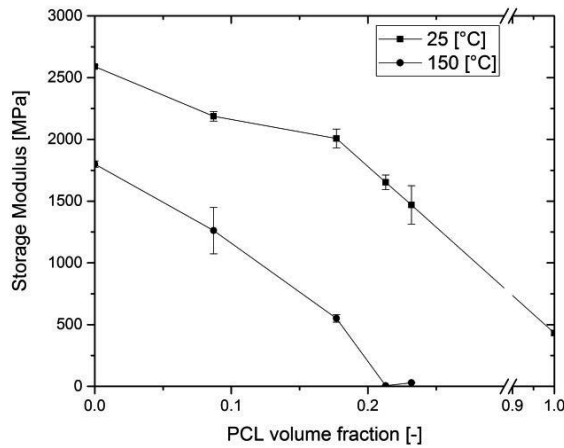


Figure 4.10: E' determined by DMA as a function of the PCL ($M_n \approx 80,000$ g/mol) volume fraction at room temperature and the healing temperature (150 °C).

The maximum stress observed during the tensile tests decreased approximately eightfold as the PCL ($M_n \approx 80,000$ g/mol) content was increased from 0 to 17.2 vol% (Figure 4.11 (a)), flattening off at about 15 MPa, which was close to the yield stress, σ_y , of pure PCL. The corresponding Young's moduli, E (Figure 4.11 (b)), were consistent with the values of E' obtained by DMA (Figure 4.10) except for the pure PCL which did not follow the same heat treatment due to its high viscosity and processing through injection moulding. As in section 4.1.1, this behaviour can be explained from observation of the fracture surfaces (observed by SEM in Figure 4.8 (b)). In particular, at high PCL contents (*Epoxy-PCL(21.3)* and *Epoxy-PCL(23.2)*), three modes of fracture co-existed (see Figure 4.13 for a schematic view): (i) failure of the epoxy-PCL interface, (ii) cohesive failure of the PCL and (iii) brittle failure of the interface between the interconnected epoxy particles. In the limit of low PCL contents (*Epoxy-PCL(8.7)*), brittle failure of the epoxy dominated, implying that the PCL particles do not promote matrix ductility, while at intermediate PCL contents (*Epoxy-PCL(17.7)*), all the fracture modes were present. At high PCL content (*Epoxy-PCL(23.2)*), cohesive failure of the PCL was mostly present. The decrease in strain-to-failure from about 4%, where the epoxy was the continuous phase, to only about 1.5% for *Epoxy-PCL(21.3)* and *Epoxy-PCL(23.2)*, where the continuous phase was essentially PCL, was attributed to severe confinement of the relatively ductile PCL by the relatively stiff, high yield-strength epoxy particles (σ_y at least 8 times that of the PCL) and brittle behaviour of the interfaces between the epoxy particles (which explains cohesive failure of the PCL on the fracture plane), rather than premature failure at the PCL-epoxy interface. Indeed, the strain-to-failure has been reported to increase with PCL content in similar systems, albeit for different cure conditions and stoichiometry, suggesting strong interfacial adhesion [144].

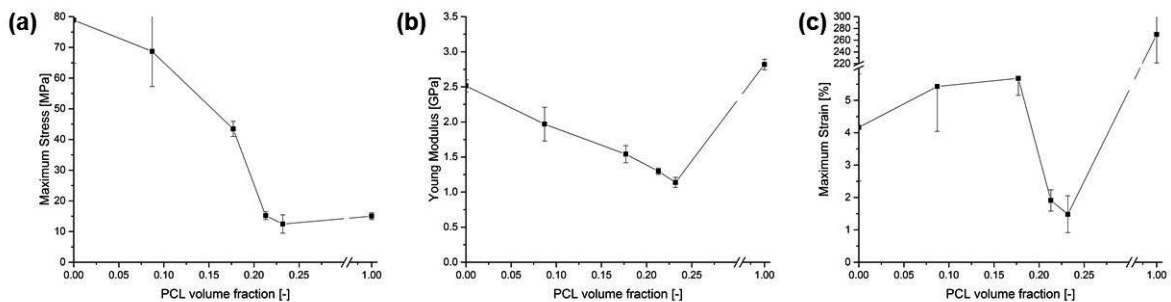


Figure 4.11: (a) Maximum stress, (b) Young's Modulus and (c) strain to failure as a function of the PCL ($M_n \approx 80,000$ g/mol) volume fraction.

Figure 4.12 shows fracture toughness, K_{IC} , from the TDCB tests as a function of the PCL ($M_n \approx 80,000$ g/mol) content. The relatively large scatter in K_{IC} was again attributed to the specimen side-grooves [292]. Consistent with the trends in the maximum stress and the strain-to-failure in the tensile tests, K_{IC} was generally observed to decrease on addition of PCL to the epoxy, although addition of ductile thermoplastics, including PCL, to an epoxy matrix has frequently been reported to result in improved fracture resistance. In the present case, K_{IC} for the unmodified epoxy was already comparable with values obtained in many optimised rubber-modified systems, accounting for the apparent absence of any toughening effect on PCL addition [144], [243]. As with the strain-to-failure in the tensile tests, the reduced K_{IC} at high PCL contents was interpreted as a confinement effect. If the epoxy particles are considered not to yield, and assuming that brittle fracture of the contacts between the epoxy particles contributes little to energy dissipation, the continuous PCL phase may be modelled as a layer of mean initial thickness d_0 , assumed to be of the order of $10 \mu\text{m}$ based on the observed morphology (epoxy particle diameters of about $20 \mu\text{m}$), confined between parallel rigid plates whose plane is perpendicular to tensile axis. Given that d_0 is very much less than the expected plastic zone size for unmodified PCL (literature values for the essential work of fracture of PCL (64 kJ/m^2) imply plastic zone sizes that would exceed the specimen dimensions in the present case [294]), it may be assumed that cracks propagating through the confined PCL layer are associated with yielding through the whole layer thickness, followed by either cohesive failure of the PCL or failure of the epoxy-PCL interface. The crack opening displacement, δ , and hence K_{IC} , may then be determined from

$$\delta = (\lambda - 1)d_0 \quad \text{and} \quad K_{IC} = \sqrt{\frac{E\sigma_y(\lambda - 1)d_0}{1 - \nu^2}} \quad (4.3)$$

where ν is the Poisson's ratio and λ is the characteristic deformation ratio of PCL, estimated to be 4 from the strain-to-failure for pure PCL in Figure 4.11 (c). Taking $\sigma_y = 20 \text{ MPa}$ for pure PCL, $\nu = 0.4$ and $E = 1.5 \text{ GPa}$ for the blends with the particulate epoxy morphology, K_{IC} is estimated to be around $1 \text{ MPa m}^{1/2}$, suggesting that this scenario may account for the results in Figure 4.12. A schematic of this PCL confinement within the phase-separated structure is shown in Figure 4.13 along with the different failure mechanisms highlighted through the fracture surfaces of Figure 4.8. The PCL plastic zone size to illustrate its premature rupture is also shown and can be related to the study of Smith *et al.* [245] (see Figure 2.39) where similar detrimental effects to the fracture toughness were observed for large thermoplastic process zones. From Figure 4.13, it is clear that not all the fracture mechanisms can be healed by the flow of PCL during the thermal treatment. While failure at the interface between epoxy particles and PCL as well as PCL cohesive failure can be healed, the interconnection between the epoxy particles cannot be reformed by the healing treatment, thus reducing potentially the load bearing capacity of the system after healing.

Even though low fracture toughness values were observed, healing (after thermal mending at $150 \text{ }^\circ\text{C}$ for 30 minutes) up to 100% and 170% for respectively *Epoxy-PCL(21.3)* and *Epoxy-PCL(23.2)* could be reached, which proved again the ability of PCL to wet and heal the crack faces. Also, the non-recovery of particle interconnections was not seen as detrimental and explained by the crack opening dependence on the PCL plastic zone size. Healing efficiency exceeding 100% was found due to the test conditions where two faces were brought back into contact during healing; due to the low modulus at the healing temperature (see DMA results, Figure 4.10), the crack surfaces were flattened, thus increasing the contact area and the energy required to propagate the crack. For this reason, *Epoxy-PCL(21.3)* was highlighted as the best candidate for thermal mending applications in these blends type.

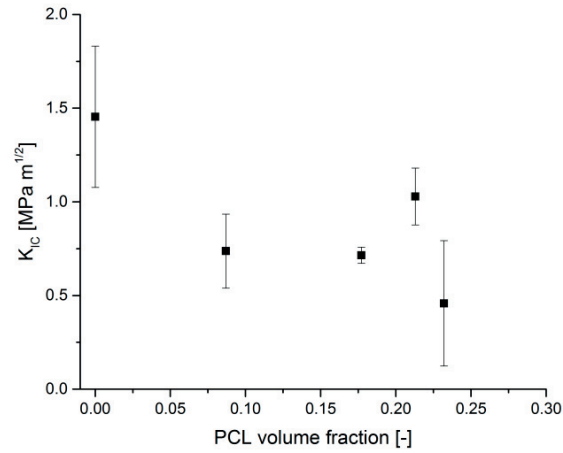


Figure 4.12: K_{IC} as a function of the PCL ($M_n \approx 80,000$ g/mol) volume fraction.

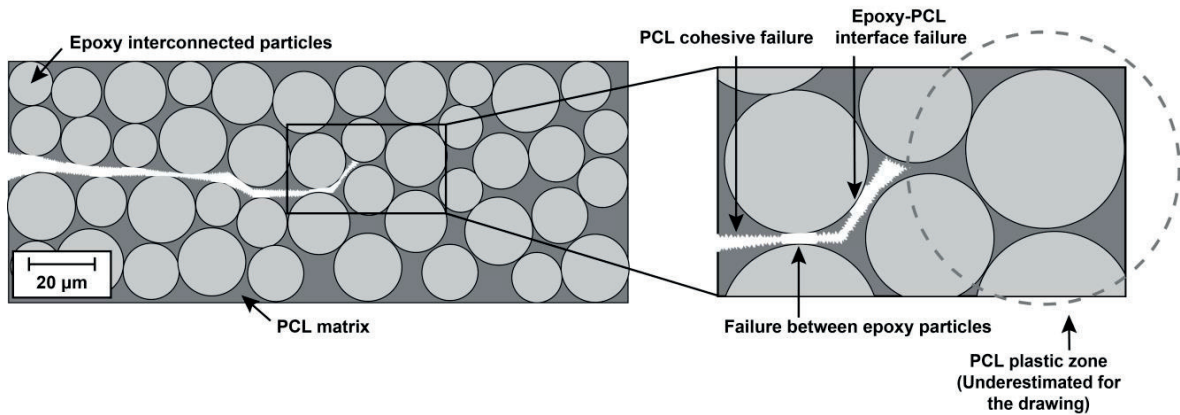


Figure 4.13: Schematic of the phase-separated structure containing epoxy-interconnected particles with a surrounding PCL matrix. When a crack propagates through the structure, different modes of failure arise and are detailed in the right close up look. The PCL plastic zone size to illustrate its premature rupture is also shown, but underestimated for the sake of the drawing.

4.1.3 PLA

PLA is a biodegradable semicrystalline thermoplastic with a T_g of around 60 °C and a T_m of around 150 °C. Its tensile strength reaches for many grades 50 MPa. It has never been used for phase separation in epoxy, but its free hydroxyl groups can allow this process. Even though the high melting temperature is critical in terms of processing, this polymer has all other required properties of Table 4.1. Procedures to process and test the specimens are the same as detailed in Chapter 3, unless otherwise mentioned. In particular, it was more difficult to dissolve PLA into epoxy as compared to PCL, therefore dissolution was performed at 170 °C for 2 hours, before decreasing the temperature to 140 °C in order to add the curing agent. Six different specimen compositions were produced including pure epoxy, pure PLA and varying the PLA content (Table 4.4). Similar types of morphologies as observed with previous blends were obtained and observed by optical microscopy and scanning electron microscopy (Figure 4.14): (i) at concentrations above 21.8 vol% PLA, the morphology consisted of a particulate epoxy phase and a co-continuous PLA phase; (ii) at concentrations up to 4 vol% PLA, the morphology consisted of a continuous epoxy phase with PLA inclusions; (iii) at concentrations between 4 and 21.8 vol% PLA, a complex morphology was observed with relatively

large co-continuous PLA and/or epoxy domains containing much smaller epoxy and PLA inclusions respectively. Notice that SEM pictures shown are the fracture surfaces obtained after tensile tests. Overall, the obtained morphologies were similar to the epoxy-PCL blends studied previously (see Luo *et al.* [7] study, section 4.1.1 and 4.1.2); however the compositions were tuned as from Figure 4.2 it is known that the critical point which determines the different morphologies appears at lower PLA concentrations as compared to PCL. Notice also that two blends including the complex morphology are presented here instead of two blends with the epoxy particulate morphology because at concentrations higher than 21.8 vol% PLA in the blends, the viscosity was too high to process the specimens.

Table 4.4: Specimen designations and the corresponding mass ratios of epoxy resin to PLA, and the overall PLA weight and volume fractions after addition of the DDS.

Specimen	epoxy to PLA	PLA weight fraction [%]	PLA volume fraction [%]
	$m_{\text{epoxy}}:m_{\text{PLA}}$	m_{PLA}	ϕ_{PLA}
Epoxy-PLA(0)	100:0	0	0
Epoxy-PLA(4.0)	95:5	3.7	4.0
Epoxy-PLA(12.3)	85:15	11.5	12.3
Epoxy-PLA(16.5)	80:20	15.5	16.5
Epoxy-PLA(21.8)	74:26	20.5	21.8
Epoxy-PLA(100)	0:100	100	100

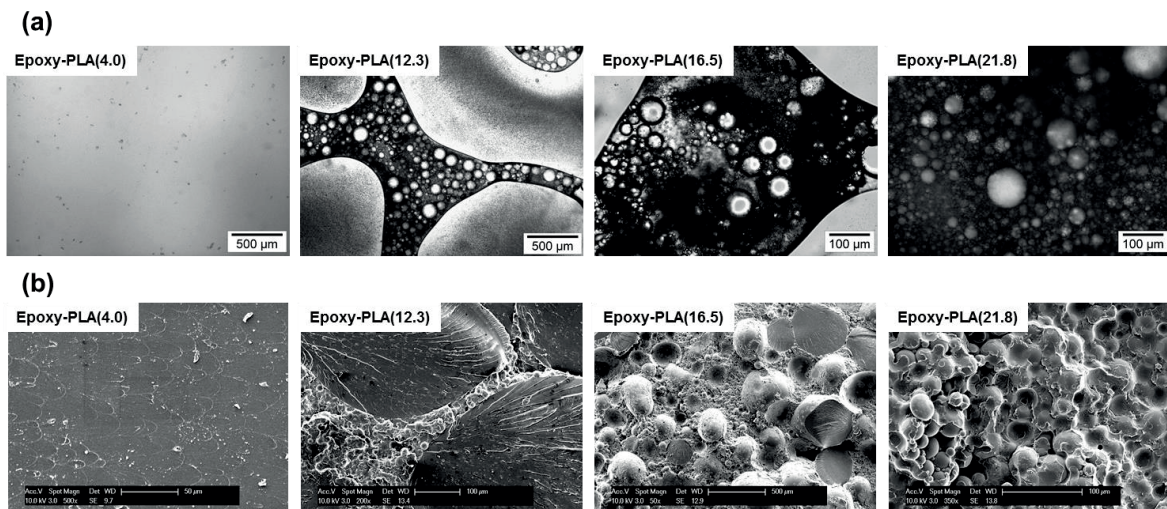


Figure 4.14: Blend morphology as a function of PLA volume fraction (*Epoxy-PLA(Various vol%)*). (a) Optical microscopy images; (b) Scanning electron microscopy images (fracture surfaces from tensile tests).

Figure 4.15 shows DSC heating scans for the different epoxy-PLA blends after cure. Three characteristic transitions were observed for all the compositions. The small enthalpic peak and step-like increase in heat capacity at about 59 °C were associated with the glass transition of the PLA, the endothermic peak at about 152 °C corresponded to melting of the PLA, whereas the small enthalpic peak and step-like increase in heat capacity at about 197 °C were associated with the glass transition of the epoxy. These transition temperatures were generally similar to those of the pure PLA and pure epoxy, indicating a high degree of phase purity and immiscibility between the two components. Notice that below a PLA concentration of 4%, only the epoxy glass transition is observed and appears slightly lowered which in this case demonstrates that phase separation was not complete and did not provide immiscible blends in the cured state.

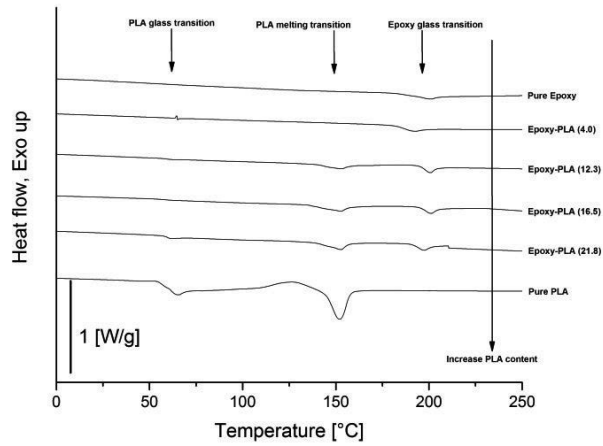


Figure 4.15: DSC heating scans for the different epoxy-PLA blends after cure.

The storage modulus, E' , is shown as a function of the PLA content in Figure 4.16 for two different temperatures: 25 °C (room temperature) and 160 °C (the targeted healing temperature, which is 10 °C higher than for epoxy-PCL blends in order to reach the thermoplastic molten state). At room temperature, an increase in E' from 2.6 to close to 2.8 GPa was observed as the PLA content increased from 0 to 12.3 vol%, which was an almost linear increase between both values of pure epoxy and PLA components, indicating no influence of phase separation in those blends. However, when reaching the establishment of the co-continuous morphology visible in Figure 4.14 (at 16.5 vol% PLA), the modulus started to decrease and reached a similar value to pure epoxy for the highest PLA concentration in the blend. At the healing temperature, E' decreased from about 1.7 to about 0.008 GPa in the same composition range, reflecting the molten state of PLA. At 160 °C, the blend therefore lost its dimensional stabilities, which was explained by the lack of contact between the epoxy particles observed in Figure 4.14 (b).

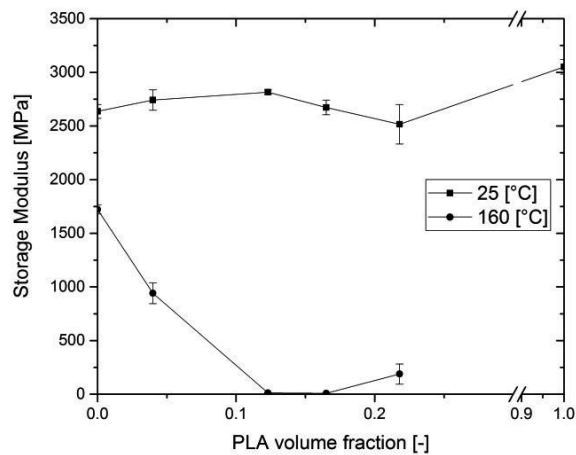


Figure 4.16: E' determined by DMA as a function of the PLA volume fraction at room temperature and the healing temperature (160 °C).

The maximum stress observed during tensile tests decreased approximately twofold as the PLA content was increased from 0 to 12.3 vol% before increasing again in the direction of pure PLA strength (Figure 4.17 (a)). The corresponding

Young's moduli, E (Figure 4.17 (b)), were consistent with the values of E' obtained by DMA (Figure 4.16). As with epoxy-PCL blends, this behaviour can be explained from observation of the fracture surfaces (observed by SEM in Figure 4.14 (b)). In particular, at high PLA contents, the lower interconnections between epoxy particles as well as the weak bonding between epoxy particles and the surrounding PLA matrix were highlighted in addition to the confined layer theory seen with epoxy-PCL blends (see section 4.1.2). The decrease in strain-to-failure (Figure 4.17 (b)) from about 4%, where the epoxy was the continuous phase, to only about 2% for high PLA contents, where the continuous phase was essentially PLA, was again attributed to the PLA confinement in between epoxy particles as strain-to-failure of pure PLA was higher than the produced blends.

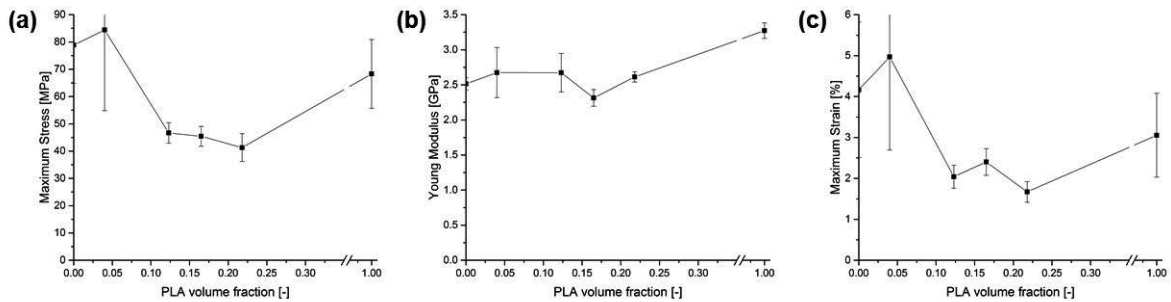
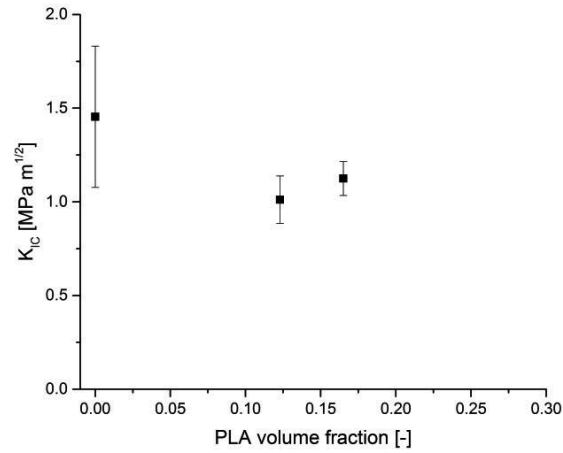


Figure 4.17: (a) Maximum stress, (b) Young's Modulus and (c) strain to failure as a function of the PLA volume fraction.

Finally, fracture toughness, K_{IC} , of these blends was assessed through TDCB tests and is depicted for each blend in Figure 4.18. Specimens containing 4 and 21.3 vol% PLA could not be tested due respectively to their high toughness, making the interface around the blend of this geometry to rupture first, and to the impossibility to process the specimens because of the high blend viscosity. At intermediate PLA content, fracture toughness however decreased, which could be related to the low strength values observed for those compositions and the weak bonding between PLA and epoxy in the cured state. This weak bonding could be supported by the observation of the fracture surfaces for those specimens (Figure 4.14 (b)), where epoxy particles were bare of PLA matrix within the complex morphology. The relatively large scatter in K_{IC} was again attributed to the specimen side-grooves [292].

Even though low fracture toughness values were observed, healing (after a thermal cycle of 160 °C for 30 minutes) reaching 137% was demonstrated for *Epoxy-PLA(11.5)*, which proved the ability of PLA to wet and heal the crack faces. Healing efficiency exceeding 100% was found due to the test conditions where two faces were brought back into contact during the healing cycle; due to the low modulus at the healing temperature (see DMA results, Figure 4.16), the crack surface was flatten, thus increasing the contact area and the energy required to propagate the crack. Notice that healing for the higher PLA concentration could not be tested as the healing cycle ruptured the specimen due to its incapacity to keep structural integrity at high temperature. Therefore, blends containing 11.5% were defined as best for thermal mending.

Figure 4.18: K_{IC} as a function of the PLA volume fraction.

4.1.4 PMMA

PMMA is a widely known thermoplastic with relatively elevated modulus and strength. Even though it is amorphous, its T_g of around 100 °C was believed to provide healing at 150 °C. Also, it is known for its ability to phase separate and create the co-continuous morphology [163]–[168], as obtained with PCL. Procedures to process and test the specimens are the same as detailed in Chapter 3, unless otherwise mentioned. In particular, it was more difficult to dissolve PMMA into epoxy as compared to PCL, therefore dissolution was performed at 170 °C for 2 hours, before decreasing the temperature to 140 °C in order to add the curing agent. Six different specimen compositions were produced including pure epoxy and pure PMMA and varying the PMMA content (Table 4.5). Similar types of morphologies as for epoxy-PCL and epoxy-PLA blends were obtained and observed by optical microscopy and scanning electron microscopy (Figure 4.19): (i) at concentrations above 17.2 vol% PMMA, the morphology consisted of a particulate epoxy phase and a co-continuous PMMA phase, the epoxy particles decreased in diameter as the PMMA concentration increased; (ii) at concentrations up to 6.7 vol% PMMA, the morphology consisted of a continuous epoxy phase with PCL inclusions; (iii) at concentrations between 6.7 and 17.2 vol% PMMA, a complex morphology was observed with relatively large co-continuous PMMA and/or epoxy domains containing much smaller epoxy and PMMA inclusions respectively. Notice that SEM pictures shown are the fracture surfaces obtained after tensile tests. Overall, the obtained morphologies were similar to the previously studied phase-separated blends (see Luo *et al.* [7] study, section 4.1.1 to 4.1.3); however the compositions were tuned as from Figure 4.2 it is known that the critical point which determines the different morphologies appears at lower PMMA concentrations as compared to PCL.

Table 4.5: Specimen designations and the corresponding mass ratios of epoxy resin to PMMA, and the overall PMMA weight and volume fractions after addition of the DDS.

Specimen	epoxy to PMMA	PMMA weight fraction [%]	PMMA volume fraction [%]
	$m_{\text{epoxy}}:m_{\text{PMMA}}$	m_{PMMA}	ϕ_{PMMA}
Epoxy-PMMA(0)	100:0	0	0
Epoxy-PMMA(6.7)	92:8	6.0	6.7
Epoxy-PMMA(12.8)	85:15	11.5	12.8
Epoxy-PMMA(17.2)	80:20	15.5	17.2
Epoxy-PMMA(20.8)	76:24	18.8	20.8
Epoxy-PMMA(100)	0:100	100	100

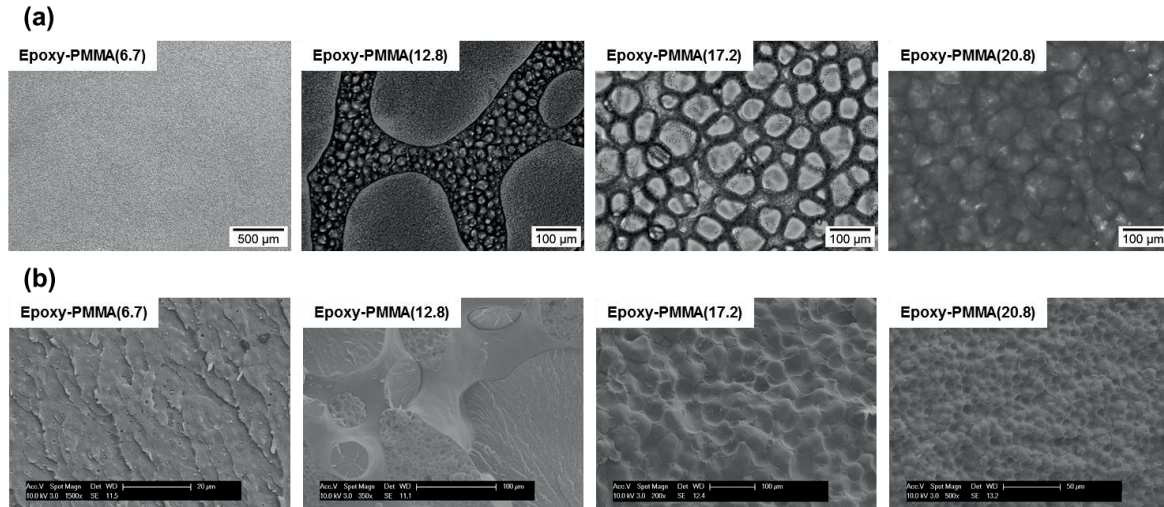


Figure 4.19: Blend morphology as a function of PMMA volume fraction (*Epoxy-PMMA(Various vol%)*). (a) Optical microscopy images; (b) Scanning electron microscopy images (fracture surfaces from tensile tests).

Figure 4.20 shows DSC heating scans for the different epoxy-PMMA blends after cure. Two characteristic transitions were observed for all the compositions. The two small enthalpy peaks at about 105 and 197 °C were associated to the glass transition temperatures of respectively PMMA and epoxy. These transition temperatures were generally similar to those of the pure PMMA and pure epoxy, indicating a high degree of phase purity and immiscibility between the two components, as for previous epoxy-thermoplastic blends.

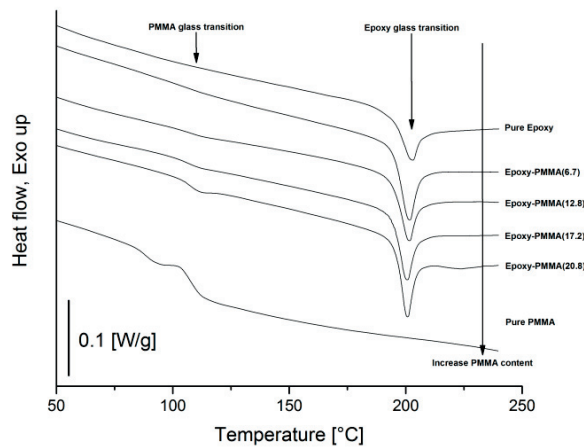


Figure 4.20: DSC heating scans for the different epoxy-PMMA blends after cure.

The storage modulus, E' , is shown as a function of the PMMA content in Figure 4.21 for two different temperatures: 25 °C (room temperature) and 150 °C (the targeted healing temperature). At room temperature, an increase in E' from 2.6 to close to 3 GPa was observed as the PMMA content increased from 0 to 20.8 vol%, which was an almost linear increase between both values of pure epoxy and PMMA components, indicating no influence of phase separation in those blends. At the healing temperature, E' decreased from about 1.75 to 0.25 GPa in the same composition range, reflecting the glassy state of PMMA. However, even at 150 °C, the blend behaved globally as a stiff elastic solid up to the highest PMMA contents investigated, and no significant dimensional instabilities were observed, indicating that

both the small amount of contacts between the epoxy particles and the intrinsic strong nature of PMMA were sufficient to maintain structural integrity at the healing temperature.

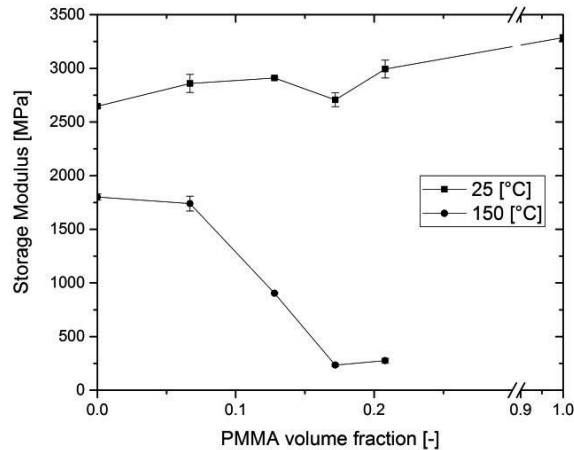


Figure 4.21: E' determined by DMA as a function of the PMMA volume fraction at room temperature and the healing temperature (150 °C).

The maximum stress observed during tensile tests decreased approximately twofold as the PMMA content was increased from 0 to 17.2 vol% before increasing again in the direction of pure PMMA strength (Figure 4.22 (a)). The corresponding Young's moduli, E (Figure 4.22 (b)), were consistent with the values of E' obtained by DMA (Figure 4.21). As for previous epoxy-thermoplastic blends, this behaviour can be explained from the fracture surfaces (observed by SEM in Figure 4.19 (b)). In particular, at high PMMA contents, lower interconnections between epoxy particles as well as a weak bonding between epoxy particles and the surrounding PMMA matrix were highlighted in addition to the confined layer theory seen in section 4.1.2. The decrease in strain-to-failure (Figure 4.22 (b)) from about 4%, where the epoxy was the continuous phase, to only about 1% for high PMMA contents, where the continuous phase was essentially PMMA, was again attributed to the PMMA confinement in between epoxy particles as strain-to-failure of pure PMMA was higher than the produced blends.

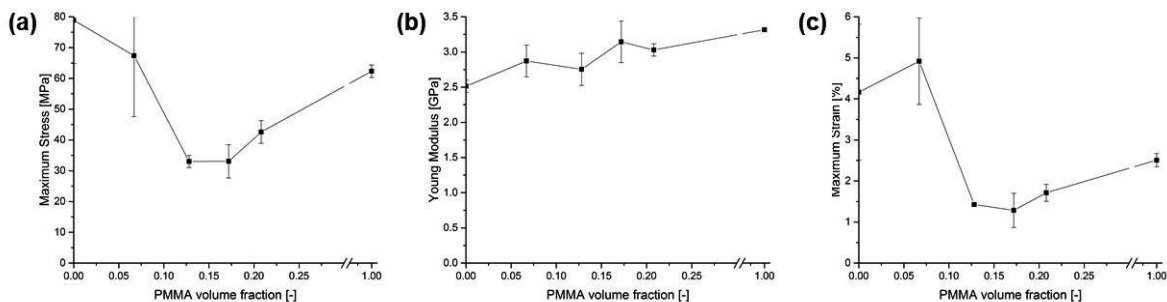


Figure 4.22: (a) Maximum stress, (b) Young's Modulus and (c) strain to failure as a function of the PMMA volume fraction.

Finally, fracture toughness, K_{IC} , of these blends was assessed through TDCB tests and is depicted for each blend in Figure 4.23. Specimens containing 6.7 vol% PMMA could not be tested due to their high fracture toughness, making the interface around the blend of this geometry to rupture first. This behaviour could be concluded from *Epoxy-PMMA(12.8)* which showed a higher fracture toughness than epoxy due to the complex morphology containing partially the phase with epoxy matrix and PMMA particles, characteristic of higher fracture toughness values as

demonstrated by other authors [55], [243]. When further increasing the PMMA content, fracture toughness decreased, which could be related to the low strength values observed for those compositions and the weak bonding between PMMA and epoxy in the cured state. This weak bonding could be supported by the observation of the fracture surfaces for those specimens (Figure 4.19 (b)), where epoxy particles were bare of PMMA matrix. The relatively large scatter in K_{IC} was again attributed to the specimen side-grooves [292].

Even though low fracture toughness values were observed, healing (after a thermal cycle of 150 °C for 30 minutes) up to 50% and 74% for respectively *Epoxy-PMMA(17.2)* and *Epoxy-PMMA(20.8)* could be reached, which proved the ability of PMMA to wet and heal the crack faces. Again, the particulate epoxy morphology could be highlighted as best for thermal mending applications.

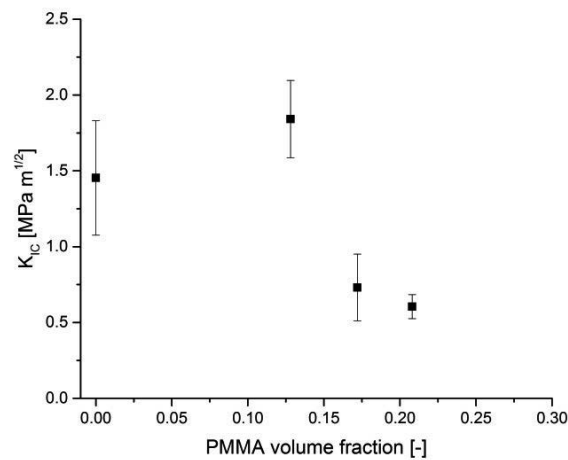


Figure 4.23: K_{IC} as a function of the PMMA volume fraction.

4.1.5 Conclusion

In the present section, four epoxy-thermoplastic blends were studied in terms of thermal properties, strength, stiffness, fracture toughness as well as recovery in fracture toughness. In terms of thermal mending (i.e. recovery in toughness), one blend in each system was highlighted: (i) *Epoxy-PCL(30.6vol%)* for the low molecular weight PCL; (ii) *Epoxy-PCL(21.3vol%)* for the high molecular weight PCL; (iii) *Epoxy-PLA(12.3vol%)* and (iv) *Epoxy-PMMA(20.8vol%)*. However, strength of those blends was also highlighted as crucial for structural integrity. To choose the most appropriate thermoplastic to be blended with epoxy and further used as a matrix for healing cracks in FRPs, those two properties must be considered. In addition, to compare with the reference material proposed by Luo *et al.* [7], one of their representative blend was processed (Epoxy with 25 vol% PCL, the PCL used was of $M_n \approx 45,000$ g/mol due to manufacturer constraints) and its strength as well as recovery in fracture toughness measured through tensile and TDCB testing (following the procedures detailed in Chapter 3). The maximum strength along with the healing efficiency measured through TDCB tests are represented for each blend in Figure 4.24, pure Epoxy is also shown. From this graph, it is then possible to highlight the best candidate to be used as a healing matrix in FRPs. PCL blends with low molecular weight ($M_n \approx 10,000$ g/mol) are discarded due to their low strength and because structural integrity during healing (150 °C) was lost (see Figure 4.5). The second obvious candidate that can be discarded is epoxy-PMMA blends. Indeed, the amorphous nature of this thermoplastic made the blends highly viscous and did not provide bleeding during the healing cycle. Blends of epoxy with the high molecular weight PCL can also be discarded due to their high viscosity during processing (inherited from the high molecular weight) as well as the loss of structural integrity during the healing cycle (see Figure 4.10). Also, these last blends are comparable to epoxy-PCL blends with $M_n \approx 45,000$ g/mol which present a lower viscosity. Epoxy-PLA blends can be of high interest to be integrated to composites because of their high strength combined with full crack recovery. However, due to the high PLA melting

temperature and thus the healing temperature too close to epoxy glass transition, structural integrity was lost during healing (Figure 4.16), which cannot be acceptable in structural applications. *Epoxy-PCL(25vol%)* blends with the medium molecular weight PCL ($M_n \approx 45,000$ g/mol) are thus most appropriate to be integrated to composites as they present a good compromise between suitable mechanical, processing and healing properties. Notice however that PLA blends could be explored using copolymers in order to decrease the melting temperature as well as the viscosity of this component or using viscosity modifiers. Before an integration to FRPs, additional insights into the phase separation mechanisms as well as blends properties are however required for the chosen blends. In particular, the blend composition must be tailored to obtain the best compromise between healing performances and structural integrity. Section 4.2 studies thermal, mechanical as well as healing properties of epoxy-PCL ($M_n \approx 45,000$ g/mol) blends over a relatively wide range of composition as compared to the study of Luo *et al.* [7] to select the healing matrix composition which will be used in the rest of this study.

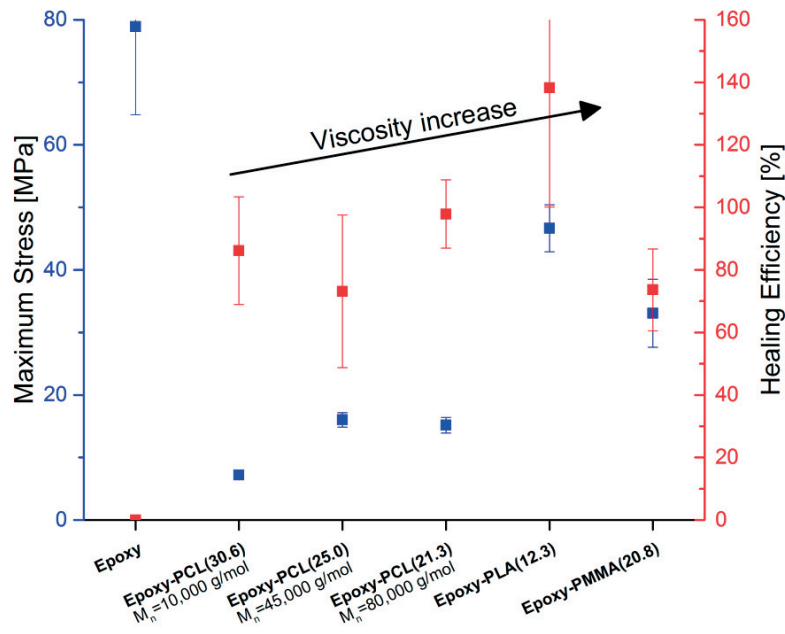


Figure 4.24: Maximum stress for the different epoxy-thermoplastic blends highlighted as best for thermal mending, along with the corresponding healing efficiency measured by means of TDCB tests. Pure epoxy and epoxy-PCL blends similar to Luo *et al.* [7] are also shown. For epoxy-PCL blends, the PCL molecular weight is provided to differentiate the blends.

4.2 Thermal mending in immiscible epoxy-PCL blends

(Adapted from ref. [295]: A. Cohades, E. Manfredi, J.-C. Plummer, and V. Michaud, "Thermal mending in immiscible poly(ϵ -caprolactone)/epoxy blends," *Eur. Polym. J.*, vol. 81, pp. 114–128, 2016)

In the present section, phase separation, mechanical properties and the crack healing capacity is investigated for immiscible PCL ($M_n \approx 45,000$ g/mol) blends with a commercial DDS-cured epoxy over a relatively wide range of PCL contents compared with previous studies [7], [135], and using a relatively mild healing temperature. This PCL was identified (see section 4.1) as the best compromise between crack healing capability and structural integrity as compared to the pure epoxy reference. Even though similar systems have been studied in [7], the phase separation mechanisms, the influence of the PCL content on the phase-separated morphology using a commercial epoxy as well as the governing failure mechanisms need to be understood before the integration as matrix in FRPs. The different amounts of PCL initially mixed with the epoxy monomer are given in Table 4.6 as the mass ratios of the two components ($m_{\text{epoxy}}:m_{\text{PCL}}$), and the weight and volume fractions of PCL determined after addition of the DDS (m_{PCL} and ϕ_{PCL}). ϕ_{PCL} is in each case given for the liquid blends, assuming a density of 1.145 g/cm³ for the PCL and a density of 1.34 g/cm³ for the epoxy-DDS. For preparation of the blends as well as characterisation methods leading to the results presented hereafter, the reader is referred to Chapter 3.

Table 4.6: Specimen designations and the corresponding mass ratios of epoxy resin to PCL, and the overall PCL weight and volume fractions after addition of the DDS.

Specimen	epoxy to PCL	PCL weight fraction [%]	PCL volume fraction [%]
	$m_{\text{epoxy}}:m_{\text{PCL}}$	m_{PCL}	ϕ_{PCL}
Epoxy-PCL(0)	100:0	0	0
Epoxy-PCL(1.7)	98:2	1.5	1.7
Epoxy-PCL(8.7)	90:10	7.5	8.7
Epoxy-PCL(13.1)	85:15	11.5	13.1
Epoxy-PCL(17.7)	80:20	15.5	17.7
Epoxy-PCL(19.5)	78:22	17.1	19.5
Epoxy-PCL(21.3)	76:24	18.8	21.3
Epoxy-PCL(23.2)	74:26	20.5	23.2
Epoxy-PCL(25.0)	72:28	22.2	25.0
Epoxy-PCL(26.9)	70:30	23.9	26.9
Epoxy-PCL(46.2)	50:50	42.3	46.2
Epoxy-PCL(66.7)	30:70	63.1	66.7
Epoxy-PCL(100)	0:100	100	100

4.2.1 Microstructural development in the blends

4.2.1.1 Determination of the cloud-point

The time to reach the cloud-point during cure was estimated by hot-stage microscopy for each specimen in Table 4.6. Figure 4.25 shows typical images from *Epoxy-PCL(21.3)* at a nominal temperature of 180 °C, for which the time to reach the cloud-point was estimated to be 26.3 min. Isothermal DSC heat flow curves normalized with respect to the total mass of the epoxy-hardener in the specimen (see Figure 4.26), were used to obtain the degree of conversion as a function of time at the same temperature, by comparing the instantaneous heat of reaction with the total heat of reaction determined from heating scans. A sharp increase in the slope of the heat flow rate curve was typically observed at intermediate times (see Figure 4.26). This was assumed to correspond to phase separation and the consequent increase in the local concentration of the reagents. As seen from Figure 4.27, the times to phase separate estimated in this way by DSC were comparable with the cloud-point times determined by hot-stage microscopy, although these latter tended to be systematically shorter. This discrepancy was attributed to inaccurate temperature

control of the hot stage (recalibration using reference materials indicated that the effective temperature of the hot stage was up to 7 °C less than the nominal temperature in this range). For consistency, therefore, the degrees of conversion corresponding to the cloud-point curves referred to in the following section were determined directly from the DSC curves.

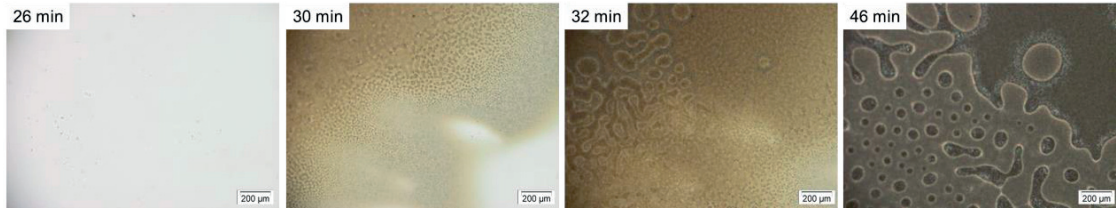


Figure 4.25: Evolution of the microstructure of *Epoxy-PCL(21.3)* as a function of cure time at a nominal temperature of 180 °C.

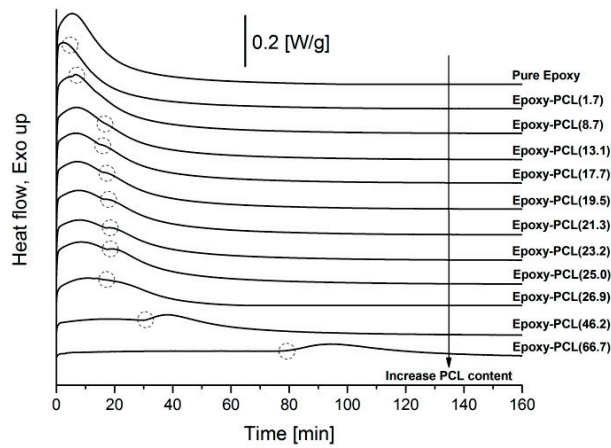


Figure 4.26: Isothermal DSC heat flow curves at 180 °C for the different blends. The dashed circles indicate the times corresponding to the onset of phase separation.

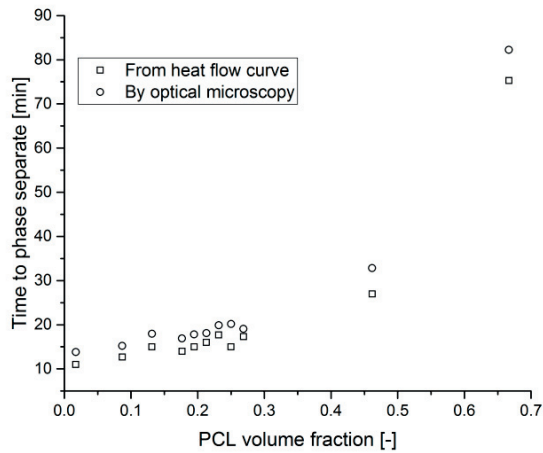


Figure 4.27: Time for phase separation determined from DSC heat flow curves (cf. Figure 4.26) and times to reach the cloud-point determined by optical microscopy as a function of the PCL volume fraction at a nominal temperature of 180 °C.

4.2.1.2 Phase behaviour

Polymerisation-induced phase separation may be described semi-quantitatively using the *Flory-Huggins* model (see section 2.4.3.1 and 4.1) and a single concentration-independent interaction parameter, χ , to account for the effect of the increase in molar mass on miscibility [134]. In the present case of a ternary blend of a polymeric modifier with an epoxy resin and a diamine hardener, the epoxy-hardener system was treated as a single monodisperse pseudo-component [134] with an initial number average molar mass, $M_n = 315$ g/mol, and no attempt was made to take into account local deviations from stoichiometry during phase separation. The molar volume of this pseudo-component may be estimated from the number average degree of polymerisation for a given degree of conversion of the epoxy groups, p , which, for a stoichiometric mixture with a four-functional hardener [134], is assumed to be given by:

$$X_n(p) = \frac{1}{1 - 2p^2} \quad (4.4)$$

The values of p corresponding to the binodal and spinodal curves were then calculated as a function of PCL content for a given value of χ as described by Williams *et al.* [134] (see section 2.4.3.1), taking the molar volume of the PCL monomer be the reference volume. The results shown in Figure 4.28 were obtained by adjusting χ to provide an approximate fit to the experimental cloud-point conversion derived from the ratio of the enthalpy at the start of phase separation (as shown in Figure 4.26) and the total enthalpy of reaction. The PCL volume fraction corresponding to the critical point, where the binodal and spinodal are cotangent, is given by:

$$\phi_{crit} = \frac{1}{1 + (Z_{PCL}/Z_{crit})^{1/2}} \quad (4.5)$$

$$Z_{crit} = \left(\frac{1}{(2\chi)^{1/2} - (1/Z_{PCL})^{1/2}} \right)^2$$

where Z_{PCL} is the ratio of the molar volume of the PCL to that of the PCL monomer, which is approximately equal to 394 in the present case ($M_n \approx 45,000$ g/mol), and Z_{crit} is the reduced molar volume of the reacted pseudo-component corresponding to the critical point. Taking $\chi = 0.12$, the value used for the fit to the data in Figure 4.28, ϕ_{crit} was estimated to be about 10.3 vol% PCL (i.e. about 9.0 wt%). This should be considered a very rough estimate given the scatter and the lack of any clear trend in the experimental data points in Figure 4.28, and the various assumptions inherent in the *Flory-Huggins* approach, e.g. those of a monodisperse system at equilibrium in which stoichiometry is respected throughout and for which χ is independent of composition. However, it provides a convenient basis for the discussion of morphological development in this system.

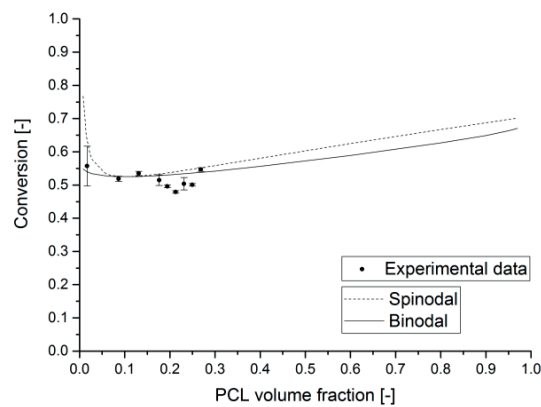


Figure 4.28: Estimates of conversions corresponding to spinodal and binodal curves as a function of the PCL volume fraction for $\chi = 0.12$ according to the *Flory-Huggins* equation (see section 2.4.3.1), along with experimental data points for the conversion at onset of phase separation.

4.2.1.3 Blend morphology

As shown in Figure 4.29 (a), three types of morphology were observed by optical microscopy, depending on the PCL content: (i) at concentrations above 23.2 vol% PCL, the morphology consisted of an interconnected particulate epoxy phase and a co-continuous PCL phase, the epoxy particles decreasing in diameter as the PCL concentration increased, as shown in Figure 4.30; (ii) at concentrations up to 13.1 vol% PCL, the morphology consisted of a continuous epoxy phase with PCL inclusions; (iii) at concentrations between 13.1 and 23.2 vol% PCL, a complex morphology was observed with relatively large co-continuous PCL and/or epoxy domains containing much smaller epoxy and PCL inclusions respectively. This type of morphology is typified by the SEM image in Figure 4.31 of an etched freeze-fracture surface from *Epoxy-PCL(19.5)*. On the left-hand side of the image, the epoxy forms a discrete particulate phase in a PCL-rich matrix, while on the right-hand side of the image the epoxy is the continuous phase and contains small cavities corresponding to PCL-rich particles removed during etching. Similar morphologies have been reported previously for this composition range [7], [135], [136], [296], and, as shown in Figure 4.29 (b), comparable results were also obtained here when Epon™ 828EL was substituted by the DGEBA used by Luo *et al.* [7], indicating phase separation to be insensitive to the molar mass per epoxide group within this range.

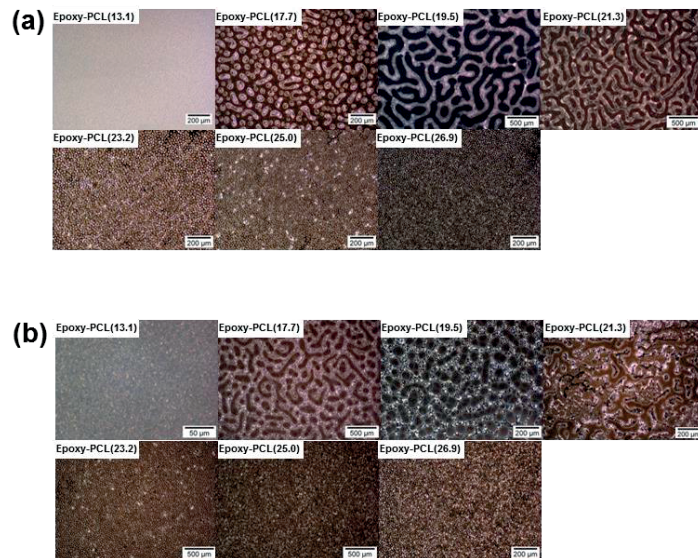


Figure 4.29: Morphology at different compositions for: (a) Epon™ 828 EL (*Momentive*) resin; (b) DGEBA (*Sigma*) resin.

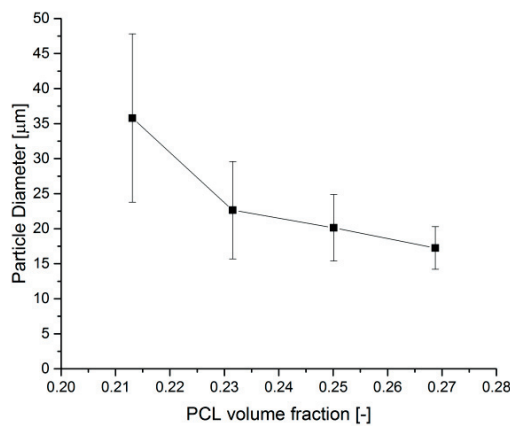


Figure 4.30: Average epoxy particle diameter in microtomed sections as a function of the PCL volume fraction.

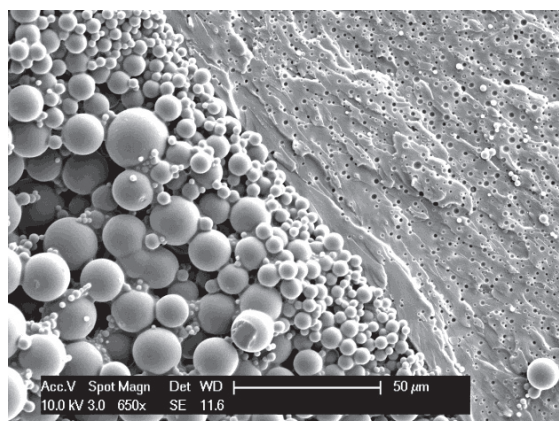


Figure 4.31: SEM image of *Epoxy-PCL(19.5)* at the interface between the coarse co-continuous domains visible in the corresponding optical micrograph in Figure 4.29.

The model phase diagram in Figure 4.28 suggested the critical point to be at about 10 vol% PCL for a reaction temperature of 180 °C, and in the vicinity of the critical point, the spinodal and binodal curves were predicted to be relatively close to each other. The dominant phase separation mechanism in this regime was therefore inferred to be spinodal decomposition rather than nucleation and growth [136]. Also, the shape of the binodal implied phase separation initially into roughly equal volumes of epoxy- and PCL-rich phases for PCL contents around and immediately above that corresponding to the critical point. It follows that co-continuous morphologies should be favoured under these conditions. Moreover, the rapid increase in viscosity of the epoxy-rich phase as the conversion increases towards the gel point at $p \approx 0.7$, is expected to stabilize the coarse morphologies resulting from the early stages of phase separation. The decrease in miscibility with further increase in conversion then results in the formation of fine precipitates within the co-continuous domains as seen in Figure 4.31, and as discussed in detail e.g. by Williams *et al.* [134]. In the present case, co-continuous morphologies were observed in the range 17 to 22 vol% PCL, whereas discrete domains of PCL-rich particles in a continuous epoxy-rich matrix dominated at 13.1 vol% PCL, indicating the PCL content at the critical point to be somewhat higher than predicted from Eq. (4.5). This is consistent with previous investigations into similar systems, for which the experimental critical point was reported to be 13.8 vol% PCL [144], [296].

4.2.1.4 Phase composition

Although the model phase diagram in Figure 4.28 implied high phase purity at equilibrium for high degrees of conversion, the observed microstructures were clearly influenced by kinetic factors. FTIR microscopy was therefore used to investigate the composition of the coarse structure in polished cross-sections from specimens containing 17.7 and 25 vol% PCL (the minimum specimen size was 12×12 μm). The absorption spectra in the wavenumber range 1680 to 1780 cm^{-1} (the carbonyl stretch band characteristic of the PCL) for specimens containing 17.7 and 25.0 vol% PCL are shown in Figure 4.32 along with spectra for the pure epoxy and PCL. The discrete particles present at 25 vol% PCL and also those present in the nominally PCL-rich domains at 17.7 vol% PCL were confirmed to show no absorption in this range, while strong carbonyl peaks were obtained from the surrounding matrix. Even so, the carbonyl peaks tended to be weaker than those obtained from the pure PCL reference specimens, presumably because of the limited lateral and vertical resolution of the FTIR microscope.

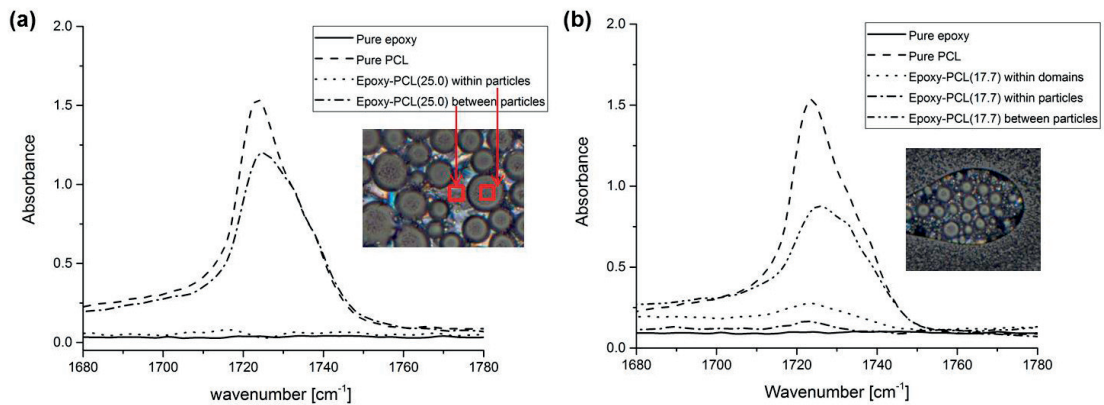


Figure 4.32: FTIR spectra in the carbonyl stretch band (wavenumbers 1680-1780 cm^{-1}) from selected regions of (a) *Epoxy-PCL(25.0)* and (b) *Epoxy-PCL(17.7)* blends. Spectra for the pure epoxy and pure PCL are also shown for comparison.

4.2.2 Thermal transitions in the cured blends

Figure 4.33 (a) and (b) show DSC heating and cooling scans for the different blends after cure. Two characteristic transitions were observed for all the compositions. The endothermic peak at about 54 °C corresponded to melting of the PCL, whereas the small enthalpic peak and step-like increase in heat capacity at about 197 °C were associated with the glass transition of the epoxy. These transition temperatures were generally similar to those of the pure PCL and pure epoxy, indicating a high degree of phase purity, consistent with the FTIR results. The somewhat reduced melting temperature and lack of a clear exotherm in the cooling curves for *Epoxy-PCL(13.1)* was attributed to the high degree of dispersion of the PCL in the epoxy matrix in this case, which may retard crystallisation. From Figure 4.33 (b), the degree of crystallinity of the blends could be determined to assess the potential detrimental effect of the curing cycle. Figure 4.34 shows the crystallinity degree of the PCL phase within the different phase-separated blends after 3h curing, compared to that of the pure PCL in the as received state and after 3h curing at 180 °C. Overall, crystallinity of the PCL is not much affected by the imposed curing cycle; hence viscosity or other relevant properties of the PCL are not expected to be greatly affected.

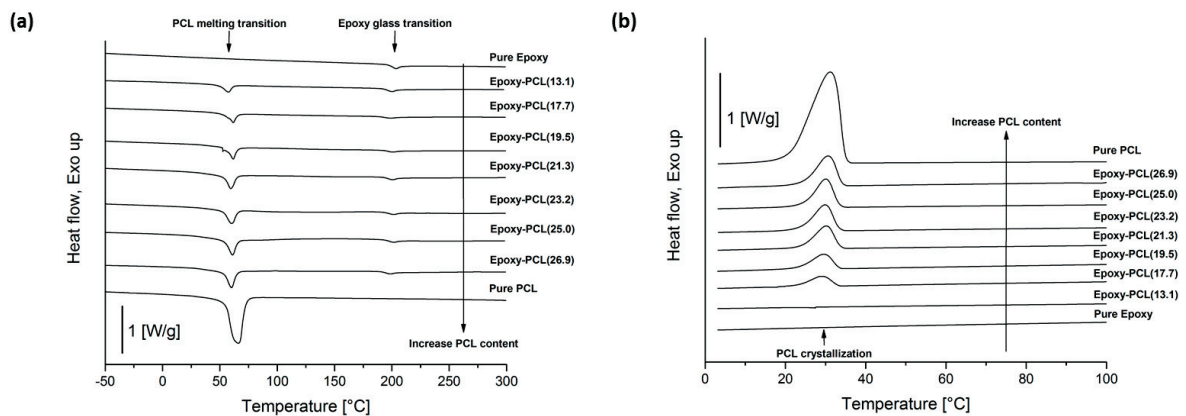


Figure 4.33: DSC heating (a) and cooling (b) scans for the different blends after cure.

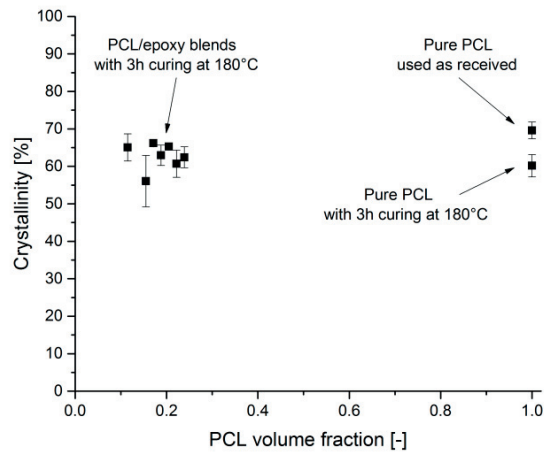


Figure 4.34: Crystallinity degree of the PCL phase within phase-separated blends after 3 h curing, as a function of the PCL volume fraction. Pure PCL as received and with 3h curing are also shown for comparison.

4.2.3 Mechanical properties

4.2.3.1 Dynamic mechanical analysis

Three distinct mechanical transitions were identified from the DMA scans, and their corresponding transition temperatures are summarized in Figure 4.35 (a) as a function of PCL content. Those at about $-25\text{ }^{\circ}\text{C}$ and $200\text{ }^{\circ}\text{C}$, denoted $T_{\alpha,\text{PCL}}$ and $T_{\alpha,\text{Epoxy}}$ respectively, were associated with the glass transitions of the PCL and the epoxy, while a third at around $75\text{ }^{\circ}\text{C}$ was attributed to melting of the PCL and is denoted $T_{\beta,\text{PCL}}$. The storage modulus, E' , is shown as a function of the PCL content in Figure 4.35 (b) for two different temperatures, $25\text{ }^{\circ}\text{C}$ (room temperature) and $150\text{ }^{\circ}\text{C}$ (the target healing temperature). At room temperature, a decrease in E' from 2.6 to close to 1.6 GPa was observed as the PCL content increased from 0 to 17.7 vol%, corresponding to the establishment of the co-continuous morphology visible in Figure 4.28. At $150\text{ }^{\circ}\text{C}$, E' decreased from about 1.75 to about 0.25 GPa in the same composition range, reflecting the molten state of the PCL. However, even at $150\text{ }^{\circ}\text{C}$, the blend behaved globally as a stiff elastic solid up to the highest PCL contents investigated, and no significant dimensional instabilities were observed, indicating the contacts between the epoxy particles to be sufficient to maintain structural integrity at the healing temperature, as found previously by Luo *et al.* [7]. In the present case, the interconnectivity of the epoxy particles at high PCL contents was also confirmed by direct observation of the thin sections used to determine the particle diameters (see Figure 4.30).

Upper (constant strain) and lower (constant stress) bound predictions of E' at $25\text{ }^{\circ}\text{C}$ based on the moduli of the pure epoxy and the PCL have also been included in Figure 4.35 (b). Comparison with the data suggested there to be a transition from a regime in which the epoxy is the continuous phase to a regime where the epoxy and PCL were effectively in a series arrangement, consistent with the observed morphologies. Hence, at the highest PCL contents, the PCL acted as a continuous layer and the bulk of the epoxy particles deformed relatively little. The relatively low E' observed at $150\text{ }^{\circ}\text{C}$ at high PCL contents, where the contribution of the PCL was presumably negligible, also indicated the particulate epoxy phase to contribute relatively little to the overall stiffness at $25\text{ }^{\circ}\text{C}$, in spite of its interconnectivity.

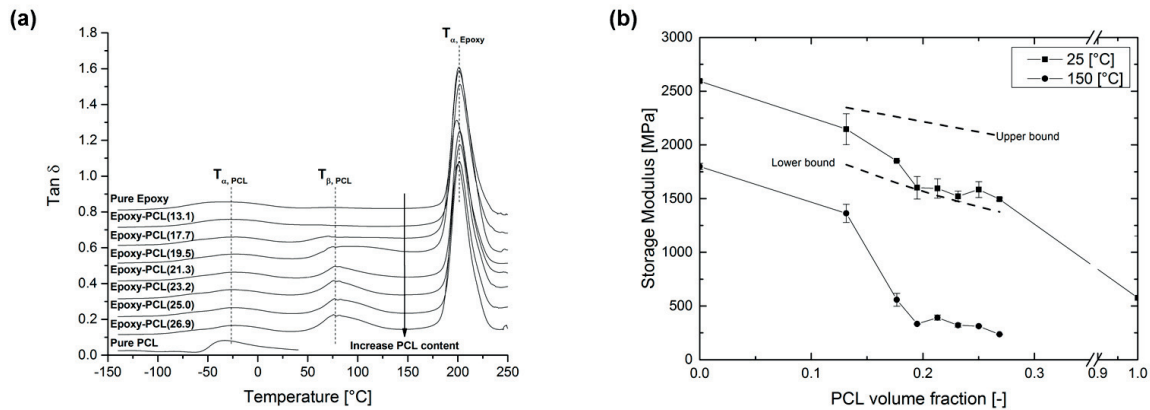


Figure 4.35: DMA results: (a) transition temperatures as a function of the PCL volume fraction. (b) E' as a function of the PCL volume fraction at room temperature and the healing temperature (150 °C), along with upper and lower bound predictions for E' as indicated.

4.2.3.2 Tensile properties

The maximum stress observed during the tensile tests decreased approximately fourfold as the PCL content was increased from 0 to 26.9 vol% (Figure 4.36 (a)), flattening off at about 20 MPa above 23.2 vol% PCL, which was close to the yield stress, σ_y , of pure PCL. The corresponding Young's moduli, E (Figure 4.36 (c)), were consistent with the values of E' obtained by DMA (Figure 4.35 (b)). As seen from Figure 4.37 (c), at high PCL contents, three modes of fracture co-existed (see also Figure 4.13 for a schematic explanation): (i) failure of the epoxy-PCL interface, (ii) cohesive failure of the PCL and (iii) brittle failure of the interface between the interconnected epoxy particles. In the limit of low PCL contents (Figure 4.37 (a)), brittle failure of the epoxy dominated, implying the PCL particles not to promote matrix ductility, while at intermediate PCL contents (Figure 4.37 (b)), all the fractures modes were present. The decrease in strain-to-failure from about 4.5%, where the epoxy was the continuous phase, to only about 2% for *Epoxy-PCL(25.0)* and *Epoxy-PCL(26.9)*, where the continuous phase was essentially PCL, was attributed to severe confinement of the relatively ductile PCL by the relatively stiff, high yield-strength epoxy particles (σ_y at least 4 times that of the PCL) and brittle behaviour of the interfaces between the epoxy particles, rather than premature failure at the PCL-epoxy interface (see section 4.1.2 and Figure 4.13). Indeed, strain-to-failure has been reported to increase with PCL content in similar systems, albeit for different cure conditions and stoichiometry, suggesting strong interfacial adhesion [144].

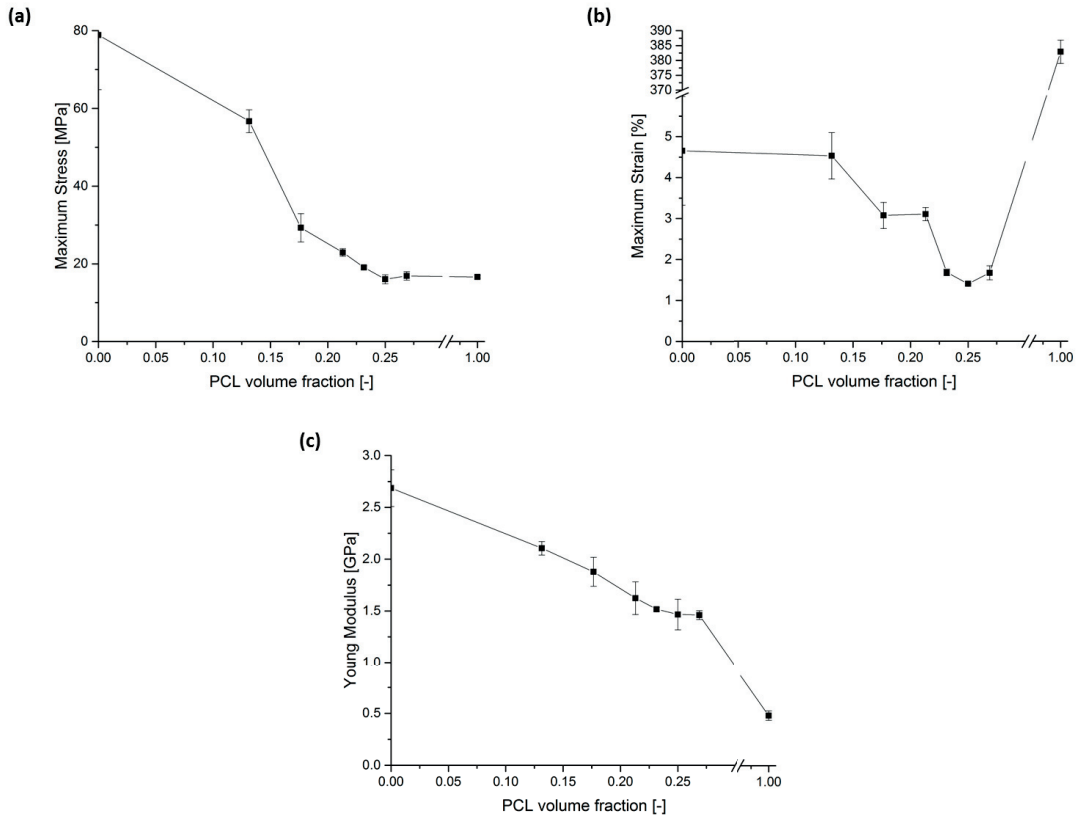


Figure 4.36: (a) Maximum stress, (b) strain-to-failure and (c) Young's Modulus as a function of the PCL volume fraction.

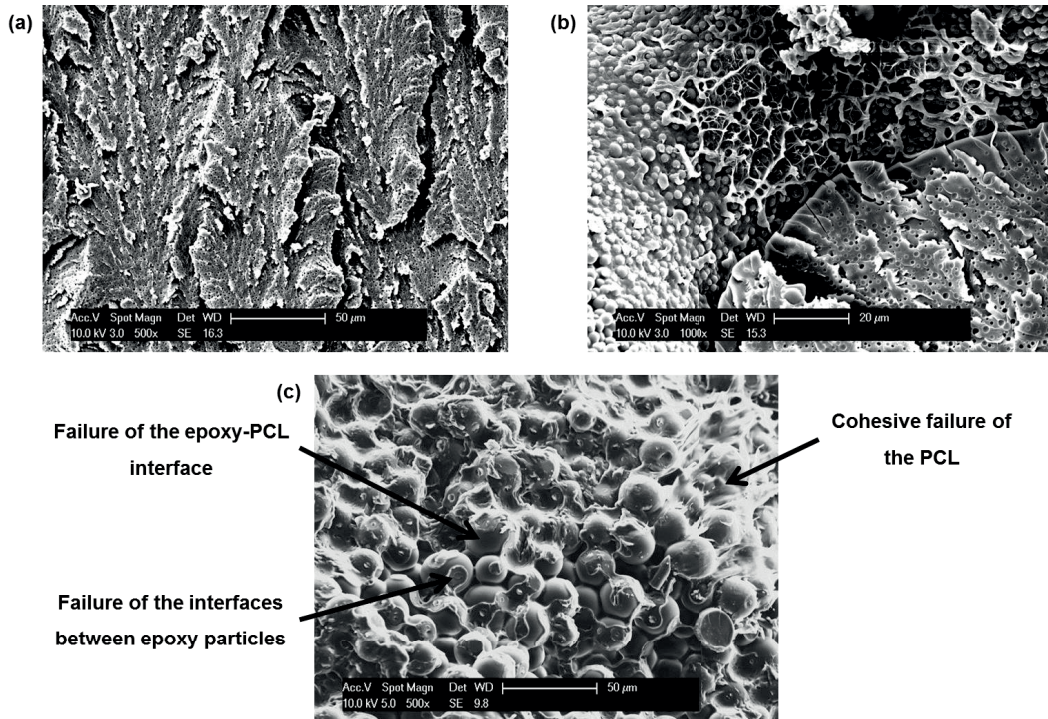


Figure 4.37: SEM image of the tensile fracture surfaces for (a) *Epoxy-PCL(13.1)*; (b) *Epoxy-PCL(17.7)* and (c) *Epoxy-PCL(25.0)*.

4.2.3.3 Fracture properties

Figure 4.38 shows K_{IC} from the TDCB tests as a function of the PCL content. For the pure epoxy, a mean value of $1.45 \text{ MPa m}^{1/2}$ was obtained, i.e. 50% higher than that reported by Lee et al. for the same epoxy subjected to a post-cure heat treatment at $250 \text{ }^\circ\text{C}$ [297], but comparable with values for commercial systems [298]. Consistent with the trends in the maximum stress and the strain-to-failure in the tensile tests, K_{IC} was generally observed to decrease on addition of PCL to the epoxy: (i) at 13.1 vol% PCL, where the PCL formed discrete inclusions in a continuous epoxy matrix, K_{IC} fell to $1.04 \text{ MPa m}^{1/2}$; (ii) K_{IC} rose slightly to $1.07 \text{ MPa m}^{1/2}$ for the coarse bi-continuous microstructures observed at intermediate compositions; (iii) K_{IC} fell to around $0.65 \text{ MPa m}^{1/2}$ for the particulate epoxy morphology. Although addition of ductile thermoplastics, including PCL, to an epoxy matrix has frequently been reported to result in improved fracture resistance, in the present case, K_{IC} for the unmodified epoxy was already comparable with values obtained in many optimised rubber-modified systems, accounting for the apparent absence of any toughening effect on PCL addition [144], [243]. As with the strain-to-failure in the tensile tests, the reduced K_{IC} at high PCL contents was interpreted as a confinement effect. This effect was detailed in section 4.1.2 (see Figure 4.13). The relatively large scatter in K_{IC} among the individual specimens, as reflected by the error bars in Figure 4.38 was again attributed to variations in the geometry of the specimen side-grooves [292].

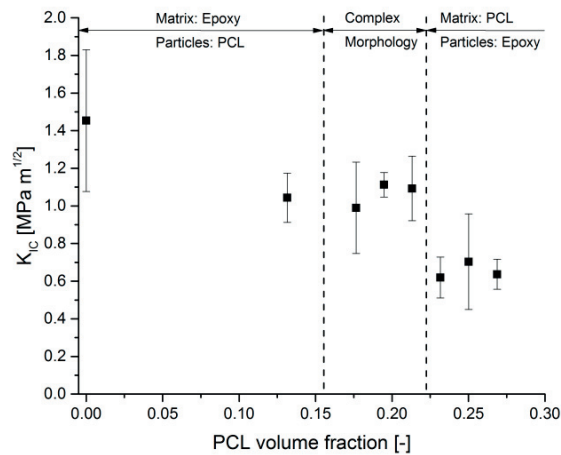


Figure 4.38: K_{IC} as a function of the PCL volume fraction.

After testing, the TDCB specimens were subjected to a healing treatment at $150 \text{ }^\circ\text{C}$ for 30 min as described in section 3.3.5. As indicated in section 4.2.3.1, all the blends behaved as stiff elastic solids at this temperature, but because of the large difference in the effective thermal expansion coefficient between the epoxy and the PCL, the unloaded crack faces tended to separate during healing. Hence, while fracture toughness recovery of up to 80% was observed for the *Epoxy-PCL(25.0)* tested after unconstrained healing, the results showed significant scatter. Compressive stresses of between 0 and 250 kPa as defined in section 3.3.5 were therefore applied to the specimens during healing and it was found that a minimum of 50 kPa was necessary to maintain closure of the crack faces for all the compositions considered. As shown in Figure 4.40, under these conditions, although the scatter was still rather high, in particular for high PCL content due to potential loss or inhomogeneity of the PCL during healing for these geometries, the healing efficiency increased as the PCL content increased, reaching a mean value of 78.5% at the highest PCL contents, although certain specimens showed healing efficiencies in excess of 100%. After healing, the fracture surfaces were covered by a continuous layer of PCL, confirming the role of PCL bleeding in the healing process. Moreover, optical observation of the crack before and after healing (Figure 4.39) indicated full recovery of the initial microstructure. The effect of multiple fracture and healing cycles was also investigated for *Epoxy-PCL(25.0)* and *Epoxy-PCL(26.9)*. Figure 4.41 shows the evolution of the healing efficiency over three successive cycles. Although there was significant scatter,

it was found that the healing efficiency decreased by less than 5% after each cycle, suggesting the present approach to be effective in the case of multiple damage events.

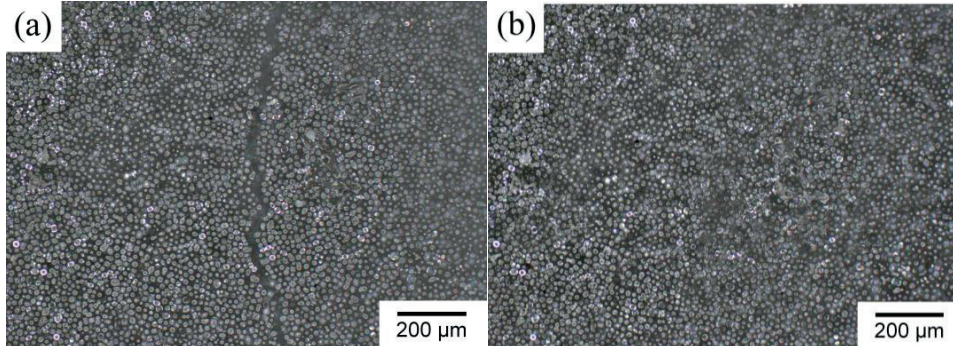


Figure 4.39: Reflected light optical microscopy of (a) a crack after testing and (b) the same crack after healing at 150 °C for 30 minutes.

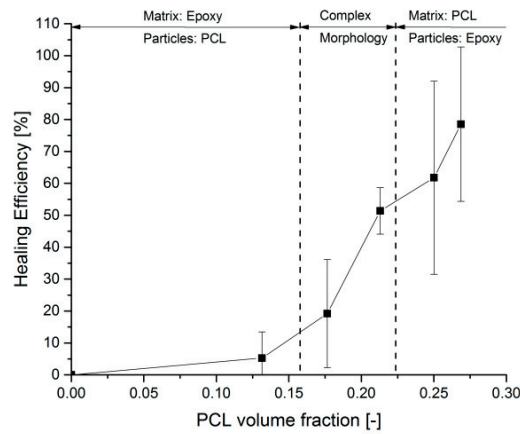


Figure 4.40: Healing efficiency as a function of the PCL volume fraction for an applied stress of 50 kPa during healing.

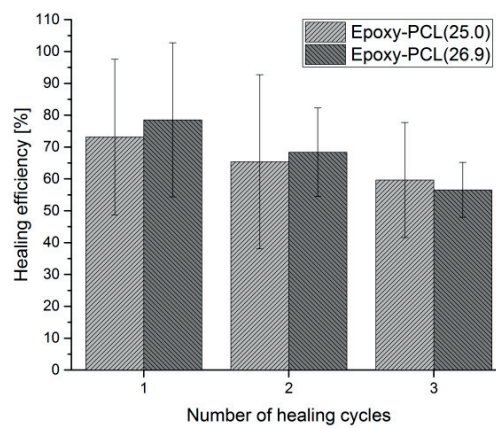


Figure 4.41: Multiple healing assessment for *Epoxy-PCL(25.0)* and *Epoxy-PCL(26.9)*.

4.2.4 Conclusion

Blends of a commercial epoxy/DDS hardener with the thermoplastic PCL ($M_n \approx 45,000$ g/mol) led to three types of morphologies after polymerisation-induced phase separation: an interconnected particulate epoxy phase and a co-continuous PCL phase at PCL concentrations greater than 23.2 vol%; (ii) a continuous epoxy phase containing PCL inclusions at concentrations of up to 13.1 vol% PCL; (iii) a complex morphology with relatively coarse co-continuous PCL and/or epoxy domains between 13.1 and 23.2 vol% PCL. These morphologies were consistent with simple model predictions, which suggested spinodal decomposition to be the dominant mode of phase separation over most of this composition range.

Increasing the PCL content reduced the dynamic and static tensile stiffness of the blends, which tended to a lower limit imposed by the presence of a continuous PCL phase at the highest PCL contents investigated. The stiffness nevertheless remained above 1 GPa, and the blends continued to behave as rigid elastic solids at the healing temperature of 150 °C, in spite of a sharp decrease in the Young's modulus at this temperature, owing to the interconnectivity of the epoxy-rich particulate phase.

A four-fold decrease in strength and a two-fold decrease in toughness were also observed for the blends containing a continuous PCL phase. These were attributed to both the high initial fracture toughness of the baseline epoxy ($1.45 \text{ MPa m}^{1/2}$), and severe spatial confinement of the nominally ductile PCL. After a moderate healing treatment at 150 °C for 30 min, toughness recovery increased strongly with PCL content, reaching 70 to 80% efficiency for blends containing 25 and 26 vol% PCL. Because healing depends on the capacity of the PCL, which shows relatively high thermal expansion on melting, to expand, flow into newly formed cracks and bridge the crack faces, efficient healing is clearly contingent on the presence of a continuous PCL phase. The PCL bleeding behaviour within specific geometries and volumes is further detailed in Chapter 5 and Chapter 7.

It follows that blends with morphologies comprising interconnected epoxy particles embedded in a continuous PCL matrix are most suited to provide a part with healing properties, while maintaining adequate mechanical properties both in service and at the healing temperature of 150 °C, i.e. above the melting point of the PCL. Moreover, because the blend is homogenous prior to cure, it is expected to be compatible with processing requirements for the matrix phase of an FRP, provided that its viscosity is not greatly increased. The analysis developed in this section also provides guidelines for the optimisation of the blend composition and the molar mass of the thermoplastic component so as to ensure healing at moderate temperatures while maintaining appropriate toughness in service. The next chapter presents the integration of epoxy-PCL blends as a healing matrix in FRPs.

Chapter 5 E-glass epoxy-PCL blends

In the present chapter, phase-separated epoxy-PCL ($M_n \approx 45,000$ g/mol or $M_n \approx 49,000$ g/mol) blends form the matrix of structural composites. In particular, FRPs were manufactured with these blends (as well as with pure epoxy for comparison) through Vacuum Assisted Resin Infusion Moulding (VARIM) at high temperature. Section 5.1 presents the assessment of phase separation kinetics within these FRPs as well as interlaminar fracture toughness and its recovery after thermal mending. Section 5.2 presents damage recovery in FRPs with these blends extended to more realistic cases of impact and compression after impact.

5.1 Thermal mending in E-glass reinforced epoxy-PCL blends

(Adapted from ref. [299]: A. Cohades and V. Michaud, "Thermal mending in E-glass reinforced Poly(ϵ -caprolactone)/epoxy blends," *Compos. Part A Appl. Sci. Manuf.*, vol. 99, pp. 129–138, 2017)

This section first explores the influence of the fibres on phase separation kinetics as well as the resulting interfacial shear strength between epoxy-PCL blends and E-glass fibres. Strength, stiffness and interlaminar fracture toughness of the produced composites were assessed through static, dynamic bending tests and Mode I DCB experiments. DCB specimens were then subjected to a thermal mending cycle at 150 °C for 30 minutes to investigate their crack healing capacity. The different amounts of PCL ($M_n \approx 45,000$ g/mol) initially mixed with the epoxy monomer are given in Table 5.1 as the mass ratios of the two components ($m_{\text{epoxy}}:m_{\text{PCL}}$), and the volume fractions of PCL determined after addition of the DDS, ϕ_{PCL} . This last figure is in each case calculated for the liquid blends, assuming a density of 1.145 g/cm³ for the PCL and a density of 1.34 g/cm³ for the epoxy-DDS. These blends were then used for composite production. The obtained fibre volume fractions within each composite are also given in Table 5.1. For preparation of the blends as well as characterisation methods leading to the results presented hereafter, the reader is referred to Chapter 3. Notice that blends with high amount of PCL (37 vol%) were also prepared to compare with blends selected in section 4.2 (i.e. with 25 vol%).

Table 5.1: Specimen designations and the corresponding mass ratios of epoxy resin to PCL, and the overall PCL volume fractions after addition of the DDS. Fibre volume fraction obtained after composite production is also given.

Specimen	epoxy to PCL	PCL volume fraction in matrix [%]	Fibre volume fraction in specimen [%]
	$m_{\text{epoxy}}:m_{\text{PCL}}$	ϕ_{PCL}	V_f
Plain	100:0	0	47.1±0.6
PCL(25)	72:28	25.0	50.1±0.2
PCL(37)	59.5:40.5	36.9	48.1±1.8

5.1.1 Microstructural development in the blends

Microstructural development of the composites during curing was assessed by hot-stage microscopy observations. Figure 5.1 shows typical images for PCL(25) at a nominal temperature of 180 °C and for different times until complete polymerisation of the structure. White lines are fibres whereas the black circle is a bubble trapped in between the glass slides. Even though the fibres seemed to serve as nucleation sites for the particles during cure (see Figure 5.1 at 22 minutes, where a layer of epoxy phase forms preferentially around the fibres), phase separation upon polymerisation of epoxy-PCL blends (i.e. particle distribution) was overall not influenced by the presence of fibres in the cured state (see Figure 5.1 at 46 minutes). At full cure (46 minutes), a thin layer of epoxy could be observed around the glass fibres. This behaviour, explained previously by Turmel and Partridge [157] in similar systems, was

attributed to preferential wetting of the epoxy on the fibres, and therefore prevented the creation of an interface between the glass fibres and the continuous PCL phase. Notice that the range in particle diameters was similar to what was observed in section 4.2.

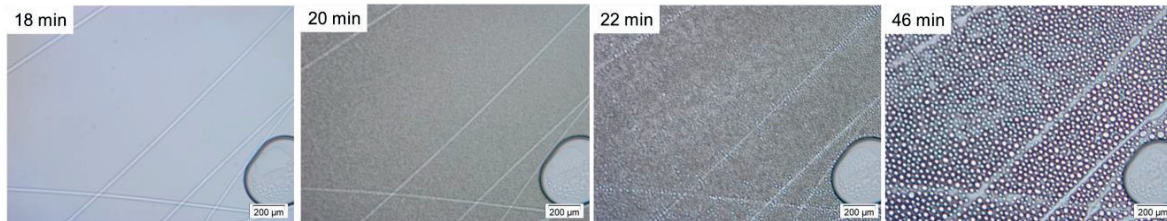


Figure 5.1: Evolution of the microstructure of *PCL(25)* in presence of glass fibres as a function of cure time at a nominal temperature of 180 °C.

The phase-separated microstructure was further assessed in presence of high fibre volume content. Transverse cuts of the cured specimens are shown in Figure 5.2, and for each image, the corresponding schematic structure is shown on the right. The quality of the composite through the VARIM process can be first highlighted as no porosities were observed (notice that the black regions in the composites with epoxy-PCL blends (Figure 5.2 (b) and (c)) were due to polishing artefacts, corresponding to the removal of softer PCL regions). The void content for the *Plain* specimens were further quantified by water immersion using ASTM D2734 [300] as $0.87\% \pm 0.60\%$, which confirmed the microscopy observations. Due to the sensitivity of PCL to water, the void content of Epoxy-PCL composites was only based on microscopy observations. In the *PCL(25)* composition (Figure 5.2 (b)), the matrix showed a two-phase structure (epoxy particles with a surrounding matrix) only where larger spaces existed in the composite, i.e. in between the plies in the resin rich regions. In these fibre-reinforced composites, phase separation was thus limited within the fibre tows, leading to a different structure between (phase-separated) and within (continuous epoxy phase) tows. This behaviour was confirmed by the measurement of epoxy particle diameters, which were of $12.60 \pm 3.66 \mu\text{m}$ in the resin rich region, greater than the distance between two fibres within a tow. This measured diameter was smaller than what has been measured in section 4.2 for neat resin systems ($20.14 \pm 4.75 \mu\text{m}$), indicating that phase separation started later due to the presence of fibres, even though these served as nucleation sites. Indeed, as the fibres were covered by a layer of epoxy, the blend equilibrium in the resin rich region might have been shifted, which delayed the start of phase separation due to the curved shape of the spinodal curve on the system phase diagram (see section 4.2, Figure 4.28). This statement was further confirmed by the variability in particle sizes and the higher concentration of small particles at the edges of the resin rich region, close to the glass fibres. In the *PCL(37)* composition (Figure 5.2 (c)) however, phase separation could be observed between and within tows of the composite. As epoxy particle diameters were $3.55 \pm 1.05 \mu\text{m}$ in this case, particles could fit between fibres within tows. Notice again that this mean diameter was slightly smaller than what has been measured in neat resin systems ($7.36 \pm 1.58 \mu\text{m}$), therefore confirming the later start of phase separation in presence of fibres. Even though phase separation was present within tows of the *PCL(37)* composition, a continuous epoxy layer could be observed around the glass fibres, demonstrating again preferential wetting of the epoxy phase [157]. Overall, the matrix phase separation, albeit constrained by the fibres, proceeded similarly to neat resins (see section 4.2), leading to similar morphological developments.

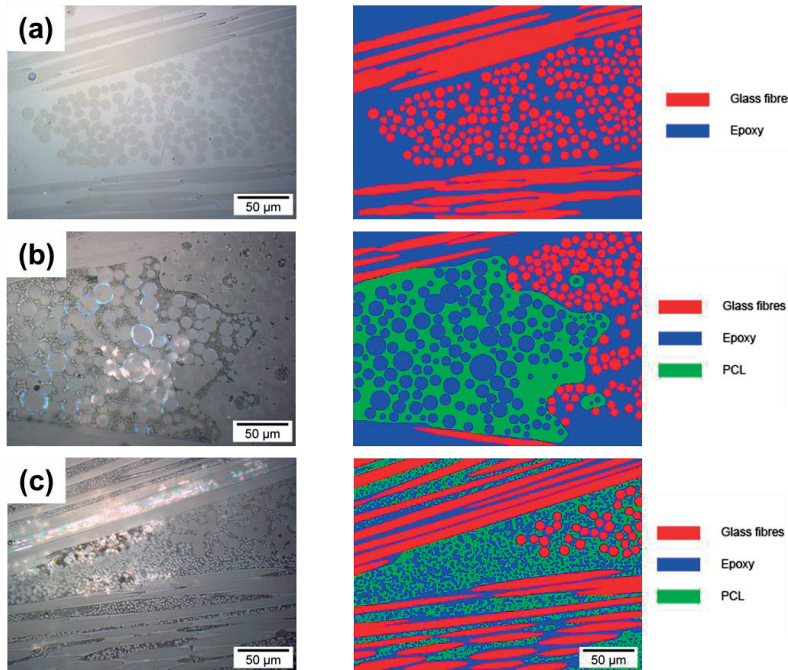


Figure 5.2: Transverse cut of the three assessed systems: (a) *Plain*; (b) *PCL(25)*; (c) *PCL(37)*. A schematic of the structure is drawn on the right of each image.

5.1.2 Thermomechanical properties

Figure 5.3 shows DSC heating scans for the different specimens after cure. Two characteristic transitions were highlighted: (i) the endothermic peak at about 54 °C corresponded to the PCL melting (not present for the *Plain* specimen); (ii) the small enthalpy peak at about 197 °C was associated with the epoxy glass transition. These transition temperatures were similar to those of the pure PCL and pure epoxy (see section 4.2), indicating a high degree of phase purity. Notice also that the lack of exothermic reaction indicated that the obtained composites were in a fully cured state. The presence of fibres therefore did not induce changes in the required curing schedules of the matrix blends determined in section 4.2.

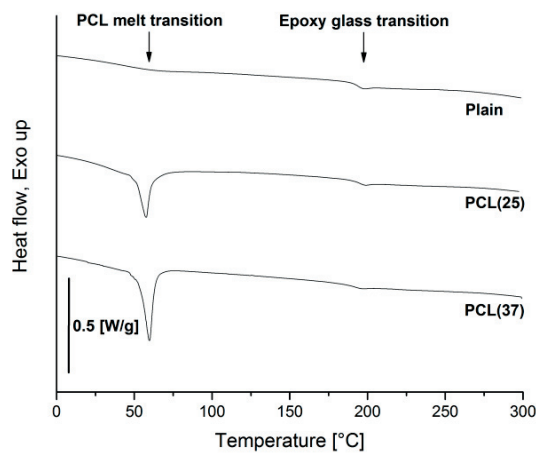


Figure 5.3: DSC heating scans for the different specimens after cure.

Traces of the bending storage modulus, E' , and the loss tangent, $\tan \delta$, as determined by DMA experiments, are shown as a function of temperature in Figure 5.4. Again, the characteristic transition temperatures (PCL glass transition and melt as well as epoxy glass transition) are invariant for the three assessed systems, indicating high degree of phase purity. More interesting are the obtained properties at room temperature and at the targeted healing temperature, 150 °C. At room temperature, a decrease in E' from 6.6 to close to 6.3 GPa was observed as the PCL content varied from 0 to 25 vol% in the matrix, indicating a nearly constant modulus between these two compositions thanks to the interconnectivity of the epoxy particles, as previously observed in neat resins (see section 4.2). The $\tan \delta$ curves indicate in the same composition range that adding PCL to the matrix improves the damping properties of the system. Increasing further the PCL content (to 37 vol% in the matrix) led however to a higher modulus decrease, down to 4.6 GPa, because at higher PCL content, the particle size and interconnectivity are lowered as already stated in section 4.2. At 150 °C, E' decreased from about 5.5 GPa for the *Plain* system to about 3.7 GPa for *PCL(25)* and about 1.5 GPa for *PCL(37)*, reflecting the molten state of the PCL. However, at that temperature, the composite specimens behaved globally as stiff elastic solids with no significant dimensional instabilities, indicating that the contacts between the epoxy particles were sufficient to maintain structural integrity, even at the healing temperature. DMA measurements are however not fully sufficient to quantify bending stiffness and strength of the tested specimens. Three point bending tests were thus performed on *Plain* and *PCL(25)* specimens at room temperature only. These tests revealed bending moduli of 15.99 ± 1.24 GPa and 15.30 ± 0.63 GPa for respectively *Plain* and *PCL(25)*, and flexural strengths of respectively 389.68 ± 31.75 MPa and 349.89 ± 26.74 MPa. At room temperature, stiffness and strength for *PCL(25)* were thus almost similar to *Plain*, again demonstrating the preservation of structural integrity while using such modified composites, but also the dominance of fibres load holding.

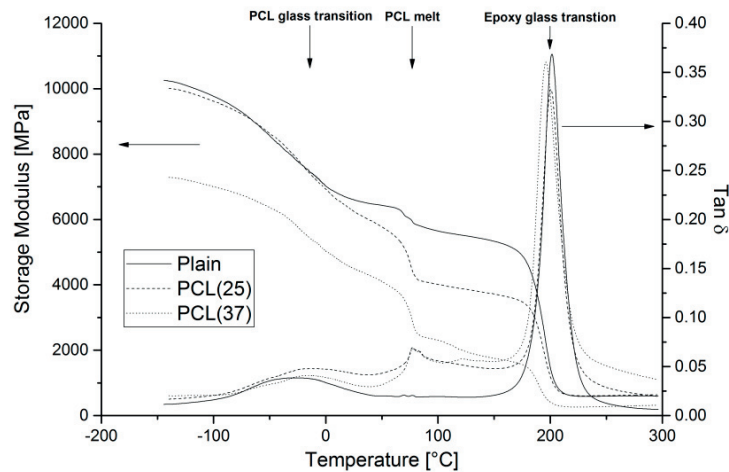


Figure 5.4: E' and $\tan \delta$ as a function of temperature for the three assessed specimens: *Plain*, *PCL(25)* and *PCL(37)*.

5.1.3 Interfacial Shear Strength determination

Interfacial shear strength (IFSS) between fibres and matrix of the assessed composites (Figure 5.5) has been determined by means of nanoindentation tests (see section 3.3.3.2 for experimental procedures and details of calculations). *Plain* specimens exhibited a mean IFSS value of 95 MPa, well above the shear strength of the epoxy matrix, but consistent with values reported in literature for similar systems [95]–[98]. While adding PCL to the matrix, the IFSS value decreased to 81 MPa and 76 MPa for *PCL(25)* and *PCL(37)* respectively, indicating lower interfacial properties when PCL was added to the system. As stated in section 5.1.1, the continuous PCL phase in the two-phase morphology did not cover the fibres due to preferential wetting of the epoxy phase on glass fibres. Therefore, interfacial shear strength in blend systems was measured between a fibre and its surrounding epoxy phase; the decrease in IFSS values when the PCL content increased originated from the surrounding softer environment taken

into account by the n parameter of the data reduction scheme (see Eqs. (2.12) and (2.13)). n values being in the present case for *Plain*, *PCL(25)* and *PCL(37)* compositions respectively of 107, 96 and 88 mm^{-1} , the previous statement is confirmed from Eq. (2.10) and the direct proportionality between E_m and n . The results show relatively large standard deviations, even though the data reduction procedure over more than 50 specimens reduces this scatter [96], for two main reasons: (i) the variation in fibre diameters ranged from 8 to 14 μm for the present case; (ii) the precision in centring the indenter with each fibre (if the indentation mark was not enough centred (on visual assessment) or if it ran over the fibre diameter, the test was discarded). Notice also that even if the surrounding fibre environment is taken into account in the model, care was taken in testing fibres in a nearly close packed arrangement, as shown in Figure 3.6 (b), to avoid further data scatter.

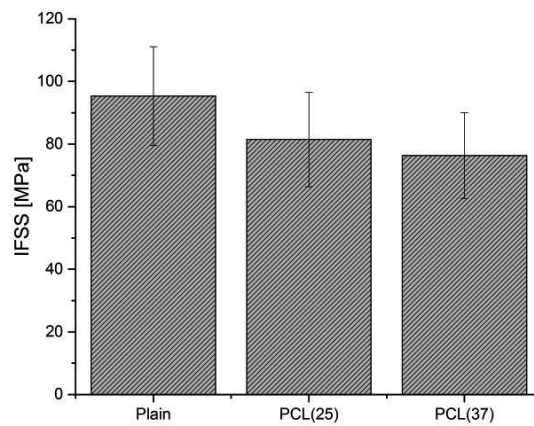


Figure 5.5: Interfacial shear strength for the three assessed systems.

5.1.4 Mode I Double Cantilever Beam Testing

5.1.4.1 Fracture properties in the virgin state

Figure 5.6 shows interlaminar fracture toughness mean values for the three types of composites. Even though a $\pm 45^\circ$ interface was tested, the toughness value obtained for the *Plain* system (1135 J/m^2) was similar to what was measured in previous studies [216]. As compared to this *Plain* system, a decrease of 40% and 58% in interlaminar fracture toughness was observed for respectively *PCL(25)* and *PCL(37)* systems. This behaviour was directly related to (i) the decrease in IFSS values when increasing the PCL content as the matrix gets more ductile and interfacial debonding between the fibres and the matrix is made easier (see section 5.1.4.3) and (ii) the intrinsic fracture toughness behaviour of the blends where the PCL, which exists as a confined layer between epoxy particles, governs the system's strength, as determined in section 4.2. Notice that the dashed line drawn between *Plain* and *PCL(25)* system values may not represent the expected behaviour, because at low PCL contents, the morphology consists of PCL particles embedded into an epoxy matrix, which could probably locally increase fracture toughness [55], [243].

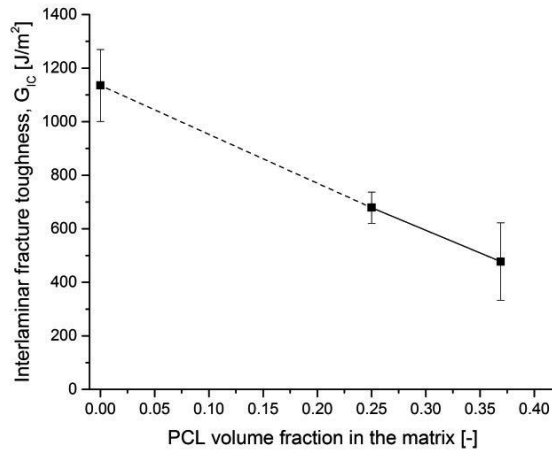


Figure 5.6: Interlaminar fracture toughness, G_{IC} , as a function of the PCL volume fraction in the matrix.

5.1.4.2 Healing efficiency assessment

Multiple healing efficiencies were first determined in terms of stiffness, based on Eq. (3.4) and are shown for *PCL(25)* and *PCL(37)* in Figure 5.7 for three healing cycles. Efficiencies for *Plain* specimens are not depicted as their value was null, as expected. Notice first that the scatter was relatively high due to the difficulty in crack faces alignment while unloading the specimen. Both *PCL(25)* and *PCL(37)* exhibited high potential for recovery in stiffness after thermal healing. After one healing cycle, *PCL(25)* recovered its stiffness by 82% whereas full recovery was observed for *PCL(37)*. Recovery in properties was higher for higher PCL contents, due to the higher expansion capability as more volume of PCL was present. Stiffness recovery was further improved over multiple testing and healing cycles, again due to the expansion capability of the PCL. Efficiencies above 100% could be observed because a propagating crack broke the interconnected particulate morphology which created a new and tougher PCL interface after healing (see section 5.1.4.3 for evidence of this behaviour on the fracture surface observations).

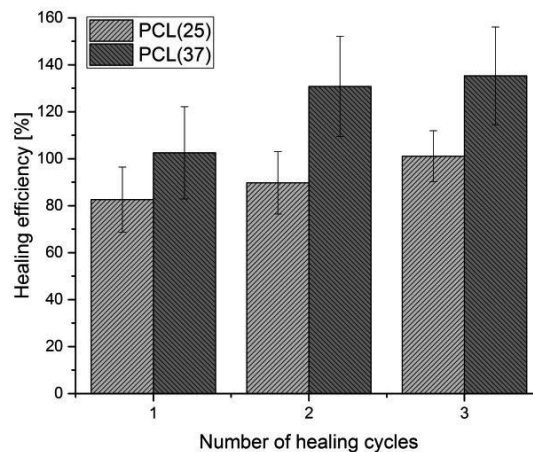


Figure 5.7: Multiple healing assessment in terms of stiffness based calculation for *PCL(25)* and *PCL(37)*.

Multiple healing efficiencies were then determined in terms of interlaminar fracture toughness, based on Eq. (3.5) and are shown for *PCL(25)* and *PCL(37)* in Figure 5.8 for three healing cycles. Efficiencies for *Plain* specimens are not

depicted as their value was null, as expected. Both *PCL(25)* and *PCL(37)* exhibited moderate recovery in toughness after thermal healing. Notice first that the scatter was relatively high due to the difficulties in (i) crack faces alignment while unloading the specimen and (ii) properly determining the advancement of the crack in the healed state (the thermoplastic often did not wet the entire specimen surface). Similar behaviour as for stiffness based calculations could be observed even if the values did not reach 100%. The co-continuous epoxy-PCL morphology was broken during the virgin cycle, which created an interface of only PCL during healing. This PCL interface provided the same initial stiffness but not the same strength and therefore toughness, as concluded in section 4.2 for neat blends. Incomplete recovery in interlaminar fracture toughness could be further understood by observing the energy release rate during crack propagation (i.e. R-curve behaviour) of the different systems for the first damage cycle as well as after thermal mending at 150 °C for 30 minutes (Figure 5.9 (a)). Energy release rate of the pristine specimens (in black in Figure 5.9 (a)) showed conventional behaviour in FRPs with a rising R-curve due to fibre bridging [66] (the rising R-curve was more pronounced for the *Plain* system due to its brittle behaviour as compared to FRPs with epoxy-PCL blends). For FRPs with epoxy-PCL blends, the steady state interlaminar fracture toughness appeared at lower levels than *Plain* specimens as expected from Figure 5.6. When testing the specimens in the healed state (i.e. after thermal mending at 150 °C for 30 minutes), the R-curves showed a two-step behaviour with two successive values of steady state interlaminar fracture toughness, which was not observed in conventional FRPs [67]. A first plateau was observed at low interlaminar fracture toughness values (50 J/m²) whereas a second plateau was found at around 250 J/m² until reaching again the interlaminar fracture toughness of the virgin specimen if the crack was further propagated. This unconventional behaviour was analysed by comparing the R-curve of the healed specimens with the specimen crack thickness during thermal healing (i.e. with the crack faces imposed to be in contact at the location of the loading blocks) (see Figure 5.9 (b) for a *PCL(25)* specimen). The crack thickness has been measured after the first DCB test when the specimen was ready for thermal mending, so it represents the gap to heal within the damaged specimen. From the study of Rodgers [285], it was possible to measure the PCL expansion capacity at the healing temperature (14% at 150 °C), and therefore determine the maximum thickness the PCL could fill considering the geometry and PCL content. For the present case, the PCL had the ability to fill a crack of 36 µm (for a *PCL(37)* specimen, this value was 53 µm), which corresponded to the value where the second steady state interlaminar fracture toughness was observed. This second plateau was therefore representative of the toughness after healing, and lead to the conclusion that incomplete crack filling occurred in the present case. Incomplete crack filling thus decreased the obtained steady state interlaminar fracture toughness. Also, the second steady state interlaminar fracture toughness step was more extensive for the *PCL(37)* as the PCL could expand more and better fill the crack gap. Finally, this second plateau appeared at a similar value for both systems, representative of the properties of the newly formed interface.

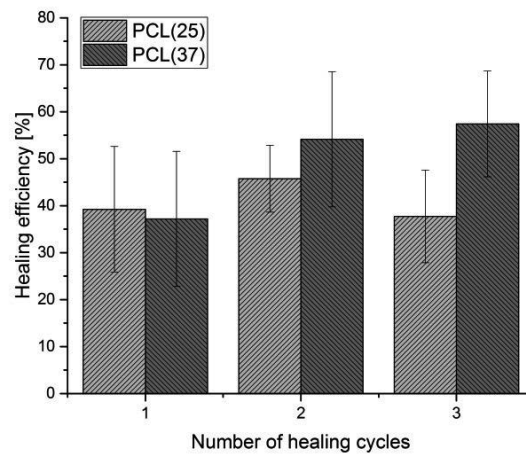


Figure 5.8: Multiple healing assessment in terms of interlaminar fracture toughness based calculation for *PCL(25)* and *PCL(37)*.

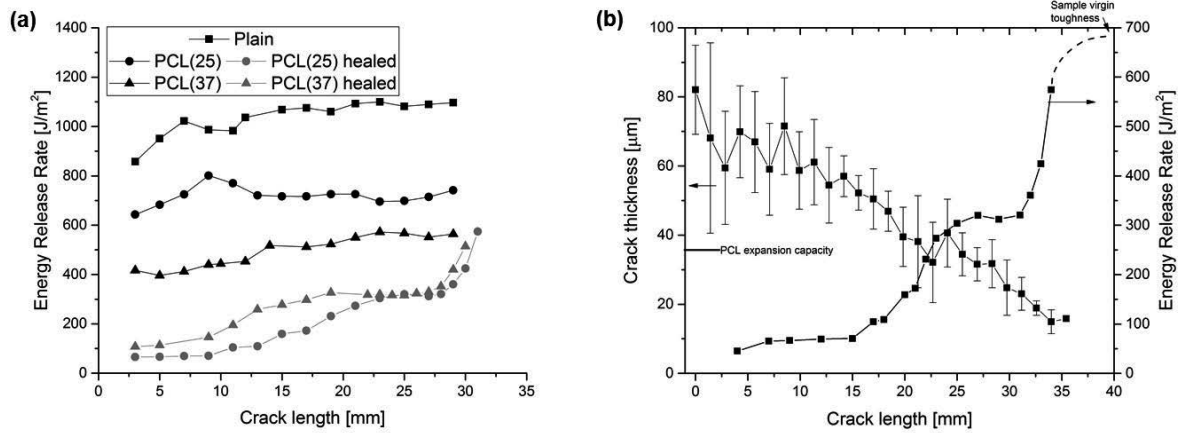


Figure 5.9: (a) R-curve behaviour for unmodified (*Plain*) and modified (*PCL(25)* and *PCL(37)*) FRPs, as well as modified FRPs after thermal mending at 150 °C for 30 minutes (*PCL(25) healed* and *PCL(37) healed*); (b) Crack thickness as a function of the crack length during healing of a *PCL(25)* specimen, superimposed with its R-curve behaviour in the healed state.

5.1.4.3 Fracture surface considerations

Fracture surface analysis was performed on the modified composites in the damaged state after 1, 2 and 4 testing cycles. The fracture surface for a *PCL(25)* specimen (Figure 5.10 (a)) after the first fracture testing cycle (*virgin*) indicated that failure has been dominated by interfacial debonding between the fibres and the matrix. This mechanism of delamination between fibre bundles and their surrounding matrix has been observed previously in many cases [65], [216], [301] for woven composites. Even though the matrix consisted of epoxy particles surrounded by a PCL matrix, there was evidence of epoxy interfacial debonding in addition to PCL cohesive failure (indicated by the arrows in Figure 5.10 (a)). As demonstrated in section 5.1.1, glass fibres were covered by a thin layer of epoxy due to preferential wetting during microstructural development, thus this interface ruptured during crack opening. Figure 5.10 (b) depicts the fracture surface of a *PCL(25)* specimen, after one healing cycle. Observations were performed in the resin rich regions, characterised by the presence of the phase-separated particulate morphology (at the intersection of fibre bundles). Whereas interfacial debonding could be observed (in the central region of Figure 5.10 (b)), as in the case after a *virgin* cycle (Figure 5.10 (a)), the surface shows evidence of PCL bleeding with partial coverage, thus explaining healing of the mechanical properties discussed in section 5.1.4.2. In addition to this central interfacial debonding, three regions, explaining the healing process, could be highlighted (shown with arrows in Figure 5.10 (b)): (i) *PCL bleeding* showed glass fibres recovered by PCL, (ii) *Trace of virgin fracture* showed epoxy interfacial debonding created during the *virgin* cycle but now covered by PCL that bled during healing, (iii) *PCL cohesive failure* showed evidence of PCL fracture after having healed the surface. These three regions thus highlighted evidence of PCL bleeding and surface coverage, however, as PCL cohesive failure could be observed only partially on the surface, PCL crack bridging could not proceed on the entire fracture surface (due to the limited PCL expansion capacity), explaining the partial toughness recovery observed in section 5.1.4.2. While in the first fracture testing cycle (Figure 5.10 (a)) epoxy interfacial debonding was dominant, PCL cohesive failure was dominant after the second fracture testing cycle (Figure 5.10 (b)) which could explain efficiencies higher than 100% observed in the stiffness based calculation as the crack has been propagated on an interface consisting now only of PCL. Figure 5.10 (c) finally shows the fracture surface of *PCL(37)* after three healing cycles. The higher PCL content for this specimen, but also the three performed healing cycles, led to higher PCL coverage on the surface (this evidence is provided by the arrows on the figure showing PCL bleeding as well as large areas of PCL cohesive failure) as well as to smaller particles as compared to Figure 5.10 (b). In addition, the dispersion in epoxy particle sizes due to the influence of fibres on the phase separation process could be observed, as for optical microscopy shown in Figure 5.2. The higher coverage in PCL for this case also explained the higher efficiencies in terms of stiffness as well as toughness based calculations.

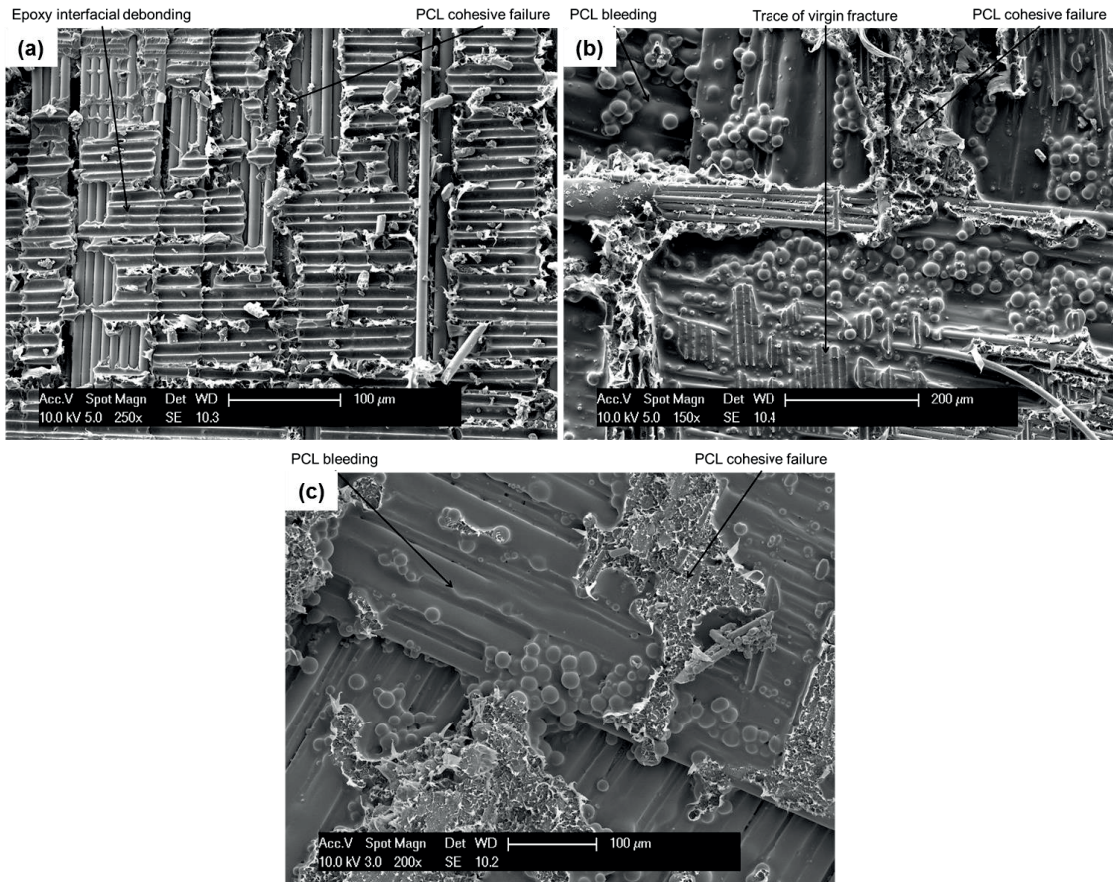


Figure 5.10: SEM image of a DCB fracture surface for (a) *PCL(25)* specimen after a virgin cycle; (b) *PCL(25)* after one healing cycle and (c) *PCL(37)* after three healing cycles.

5.1.5 Conclusion

Glass fibre-reinforced epoxy-PCL ($M_n \approx 45,000$ g/mol) composites with fibre volume fractions around 50 vol% were successfully processed through Vacuum Assisted Resin Infusion Moulding at elevated temperature. Due to preferential wetting of the epoxy on the glass fibres, these were recovered by a small layer of epoxy, and not by the expected PCL phase. While phase separation and development of the epoxy particulate morphology could happen in the resin rich regions of the reinforcement, it was completely prevented within the fibre tows due to space constraints when epoxy particle diameters were higher than the mean distance between two fibres within tows. These space constraints were observed as less critical for higher PCL contents as diameters of the epoxy particles were smaller, which allowed particles to be inserted within fibre tows. Even though each individual fibre was surrounded by a thin epoxy layer, interfacial shear strength decreased with the increase in PCL content because of the surrounding softer environment in the phase-separated epoxy-PCL matrices.

The presence of PCL in the composites did not lead to a significant difference in room-temperature storage modulus, flexural modulus and strength, as compared to *Plain* systems, whereas Mode I DCB tests revealed a large decrease in interlaminar toughness when PCL was added to the system. This decrease was attributed to the decrease in interfacial shear strength values and by the intrinsic fracture toughness of the blends where the PCL is present as a confined layer in between the epoxy particles, as previously determined in Chapter 4. Mode I DCB testing further allowed the determination of the healing efficiencies in terms of stiffness and toughness over several cycles. For both composites modified by PCL, higher efficiencies were observed for higher PCL contents as well as for a higher number of healing cycles due to the higher PCL coverage (thanks to its ability to bleed and expand within the crack) on the specimens

fracture surface during healing. In terms of toughness, efficiencies obtained were lower due to incomplete crack filling by the PCL phase affecting the R-curve behaviour.

Even though phase separation was affected by the presence of fibres in composites, it can be concluded from the present findings that 25 vol% of PCL within the matrix provides suitable healing efficiencies without any deterioration in modulus or strength of the composite. However, toughness is considerably decreased by the presence of PCL due to its lower intrinsic strength. This model system thus demonstrates the feasibility and interest of processing self-healing composites based on this concept. Providing that its strength competes with reference epoxy systems, this system is promising for healing damage events such as low energy impacts where matrix cracks dominate.

5.2 Damage recovery after impact in E-glass reinforced epoxy-PCL blends

(Adapted from ref. [302]: A. Cohades and V. Michaud, "Damage recovery after impact in E-glass reinforced Poly(ϵ -caprolactone)/epoxy blends," *Compos. Struct.*, vol. 180, pp. 439–447, 2017)

In the present section, healing of impact damage in FRPs with phase-separated epoxy-PCL blends as a matrix and woven E-glass fibres as reinforcement is investigated. Low velocity impact damage is of main concern in aircrafts where damage events can be attributed to operational or maintenance activities and tends to decrease strength, durability and stability of the structure [1]. For example, in graphite-epoxy systems, barely visible impact damage (produced by low velocity impacts) can lead to tensile and compressive strength losses up to respectively 50% and 60% [303]. These impact damage events are most often created by dropped tools, which led in the aircraft industry to the formulation of a damage resistance requirement for primary laminate structure of 5.4 J impact energy [303]. Considering the typical weight of a hammer (500 g) falling from 1 m height, the damage requirement is respected, however stresses are generated and higher impact energies are easily reached through such events; there is thus a high interest in healing autonomously impact damage events created by low velocity impact energies (up to 20 J). To assess such prospect, FRPs were manufactured with a 25 vol% PCL blend (as well as with pure epoxy for comparison) through VARIM at high temperature. Different damage severities have been imparted to the specimens by low-velocity impact tests from 8.5 up to 34 J (to meet the requirements stated above), and the healing capacity, after a thermal mending cycle at 150 °C for 30 minutes, has been measured with three complementary methods: (i) recovery of impact damage area by means of C-scans, (ii) theoretical crack thickness closure by optical microscopy observations and (iii) recovery in compressive residual strength after an impact event. Notice that a slightly different PCL ($M_n \approx 49,000$ g/mol) was used for convenience due to the high amount of specimens needed for compression after impact tests, but intrinsic properties (morphology, thermomechanical, strength and fracture toughness) of these blends were measured and found to be similar to epoxy-PCL blends studied in section 4.2.

Two types of matrix have been prepared: (i) pure epoxy resin, (ii) epoxy-PCL blends containing 25 vol% of PCL. These blends were then used for composite production. Composites made of pure epoxy are named "*Plain*" in the following and contained a fibre volume fraction of $45.4 \pm 0.7\%$ whereas composites made of epoxy-PCL blends are named "*PCL(25)*" in the following and contained a fibre volume fraction of $48.0 \pm 0.7\%$. For preparation of the blends as well as characterisation methods leading to the results presented hereafter, the reader is referred to Chapter 3.

5.2.1 Impact testing

The impact force as well as impact energy levels during tests are presented in Figure 5.11 for the *Plain* and *PCL(25)* systems. As expected, as the impact energy increased, the peak load as well as the energy during test increased. The load increased for both cases with some oscillations until the peak load before a smooth decrease until reaching zero. This behaviour, typical of conventional FRPs [1], [72], [304]–[306] was attributed to growing ply delamination in the specimen during impactor penetration while during rebound no further delamination and thus no peak in the load curve was present. The first peak in the load response is representative of the first delamination within the specimen (i.e. Hertzian failure [304], [307]) and appeared earlier (at lower load) for the *PCL(25)* system. Indeed, resistance to crack propagation (i.e. toughness) was lower for the *PCL(25)* composite as compared to the *Plain* case (see section 5.1). This lower resistance to crack propagation and thus delamination was further confirmed by the amount of peaks observed on the force-time curves for both cases and by the measurement of the damage area (see section 5.2.2). In addition, this first load drop is related to matrix strength [308], again consistent with the fact that the matrix in *PCL(25)* specimens was of lower strength, as demonstrated in section 4.2. While Hertzian failure was more difficult to detect in *Plain* specimens, *PCL(25)* ones demonstrated that the position of the first load drop was constant for varying impact energies, as reported in earlier studies [309]. Still focusing on the load curve, the peak load appeared later for the *PCL(25)* as compared to the *Plain* specimens, indicating that more damage was accumulated within the *PCL(25)* system, again in accordance with the composite intrinsic toughness and its lower resistance to delamination. The level of impact force at which this peak load appeared was different for the two assessed systems and did not follow the

same trend between the three impact energies used. This behaviour, observed previously elsewhere [74], [307], indicated a difference in strain-rate sensitivity between the two matrices.

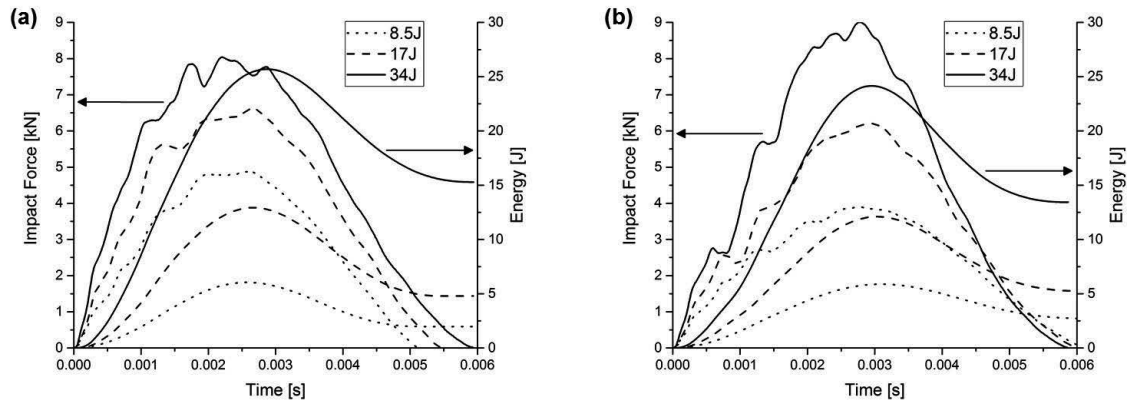


Figure 5.11: Impact force and energy as a function of time for three different impact energies, for (a) *Plain* system and (b) *PCL(25)* system.

Impact energy during test was calculated from the force-time curves following ASTM standard D7136 [72] and is shown in Figure 5.11 (right axis) for the two assessed systems. Energy increased up to a peak value before being partly restituted to the impactor and reaching a final value which can be considered as the amount of dissipated energy by the impactor within the impacted specimen. However, this last quantity does not consider the possibility for other energy consumption mechanisms to take place, including friction with the linear guide during falling, deformation of the grips, energy transfer to the impactor or the base machine [305]. Energy dissipation was therefore quantified by measuring the inbound and rebound velocities of the impactor with the help of light gates placed right above the specimens. The energy dissipated during the entire impact process is represented in Figure 5.12 for the three different energies and appeared to be invariant between the two assessed systems. Indeed, while the delamination area between two specimens made of two different matrices can be different because of their intrinsic delamination resistance, the energy absorption mechanism during impact is mainly related to the capacity of the fibres to absorb energy [308]. For two specimens having different matrices, but similar lay-up, reinforcement architecture and number of plies, the magnitude of energy dissipation will thus be the same [310]. It has been demonstrated that fibre volume fraction has an influence on the impact response of composites [311], however, it is important to remember that in a concern to create the same damage amount in each specimen before the healing process, the impact energies were adjusted to take into account variations in the thickness of individual specimens (Eq. (3.6)) and therefore the variation in impact properties resulting from a variation in fibre volume fraction should have been avoided.

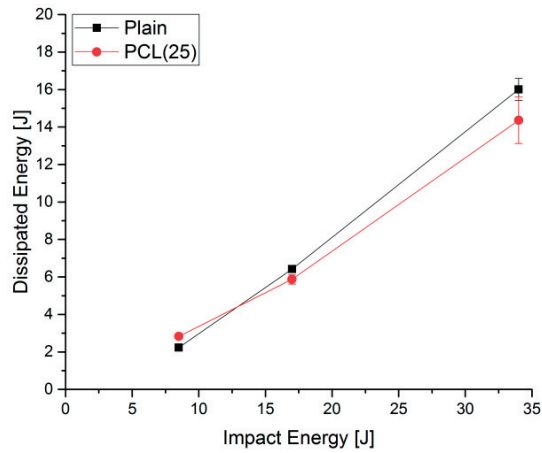


Figure 5.12: Dissipated energy during impact as a function of the impact energy, for *Plain* as well as *PCL(25)* systems.

Figure 5.13 presents the impact force as a function of the composite deflection response (integrated from the force-time histories) for the two assessed systems and the three impact energies. Oscillations, as in Figure 5.11, were characteristic of damage initiation and propagation within the specimens and were found to be lower for lower impact energy levels. This plot is of interest as its slope indicates the stiffness of the specimen, which by evidence is the same within each specimen for the three different energies. However, stiffness differs between *Plain* and *PCL(25)*, indicating that it was different for the two assessed systems, as expected from sections 4.2 and 5.1. Quantification of stiffness was however not performed here as many assumptions, which might bias the results, were performed during the curve determination [305]: neglecting friction between the impactor and the specimen, the damping effect in the structure, the gravity during the impact event, or assuming the impactor as a rigid body.

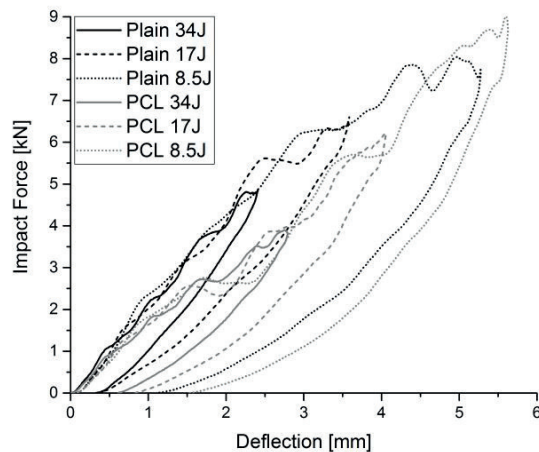


Figure 5.13: Impact force as a function of the deflection response for *Plain* and *PCL(25)* systems as well as three impact energies: 34, 17 and 8.5 J.

In addition to the analysis of the force-time histories during the impact event, the observation of the damage shape was performed through optical images (Figure 5.14). The impact showed a typical nut shape, both for *Plain* and *PCL(25)* systems, in accordance with the stacking sequence used [312]. The damage area was higher for *PCL(25)*

because of its lower resistance to crack propagation, as discussed before. Also, the damage was larger on the back face of the laminate, a combined effect between top and bottom surface where the impact event induced respectively compressive and tensile stresses, as already discussed elsewhere [313]. As the optical images shown in Figure 5.14 display translucent specimens, the true observed damage area was not influenced by larger back face damage. These images were taken before and after a thermal mending cycle at 150 °C for 30 minutes and showed the capacity of the modified composites (*PCL(25)* specimens) to heal impact induced damage. However, as quantification of the damage extent through these optical images was not conclusive due to the inability to exactly determine matrix microcracking (i.e. the exact surrounding of the damage), C-scans were performed.

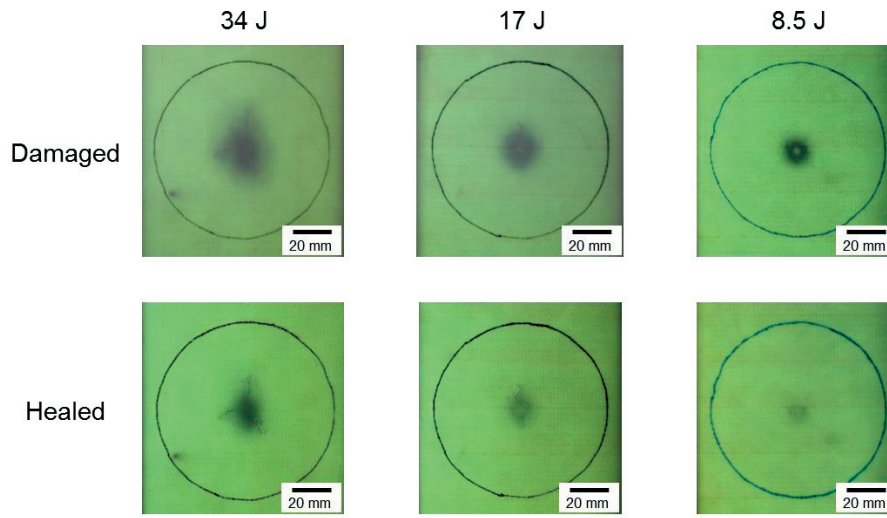


Figure 5.14: Front face optical image of *PCL(25)* specimens after impact (*Damaged*) and after a thermal mending cycle of 30 minutes at 150 °C (*Healed*) for three impact energies: 34, 17 and 8.5 J.

5.2.2 C-scans

Figure 5.15 depicts the impact damage area as measured by C-scans on *Plain* and *PCL(25)* specimens impacted at the three different energies. As expected from the impact behaviour (see Figure 5.11), the damage extent, linked to the system intrinsic toughness and strength, was higher in *PCL(25)* specimens as compared to *Plain* ones. However, the progression in damage area for the two systems did not follow the same trend: at low impact energies, the slope of the curve was nearly the same for the two systems while it was different at higher energies. During the impact event, many different modes of failures are found in FRPs, including [74], [314]: matrix damage, delamination and fibre damage. These three modes appear successively during the impact event and when increasing the impact energy. While at low energies, matrix cracking occurs due to compression, tension or shear, delamination is produced by interlaminar stresses. These two modes depend on the material's toughness and do not give rise to the same damage progression, which explained the damage area evolution observed in Figure 5.15.

C-scans of specimens impacted at the three energies were performed before and after a thermal mending cycle at 150 °C for 30 minutes. This procedure, realised on at least three specimens per condition, allowed determining the capacity for damage area recovery of *PCL(25)* specimens following Eq. (3.7). Examples of C-scans before (*Damaged*) and after the healing cycle (*Healed*) are depicted in Figure 5.16 for the three impact energies, colours represent the sound intensity and damage was defined when 80% of the sound intensity was lost. Even though the damage area could not be fully recovered, the efficiency of the thermal mending cycle increased as the impact energy decreased. Indeed, for impact energies of 34, 17 and 8.5 J, the healing efficiency in terms of damage area recovery was respectively of $39.9 \pm 0.6\%$, $55.4 \pm 2.7\%$ and $94.8 \pm 2.7\%$. At high impact energy, two mechanisms were responsible for the incomplete recovery of damage: (i) fibre deformation and damage and (ii) formation of large cracks. The repair

system being efficient only in the matrix, fibre deformation and damage will be permanent within such a structure after impact damage at high energy, showing the limitation of this healing mechanism. However, at low energies, when the impact event induced only matrix microcracking, incomplete healing was also observed. The expansion capacity of PCL (14% at 150 °C) in such a system varies between 35 and 53 microns (see section 5.2.3 for calculations), therefore the impact event should have induced some thicker cracks which could not be healed. At low damage extent, the echo signal from the C-scan was reflected and gave information on the transverse crack thickness. In a large damage however, the echo signal was blocked and could not provide information on the crack thickness distribution within the specimen. Transverse cuts of the damaged specimens were thus performed (see section 5.2.3) to provide understanding of the healing mechanism of such system after impact damage.

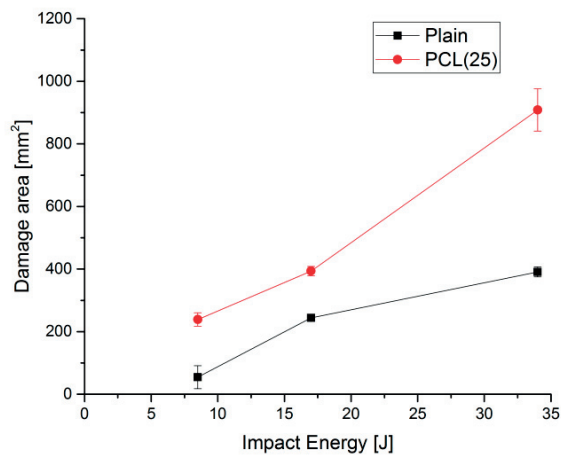


Figure 5.15: Damage area measured by C-scan analysis as a function of the impact energy, for *Plain* as well as *PCL(25)* systems.

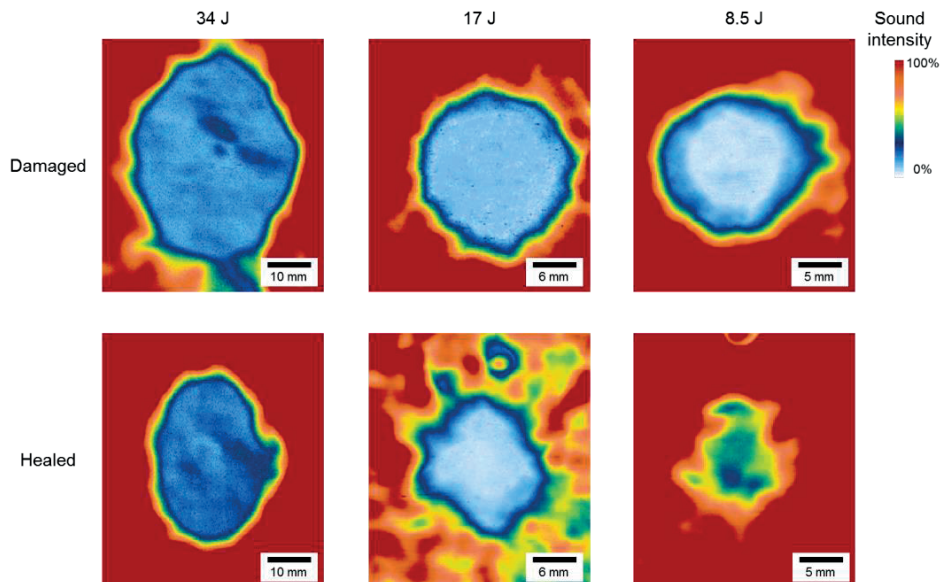


Figure 5.16: C-scan images of *PCL(25)* specimens after impact (*Damaged*) and after a thermal mending cycle of 30 minutes at 150 °C (*Healed*) for three impact energies: 34, 17 and 8.5 J.

5.2.3 Morphological characterisation

Figure 5.17 shows reconstructed cross-sectional area taken from 200 optical microscopy images, for the three impact energies assessed in *PCL(25)* specimens in the damaged state (i.e. unhealed). As for impact data and C-scans, when the impact energy decreased, the amount of damage (i.e. cracks) decreased. This mapping also revealed the type of damage mechanism (matrix damage, delamination and fibre damage [74], [314]) occurring at each impact energy: (i) at 8.5 J, only matrix microcracks could be observed, (ii) at 17 J, some delamination was also present, (iii) at 34 J, higher amount of delamination was present and fibre damage appeared. 34 J energy led to a pine tree pattern, typical in FRPs [312]. Notice also that the infusion quality of the composites could be confirmed within the undamaged zones, showing no porosities, as expected from section 5.1.

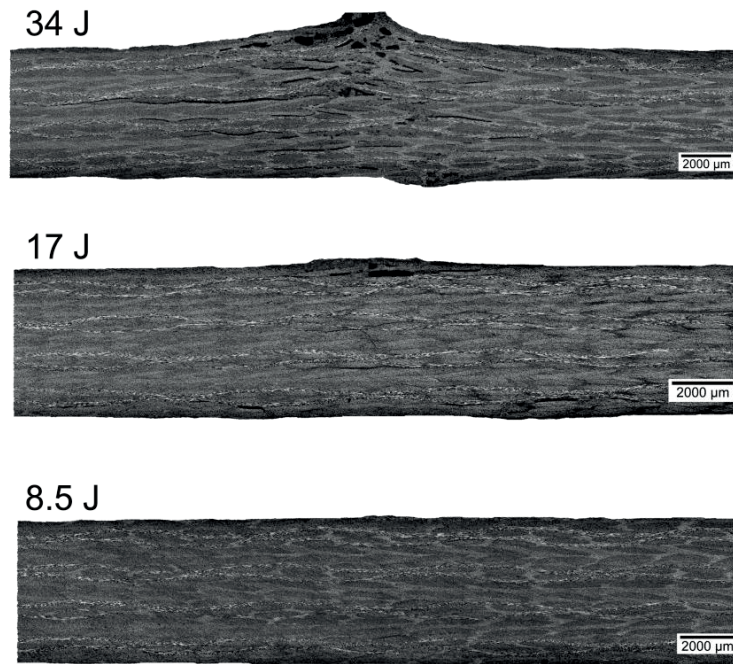


Figure 5.17: Transverse cut optical microscopy mapping of *PCL(25)* system impacted at energies of 8.5, 17 and 34 J.

From the maps in Figure 5.17, the crack thickness distribution due to the impact event was measured for the three impact energies. Thickness distribution over each specimen is depicted in Figure 5.18 and fitted with a standard Gaussian procedure. As expected from optical observations, the amount and size of cracks increased when the impact energy increased. Knowing the amount and size of cracks further allowed determining a theoretical healing efficiency from the theoretical PCL volume expansion within each specimen. Indeed, from the study of Rodgers [285], PCL has a volume expansion capacity of 14% at 150 °C (i.e. the healing temperature). In addition, from C-scans data, it is known that the damage area was on average of 2.39, 3.94 and 9.08 cm² for impact energies of respectively 8.5, 17 and 34 J. Assuming that these damage areas were present on the entire thickness of the laminate (i.e. 15 interfaces) and knowing specimen dimensions, the PCL expansion capacity over the specimen free surfaces, and thus its crack filling capacity for impacts of 8.5, 17 and 34 J could be determined and was respectively of 53, 47 and 35 µm. As the energy of impact increased, the PCL filling capacity was therefore theoretically decreased because of a higher amount of free surfaces for the PCL to expand and thus less through thickness expansion capacity. Using the crack thickness distribution of Figure 5.18, the PCL could thus fill 99.1%, 69.9% and 32.3% of the cracks created by impact events at energies respectively of 8.5, 17 and 34 J. These data correlated well with damage area recoveries observed by C-scans.

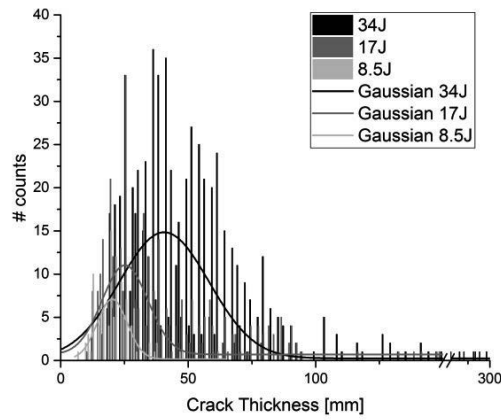


Figure 5.18: Crack thickness distribution corresponding to the optical microscopy mapping of Figure 5.17.

Calculating the crack filling capacity of PCL for different specimen geometries (DCB in section 5.1 and impact here) and for different damage amounts (i.e. with varying specimen free surfaces) raised the question of how large should the heated volume be for the PCL to bleed. It is known that PCL expands by 14% at 150 °C [285], but the corresponding expansion thickness of a given element varies with (i) the volume of the heated element and (ii) the quantity of free surfaces available for the PCL to bleed. The PCL expansion thickness capacity on the free surfaces of a given heated element is shown as a function of its area to volume ratio in Figure 5.19. Calculations were performed for epoxy-PCL(25vol%) blends as a bulk resin or when inserted into a composite with 50% fibre volume fraction. The area to volume ratio in Figure 5.19 is also linked to the volume of a cubic element with such ratio. As expected, the PCL expansion thickness decreases when the area to volume ratio increases, which directly links to the increasing volume of a cubic element. Also, this thickness is larger for the *Pure resin* case as compared to the *Composite* case at equal volume, due, obviously, to the presence of fibres. For DCB and impact specimens studied in the present work, the area to volume ratio laid between 5 and 9, corresponding to respectively around 15 and 25 μm expansion thickness, half of the crack filling capacity determined previously as expansion on only one surface was considered here. The area to volume ratio needs thus to be considered while designing an FRP part as it can be a limiting factor in the PCL expansion and thus crack filling/healing capacity.

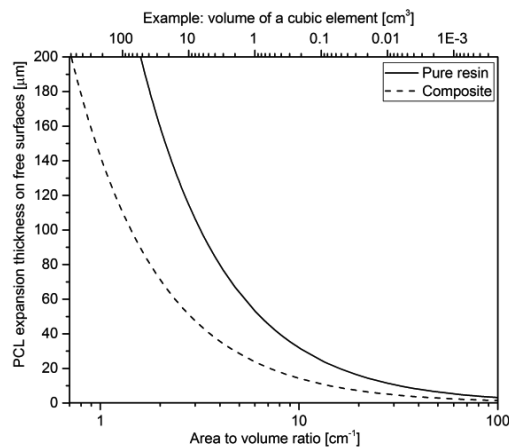


Figure 5.19: PCL expansion thickness on the free surfaces of a heated element with varying area to volume ratio for epoxy-PCL(25) blends as *Pure resin* or in the *Composite* (with $V_f=50\%$). The top scale links the area to volume ratio to the example of a cubic element with varying volume.

5.2.4 Compression After Impact (CAI)

CAI strength has been recognized since many years as the property suffering the largest from impact damage as compared to undamaged materials [312], quantification of damage recovery through this technique is thus of great interest. Figure 5.20 depicts the compressive residual strength of *Plain*, *PCL(25)* specimens in the damaged state (i.e. after the impact event) and *PCL(25)* specimens in the healed state (i.e. after the impact event and a healing cycle at 150 °C during 30 minutes) as a function of the impact energy level. Compression properties of the specimens in the undamaged state (i.e. at 0 J impact energy) were also tested as reference. Each condition was tested with at least three specimens. For both systems, as the impact energy increased, the compressive residual strength decreased due to the higher amount of damage provided during the impact event. *PCL(25)* specimens exhibited for each impact energy, a lower compressive residual strength as compared to *Plain* ones. CAI strength is related to two phenomena [315]: buckling of the impact damage area and crack propagation next to the point of impact before fibre and specimen failure. Thermoplastic based composites demonstrated elsewhere [316] higher CAI strength as compared to thermoset based composites, the higher toughness (i.e. resistance to crack propagation) of thermoplastic composites being the driving force for this improved behaviour. As demonstrated in sections 4.2 and 5.1, resistance to crack propagation in epoxy-PCL matrices (neat as well as when integrated to FRPs) was lower as compared to epoxy ones because the PCL stayed as a confined layer in between the epoxy particles within the structure which prevented matrix strain. The difference in compressive behaviour between the two systems was constant up to 17 J energy and then decreased because at higher impact energies, fibre failure induced by impact influenced the compressive residual properties. Nevertheless, CAI strength values observed for the assessed systems were in the range of conventional values in FRPs [315]–[317] thanks mainly to the woven reinforcement and the high volume fraction of fibres. Notice that F_{CAI} for the *Plain* specimens at 8.5 J energy is depicted in grey in Figure 5.20 because failure occurred by end brooming, thus leading to an invalid measurement according to the ASTM standard.

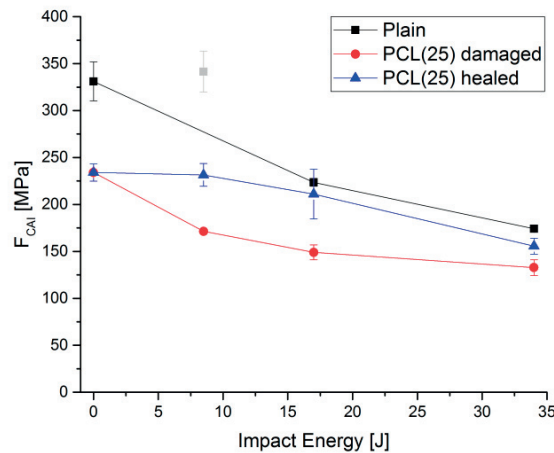


Figure 5.20: Compressive residual strength as a function of the impact energy for *Plain*, *PCL(25)* in the damaged state and *PCL(25)* in the healed state.

Recovery in CAI strength was assessed on some *PCL(25)* specimens, damaged and successively healed by a thermal mending cycle at 150 °C for 30 minutes. In Figure 5.20, the effect of this healing cycle (*PCL(25) healed*) is superimposed with damaged *Plain* and *PCL(25)* specimens. The healing efficiencies could then be calculated by Eq. (3.8) and were of $95.9 \pm 6.0\%$, $73.0 \pm 10.4\%$, $22.4 \pm 0.5\%$ for impact energies respectively of 8.5, 17 and 34 J. As expected from C-scan tests and optical microscopy, at low impact energies, PCL could fill the impact induced cracks whereas at high impact energies it could not due to its limited expansion capacity. High recovery of CAI strength at low impact energy was further confirmed by the fact that on all specimens in the damaged state, compressive failure

occurred through the impact damage (see Figure 5.21 (a)) while on all specimens in the healed state, failure occurred by end brooming (see Figure 5.21 (b)). However, healing efficiency values did not reach 100% due to the destructive nature of CAI testing which required different specimens for each condition, thus creating an additional standard deviation. Also, as demonstrated by Slattery *et al.* [317], test geometry and buckling in CAI tests are really sensitive to scaling effects, thus if repair has to be validated for a real structure, dimensions of the CAI specimens have to be as close as possible to those of the targeted structure.

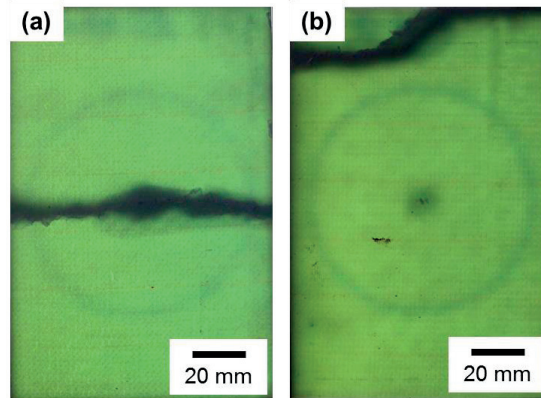


Figure 5.21: Back face optical image of CAI specimens from the PCL(25) system impacted at 8.5 J (a) not healed and (b) healed.

5.2.5 Healing efficiency comparison

Impact damage healing efficiency has been quantified by means of C-scans through recovery in damage area as well as CAI strength recovery, but also theoretically estimated knowing the expansion capacity of PCL and the crack thickness distribution within the impact damage. Healing efficiency values for these three methods are superimposed in Figure 5.22 as a function of the impact energy. At low impact energy, thanks to the expansion capacity of PCL to fully bridge the crack gap, the overlap between the three methods is almost perfect. At higher impact energies however, the difference between the three methods was higher. Owing to the different nature of these three characterisation methods, the overlap could be considered as sufficient to confirm the observed trend, as well as to validate the theoretical crack filling estimation.

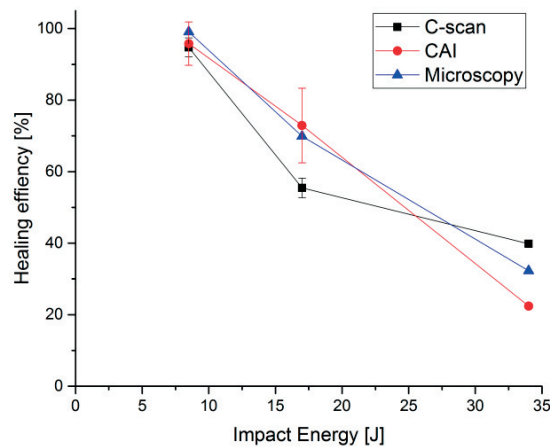


Figure 5.22: Healing efficiency as a function of the impact energy, for three characterisation techniques: (i) damage area determined by C-scan; (ii) compression after impact tests; (iii) crack thickness distribution by optical microscopy observations.

5.2.6 Conclusion

Glass fibre-reinforced epoxy-PCL ($M_n \approx 49,000$ g/mol) composites with fibre volume fractions around 50 vol% were successfully processed through the VARIM process at elevated temperature. Specimens were used to assess the impact response of such systems, characterise their damage area recovery as well as their potential for recovery of compressive residual strength. As expected from section 5.1, resistance to crack propagation was lower for epoxy-PCL composites as compared to pure epoxy composites because Hertzian failure appeared earlier and the amount of peaks in the load-time histories (representing delamination events) was higher. Also, damage accumulation was higher in epoxy-PCL systems as the peak load appeared later in the load-time histories.

This lower resistance to crack propagation was further confirmed by C-scan analysis where epoxy-PCL composites showed a damage area 2.5 times larger at 34 J impact energy. C-scans were performed before and after a thermal mending cycle at 150 °C for 30 minutes, and demonstrated a damage area recovery from 40% up to 90%. Incomplete recovery has been attributed to fibre damage, which could not be healed, and formation of rather thick cracks, which could not be healed by PCL due to its limited expansion capacity. Transverse cuts of specimens impacted at the three energy levels showed typical damage shapes in FRPs and the determination of transverse crack distribution within epoxy-PCL composites revealed crack thicknesses ranging from few μm up to 300 μm . The theoretical PCL expansion capacity of PCL further emphasized that, depending on the energy level, 32 to 99% of the cracks could be bridged, thus confirming C-scans analysis. In addition, epoxy-PCL composites were able to recover between 22 and 96% of compressive residual strength after low-velocity impact damage, in accordance with C-scan and optical microscopy observations, even though these showed lower resistance to crack propagation as compared to pure epoxy composites (a CAI strength decrease by 29% in undamaged specimens).

Although epoxy-PCL composites demonstrated lower compressive residual strength as compared to pure epoxy composites, the used woven reinforcement and the high fibre volume fraction provided CAI strength values close to those encountered in conventional FRPs. In addition, the developed system allowed full healing of an impact damage of 8 J, corresponding to the main concern of maintenance activities in the composite industry (e.g. dropped tools). Epoxy-PCL composites, providing their manufacturing feasibility through conventional industrial processes, their acceptable impact damage resistance and their ability to fully heal low-velocity impact damage, can thus be of interest in composite structures that are subjected to moderate loads and not easily accessible to repair. In order to repair composite structures that are subjected to higher loads and thus contain larger damage volumes, there is however the need to reduce the crack sizes before the healing process can take place. An innovative strategy to solve this problem is proposed in the next chapter.

Chapter 6 Stitched SMA wires for enhanced damage recovery of self-healing FRPs

(Adapted from ref. [318]: A. Cohades, N. Hostettler, M. Pauchard, C. J. G. Plummer, V. Michaud, "Stitched shape memory alloy wires enhance damage recovery in self-healing fiber-reinforced polymer composites," *SUBMITTED, 2017* and from ref. [319]: A. Cohades, M. Pauchard, and V. Michaud, "Impact resistance and recovery in SMA stitched E-glass reinforced Poly(ϵ -caprolactone)/epoxy composites," *Proc. ICCM21, 2017*)

The need to reduce the damage volume before the healing process takes place was highlighted in the previous chapter in order to reach healing of larger damage levels. Borrowing from standard medical practice for the treatment of wounds, an improved strategy might be to close cracks whose thickness is above a certain threshold by applying sutures prior to activation of the healing process. SMA wires inserted into FRPs through stitching of the dry fabric before impregnation provide a means of achieving this. SMA wires that have been stretched and partly debonded subsequent to crack propagation are able to recover their initial length on heating and/or exert a stress that may reach several hundred MPa, effectively closing the cracks. In this chapter, a combined healing strategy applied to FRPs with two functionalities is investigated (Figure 6.1): (i) epoxy-PCL(25vol%) blends as matrix to provide healing and (ii) stitched NiTiCu SMA wires to close cracks. FRPs were manufactured with the healing matrix through the VARIM process at high temperature and SMA wires were stitched transversally to the stacked preform before the VARIM process. The SMA intrinsic properties were first assessed through DSC and contact angle measurements. Mechanisms of crack closure were secondly determined through pull-out tests of SMAs in resins as well as in FRPs, which allowed determining a stitching design for further integration to FRPs. Then Mode I DCB testing and low-velocity impact tests at three impact energy levels were performed and the damage area recovery of these smart systems assessed by means of optical analysis and C-scans after thermal mending at 150 °C for 30 minutes.

When preparing *Epoxy* and *Epoxy-PCL(25vol%)* blend-based FRPs (referred to respectively as *GF-Epoxy* and *GF-Epoxy-PCL* in what follows) with stitched SMA wires, these latter were first stitched into the dry fabric (a woven twill 2x2 E-glass fabric) with a commercial sewing machine at a point density of 700 SMA wires/m², which is expected to provide recovery stresses of up to 4000 N/m². The resulting average distances between two stitched lines and between two needle knots were 4.49 ± 0.75 mm and 3.94 ± 0.78 mm respectively. The VARIM process was then used to prepare specimens for Mode I fracture tests and for impact tests. The fibre volume fraction was 46.68 ± 0.71% and the SMA volume fraction was 0.33 ± 0.02% for the *GF-Epoxy* specimens, whereas for the *GF-Epoxy-PCL* specimens, the fibre volume fraction was 47.03 ± 1.07% and the SMA volume fraction was 0.41 ± 0.01%. Notice that PCL with $M_n \approx 45,000$ g/mol was used for Mode I fracture tests and PCL with $M_n \approx 49,000$ g/mol was used for impact tests, as in Chapter 5. For preparation of the specimens as well as characterisation methods leading to the results presented hereafter, the reader is referred to Chapter 3.

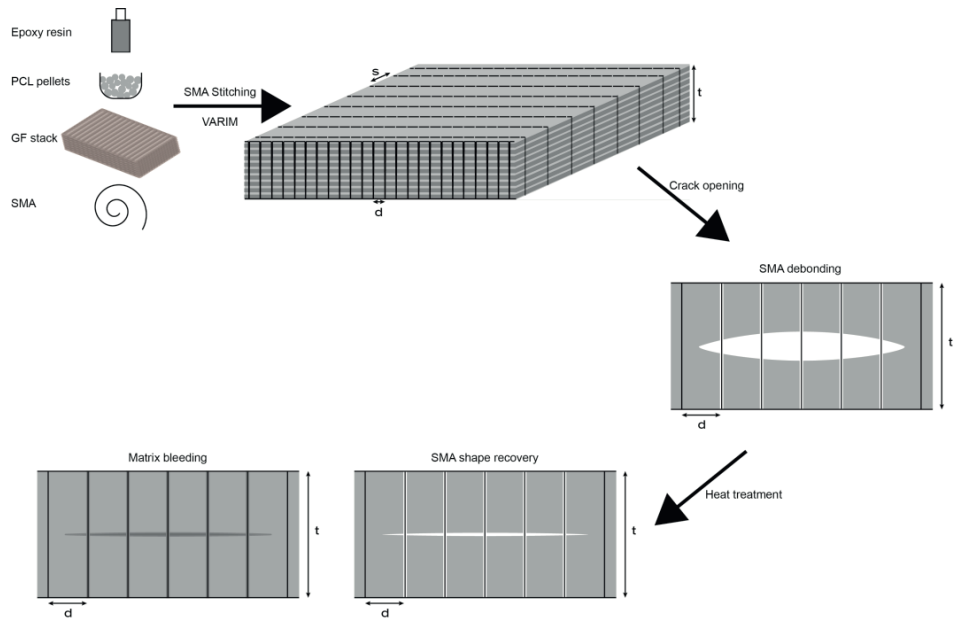


Figure 6.1: Illustration of the proposed healing system and its process to efficiently close and heal cracks.

6.1 Stitching design formulation

6.1.1 SMA wire characterisation

In addition to the SMA wire intrinsic properties given in Table 3.1, thermal transitions as well as contact angles with the used matrices were determined. An example of DSC heating and cooling scans (-80 to 200 °C at 10 °C/min) of the NiTiCu wire is depicted in Figure 6.2. The four characteristic transitions were well observed and were defined as: the start and finish temperatures upon heating of the martensite to austenite transformation, denoted respectively as A_s and A_f ; and the start and finish temperatures upon cooling of the austenite to martensite transformation, denoted respectively as M_s and M_f . The measured values are given in Table 6.1 and were in agreement with previous studies [6], [210] even though some slight variations were noticed and explained from the different batch natures.

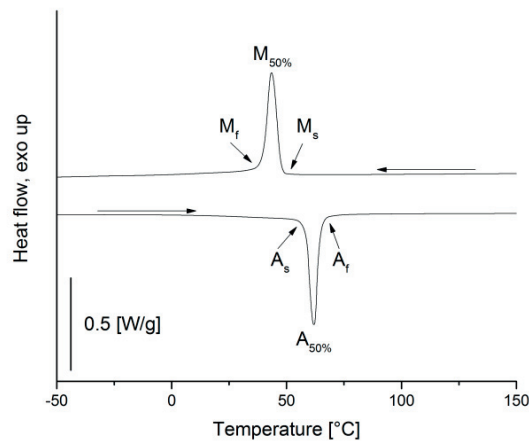


Figure 6.2: DSC heating and cooling scans for NiTiCu SMA wire. Martensite and Austenite characteristic temperatures are also indicated in the graph.

Table 6.1: NiTiCu wire characteristic transition temperatures determined by DSC.

	A_s	$A_{50\%}$	A_f	M_s	$M_{50\%}$	M_f
T [°C]	58.68	61.81	64.4	48.1	44.01	39.65

Small droplets of matrices (*Epoxy* and *Epoxy-PCL*) were deposited on cleaned SMA wires with the help of a syringe tip and then cured for 3h at 180 °C. Mean contact angle results, determined with the method of Carroll [280], are as follows:

- $\theta_{\text{Epoxy}} = 46^\circ \pm 7^\circ$
- $\theta_{\text{Epoxy-PCL}} = 40^\circ \pm 15^\circ$

The contact angles are below 90°, indicating that both resins had the ability to wet the wires. This behaviour was representative of the good compatibility between both components showing promise to high IFSS values as compared to non-wetting resins. The lower angle found in *Epoxy-PCL* specimens indicated better compatibility with SMAs as compared to *Epoxy* specimens. Notice that the observed scatter was attributed to possible errors in the alignment of the wires with respect to the angle of view. Also, the higher standard deviation with *Epoxy-PCL* blends came from the irregular structure of epoxy particles that may have altered a consistent measurement of the droplet diameter (indeed the meniscus at both ends of the droplet was less well defined as compared to specimens with pure epoxy resin, see Figure 3.7 for *Epoxy-PCL* blends on an SMA wire).

6.1.2 Interfacial behaviour of the SMA

Three parameters, sketched in Figure 6.1, are important for the design of the SMA stitches: the stack thickness, the stitching density in the specimen plane, and the interface strength, which should be tailored to promote partial debonding, and hence avoid irreversible deformation of the SMA in the vicinity of the crack. In order to optimise this latter parameter, the pull-out behaviour of the SMA wire from the pure resins (*Epoxy* and *Epoxy-PCL* blends) and the corresponding FRP composites was investigated.

6.1.2.1 Interfacial behaviour of SMA wires in pure resins

Pure epoxy (*Epoxy*) and blends of epoxy and 25 vol% PCL (*Epoxy-PCL*) were prepared following the procedure reported in Chapter 3, and poured into silicon moulds. Either straight lengths or loops of the SMA wires were previously inserted (see Figure 3.5) and the resin cured for 3 h at 180 °C. Figure 6.3 (a) shows the surface of a fractured specimen, highlighting the circular trajectory of an SMA loop. In each case, the force-displacement curve from the pull-out tests showed an elastic regime, followed by a plateau associated with detwinning of the martensitic phase in the SMA (Figure 6.4). The force then increased to a maximum, which coincided with debonding. For both resin systems, the peak force was higher for the loop geometry than for the straight geometry for a given wire embedded length. The yield stress of the PCL (see section 4.2) resulted in flow of the matrix along the SMA wire during pull-out (Figure 6.3 (b) and Figure 6.3 (c)), leading to stick-slip behaviour (Figure 6.4 (b)). Figure 6.3 also illustrates the microstructure obtained with *Epoxy-PCL* blends, i.e. interconnected epoxy particles in a PCL matrix, in accordance with section 4.2.

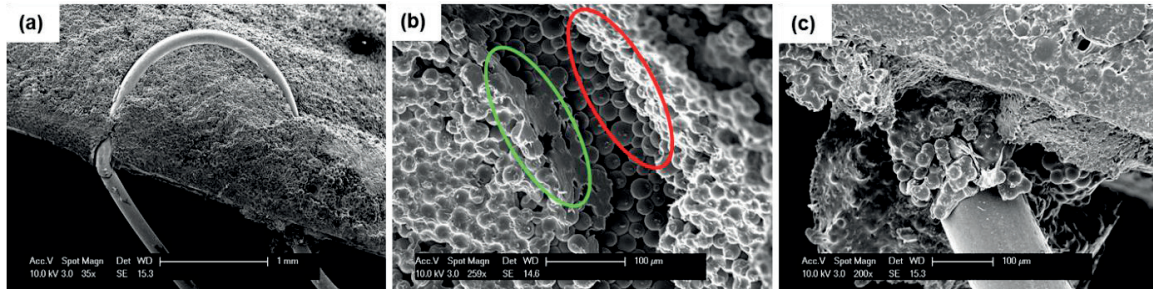


Figure 6.3: (a) SEM image of a fractured pull-out specimen prepared from *Epoxy-PCL*; (b) SEM image of a pull-out specimen prepared from *Epoxy-PCL* in which the wire has been removed and the morphology provides an indication of the stress distribution in the loop geometry (a region of compressive deformation is circled in green and a region of tensile deformation is circled in red); (c) SEM image from the top surface of a pull-out specimen prepared from *Epoxy-PCL* showing matrix material drawn out of the specimen by the wire during testing.

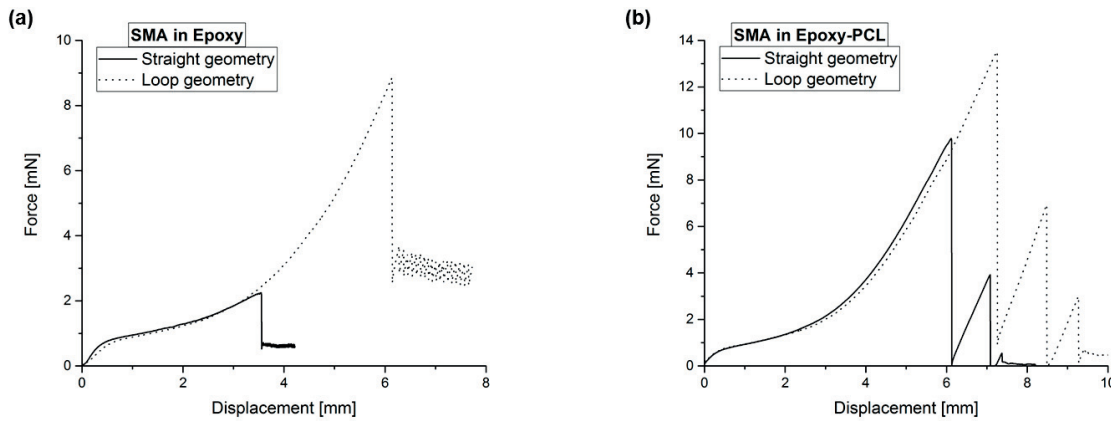


Figure 6.4: Typical force-displacement curves during a pull-out test. (a) Straight and loops geometries in pure *Epoxy*; (b) Straight and loops geometries in *Epoxy-PCL* blends. The embedded length was 3 mm for every represented curve.

The apparent IFSS, τ_a , between the resins and the SMA wires was determined as a function of the embedded length for both resins and both geometries (Figure 6.5) from the force-displacement curves according to Eq. (2.6) in section 2.2.2.1. The IFSS for the *Epoxy-PCL* blends was higher than for *Epoxy* in both geometries. This was attributed to the relatively high ductility of the PCL, and the observation of lower contact angles between the SMA wires and cured *Epoxy-PCL* blends (40°) than between the SMA wires and cured *Epoxy* (46°). The modified stress distribution (compressive and tensile deformation zones through the channel length, as illustrated in Figure 6.3 (b)) and increased pull-out friction associated with the loop geometry led to a higher IFSS at similar embedded lengths. The ability of the *Epoxy-PCL* specimens to heal the interface with the SMA wire after a thermal mending cycle of 30 minutes at 150°C was also assessed from successive pull-out tests. Although full recovery was not observed because of the significant amounts of matrix drawn out during the initial tests (Figure 6.3 (c)), it was shown (Figure 6.5 (a)) that the IFSS of the healed specimens could reach values similar to those of the *Epoxy* matrix in the straight geometry. Healing of the SMA-matrix interface is therefore also expected when healing microcracks generated through impact loading, as in the present work. However, because the SMA wires were further integrated into the FRPs as stitches, it was also necessary to assess their pull-out behaviour in the presence of reinforcement fibres, because fibres have been shown to influence phase separation (see section 5.1).

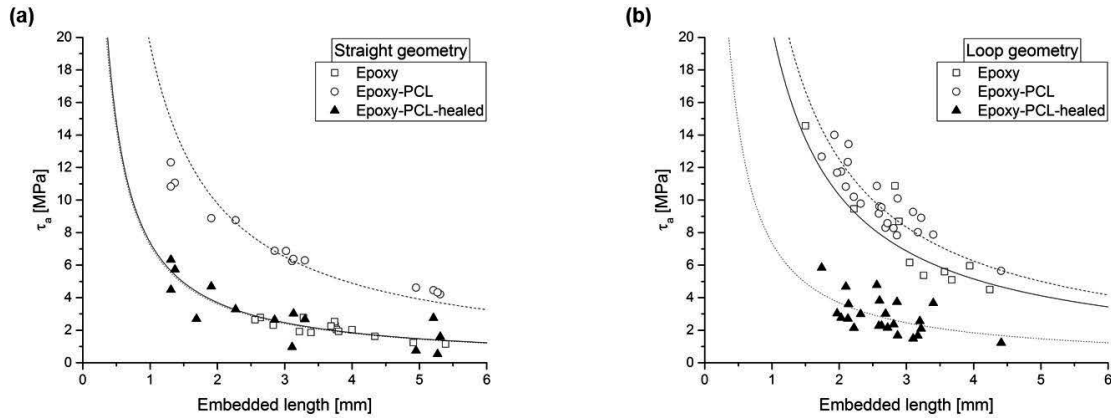


Figure 6.5: Apparent IFSS as a function of the interfacial shear strength for different matrices and (a) straight SMA wires; (b) SMA loops.

Intrinsic IFSS, τ_i , is by definition the apparent IFSS, τ_a , at a zero embedded length. Mendels model (Eq. (2.6)) was used to find this quantity for each system, which is given in Figure 6.6 (a) for the straight geometry and Figure 6.6 (b) for the loop geometry. The observed differences followed the same behaviour as for the apparent IFSS: higher values for *Epoxy-PCL* specimens due to the difference in failure modes with the SMAs (cohesive failure for *Epoxy-PCL* and adhesive failure for *Epoxy* specimens). Notice that thanks to the observed adhesive failure between the wire and the matrix (observed by SEM), the values found for the *Epoxy* straight specimens were in accordance with previous studies [241]. Also, comparing the graphs in Figure 6.6 highlights the higher importance of the loop geometry on the IFSS values for the stiff epoxy as compared to the weaker *Epoxy-PCL* system (the magnitude of τ_i are inversed between *Epoxy* and *Epoxy-PCL* when testing as loops).

Determining intrinsic IFSS through Eq. (2.6) is quite straightforward; however taking into account internal stresses (Eq. (2.7)) requires knowing the temperature difference ΔT , which can vary as its determination is either made between the curing and the testing temperature or between the glass transition and the testing temperature. Here, the influence of internal stresses was determined by the data fits shown in Figure 6.5. This fit was performed between the apparent IFSS values and the intrinsic one (at zero embedded length). Then the temperature difference, ΔT in Eq. (2.7), was adapted to fit at best the apparent IFSS values. Varying this quantity did not show any significant difference and therefore internal stresses were neglected in the present work. Notice that interfacial shear strength between SMA wires and a surrounding matrix is dependent on the martensite twinning amount as related by Sparnins *et al.* [241]. Due to the geometries and temperature cycles used in the present work, the martensite had most probably various amounts of twinning, even though annealing cycles were performed. This behaviour participated to the observed standard deviations.

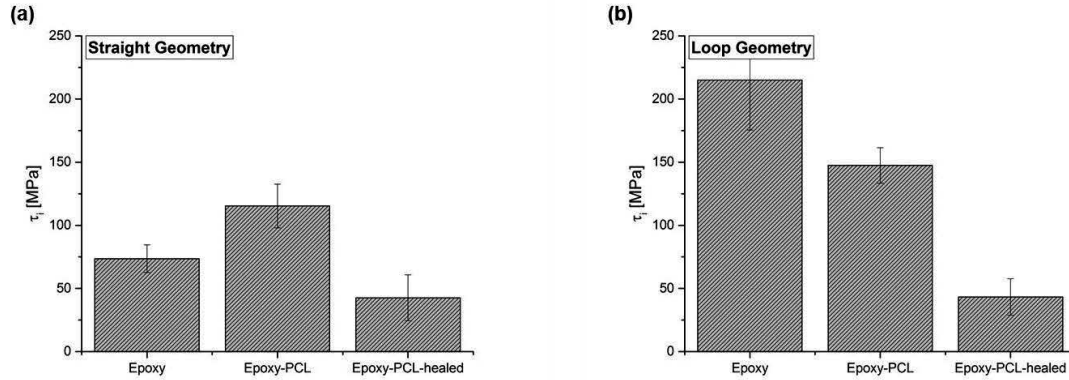
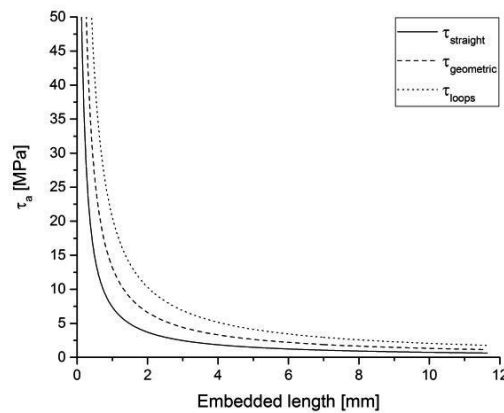


Figure 6.6: Intrinsic IFSS for (a) straight specimens; (b) loop specimens.

The evolution of apparent IFSS between the loop and straight geometries as a function of the embedded length in Figure 6.5 seemed to be similar. Therefore, the possibility to model the IFSS property in the loop case can be explored by simply knowing it in the straight case and the link that exists between the two. Assuming that shear strength in the loop geometry is simply defined as the sum between shear strength in the straight geometry and a shear strength called “geometrical”, IFSS in the loop case can be modelled by:

$$\tau_{loop} = \tau_{straight} + \tau_{geometrical} = \tau_{straight}(1 + \xi) \quad (6.1)$$

where $\tau_{geometrical}$ was further defined as a factor ξ times the shear strength in the straight case, $\tau_{straight}$. Figure 6.7 shows, graphically, for an *Epoxy* specimen, the apparent IFSS in the straight and loop geometries as well as the “geometrical” IFSS. Through this representation, a $\tau_{geometrical}$ appears, that links IFSS values in the two geometries. This “geometrical” IFSS can be expressed as a function of the straight IFSS and a factor ξ (Eq. (6.1)). This definition is convenient as the ξ factor is constant with the embedded length. Even though the ξ factor is different between the two assessed resins because it depends on the intrinsic material properties (strength and/or modulus), this model demonstrates that shear strength between SMAs and any matrix can be quantified by performing simple pull-out tests, knowing the geometrical factor and its dependency to intrinsic material properties. Further tests would be here needed to accurately determine the origin of ξ .


 Figure 6.7: Apparent IFSS for straight and loop specimens and the corresponding geometrical IFSS as a function of the embedded length for *Epoxy* specimens.

6.1.2.2 Interfacial behaviour of SMA wires in FRPs

Glass fibre-reinforced pull-out specimens in the loop and straight geometries were prepared by the VARIM process with a fibre volume fraction of 50%. Embedded lengths of 1.5 to 5 mm were tested and although debonding was observed in the straight geometry, in the loop geometry the wires broke before debonding from the FRP block at forces corresponding to the failure strength of the SMA wire, as determined previously [9], [210]. This was attributed to constraints imposed by the glass fibres, which resulted in deformation of the loops. The curved tip of the syringe used to place the SMA wires, intended to simulate the needle used later for stitching, modified the spacing of the glass fibres, creating a channel of nearly 500 μm in width (Figure 6.8 (a)). At the same time, the loops adopted a rectangular shape, as seen from Figure 6.8 (b). The SMA wires were strongly anchored at the vertices of these rectangular loops with respect to sliding. However, away from the vertices, the wires were inferred to debond, because: (i) the IFSS values in the straight geometry of up to 200 MPa were much lower than the tensile strength of the SMA wire of about 800 MPa; (ii) there was direct evidence for debonding in the form of voids and tearing of the matrix around the wires (Figure 6.8 (a)). In a stitched composite, this anchoring should ensure uniform strains in the SMA across the whole of the FRP specimen thickness, leading to enhanced crack closure capacity after a damage event. Under these conditions, assuming a 5 mm thick FRP plate and a strain to failure for the SMA wires of 7.4% [9], and that the wires are stitched through the entire plate thickness with loops at both ends, the maximum crack thickness that can be closed without SMA failure is estimated to be 370 μm . Furthermore, given that the recovery stress for the SMAs is 340 MPa [9], each actuated SMA wire will exert a compressive force of about 6 N on the crack faces, resulting in a recovery stress of 4000 N/m^2 for the stitching design shown in Figure 6.1 with $t = 5 \text{ mm}$, $s = 4 \text{ mm}$, and $d = 4 \text{ mm}$.

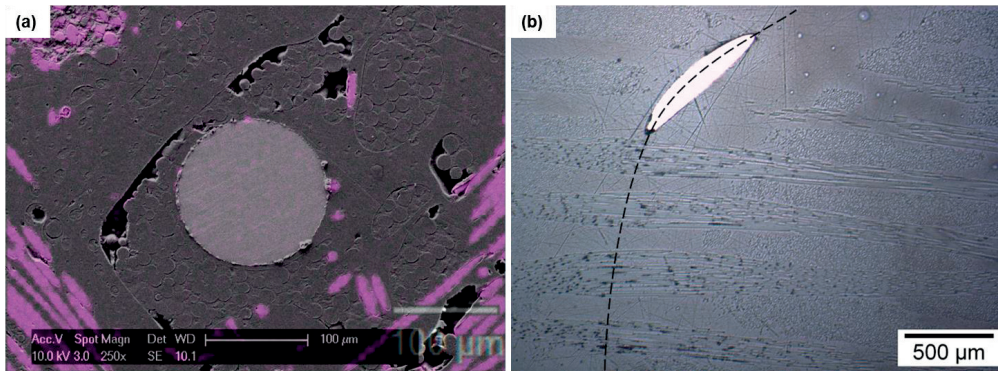


Figure 6.8: (a) SEM image of the cross-section of a polished specimen of an *Epoxy-PCL* blend containing glass fibre reinforcement; the pink areas indicate the presence of Si (determined by EDX analysis) and hence the location of the glass fibres. (b) Optical microscopy image of a polished specimen containing glass fibre reinforcement, *Epoxy* resin and an SMA wire inserted with the loop geometry (the dashed line indicates the trajectory of the wire).

6.2 Mode I Double Cantilever Beam Testing of SMA stitched composites

6.2.1 Fracture behaviour of composites containing stitched SMA wires

Mode I double cantilever beam (DCB) tests were used to assess the fracture behaviour of *GF-Epoxy* and *GF-Epoxy-PCL* in the presence of the SMA stitches. The specimens were free of SMA over the first 2 cm of the crack path, but stitched over the remainder of the crack path so as to ensure stable growth of the crack in a zone free of wires before it reached the zone stitched with the SMA. Load displacement traces, a typical example of which is shown in Figure 6.9 (a), showed an initial increase in load with displacement up to the onset of propagation of the crack in the SMA-free zone. When the crack reached the zone containing the SMA, the load started to increase again showing initially elastic behaviour, followed by a plateau associated with detwinning of the martensitic phase in the SMA. Once the SMA wires reached their failure strain, they broke (Figure 6.9 (c)), resulting in discontinuous drops in the load (Figure 6.9 (a)). The R-curve was also determined from measurements of the crack length during each test, as shown in Figure 6.9 (b) for

both systems. As with the load-displacement traces, the R-curves reflected differences in behaviour in the SMA-free zone and in the zone containing the SMA wires. In the SMA-free zone, the R values were similar to those determined previously for these materials (see section 5.1), whereas in the zone containing the SMA wires, R increased by a factor of about three for both *GF-Epoxy* and *GF-Epoxy-PCL* and showed discontinuities corresponding to the failure of individual SMA wires. Consistent with previous results (see section 5.1), the crack resistance of *GF-Epoxy* was generally greater than for *GF-Epoxy-PCL*. These tests also confirmed the SMA wires to debond over the whole of the thickness of the FRPs, and subsequently break when their strain to failure was exceeded. Moreover, they indicated that the crack propagation length should not exceed a certain threshold length (2.4 cm in the present case) if SMA breakage is to be avoided and their capacity for crack closure after thermal treatment is to be maintained. The presence of broken SMA wires subsequent to more extensive propagation would prevent reduction of the crack face separation to less than 150 μm (the diameter of the SMA wires), thus compromising efficient crack healing by the matrix.

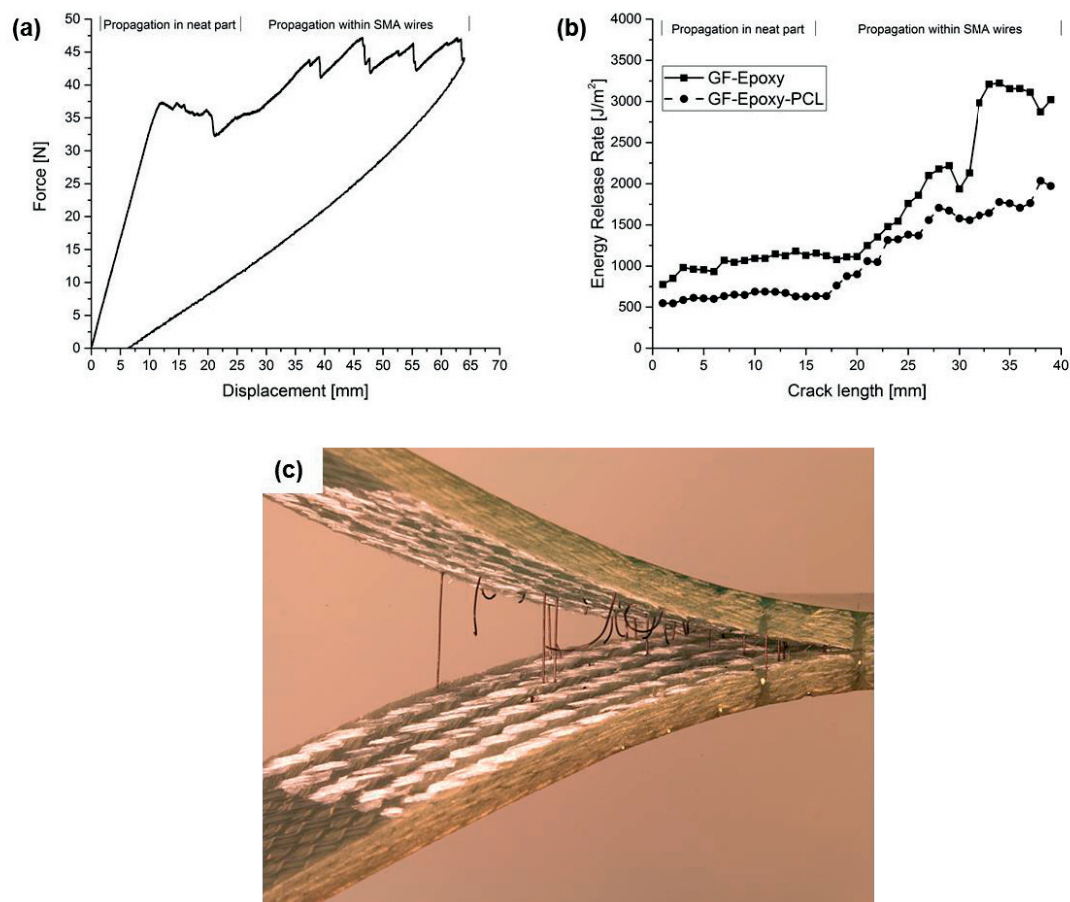


Figure 6.9: (a) Typical loading-unloading curve from a DCB test on *GF-Epoxy* in the presence of SMA wires; (b) Typical R-curves from DCB tests on *GF-Epoxy* and *GF-Epoxy-PCL* in the presence of SMA wires; (c) *GF-Epoxy* DCB specimen after crack propagation over a distance of 4 cm showing breakage of the SMA wires.

6.2.2 Crack closure and stiffness recovery

The same DCB experiments were used to quantify the capacity of the SMA wires to close cracks and the associated stiffness recovery after a 30 minutes thermal mending cycle at 150 $^{\circ}\text{C}$. The crack face separations in at least three damaged specimens of each type of material were measured by optical microscopy, before and after activation of the SMA wires by the thermal mending cycle. Figure 6.10 (a) shows typical crack profiles before and after activation in *GF-*

Epoxy and Figure 6.11 (a), Figure 6.12 (a) typical crack profiles before and after activation in *GF-Epoxy-PCL* (for respectively unclamped and clamped specimens during the thermal mending) where bleeding of the PCL from the matrix can also be observed in the healed specimens (lower image). The crack face separations as a function of the crack length (distance along the crack) were in each case compared with those observed in unstitched specimens in order to determine the effect of the SMA wires.

In section 5.1, specimens were clamped at the loading blocks during thermal mending. With the use of SMA wires, specimens were initially left as unclamped during the thermal mending cycle in order to assess the crack closure capacity of the wires only. Analyses of the crack face separation in FRPs based on the unmodified epoxy matrix (*GF-Epoxy*) with and without the stitched SMA wires are shown in Figure 6.10 (b) and (c), in each case for three specimens subjected to damage followed by thermal healing. In the vicinity of the SMA wires (i.e. close to the crack tip), the crack face separation was found to be reduced by around 100 μm , and the crack opening at the tip of the original starter crack (the limit of the release film), was also reduced by around 150 μm (Figure 6.10 (b)) after thermal treatment. No crack closure was observed after the thermal treatment in specimens without the SMA wires (Figure 6.10 (c)). Comparison of Figure 6.10 (b) and (c) thus demonstrated the ability of SMA wires to partially close cracks when integrated as stitches in FRPs. Because these specimens were based on unmodified epoxy rather than the healing matrix, the observed crack closure was due to recovery of the SMA wires alone. The initial crack opening at the tip of the original starter crack (the limit of the release film) was nevertheless greater in specimens with stitched SMA wires than in specimens without SMA, owing to the presence of strained and/or broken SMA wires between the crack faces, which obstructed crack closure immediately after release of the applied load.

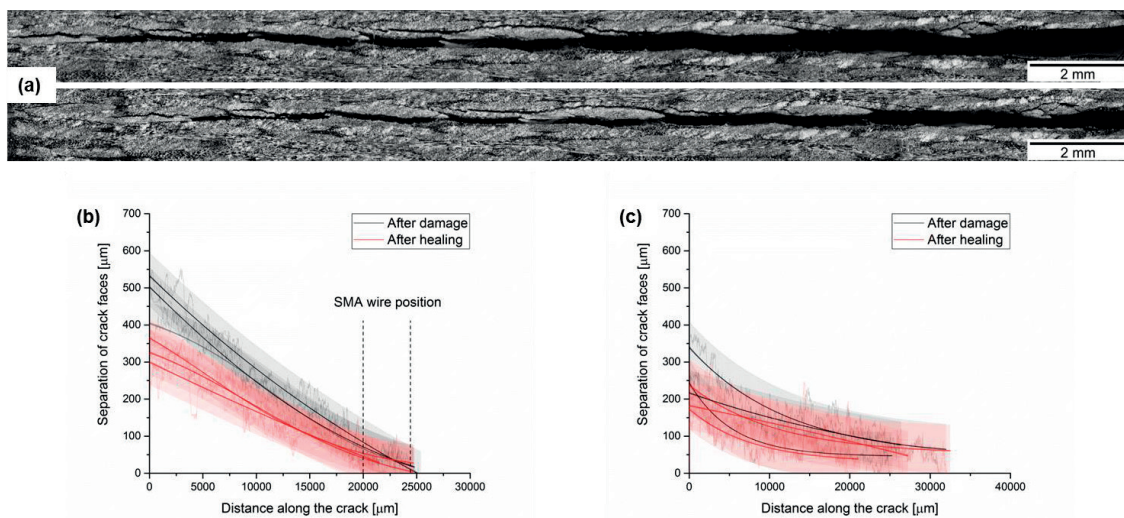


Figure 6.10: (a) Optical micrographs of the crack in a *GF-Epoxy* DCB specimen: (top) after damage; (bottom) after damage and healing at 150 °C for 30 minutes. Separation of the crack faces as a function of crack length in *GF-Epoxy-PCL* after damage (in black) and after damage and healing (in red) for (b) specimens stitched with SMA wires, whose positions are indicated by the dashed lines, and (c) specimens without stitched SMA wires. The original data for the separation of the crack faces, also shown in the figure, were fitted using a standard Boltzmann procedure with a 95% confidence band.

Measurements of the crack face separation in FRPs based on the epoxy-PCL healing matrix (*GF-Epoxy-PCL*) with and without the stitched SMA wires are shown in Figure 6.11 (b) and (c), in each case for three specimens subjected to damage followed by healing. In the vicinity of the SMA wires (i.e. close to the crack tip), the crack face separation was found to be reduced from 200 μm to zero and the crack opening at the tip of the original starter crack (the limit of the release film), was also reduced from 600 μm to 150 μm (Figure 6.11 (b)). This large reduction in crack face separation was a combined effect of (i) the SMA wires and (ii) internal stresses induced during specimen fracture, which were released during the thermal mending cycle. This second effect was demonstrated by analysis of specimens without SMA wires (Figure 6.11 (c)), in which crack closure close to the crack tip location was observed to be reduced by

around 40 μm (the PCL bleeding capacity), whereas at the crack origin, the crack opening decreased from 450 μm to 150 μm . This behaviour was only observed for specimens with the healing matrix (*GF-Epoxy-PCL*), and was attributed to the lower intrinsic strength of the latter, which also resulted in a larger damage volume than in specimens with the pure epoxy matrix (*GF-Epoxy*). Although the specimens with the healing matrix showed some damage volume reduction during thermal mending owing to release of internal stresses and bleeding of the epoxy-PCL matrix, comparison of Figure 6.11 (b) and (c) highlights the ability of the SMA to fully close cracks with crack face separations of up to 200 μm when integrated as stitches in FRPs, a comparable performance to that observed in pure epoxy FRPs (*GF-Epoxy*) containing stitched SMA wires. Complete crack healing was nevertheless not achieved in the present case because of the large maximum crack face separations. Full crack healing in this geometry would require clamping of the loading blocks, as in section 5.1, in order to limit the maximum crack face separation to 200 μm prior to activation of the SMA wires and bleeding of the PCL into the crack.

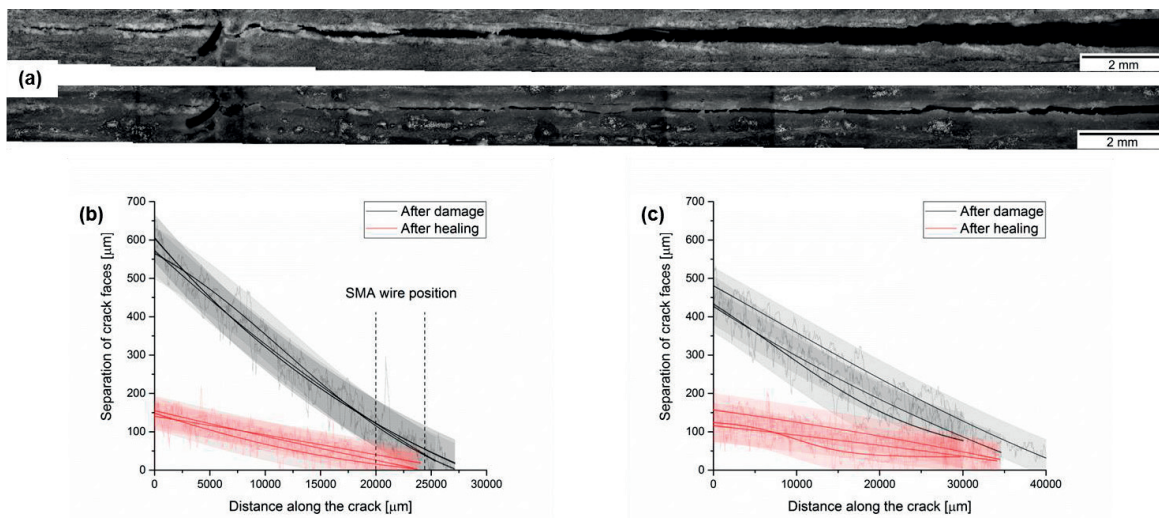


Figure 6.11: (a) Optical micrographs of the crack in a *GF-Epoxy-PCL* DCB specimen: (top) after damage; (bottom) after damage and healing at 150 °C for 30 minutes. Separation of the crack faces as a function of crack length in *GF-Epoxy-PCL* after damage (in black) and after damage and healing (in red) for (b) specimens stitched with SMA wires, whose positions are indicated by the dashed lines, and (c) specimens without stitched SMA wires. The original data for the separation of the crack faces, also shown in the figure, were fitted using a standard Boltzmann procedure with a 95% confidence band.

In order to reduce the damage volume without bringing the propagated crack faces into close contact, and to be consistent with previous investigations (see section 5.1), the specimens were clamped at the location of loading points during the thermal mending cycle. Crack closure was investigated for clamped *GF-Epoxy-PCL* specimens with and without the SMA wires, and results are given in Figure 6.12 (b) and (c) for three specimens that had each undergone three successive fracture testing and thermal mending cycles. The SMA wires were able to bring the crack faces into close contact for initial crack face separations of up to 200 μm , whereas in the absence of the SMA, crack closure due to bleeding of the PCL from the matrix was only effective for crack face separations of up to 40 μm , as reported previously (see sections 5.1). Although the crack face separations at the origin (the limit of the release film that formed the starting point for delamination) were higher in specimens with stitched SMA wires than in specimens without SMA owing to the wires that were in the strained stage as well as the presence of some broken wires, which obstructed crack closure when releasing the test load, the wires allowed bringing larger cracks in close contact before sealing them by the healing matrix. This healing behaviour is repeatable as demonstrated for 3 successive cycles.

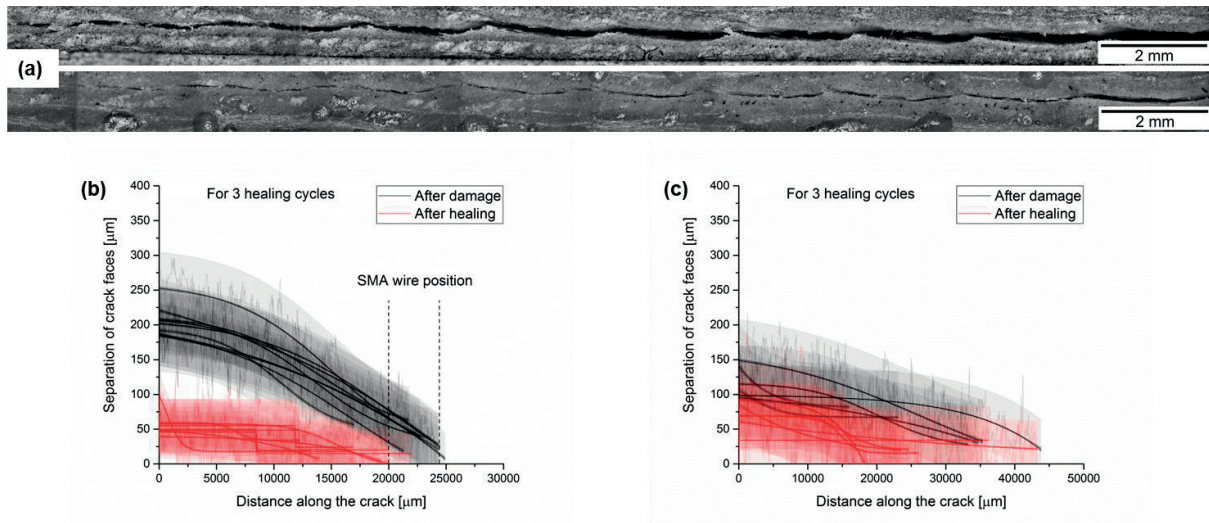


Figure 6.12: (a) Optical micrograph of an interply crack in a *GF-Epoxy-PCL* DCB specimen: after crack propagation (top); after crack propagation followed by healing at 150 °C for 30 minutes (bottom). Separation of the crack faces as a function of crack length in *GF-Epoxy-PCL* specimens after crack propagation (black) and after crack propagation and healing (red) in: (b) specimens stitched with SMA wires (the dashed lines indicate the position of the SMA wires); (c) specimens without SMA wires. The results in (b) and (c) are for specimens subjected to three successive damage and healed cycles. During healing, the specimens were clamped at the loading points. The original data for the separation of the crack faces, also shown in the figure, were fitted using a standard Boltzmann procedure with a 95% confidence band.

The capacity of SMA stitches to close cracks and improve the healing efficiency of the epoxy-PCL matrix was further demonstrated by comparing the load-displacement traces from tests on virgin (undamaged) specimens with those obtained after crack propagation and thermal healing. Representative load-displacement traces from *GF-Epoxy-PCL* with and without the SMA wires after three successive damage and healing cycles are shown in Figure 6.13 (a) and (b), respectively. Crack propagation took place at a higher load for healed specimens stitched with SMA wires than for healed specimens without the SMA wires. This behaviour demonstrated that the stitched SMA wires were able to reduce the separation of the crack faces significantly, facilitating subsequent sealing with the matrix and increasing the total healed crack area compared with that in specimens without SMA wires. Full recovery was nevertheless not possible in this configuration, where the crack path included parts of the specimen that were not stitched with SMA wires, and in which the crack width was too large for healing to be effective.

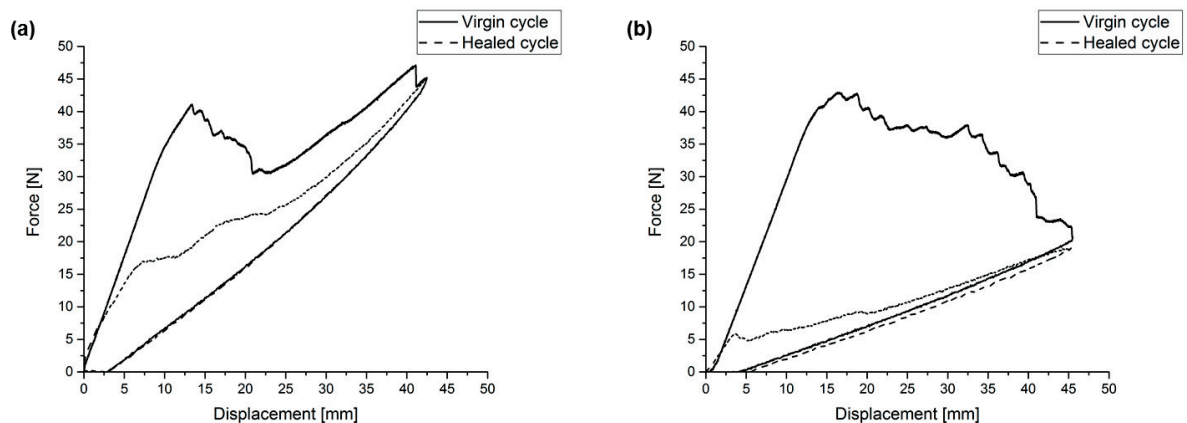


Figure 6.13: Loading and unloading cycles for DCB specimens in the virgin and healed states: (a) *GF-Epoxy-PCL* stitched with SMA wires, (b) *GF-Epoxy-PCL* without SMA wires. The cycles shown for healed specimens were obtained after three successive damage and healing cycles.

6.3 Impact damage of SMA stitched composites

6.3.1 Preliminary study

Preliminary impact experiments have been performed on SMA stitched composites made of a low toughness epoxy resin (epoxy-DETA), which was cured at room temperature and post-cured at 45 °C. Specimens preparation followed the procedures described in Chapter 3 and the specimens contained a fibre volume fraction of $48.19 \pm 0.41\%$ and an SMA volume fraction of $0.40 \pm 0.001\%$. Impacts have been performed at three nominal energies (34, 17 and 8.5 J) and specimens were then subjected to the heat treatment at 150 °C in order to assess the recovery in the damage area quantified by binarized optical images. Binarized images before (*Virgin*) and after (*Heat treated*) the heat treatment are shown for the three impact energies in Figure 6.14. The black region is the impacted area, whereas the black lines show the SMA wires stitched within the system. The heat treatment allowed reducing the impacted area by 56.0%, 58.9% and 62.5% for respectively 34, 17, and 8.5 J impact energies. Even though the recovery of the impacted area was not complete, the reduction achieved when inserting SMA wires at 17 J gave a similar impacted area as unstitched specimens impacted at 8.5 J (see section 5.2). Considering the ability of epoxy-PCL composites to fully recover impacts of 8.5 J energy (as determined in section 5.2), using SMA wires were thus expected to improve the healing ability of specimens combining a healing matrix and SMA stitches. However, this behaviour needed to be confirmed for impact specimens containing epoxy-PCL blends (i.e. *GF-Epoxy-PCL* specimens) as well as the pure epoxy cured with DDS (i.e. *GF-Epoxy* specimens). Impact tests as well as damage recovery assessment (after thermal mending) through optical and C-scan analysis are presented hereafter for *GF-Epoxy* and *GF-Epoxy-PCL* systems.

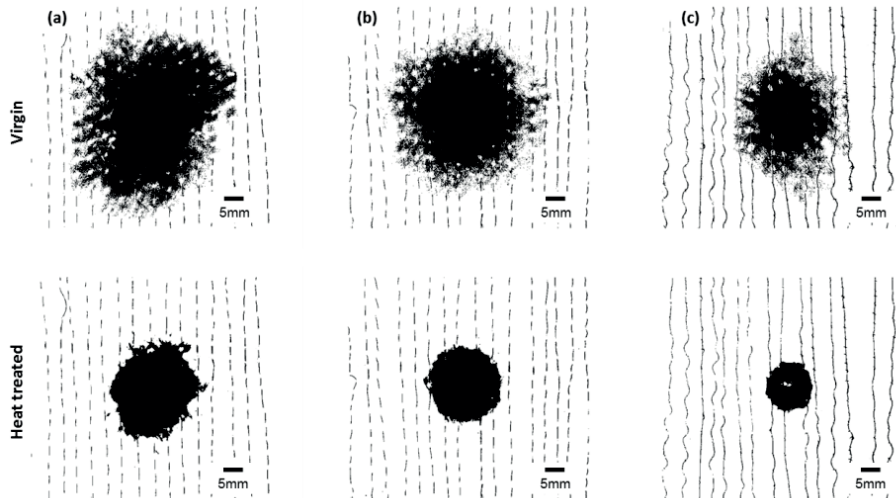


Figure 6.14: Binarized optical images of impacted specimens made of epoxy-DETA resin, at impact energies of (a) 34, (b) 17 and (c) 8.5 J. Images are shown before (*virgin*) and after (*heat treated*) a thermal mending cycle of 30 minutes at 150 °C.

6.3.2 Impact testing

The impact forces as well as energy levels during an impact are represented as a function of time for representative specimens of *GF-Epoxy* and *GF-Epoxy-PCL* systems in Figure 6.15 (left axis for impact forces and right axis for energy levels). As expected, when the impact energy increased, the peak load as well as the energy during test increased. In both cases, a maximum on the curve could be observed, representative of the maximum penetration depth of the impactor. The load curve showed oscillations before this maximum for both systems (*GF-Epoxy* and *GF-Epoxy-PCL*) as well as for the three impact energies, while a smooth decrease down to zero load was observed after this maximum. This behaviour is well known in conventional FRPs [1], [304]: oscillations are attributed to growing ply delamination during penetration of the impactor within the specimen while no further delamination occurs during rebound of the

impactor (i.e. after the peak load). Still focusing on the load response, the first oscillation was representative of the first delamination within the specimen (also called Hertzian failure [304]) and appeared earlier for *GF-Epoxy-PCL* specimens. This behaviour was attributed to the lower resistance to crack propagation (i.e. toughness) as well as to the lower strength of this healing matrix, as determined in sections 4.2 and 5.1. Another characteristic behaviour of a difference in delamination resistance between these two systems can be highlighted through the time at which the peak load is reached. Indeed, the peak load was reached later in *GF-Epoxy-PCL* specimens as compared to *GF-Epoxy* specimens, which indicated that the healing matrix accumulated more damage due to its lower delamination resistance before rebound of the impactor.

Impact energy levels during tests also increased up to a maximum value, before decreasing and reaching a final value. This decrease corresponded to the energy restituted to the impactor by the specimen and the final observed value could be defined as the dissipated energy by the impactor within the impacted specimen. The energy levels have been calculated following the ASTM standard D7136 [72], however, this calculation does not consider other energy consumption mechanisms such as friction within the machine guides, energy transferred during test directly to the impactor and the base machine, or deformation of the grips [305]. In order to counter those effects, the inbound and rebound velocities have also been determined in the present study. These are given in Table 6.2 (as well as mean values of maximum load observed) and the similarity between *GF-Epoxy* and *GF-Epoxy-PCL* specimens was attributed to the fact that energy absorption mechanisms are mainly related to the capacity of the reinforcing fibres to absorb energy [308]. As compared to previously determined data on specimens without SMA stitches (see section 5.2), the dissipated energy increased up to 34% (at the lowest impact energy considered) for both assessed systems, indicating improved damping properties in the presence of the SMA [3], [320].

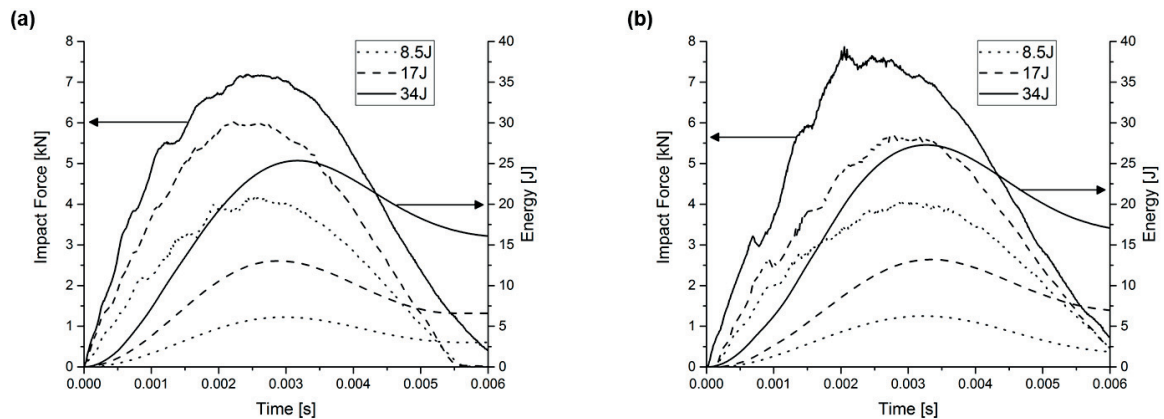


Figure 6.15: Impact force and energy as a function of time for three different impact energies, for (a) *GF-Epoxy* specimens and (b) *GF-Epoxy-PCL* specimens.

In Table 6.2, the maximum load and the energy dissipated during impact are given for the three impact energies as well as for the two assessed systems. A relatively high standard deviation can be observed for every value, greater than that achieved with the tests performed previously on systems without SMA stitches (see section 5.2). This deviation was attributed to the position of the impact as referred to the position of the SMA stitched lines in the specimens. Two extreme cases are shown in Figure 6.16 for *GF-Epoxy* specimens: (i) an impact lying exactly on an SMA stitched line (Figure 6.16 (a)) and (ii) an impact lying exactly in between two SMA stitched lines (Figure 6.16 (b)). The shape of the damage area is different for these two cases: (i) the impact is long and the damage area seems to have followed the stitched lines, thus energy dissipation was directed through the SMA stitches, and (ii) the impact has a rounder shape and the damage area seems to have propagated more within the composite. However, the measure of damage areas (through binarization of the optical image, see section 6.3.3) in every specimens for the three impact energies revealed values in the same range whether the impact was lying on an SMA or not. From the present findings, it can be concluded that the impact position with respect to the SMA stitched lines influences the damage

shape, and to a lower extent the damage level. This influence may lead to the standard deviation observed within the impact data. Finally, the quality of the stitching pattern achieved with the sewing machine can be observed from Figure 6.16.

Table 6.2: Maximum load (F_{max}) and dissipated energy (E_{diss}) during impact at three nominal energies (34, 17 and 8.5 J) for *GF-Epoxy* and *GF-Epoxy-PCL* specimens.

Specimen	Impact energy [J]	F_{max} [kN]	E_{diss} [J]
<i>GF-Epoxy</i>	34	7.09 (0.19)	15.96 (0.69)
	17	5.69 (0.28)	6.92 (0.21)
	8.5	4.58 (0.43)	2.46 (0.22)
<i>GF-Epoxy-PCL</i>	34	7.51 (0.27)	16.81 (1.27)
	17	5.67 (0.11)	6.93 (0.63)
	8.5	4.12 (0.55)	3.40 (0.28)

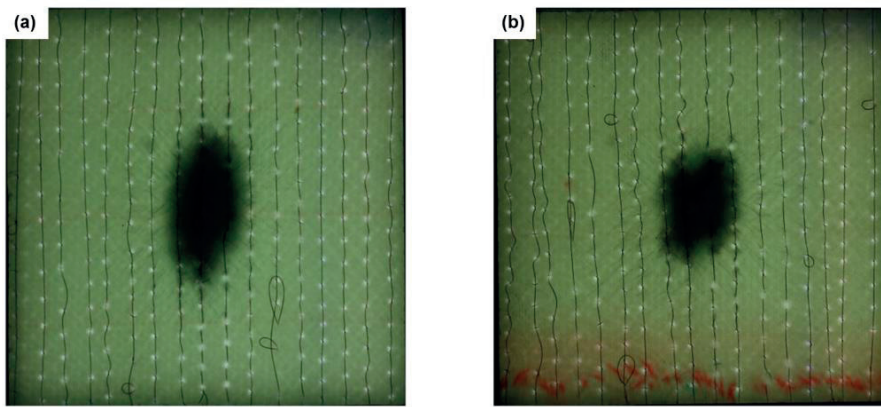


Figure 6.16: Back face optical image of *GF-Epoxy* specimens impacted at 34 J energy: (a) impact on an SMA stitched line and (b) impact in between two SMA stitched lines.

6.3.3 Impact damage recovery through optical analysis

Recovery of the impact damage area has been first quantified for *GF-Epoxy* specimens, which were used to demonstrate the capacity of the SMAs to close cracks only (no healing matrix and thus no crack sealing could occur). Optical images were binarized and the impact damage isolated; the comparison of the impact area before (*Virgin*) and after (*Heat treated*) thermal mending allowed determining the SMA capacity to close cracks, which changed the image light contrast and thus the binarization threshold (Figure 6.17). This experiment is similar to the preliminary study presented in section 6.3.1, however the composite was here made of the epoxy resin used to create the epoxy-PCL healing blends (i.e. cured with DDS). As this epoxy is tougher than that cured with DETA, the observed damage areas for each impact energy in Figure 6.17 are smaller as compared to Figure 6.14.

Subjecting the specimens to a thermal treatment at 150 °C for 30 minutes demonstrated little recovery for impacts at 8.5 J whereas no impact damage recovery was observed at higher energies. This behaviour, not in accordance with the preliminary study presented in section 6.3.1 was attributed to the difference in toughness between the two epoxy matrices, but also to the different curing conditions. Indeed, specimens in the preliminary study (see section 6.3.1) have been post-cured at 45 °C before impact. Subjecting those specimens to a thermal treatment at 150 °C after impact could therefore have annealed internal stresses, which reduced the damage area. The contrast obtained by this optical analysis might not have been strong enough to detect visual differences in crack closure within impacted specimens.

Recovery of impact damage area by optical observations was further assessed for *GF-Epoxy-PCL* specimens and is shown in Figure 6.18 for the three impact energies before (*Virgin*) and after (*Heat treated*) the thermal mending cycle

at 150 °C for 30 minutes. As compared to *GF-Epoxy* specimens, which are relatively translucent (see Figure 6.16), *GF-Epoxy-PCL* specimens are opaque due to the PCL. Full recovery of impact damage was observed for low impact energy (8.5 J) whereas at higher impact energy, a trace of the impact, even though smaller than the initial impact, was still present after the thermal mending cycle. Incomplete recovery at high impact energy levels was attributed to fibre rupture and larger crack formation, which could not be healed due to the limited expansion capacity of PCL. Isolating the impact damage through binarization was not possible for *GF-Epoxy-PCL* (see Figure 6.18) due to the opacity of the specimens and thus no healing efficiency could be quantified. No conclusion could therefore be drawn on the SMA crack closure ability in impact damage specimens and improved PCL healing capacity as: (i) the crack closure behaviour in *GF-Epoxy* specimens could not be confirmed and (ii) the impact could not be isolated in *GF-Epoxy-PCL*, thus no healing efficiency quantified. Quantifying the ability of SMA stitches to close impact damage events in composites through optical image observation was thus limited by the contrast difference in transparent as well as in opaque specimens, a technique like C-scan would thus be of higher interest to exactly determine the damage contour. Impact damage recovery by means of C-scans is presented in the next section.

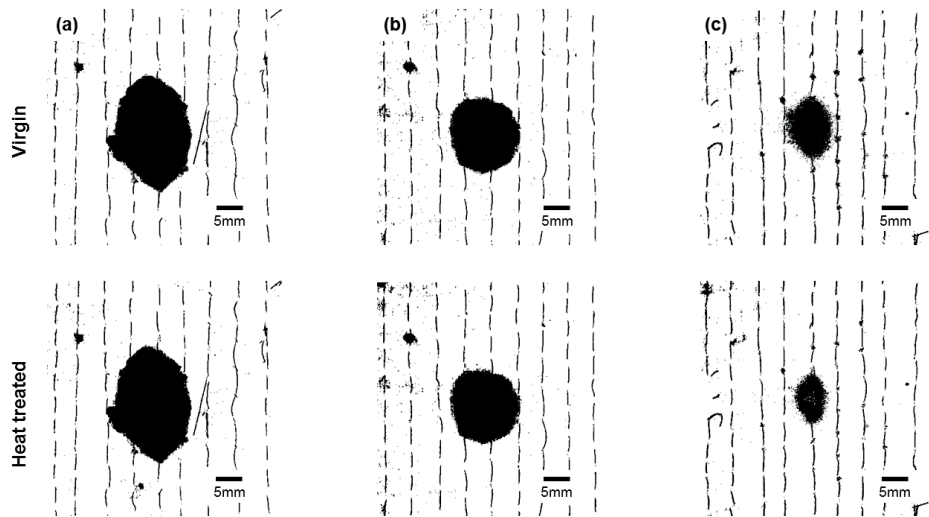


Figure 6.17: Binarized optical image of impacted *GF-Epoxy* specimens, at nominal impact energies of (a) 34, (b) 17 and (c) 8.5 J. Images are shown before (*virgin*) and after (*heat treated*) a thermal mending cycle of 30 minutes at 150 °C.

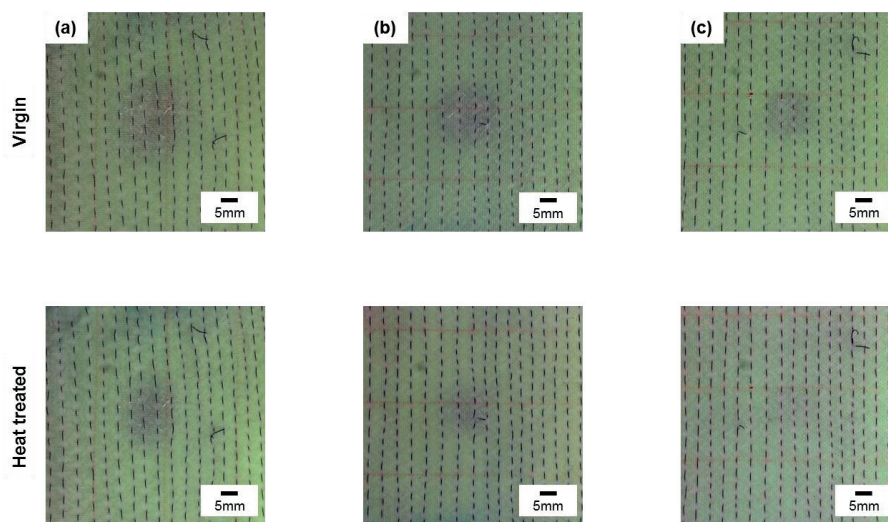


Figure 6.18: Front face optical image of impacted *GF-Epoxy-PCL* specimens, at impact energies of (a) 34, (b) 17 and (c) 8.5 J. Images are shown before (*virgin*) and after (*heat treated*) a thermal mending cycle of 30 minutes at 150 °C.

6.3.4 Impact damage recovery through C-scan analysis

C-scans of the damaged specimens confirmed the damage area to increase with increasing impact energy. The damage areas in *GF-Epoxy-PCL* FRPs were greater than those in the *GF-Epoxy* FRPs by factors of 1.5, 1.6 and 4.6 for impact energies of 34, 17 and 8.5 J respectively (see Figure 6.19 where the damage areas determined in section 5.2 for FRPs without SMAs are also shown). The greater damage areas for *GF-Epoxy-PCL* were again attributed to the lower intrinsic toughness and strength of the matrix. However, whereas at low impact energies, damage in composite laminates is generally dominated by matrix cracking and the damage area depends strongly on matrix properties, delamination and fibre damage are more extensive at higher impact energies, and the damage area increasingly depends on the properties of the fibres. This accounted for the relatively large differences in the response of the *GF-Epoxy-PCL* and *GF-Epoxy* FRPs at low impact energies. Overall, the damage areas were similar to those obtained with previous investigations on FRPs without SMA wires (see section 5.2 which values are also reported in Figure 6.19), with the exception of *GF-Epoxy-PCL* at an impact energy of 34 J, for which the damage area was reduced by a factor of about 1.5 in the presence of the SMA wires. The impact damage area was therefore not greatly affected by the presence of the SMAs up to a certain damage threshold, above which the stitched SMA wires were inferred to limit the growth of fibre dominated damage. The insensitivity of the damage area to the presence of stitched SMA wires at low impact energies was also demonstrated by Vachon *et al.* [235] for similar systems. In the present case, the position of the point of impact with respect to the lines of SMA stitches was found to influence the shape of the damage zone, but not the damage area itself, and is therefore not taken into account in the remainder of this discussion (see section 6.3.2) even though it may have contributed to the observed standard deviation.

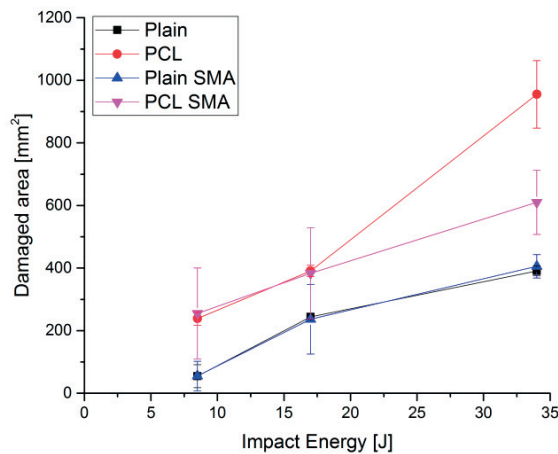


Figure 6.19: Damage area measured by C-scan analysis as a function of the impact energy, for *GF-Epoxy-PCL* (named *Plain SMA*) and *GF-Epoxy* (named *PCL SMA*) SMA stitched FRPs, and compared to the ones for *Plain* and *PCL(25)* FRPs without SMA wires determined in section 5.2.

Both the *GF-Epoxy* and *GF-Epoxy-PCL* FRPs were subjected to thermal healing. Although effective healing was not expected for the *GF-Epoxy* matrix, the SMA wires were still potentially able to close cracks in the damage zone, and hence restore transmission of the C-scan sound wave after the healing treatment. In these specimens, the apparent healing efficiencies, expressed as the ratio of the damage area in the healed state to that immediately after impact, were $34.7 \pm 1.3\%$, $76.4 \pm 3.6\%$ and $99.8 \pm 0.3\%$ for impact energies of 34, 17 and 8.5 J, respectively. The lack of apparent healing at the higher impact energies was assumed to be due to the presence of larger cracks, a loss in the closure capacity of the SMA wires, which broke at extensions greater than $370 \mu\text{m}$ (i.e. at their failure strain of 7.4%), and increased deformation and breakage of the glass fibres and SMA wires, preventing full crack closure.

Damage recovery was more extensive in the *GF-Epoxy-PCL* FRPs stitched with SMA wires, for which the healing efficiencies were $48.7 \pm 3.5\%$, $85.3 \pm 4.1\%$ and $99.8 \pm 0.3\%$ for impact energies of 34, 17 and 8.5 J, respectively. Examples of C-scans for *GF-Epoxy-PCL* specimens before (*Damaged*) and after the healing cycle (*Healed*) are given in Figure 6.20 for the three different impact energies. The colours represent the sound intensity and damaged regions were defined to regions in which 80% of the transmitted sound intensity was lost. The higher healing efficiencies in *GF-Epoxy-PCL* than in *GF-Epoxy* were attributed to the expansion capacity of PCL (14% at 150 °C), which could theoretically bridge cracks with crack face separations of between 93 and 126 μm depending on the damage level (as estimated, like in section 5.2, from the free surfaces available for the thermoplastic to expand, the overall specimen dimensions, and the damage area determined by C-scan, and assuming that the damage area was the same for every layer of the specimen). The lack of healing at higher impact energies was again attributed to increased deformation and fibre breakage, which prevented full crack closure.

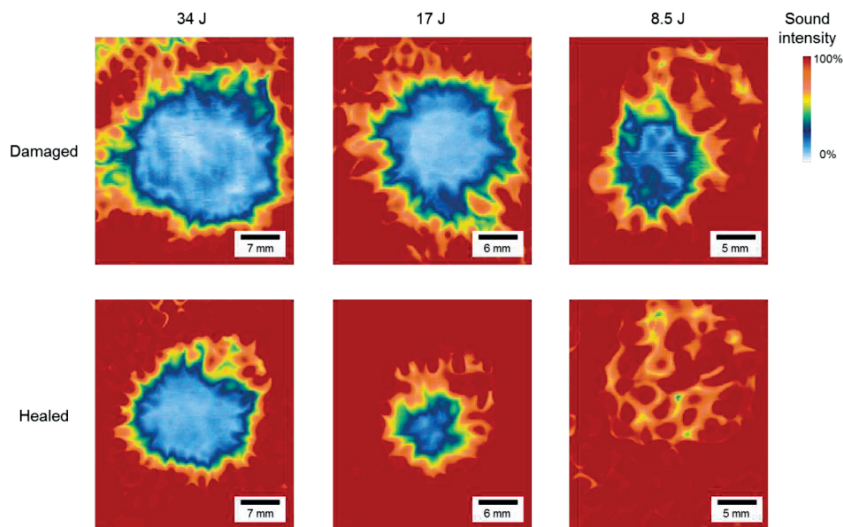


Figure 6.20: C-scan images of *GF-Epoxy-PCL* FRP specimens containing SMA wires after impact (*Damaged*) and after impact followed by a thermal mending cycle of 30 minutes at 150 °C (*Healed*) for impact energies of 34, 17 and 8.5 J.

The capacity of both systems (*GF-Epoxy* and *GF-Epoxy-PCL*) to recover from impact damage after a thermal mending cycle at 150 °C for 30 minutes was also compared with previous observations (Figure 6.21) from the same systems without SMA wires (determined in section 5.2) (for *GF-Epoxy* without SMA wires, the damage recovery was null and is thus not shown here). Overall, the damage area recovery increased by up to 55% on introducing stitched SMA wires to *GF-Epoxy-PCL* composites, demonstrating synergy between the healing effect of the matrix and actuation of the SMA. From the previous investigations (see section 5.2) of the systems without SMA wires, the recovery of resistance to compression after impact is also expected to scale in a similar manner.

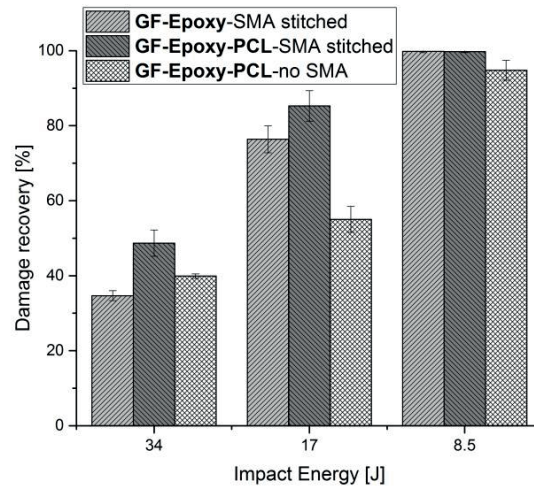


Figure 6.21: Comparison of damage area recovery in composites containing stitched SMA wires (*GF-Epoxy-SMA stitched*, *GF-Epoxy-PCL-SMA stitched*) and composites without SMA wires (*GF-Epoxy-PCL-no SMA*, from section 5.2), for three different impact energies.

6.4 Conclusion

Combining stitched SMA wires with an epoxy-PCL healing matrix in FRP composites provides the structure with the capacity to close and seal cracks after a damage event on heat treatment at a moderate temperature. SMA stitched glass fibre-reinforced epoxy-PCL composites with fibre volume fractions around 50 vol% were successfully processed through semi-automatic sewing of the SMA wires on the dry fabric followed by the VARIM process at elevated temperature. Through pull-out testing, it has been demonstrated that wires can debond in FRPs when placed perpendicular to the fibres whereas the wire deformation was completely blocked in the bend stitches. In a stitched composite, this anchoring should ensure uniform strains in the SMA across the whole of the FRP specimen thickness, leading to enhanced crack closure capacity after a damage event. This led to formulate a stitching pattern with a point density of 700 SMAs/m², which could provide recovery forces up to 4000 N/m². This design demonstrated, in Mode I crack propagation, that for a crack opening of 200 µm, SMA wires were overall able to bring the crack faces in close contact when activated through the heat treatment and over at least three cycles. The repair capacity of these smart specimens was then demonstrated for low-velocity impacts at three energy levels (34, 17 and 8.5 J). C-scans of the impact damage were performed before and after a thermal mending cycle at 150 °C for 30 minutes on stitched composites with a pure epoxy matrix but also on those with the epoxy-PCL healing matrix. The SMA stitched composites made of the pure epoxy matrix demonstrated a damage area recovery from 35 up to 100% depending on the impact energy level, thus SMA stitches had the ability to close and bring into contact crack faces thanks to their shape memory effect. It was finally demonstrated that cracks could be sealed and the damage area recovery improved with the epoxy-PCL healing matrix as the use of this matrix in SMA stitched composites demonstrated a recovery ranging from 50 up to 100% depending on the impact energy level thanks to the capacity of the PCL to expand within the crack and seal it. At 17 J energy, the recovery represented a 55% improvement over unstitched epoxy-PCL composites, and degrees of healing well beyond those hitherto reported for this range of impact energies.

This approach hence provides a potential solution to one of the major current issues in ensuring adequate composite service lives, namely matrix microcracking subsequent to low-velocity impact damage. The fibre-reinforced epoxy-PCL composites stitched with SMA wires described here have compressive strengths similar to those of conventional FRPs, and show almost complete recovery from impact damage events with energies of up to 17 J, without the need to include ancillary pumping devices. This achievement is possible through the combined effect of: (i) an epoxy-PCL healing matrix that is able to repeatedly expand and fill microcracks after multiple damage events; (ii) stitched SMA

wires that autonomously close cracks whose initial crack face separation is too large to be effectively filled by expansion of the PCL. These smart materials are particularly promising for composite structures that are not easily accessible to repair. Moreover, they may be produced using techniques close to conventional industrial processes, and show acceptable levels of initial damage resistance and improved damping properties.

Chapter 7 Alternative methods for PCL introduction to FRPs

Using phase-separated Epoxy-PCL blends as a matrix for FRPs demonstrated the resistance to crack propagation (i.e. toughness) to be reduced as compared to conventional pure epoxy FRPs (see Chapter 5). In the present chapter, two alternative methods to introduce the PCL into FRPs are proposed. The first one (section 7.1) consists in producing PCL microparticles and inserting them within the composite, using epoxy resin and curing conditions that avoid phase separation and keep the PCL intact within the structure. The second approach (section 7.2) consists in using the PCL as nanofibre veils to be inserted in between each layer of the FRP prior to resin infusion and tuning the obtained morphology by varying the curing conditions.

7.1 PCL microparticles introduction to FRPs

This section focuses on the integration of PCL microparticles into woven E-glass reinforced epoxy to assess healing through DCB experiments. An oil-in-water solvent evaporation technique is employed to create microparticles from PCL pellets without affecting their intrinsic properties. A method of integration of these microparticles within the composite prior to processing, consisting in the functionalisation of the reinforcement fabrics by manual sieving, is then explored, based on previous studies [216], [217]. The VARIM process and the composite cure were performed at low temperature to avoid phase separation of the thermoplastic so as to solely assess the thermoplastic second phase addition in the matrix (as opposed to Chapter 5 and Chapter 6). Notice that this work was performed in collaboration with Erica Manfredi and also presented in her thesis work, as an alternative to capsule based healing [56].

Three types of composite plates were produced varying the loading of PCL microparticles: 0, 15 and 30 wt% over the local ply matrix. For comparison, one composite plate containing a PCL film of 150 μm thickness in the middle layer was produced. FRPs preparation for DCB specimens production followed the same procedure as presented in Chapter 3. The PCL microparticles were sieved into the central ply of the preforms on a surface of 40x300 mm^2 next to the release film used to create the starter notch, which reduced considerably the material amount to use without affecting the measured toughness properties (for the composite with PCL film, this last was applied on the preforms and covered the same surface as microparticles). The composites were cured for 24h at 25 $^{\circ}\text{C}$ followed by a post-cure at 45 $^{\circ}\text{C}$ for 24h, which allowed complete polymerisation of the matrix (from the work of Kirkby [6]) while avoiding melting of the PCL. For more details on the preparation of the specimens as well as characterisation methods leading to the results presented hereafter, the reader is referred to Chapter 3.

7.1.1 PCL microparticles production

The PCL used ($M_n \approx 45,000 \text{ g/mol}$) was initially under the form of pellets. Microparticles of PCL with diameters ranging from 125 to 250 μm were thoughts as model system, and to provide a compromise between resistance to crack propagation and melt flow during healing. Three procedures were tested to produce these microparticles: (i) grinding and “freeze grinding” PCL pellets with pestle and mortar, (ii) oil-in-water emulsion as for self-healing microcapsules [209], (iii) oil-in-water solvent evaporation. The PCL being extremely soft, grinding or even freeze grinding with the help of liquid nitrogen did not allow the formation of PCL particles. Therefore, the same technique as that used for the production of EPA filled microcapsules with a UF shell was assessed [209] (point (ii) above), except that EPA was replaced by PCL and the UF component was removed. The procedure consisted in mixing PCL with EMA (ethylene maleic copolymer solution) and H_2O at 80 $^{\circ}\text{C}$ with an overhead stirrer at 400 rpm. During cooling, PCL aggregated and

formed a solid mass. This aggregation could come from a too weak dispersing agent; therefore EMA was replaced by SDS (sodium dodecyl sulphate). Some particles in the right range of diameters were obtained with SDS, but most of it aggregated as in the previous case. A third procedure (point (iii)) was thus assessed to create these microparticles. This procedure was similar to an oil-in-water emulsion except that PCL was initially dissolved in dichloromethane (DCM) before creating the particles in an emulsion and evaporating the used solvent. This procedure was described by Tuli *et al.* [321], [322] and was as follows:

- Dissolution of PCL (300 mg) into DCM (3mL) using a stirrer;
- Add the dissolved PCL into 1% (w/v) aqueous PVA (40 mL) solution;
- Stir the emulsion at 1300 rpm (defined for the targeted diameter, but could be increased-decreased for smaller-bigger diameters) with an overhead stirrer for 4 hours until all DCM was evaporated;
- Wash the obtained particles with H₂O;
- Leave the particles to dry for 24h;
- Sieve the particles to obtain the diameter range of 125-250 μm .

Notice that the emulsion foamed extensively during stirring at 1300 rpm. Similar to the case of microcapsules production [209], 4 drops of octanol were added into the emulsion to prevent foaming so as to reach higher production rates.

Diameters of the obtained microparticles were controlled by optical microscopy; an example is given in Figure 7.1.

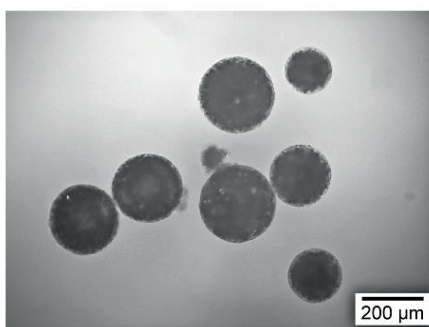


Figure 7.1: Optical microscopy of PCL microparticles prepared by an oil-in-water solvent evaporation technique after sieving in the range 125-250 μm .

Tuli *et al.* [321], [322] stated that 4 hours are enough for solvent evaporation, but this needed to be confirmed to ensure that no solvent was left around the obtained particles. In addition, the effect of octanol on the obtained microparticles had to be assessed. DSC analysis was performed on three different specimens: (i) PCL as received by the manufacturer, (ii) PCL microparticles formed by following exactly Tuli *et al.* procedure, and (iii) PCL microcapsules formed by following Tuli *et al.* procedure and adding drops of octanol to prevent foaming. Sets of the three specimens underwent a temperature ramp from -150 to 150 $^{\circ}\text{C}$ at 10 $^{\circ}\text{C}/\text{min}$ to cover T_g , T_m as well as T_c of PCL. Superimposing the different heat flow curves (see Figure 7.2) showed that neither the T_g nor the T_m of the three PCL specimens were affected. A small difference in the crystallisation temperature was observed for the PCL in the "as received" state, and was attributed to potential treatments applied during manufacturing, which were erased during dissolution of PCL prior to microparticles formation. Characteristic temperatures of PCL were not affected by the oil-in-water solvent evaporation process, and thus a priori neither the molecular weight nor the mechanical properties. The oil-in-water solvent evaporation process tuned by octanol is thus an efficient technique to produce microparticles of PCL, where diameters can be varied by varying the process stirring rate.

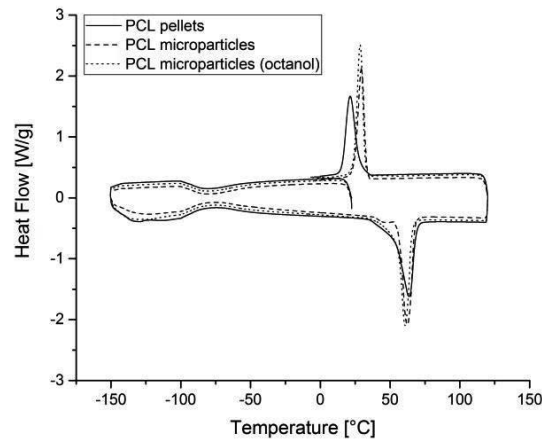


Figure 7.2: Heat flow curves for: (i) PCL pellets, as manufactured, (ii) PCL microparticles after oil-in-water solvent evaporation (PCL microparticles), (iii) PCL microparticles after oil-in-water solvent evaporation tuned with octanol (PCL microparticles (octanol)).

7.1.2 Fracture properties in the virgin state

Figure 7.3 shows the measured interlaminar fracture toughness in Mode I DCB tests for various particle loading conditions. The corresponding values are presented in Table 7.1 where the volume fraction of each tested system is also shown. Interlaminar fracture toughness of the FRPs was decreased by 10 and 80% for particle loadings of 15 and 30 wt% respectively. The literature presented in Chapter 2 showed that thermoplastic particles inside FRPs are used to increase interlaminar fracture toughness of the part [243]. However, this is normally achieved through phase separation leading to a matrix of epoxy with small thermoplastic particles well bonded to the epoxy. Bonding between the epoxy resin and the PCL is thus not sufficient here due to the low process temperature. Also, microparticles are usually in the order of a micrometre in diameter to provide toughening and were thus here too large [243]. The phenomenon of reduced toughness due to crack propagation between the continuous phase and the particulate reinforcing phase was also well investigated by Smith in his thesis work [323]. Interlaminar fracture toughness of the composite specimens containing the PCL film showed a value of $219.7 \pm 95.5 \text{ J/m}^2$, similar to the specimens with PCL microparticles loading of 30 wt%, and was again explained by a lack of bonding between PCL and epoxy.

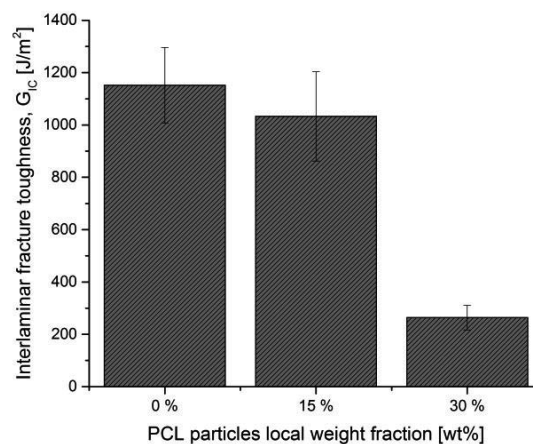


Figure 7.3: Interlaminar fracture toughness for specimens tested in Mode I, as a function of the local capsule weight fraction.

Table 7.1: Mode I interlaminar fracture toughness values of specimens containing 0, 15, 30 wt% PCL microparticles over the local ply matrix. Relative fibre volume fractions are also indicated.

Particles local fraction [wt%]	V_f [%]	Interlaminar fracture toughness [J/m^2]
0	55.0 ± 0.010	1152.0 ± 143.9
15	45.2 ± 0.027	1032.8 ± 170.7
30	51.8 ± 0.029	263.9 ± 46.8

7.1.3 Fracture properties in the healed state

After testing the virgin properties, the specimens were heated during 30 minutes at 150 °C before another loading-unloading cycle to assess healing. Notice that specimens were left as unloaded during healing but only with the crack faces imposed to be in contact at the position of the loading blocks in order to reduce the crack size to nearly 100 μm . Typical loading-unloading cycles for virgin and healed specimens are superimposed in Figure 7.4 for one specimen loaded with 30 wt% particles in the FRP. As expected, the presence of the stick-slip behaviour, typical for FRPs [65], [324], was observed during virgin testing. Some recovery of the resistance to crack propagation was observed by comparing the slopes of the virgin and healed cycles, and could be quantified.

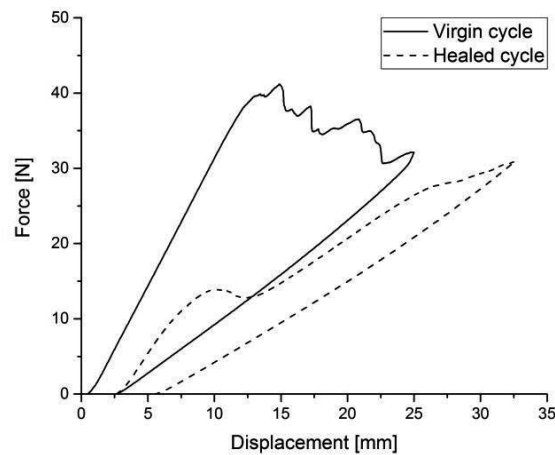


Figure 7.4: Typical DCB curves showing the loading/unloading cycles of virgin and healed composite specimens, typical specimen modified with PCL particles 30 wt%.

Whereas healing efficiency in terms of interlaminar fracture toughness could not be determined due to the impossibility to follow the crack advancement during the test in the healed state, healing efficiency in terms of stiffness could be determined and was of $30 \pm 19\%$ and $34 \pm 18\%$ for respectively 15 and 30 wt% microparticles loading. Two main factors could explain these low healing efficiencies: (i) impossibility for the PCL to flow into the crack at the healing temperature; (ii) impossibility for the PCL to fill the crack gap. These elements are further detailed below:

- (i) Viscosity measurements (by plate rheometer AR 2000 from *TA Instrument* at a frequency of 1 s^{-1} and at 150 °C), showed a value for the PCL of 39.5 Pa·s, corresponding to the thermoplastic EVA assessed by Pingkarawat *et al.* [188] where full recovery of fracture properties was observed. The viscosity of PCL was therefore enough low at the healing temperature to flow and wet the crack faces. However, it was shown in section 5.2.3 that efficient healing is also contingent on the presence of a continuous phase, which was not the case here.

- (ii) From the study of Rodgers [285] and section 5.2.3 of the present work, it was possible to determine the PCL expansion ability at the healing temperature. In the present case, PCL would have had the ability to expand by $30\ \mu\text{m}$ on both crack faces if the PCL was as a continuous phase, which was not the case due to the nature of the particles. However, non-zero efficiency values were obtained as the reduced thickness close to the crack tip could be healed. PCL particles could melt and provide some flow and thus partial coverage of the crack faces during healing, which was observed by SEM (see Figure 7.5).

Notice finally that for the composite plate containing the PCL film, the obtained healing efficiency was of $102 \pm 4\%$. This full recovery of property was explained by the ability of the PCL to flow as it was present on the entire crack surface.

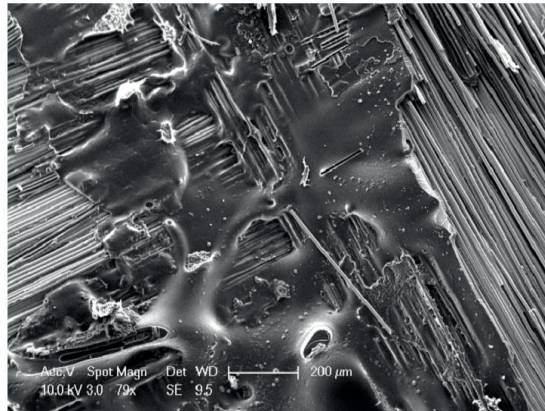


Figure 7.5: SEM image of the crack face of a specimen containing 30 wt% PCL particles over the ply matrix. Prior to imaging, the specimen has been tested, healed and re-tested.

7.1.4 Conclusion

This small benchmark on PCL microparticles integration into FRPs raised the importance of the molecular interactions that can happen between PCL and epoxy (through phase separation or not) as low fracture toughness and healing properties were demonstrated in the present case. Also, it confirmed that efficient healing is clearly contingent on the presence of a continuous PCL phase to allow volume expansion. Two paths are thus favoured to use PCL as healing agent in FRPs: (i) allowing molecular interaction between PCL and epoxy in the melt state (without phase separation) by increasing the curing temperature above the melting temperature, as performed in the study of Pingkarawat *et al.* [188] for other thermoplastic systems; (ii) creating a blend of epoxy and PCL through phase separation, as performed in the study of Luo *et al.* [7] and seen in the present work through Chapter 4 to Chapter 6. Using PCL as nanofibres in combination to a phase separation process is explored in the next section as it may allow the presence of the PCL as a continuous phase and thus provide both toughness and healing of the composites for the ultimate combined philosophy of damage prevention with damage management.

7.2 PCL nanofibre enhanced E-glass/epoxy composites

(Adapted from ref. [325]: A. Cohades, L. Daelemans, C. Ward, T. Meireman, W. Van Paepegem, K. De Clerck, V. Michaud, "Size limitations on achieving tough and healable fibre-reinforced composites through the use of thermoplastic nanofibres," *SUBMITTED, 2017*)

This section explores the potential of using PCL under the form of nanofibres to provide toughening to FRPs while keeping the healing functionality seen through Chapter 4 to Chapter 6. Indeed, in those chapters, reduction in toughness was highlighted as the major drawback of epoxy-PCL FRPs. It is proposed to interleave high enough amounts of PCL nanofibres into woven E-glass fibre epoxy composites to obtain phase-separated microstructures as obtained through Chapter 4 to Chapter 6. A PCL of molecular weight $M_n \approx 80,000$ g/mol (vs. $M_n \approx 45,000$ g/mol used previously for phase-separated blends) is used which is necessary to reach a stable and continuous electrospinning process. This higher molecular weight PCL demonstrated phase-separated microstructures with epoxy resin [135], [136] and healing properties as indicated earlier, in bulk epoxy specimens made from a phase-separated blend (see section 4.1.2). By keeping the cure temperature close to the PCL melting point (using a different epoxy resin than in Chapter 4 to Chapter 6, *RIM 135* cured with *RIMH 137*), the possibility to reach a biphasic matrix structure made of both (i) a phase-separated morphology consisting of epoxy particles and a surrounding PCL matrix that can be efficient for crack healing and (ii) a nanofibrous PCL structure barely affected by the curing process, which can provide toughening to the composite part, is investigated. This would allow the design of FRP applications combining improved damage tolerance as well as autonomous repair when necessary. This concept was first explored with bulk resin specimens through thermal and microscopy analysis to assess the influence of nanofibres on the phase separation process. FRPs were then processed with the VARIM process and interlaminar toughness of the produced composites was assessed through Mode I DCB experiments. The specimens were finally subjected to a thermal mending cycle at 150 °C for 30 minutes to investigate their crack healing capacity.

Four types of model samples made of nanofibres and epoxy resin with two different compositions (20 or 25 vol% of PCL nanofibres with respect to epoxy resin) and two curing conditions to obtain phase-separated microstructures (60 °C or 80 °C curing for 24h followed by a post-cure at 80 °C for 15h) were produced. Phase separation was assessed by DSC and microscopy analysis. Five composite plates were then produced by the VARIM process, and their different process conditions, content, final fibre and nanofibre volume fractions are summarized in Table 7.2. PCL nanofibre veils of 30 gsm were placed in between each dry reinforcement layer using a template to ensure their exact positioning. A part of the plate without nanofibres was used to provide reference (non-modified) specimens. A target glass fibre volume fraction of 50 vol% and a final plate thickness of 5 mm were sought, which corresponds theoretically to nearly 20 vol% of PCL nanofibres with respect to the total epoxy matrix volume. Infusion was performed with the epoxy resin at room temperature (to avoid any PCL melting and diffusion) before placing the composite plate to cure at the desired temperature (room temperature, to fully preserve the nanofibres and provide comparison with previous work [11], 60 or 80 °C to cure close to or above the melting point of PCL) for 24h. An additional composite plate with two PCL nanofibre veils of 30 gsm placed in between each reinforcement layer (thus corresponding to 60 gsm of nanofibres) and cured at 60 °C was manufactured to assess the influence of the PCL volume content. Also, a composite plate without nanofibres and cured at room temperature was manufactured to have enough reference specimens. Each composite plate underwent a post-curing treatment for 15h at 80 °C. Previous work showed that after the post-curing stage, the composite had the same room temperature mechanical properties, whatever the cure temperature (room temperature, 60 °C or 80 °C). For further details on preparation of the specimens as well as characterisation methods leading to the results presented hereafter, the reader is referred to Chapter 3.

Table 7.2: Specimen designations, composition, curing conditions and the corresponding fibre volume fraction obtained after composite production as well as nanofibre (NF) volume fraction with respect to the matrix.

Specimen	Composition	Curing	Post-curing	V_f [%]	V_{NF} in matrix [%]
<i>GF-Epoxy-RT</i>	Pure epoxy	RT	80 °C	49.40 ± 0.22	0
<i>GF-Epoxy-NF-RT</i>	30 gsm NF throughout	RT	80 °C	36.41 ± 3.40	11.91 ± 1.80
<i>GF-Epoxy-NF-60</i>	30 gsm NF throughout	60 °C	80 °C	46.87 ± 1.61	17.47 ± 0.91
<i>GF-Epoxy-NF60-60</i>	60 gsm NF throughout	60 °C	80 °C	39.01 ± 2.22	22.79 ± 2.17
<i>GF-Epoxy-NF-80</i>	30 gsm NF throughout	80 °C	80 °C	45.57 ± 2.14	17.75 ± 1.54

7.2.1 Phase separation in unreinforced epoxy-PCL nanofibre blends

Figure 7.6 shows DSC heating scans for the different blends after cure, for pure PCL nanofibres and pure epoxy for comparison. Two characteristic transitions were observed for all the compositions. The endothermic peak at about 54 °C corresponds to melting of the PCL, whereas the small enthalpic peak and step-like increase in heat capacity at about 85 and 90 °C are associated with the glass transition of the epoxy. These transition temperatures were generally similar to those of the pure PCL nanofibres and pure epoxy, indicating a high degree of phase purity. However, the reduced PCL melting peak for the 80 °C specimens indicated less degree of phase purity for that condition and thus higher miscibility of the two components in the cured state. Notice that (i) the two different glass transition temperatures for epoxy are attributed to the different curing temperatures and (ii) DSC scans were also performed on bulk PCL samples (i.e. before the electrospinning process) and were similar to those of PCL nanofibres, indicating that thermal transitions are unaffected by the electrospinning process.

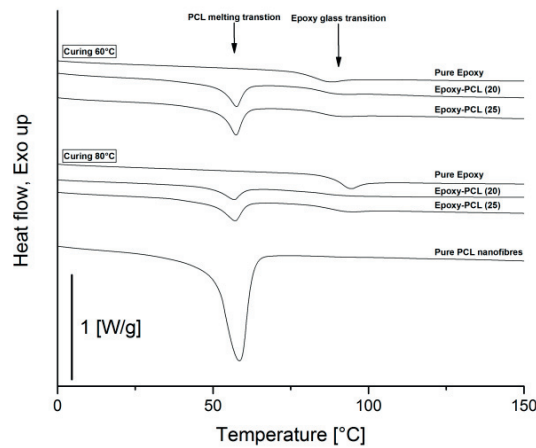


Figure 7.6: DSC heating scans for the different blends after cure. PCL volumetric ratio is shown in brackets and the curing temperatures are also indicated.

Cross-sections of the four epoxy-PCL nanofibre samples were polished and observed by optical microscopy. Figure 7.7 shows on the left an optical micrograph of an epoxy-PCL nanofibre specimen containing 20 vol% of PCL, cured at 60 °C. Three distinct regions can be observed: (i) on the left side, "Epoxy rich" region contains pure epoxy resin free of PCL; (ii) the darkest region on the right (NF Rich) shows pure PCL nanofibres within the epoxy resin and (iii) the central part "Phase-separated domains" shows two different phase-separated morphologies, epoxy particles in a PCL matrix and a domain-like morphology, as expected from Chapter 4. A close up of this micrographic map showing the transition between these two morphologies is given on the right side of Figure 7.7 and illustrates the domain-like

morphology at the bottom and the epoxy particles within the PCL matrix at the top. Epoxy particles are small and around 1 μm in diameter (smaller than the 20 μm ones obtained in Chapter 4 for similar materials) due to the interplay between reaction kinetics and PCL diffusion with the resin used here and thus the low time for nucleation and growth of the particles during phase separation. Overall, the obtained structure was not regular over the entire sample, demonstrating that epoxy resin could not dissolve all the nanofibres during the curing process, thus creating a gradient in PCL composition, resulting in different phase-separated morphologies. This irregular morphology is worth testing towards combined healing and toughness improvement as it combines phase-separated regions for healing and nanofibre regions for toughening.

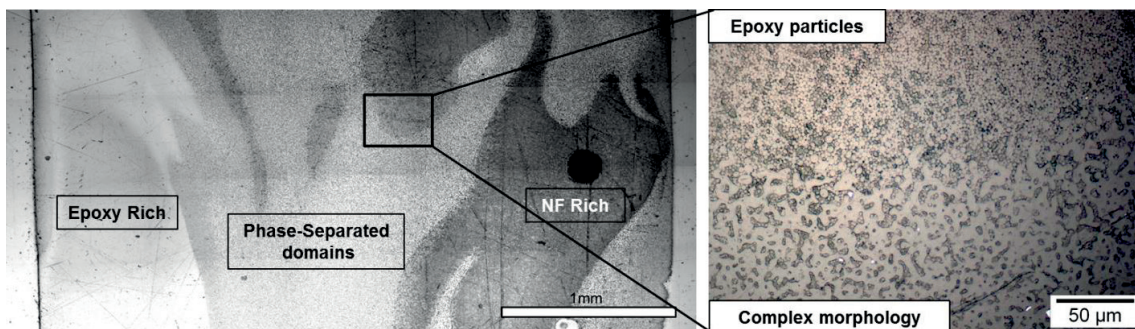


Figure 7.7: Micrographic map of PCL nanofibres (20 vol%) in epoxy resin cured at 60 °C for 24h and post-cured for 15h at 80 °C. Close up on the right showing the transition between two phase-separated morphologies.

The resin specimens were fractured and observed under SEM. Figure 7.8 (a) depicts a low magnification SEM image of the fracture surface of an epoxy-PCL nanofibre specimen containing 20 vol% of PCL and cured at 60 °C where the two morphologies observed by optical microscopy are highlighted (domain-like morphology at the top right of the image and particle-like structure everywhere else). Figure 7.8 (b), a close up of the transition between the two morphologies, confirms the PCL composition gradient observed under optical microscopy. Figure 7.8 (c) and (d) illustrate the different particle sizes, corresponding to a PCL composition gradient as distance increases from the initial veil position (the effect of the PCL blend composition on the obtained epoxy particle diameter was already well investigated in section 4.2).

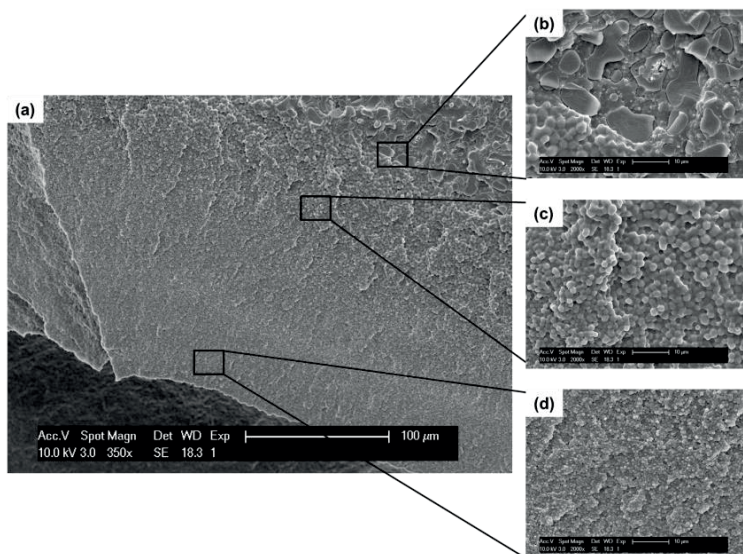


Figure 7.8: PCL nanofibres (20 vol%) in epoxy resin cured at 60 °C for 24h and post-cured at 80 °C for 15h. (a) Overall surface; (b) close up showing the complex phase-separated morphology; (c) close up showing large epoxy particles in PCL matrix and (d) close up showing smaller epoxy particles in PCL matrix.

Epoxy-PCL nanofibre specimens containing 25 vol% of PCL and cured at 60 °C showed similar microstructures but with a higher overall concentration of phase-separated epoxy-interconnected particles surrounded by a PCL co-continuous phase. Microscopy images will therefore not be depicted here. Also, the two samples cured at 80 °C contained uniform phase-separated regions (with about 1 µm diameter epoxy particles) through the microscopic analysis, demonstrating the immiscibility of the two components in the cured state, even though DSC analysis (Figure 7.6) demonstrated less degree of phase purity within these phases.

7.2.2 Fracture properties of epoxy-PCL nanofibre composites

Table 7.2 indicates the overall fibre and nanofibre volume fractions with respect to resin for each cured composite plate. While for the reference composite plate, the fibre volume fraction was close to the targeted value (i.e. 50%), it varied for the systems containing nanofibres since the nanofibrous veils obstructed nesting of the reinforcement layers during compaction, thus increased the overall thickness of the specimens. This effect was high for the plate cured at room temperature, whereas for the composites cured at 60 °C and 80 °C, it was lower as PCL nanofibres partly melted during the curing process. This behaviour influenced the volume fraction of the reinforcing glass fibres, but also the final nanofibre volume fraction with respect to the epoxy resin. At room temperature, the resulting nanofibre volume fraction with respect to the epoxy matrix was only 12% (whereas it was targeted at 20%) whereas for the composites cured at 60 °C and 80 °C, it was 18%, not differing much from the targeted value thanks to PCL melting. When using 60 gsm of nanofibres, the amount of PCL not dissolved was overall increased, thus preventing compaction which lowered the fibre as well as nanofibre volume fractions.

Figure 7.9 shows interlaminar fracture toughness mean values for the processed composites. For the reference pure epoxy composite (i.e. *GF-Epoxy-RT*), these were in the range of previous results with the same woven reinforcement (see section 5.1 and ref. [216]), but slightly higher because the epoxy resin matrix had a higher toughness than the *Epon 828* used throughout Chapter 4 to Chapter 6. When integrating 30 gsm nanofibres in between each FRP layer, toughness values increased by between 43 to 48% for the different systems. For the composites cured at room temperature (i.e. *GF-Epoxy-RT*), toughness increase was attributed to microcracks bridging by the nanofibres, similar to the work of Daelemans *et al.* [11]. For systems with 30 gsm nanofibres and cured at higher temperatures (i.e. *GF-Epoxy-NF-60* and *GF-Epoxy-NF-80*), the nanofibres have dissolved (partially) into epoxy resin before being phase-separated during cure. The resulting irregular microstructure also led to increased toughness, although with a higher observed standard deviation. When increasing the PCL nanofibres to 60 gsm (*GF-Epoxy-NF60-60*), a higher increase in interlaminar fracture toughness was demonstrated and attributed to the higher concentration of PCL as well as the higher thickness of the specimens. It is known that increasing thickness of DCB specimens increases interlaminar fracture toughness due to the increase of bending stiffness [326]. For specimens with higher nanofibre content (*GF-Epoxy-NF60-60*), nesting prevention by the nanofibres increased specimen thickness by up to 1 mm, reflecting a similar increase in interlaminar fracture toughness as in [326]. The specimen thickness variation due to the irregular microstructure also participated in the observed standard deviations. Note that specimens free of nanofibres for each curing condition provided toughness values similar to that measured on the reference epoxy composite plate, thus confirming that the different curing conditions, followed by similar post-curing, did not affect composite toughness.

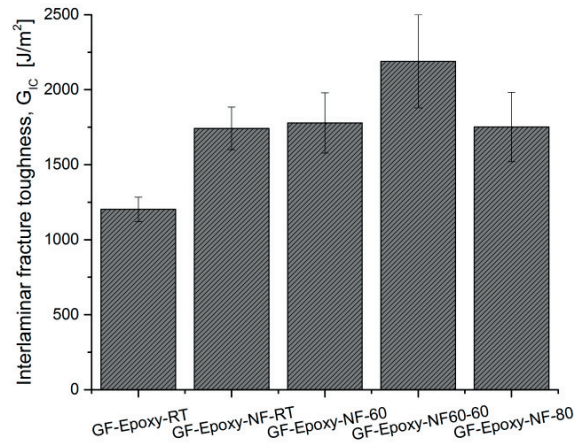


Figure 7.9: Interlaminar fracture toughness for the different assessed composites. See Table 7.2 for details on specimens naming.

Figure 7.10 shows the fracture surface of a 30 gsm nanofibre enhanced composite specimen cured at room temperature (i.e. *GF-Epoxy-NF-RT*). As expected, room temperature curing (followed by the usual post-cure at 80 °C) allowed keeping the nanofibres fibrous structure intact, in accordance with [11]. Cohesive failure of the PCL (in white) was dominant on the fracture plane, and led to the increase in toughness as compared to the reference system (see Figure 7.9). Also, many interlaminar crossings were observed which contributed to the overall failure of the PCL, as explained in [11].

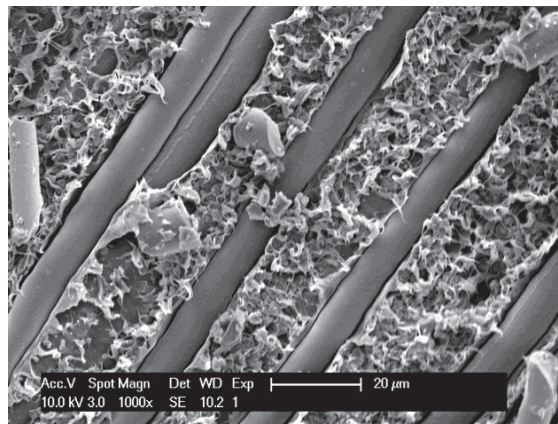


Figure 7.10: Virgin fracture surface of a nanofibre enhanced composite sample cured at room temperature (i.e. *GF-Epoxy-NF-RT*).

Figure 7.11 (a) shows the fracture surface of a 30 gsm nanofibre enhanced composite specimen cured at 60 °C (i.e. *GF-Epoxy-NF-60*). Glass fibre traces, around which nanofibrous veils were most probably shaped, are well observed. Three types of phase-separated microstructures were observed on the crack plane, illustrated in close up pictures Figure 7.11 (b) to (d). It is not excluded that some nanofibres stayed intact during the curing process (as observed in neat resin systems, see previous section); however, these were not observed on the crack plane. On the left of Figure 7.11 (a) (close up Figure 7.11 (c)), a microstructure consisting of an epoxy matrix with PCL inclusions is observed. This area corresponds to the central plane of two neighbouring glass fibres (i.e. intralaminar) where PCL can hardly be present due to the (not instantaneous) dissolution and migration process from the interlaminar region; the resulting phase separation morphology corresponds to a low thermoplastic concentration (see Chapter 4). While moving away from the intralaminar region towards the interlaminar region (i.e. at the right of Figure 7.11 (a)), a higher concentration of

PCL was present, as the nanofibrous veils were originally interleaved between the reinforcing layers. As the PCL concentration increased towards the right of Figure 7.11 (a), the domain-like morphology first appeared (Figure 7.11 (b)) before the morphology consisting of epoxy particles in a PCL matrix, characteristic of high PCL concentration, was reached (Figure 7.11 (d)). Overall, the gradient of phase-separated morphologies was consistent with that in neat resin systems (see Figure 7.8), and even though no nanofibre-like structure could be observed on the crack plane, the toughness value (see Figure 7.9) was high. When increasing the PCL nanofibre content (i.e. *GF-Epoxy-NF60-60*), the phase-separated microstructure consisting only of epoxy particles in a PCL matrix was obtained (no gradient in phase-separated morphologies), see section 7.2.3 for fracture surfaces, and also led to high toughness values. This increase in fracture toughness with phase-separated morphologies was not consistent with what has been observed throughout Chapter 4 to Chapter 6, but was attributed to the fine microstructure, where epoxy particles are around 1 μm diameter, as opposed to 20 μm in Chapter 4 to Chapter 6. In rubber modified epoxy (with phase-separated rubber particles inside a continuous epoxy phase), it is known that rubber particles of the order of 1 μm are needed to provide a toughening effect through combined shear and craze deformations [243]. However, the crack propagation mechanisms for a phase-inverted microstructure (i.e. the present case) are different as particles are the epoxy phase, in higher concentration and interconnected; to the author's best knowledge this toughening effect in FRPs has never been reported for such microstructure. Toughness increase was thus attributed to the fine microstructure which resulted in a combined effect of (i) PCL crack bridging, similar to the effect of nanofibres, as there was no statistical difference in toughness increase between the particle like morphology (*GF-Epoxy-NF-60* specimens) and the nanofibre structure (*GF-Epoxy-RT* specimens) and (ii) large scale tortuosity due to interlaminar crossing of the crack path.

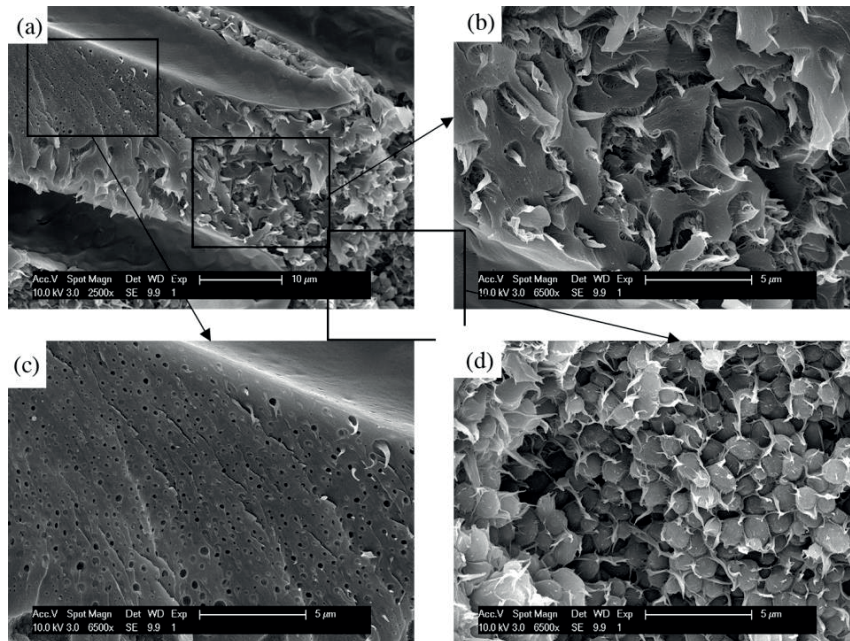


Figure 7.11: Virgin fracture surface of a nanofibre enhanced composite specimen cured at 60 °C (i.e. *GF-Epoxy-NF-60*). (a) low magnification image showing three distinct regions: (b) close up of the domain-like morphology; (c) close up of the morphology consisting of epoxy matrix with PCL particles and (d) close up of the morphology consisting of epoxy particles with a surrounding PCL matrix.

Figure 7.12 shows the virgin fracture surface of a nanofibre enhanced composite specimen cured at 80 °C (i.e. *GF-Epoxy-NF-80*). The close up on the right shows that, overall, only a fine domain-like morphology was present within this system and the toughness increase mechanism was similar to that identified for the specimens cured at 60 °C. The uniform morphology resulted from the higher curing temperature and better dissolution of PCL which could diffuse

and provide an overall constant concentration (slightly lower than the 20 vol% aimed) corresponding to that providing the domain-like structure during phase separation as opposed to an epoxy particle phase-separated microstructure.

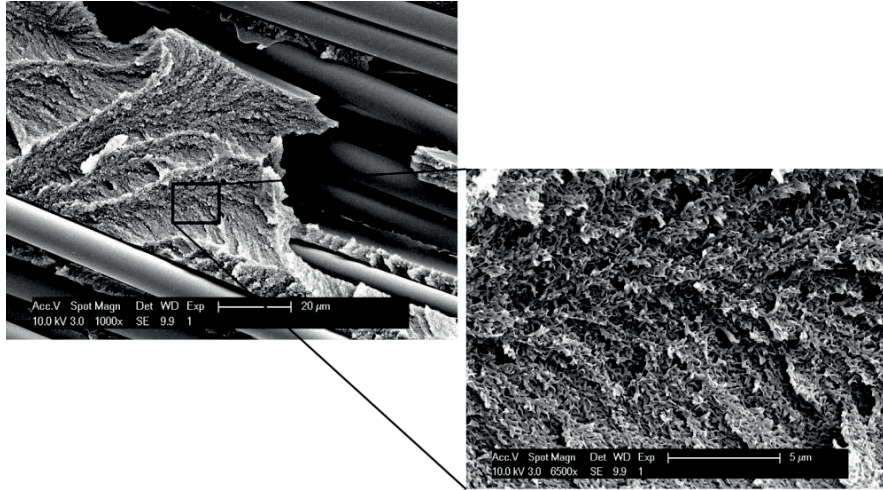


Figure 7.12: Virgin fracture surface of a nanofibre enhanced composite specimen cured at 80 °C (i.e. *GF-Epoxy-NF-80*). Close up on the right to show the domain-like morphology.

7.2.3 Healing efficiency assessment of epoxy-PCL nanofibre composites

Delaminated specimens of the different composite plates were then clamped at the loading blocks and healed at 150 °C for 30 minutes in accordance with section 5.1. A typical DCB curve showing the loading/unloading cycles of *virgin* and *healed* composite specimens is provided in Figure 7.13. The loading part of the *healed* cycle following the unloading part of the *virgin* cycle is characteristic of no crack healing. For every heat-treated specimen, such curves were obtained demonstrating that no healing could take place within the nanofibre enhanced composites.

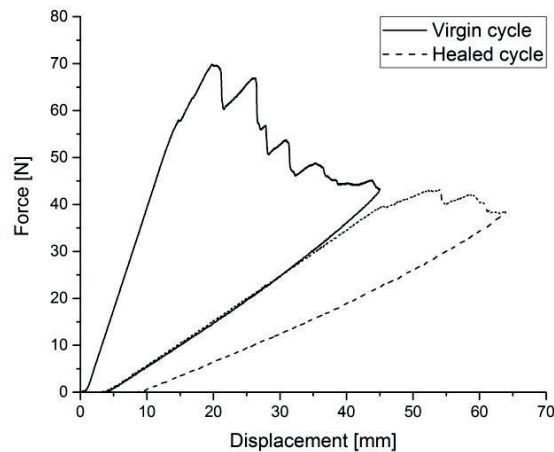


Figure 7.13: Typical DCB curves showing the loading/unloading cycles of virgin and healed composite specimen, example of a *GF-Epoxy-NF-60* specimen.

To understand the inability of the specimens to heal the propagated cracks, observations of the fracture plane after healing were performed. The analysis was restricted to specimens cured at 60 °C as these contained the phase-separated microstructure most favourable for healing applications (i.e. epoxy particles in a PCL matrix) as determined

in Chapter 4 to Chapter 6. Figure 7.14 shows the fracture surface of a nanofibre enhanced composite specimen containing 30 gsm nanofibres and cured at 60 °C (i.e. *GF-Epoxy-NF-60*), after healing and re-testing, on a region where the phase-separated morphology consisting of epoxy particles with a surrounding PCL matrix is well observed. Although some bleeding of PCL is observed which would lead to crack healing as in section 5.1, the amount of bleeding was very low, not present on the entire fracture plane and restricted to only a few microns in thickness, compared to the predicted thickness of 36 µm of PCL expected from section 5.1.

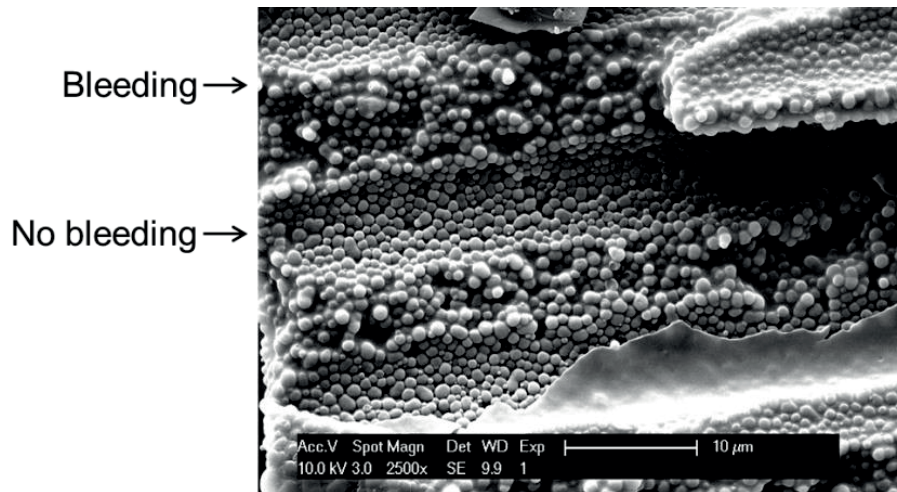


Figure 7.14: Healed fracture surface of a nanofibre enhanced composite specimen cured at 60 °C (i.e. *GF-Epoxy-NF-60*) showing the morphology consisting of epoxy particles with a surrounding PCL matrix.

A first possible explanation of the low bleeding observed here, is a lack of interconnection of the PCL phase across the entire thickness of the composite specimen, resulting in only a small volume of PCL capable to expand, since flow of PCL is obstructed in the micro-sized network. To assess this hypothesis, transverse cuts of the composite specimens were polished and observed under optical microscope. Figure 7.15 (a) shows the crack created during DCB testing at the bottom of the image and the void-free composite cut. A close up of the cross-section (Figure 7.15 (b)) confirms that a major part of the resin area appears to be phase-separated (dark grey regions). This phase-separated structure, beneficial for healing, was thus fully interconnected throughout the composite laminates and volume expansion of PCL should be able to occur. Composites containing nanofibre veils of 60 gsm (*GF-Epoxy-NF60-60*) consisted fully of phase-separated epoxy particles with a co-continuous PCL matrix (Figure 7.16 (a)), yet no significant healing could be achieved after thermal treatment in these specimens either. A close up of the fracture surface of a "healed" specimen on a resin rich region, Figure 7.16 (b), demonstrates that a small extent of bleeding took place, whereas considering the PCL concentration, its expansion capacity at the healing temperature (i.e. 14% at 150 °C) and the specimen dimensions, the crack surface should have been covered by a layer of nearly 65 µm thick (see Chapter 5 for details on this calculation). As compared to section 5.1 where a similar phase-separated morphology could bleed and provide high amount of crack healing in DCB specimens, two major physical differences should be noted: (i) PCL is introduced in the form of nanofibrous veils, where polymer chains have been stretched during electrospinning and could show some shape memory leading to shrinkage upon heating; (ii) the phase-separated morphology after curing has characteristic phase sizes of about 1 µm in diameter (compared to 20 µm found in Chapter 4 to Chapter 6) due to the curing kinetics of the resin hence the short time for nucleation and growth of the particles during phase separation. Both hypotheses are assessed in the two next sections.

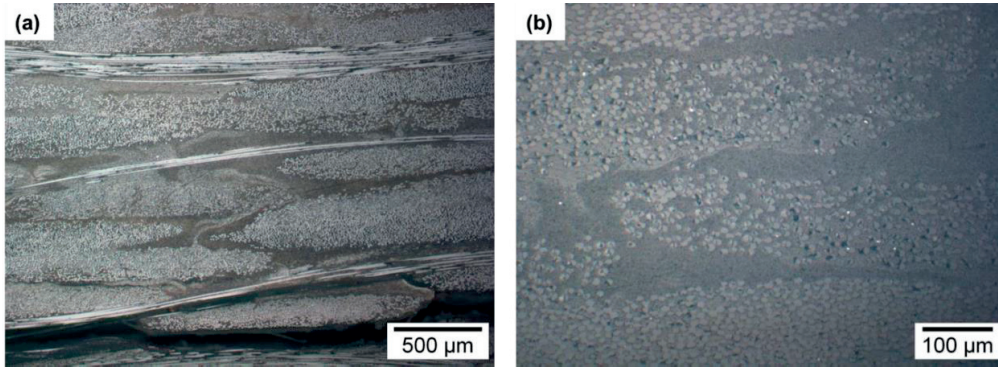


Figure 7.15: (a) Polished cross-section optical micrograph of a nanofibre enhanced composite specimen cured at 60 °C (i.e. *GF-Epoxy-NF-60*) showing phase separation on the entire specimen thickness and away from the crack path (shown at the bottom). (b) Close up of the same specimen.

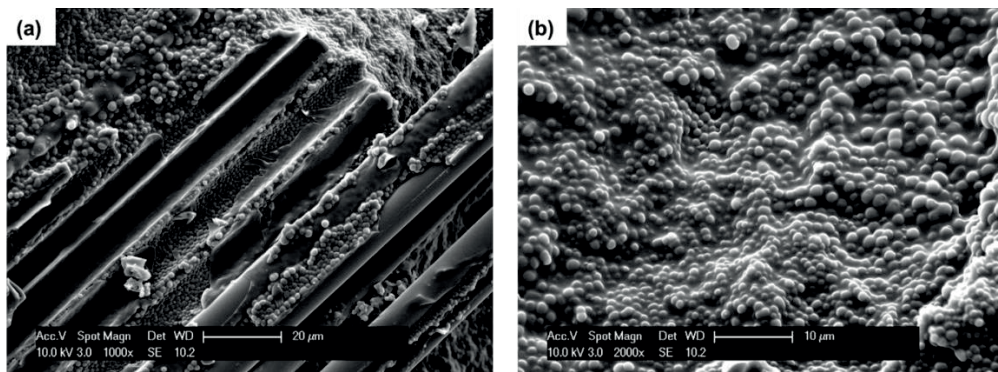


Figure 7.16: Healed fracture surface of a nanofibre enhanced composite specimen cured at 60 °C with 60 gsm nanofibres in between each fabric layer (i.e. *GF-Epoxy-NF60-60*) showing the morphology consisting of epoxy particles with a surrounding matrix.

7.2.4 Effect of nanofibre induced shrinkage on the bleeding mechanism

Hypothesis (i) (nanofibres shape memory leading to shrinkage upon heating) is first checked by considering the fracture surface of the healed sample *GF-Epoxy-NF-60* (Figure 7.17) in the region of low thermoplastic content, similar to that shown in virgin state at Figure 7.11 (a)-(b)-(c). The protruding stretched PCL observed in Figure 7.11 have indeed disappeared after healing, pointing to potential shrinkage back into the channels.

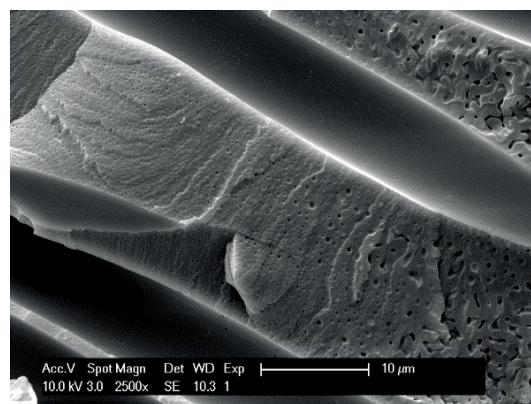


Figure 7.17: Corresponding healed fracture surface of the nanofibre enhanced composite specimen cured at 60 °C (i.e. *GF-Epoxy-NF-60*) shown previously in Figure 7.11.

To observe this shrinkage effect on nanofibre veils, small specimens (a circle and rectangular shape, see Figure 7.18 (a)) were heated to 60 °C for 1h. Due to the residual stresses contained into the nanofibres, the veils shrunk during heating (Figure 7.18 (b)). DMA tests on similar specimens, at a constant temperature of 60 °C allowed quantification of the veils contraction (Figure 7.18 (c)). Since the veils consist out of randomly oriented nanofibres, the test was not completely representative of the behaviour of single nanofibres. However, it showed that the veils shrunk considerably (about 7% in length by DMA) when they were heated near their melting point. An interesting feature of this thermal treatment is that the temperature was higher than the melting point of PCL identified by DSC analysis (see Figure 7.6) but no apparent melting of the nanofibre veils could be observed during treatment (which would result in a more transparent film-like specimen), most probably due to the high stretching of the polymer chains. In the present section, the dissolution of PCL nanofibres within the epoxy (prior to phase separation) was performed during curing of the FRPs. Due to the high viscosity of PCL and the fast curing kinetics of the resin, the residual stresses could have been locked within the microstructure. This limited their thermal expansion during crack healing at 150 °C and thus also the pressure build-up within the system which negatively affected the bleeding mechanism.

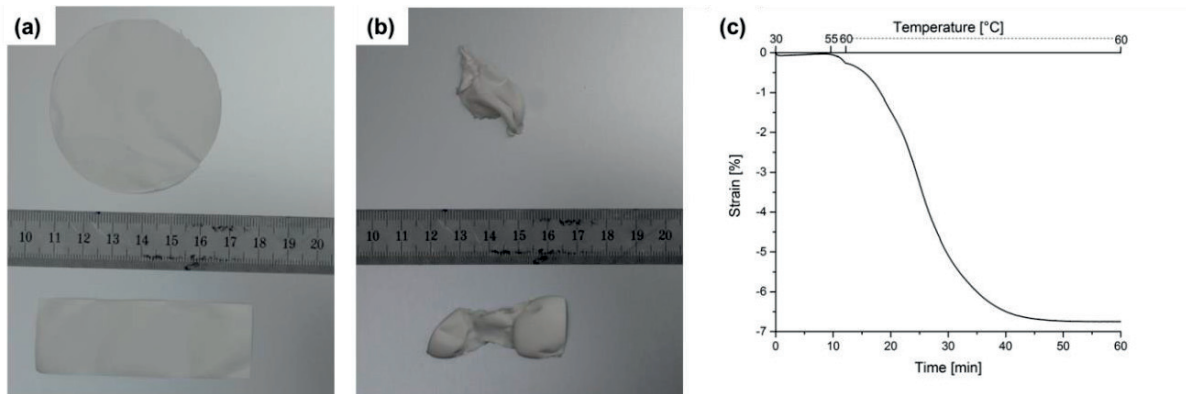


Figure 7.18: Nanofibrous veils (a) before and (b) after heating at 60 °C for 1h. (c) Corresponding cycle in DMA tension test.

7.2.5 Size effect of the particle microstructure on the bleeding mechanism

Hypothesis (ii) (fine phase-separated microstructure preventing PCL flow) was investigated by measuring the linear expansion of resin specimens during a heating ramp in the DMA. Figure 7.19 shows the obtained strain versus temperature for (i) pure epoxy used in section 4.2 (*Pure epoxy Epon 828*); (ii) pure epoxy used throughout the present section (*Pure epoxy RIM 135*); (iii) epoxy-PCL blends containing 20 vol% of PCL studied in section 4.2 (epoxy particles of 20 µm diameter) (*Epoxy Epon 828/PCL*) and (iv) epoxy-PCL blends containing 20 vol% of PCL nanofibres presented in section 7.2.1 (epoxy particles of 1 µm diameter) (*Epoxy RIM 135/PCL*). In section 4.2, the epoxy and blends were cured at 180 °C, which provided an epoxy T_g (190 °C) well above the healing temperature (150 °C) whereas in the present section, the epoxy and blends were cured at 80 °C max, which provided an epoxy T_g (90 °C) below the healing temperature. Specimens containing the epoxy *RIM 135* showed as expected a change in slope at around 90 °C corresponding to their T_g , whereas that of *Epon 828* specimens was not observed in the covered temperature range. PCL melting takes place at around 60 °C. The comparison of the slopes beyond 60 °C in both systems (as marked on each curve) reveals the PCL capacity to bleed. Indeed, in both samples containing *Epon 828* resin, without and with PCL, the slopes are similar and correspond to the CTE of the epoxy phase, as the molten PCL phase freely flows out of the epoxy network (see section 4.2). Oppositely, in specimens made with the *RIM 135* resin, the slopes differ more as the PCL, in this phase-separated system, remains retained in the confined rubbery epoxy structure, thus increasing the global specimen expansion.

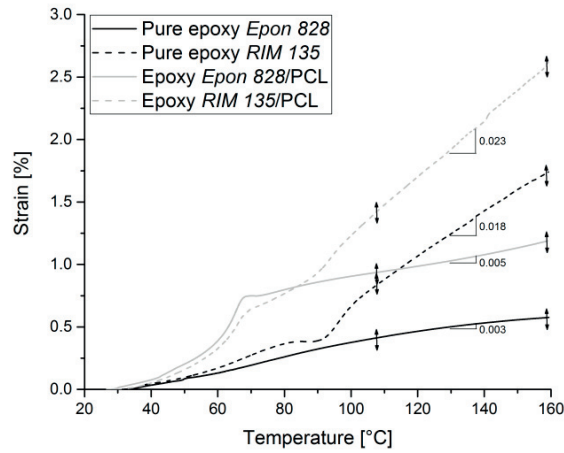


Figure 7.19: Comparison of sample strain as a function of temperature for epoxy-PCL nanofibre blends and the corresponding pure epoxy (Pure epoxy RIM 135 and Epoxy RIM 135/PCL) with samples processed in section 4.2 (Pure epoxy Epon 828 and Epoxy Epon 828/PCL). Slope of the pseudo linear plateau between the two arrows for each specimen is also showed.

In addition, flow of PCL in the porous network created by the phase-separated microstructure is possible if the pressure generated by its expansion during heating at 150 °C overcomes the capillary pressure as well as the required pressure for its flow within the channels of the porous network. The pressure generated by PCL was estimated as 184 MPa, based on its volume expansion at 150 °C (14%) and its liquid bulk modulus at the same temperature (1.31 GPa). Detailed calculations of the PCL expansive pressure and the PCL bulk modulus in the liquid state are provided in [7] and [285].

In a network of epoxy particles with 1 μm diameter, the capillary pressure reaches around 100 kPa (calculated from the *Young-Laplace* equation considering a standard PCL surface tension of around 30 mN/m). The capillary pressure is thus not a limiting factor for the PCL to flow within the phase-separated network. Then, considering the porous structure (made of particles of a given diameter D), the time t for the PCL to flow within a specimen of thickness $2L$ under a pressure difference ΔP is given by Darcy's law, using the *Carman-Kozeny* equation to describe the pore network permeability:

$$t = \frac{150\eta(1 - \varepsilon)^2 L^2}{\Delta P \Phi^2 D^2 \varepsilon^2} \quad (7.1)$$

where η is the PCL viscosity, ε the network porosity, L the flow length, ΔP the pressure drop over the porous medium, Φ the sphericity and D the particle diameter. Considering the case of a 5 mm thick DCB specimen with a propagated crack in the middle, the flow length L is assumed to be 2.5 mm. The pressure drop ΔP is assumed to be 184 MPa in the present case (even though this is a very rough upper limit as the pressure generated by PCL melting decreases during the bleeding process). As observed in Figure 7.8, the sphericity Φ of the epoxy particles can be assumed to be 1. Porosity ε is further calculated as 20.7% based on the weight fractions (20.1% of PCL for the composites with 60 gsm PCL nanofibres) and densities of epoxy and PCL (taken from section 4.2).

Figure 7.20 presents the time, calculated by Eq. (7.1), for the PCL to flow across the thickness of the epoxy particle network as a function of the particle diameter, for the case of a DCB specimen (5 mm thick, considering the PCL flow over half the specimen thickness, which provides a higher bound to the calculation). Viscosities were measured by rheological experiments in continuous mode (plate rheometer AR 2000 from *TA Instrument*) at a frequency of 1 s^{-1} and at 150 °C, and for two types of PCL: (i) that used in section 4.2 with $M_n \approx 45,000 \text{ g/mol}$ ($\eta = 39.5 \text{ Pa}\cdot\text{s}$) and (ii) that used for the nanofibres in the present section with $M_n \approx 80,000 \text{ g/mol}$ ($\eta = 4819 \text{ Pa}\cdot\text{s}$). For the high molecular weight PCL

(and thus the higher viscosity), the time to flow through half of the specimen thickness is estimated to around 100 hours, which is far more than the 30 minutes thermal treatment applied for healing. The lack of bleeding (and thus of crack healing) observed during the present assessment with DCB testing as well as on the DMA tests of Figure 7.19 (*epoxy RIM135/PCL* specimens) is thus explained by the long time required for the PCL to flow through the network of epoxy particles. Increasing the particle size would thus allow easier PCL flow (and thus higher amount of healing), decreasing to 6 minutes at 30 μm diameter. If the PCL viscosity is decreased, the overall time for the PCL to flow through the phase-separated epoxy particle network of any size is reduced, which explains the high healing capacity found for the systems studied throughout Chapter 4 to Chapter 6. Considering that toughness of the systems was reduced with epoxy particles of around 20 μm diameter (see Chapter 4 to Chapter 6), whereas in the present case, a fine microstructure (around 1 μm diameter) provided an increased toughness, using the lower viscosity PCL in FRPs with a fine microstructure through the use of PCL nanofibres could provide toughness as well as healing. However, the production of PCL nanofibres with a lower molecular weight is very challenging as molecular entanglements needed for a stable and continuous electrospinning process are not achieved, leading to unstable electrospinning behaviour.

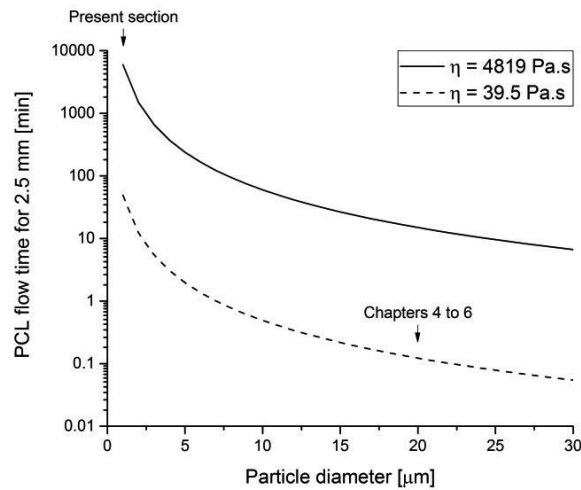


Figure 7.20: PCL flow time, calculated with Eq. (7.1), through a porous medium of 2.5 mm thickness as a function of the media particle diameter and for two different PCL viscosities. Arrows show two specific cases: (i) systems studied in the present section and (ii) systems studied throughout Chapter 4 to Chapter 6.

7.2.6 Conclusion

PCL electrospun nanofibrous veils were interleaved in glass fibre-reinforced epoxy composites in order to assess the possibility to provide both toughening and healing at the same time. Resin model samples were first produced and cured at 60 $^{\circ}\text{C}$ to obtain a combined microstructure consisting of phase-separated regions (epoxy particles surrounded by a PCL matrix) ideal for crack healing as well as retaining intact nanofibres ideal for interlaminar toughening. Thermal properties of this matrix confirmed the immiscibility of PCL and epoxy in the cured state, in principle allowing the PCL to expand and bleed to its full capacity during healing.

Glass fibre-reinforced epoxy composites interleaved with PCL nanofibres were further successfully produced by the VARIM process with a slightly lower fibre volume fraction (40%) than expected due to the use of nanofibres which prevented compaction and nesting of the glass fibre reinforcement. Mode I DCB testing revealed higher toughness (up to 48%) for the 30 gsm nanofibre enhanced composites as compared to pure epoxy composites. Crack surface analysis further showed that the use of 60 gsm PCL nanofibres and curing at 60 $^{\circ}\text{C}$ led to the presence of a fully phase-separated microstructure consisting of epoxy particles surrounded by a PCL matrix. Due to the interplay between reaction kinetics and PCL diffusion with the resin used, the epoxy particles were much smaller (1 μm diameter) than

expected from Chapter 4 to Chapter 6, leading to increased toughness of the produced specimens. The fine microstructure provided (i) microcracks bridging by the PCL and (ii) a tortuous crack path. A thermal treatment at 150 °C for 30 minutes was then applied on the specimens to assess the capacity of the PCL to bleed, flow and bridge the crack faces, thus healing the crack. However, no healing could be obtained due to two limiting factors: (i) the residual stresses in the nanofibres due to electrospinning which led to shrinkage during healing and thus limited the PCL expansion capacity; (ii) high PCL viscosity which prevented its flow in such a fine microstructure of epoxy-interconnected particles at the time scale of the healing experiment. Modelling of the flow through the Carman-Kozeny equation demonstrated that the use of a lower viscosity PCL under the form of nanofibres, should allow crack healing and high toughness properties.

Chapter 8 Cost modelling and industrial viability

Phase-separated epoxy-PCL composites (with or without stitched SMA wires) (Chapter 4 to Chapter 6), considering their manufacturing feasibility through conventional industrial processes, their mechanical properties in the range considered acceptable for structural materials and their ability to fully heal low-velocity impact damage, demonstrated strong relevance for composite structures that are subjected to moderate loads and not easily accessible to repair. However, the materials cost increase associated with these added functionalities as well as their potential to be scaled-up in terms of manufacturing and the associated cost difference need to be assessed to further validate the concept. In the present chapter, the added cost to produce FRP parts with the healing matrix (epoxy-PCL) and/or with stitched SMA wires is first calculated and the industrial viability of SMA wires stitching then demonstrated through the use of an industrial embroidery machine.

The cost modelling presented hereafter is based on the work of Verrey [327]. The production process considered is Resin Transfer Moulding (RTM) and calculations are made for a number of parts produced per year varying between 10,000 and 100,000. The smart composites studied in the present work are composed of two added functionalities: the healing matrix and SMA wires. These functionalities can be of interest when used separately or in combination and thus the cost increase related to each functionality must be assessed. Also, the production costs must be compared to a baseline product, which is defined here as an epoxy based FRP. Four scenarios are thus considered:

1. RTM with glass fibres epoxy
2. RTM with glass fibres epoxy-PCL
3. RTM with SMA stitched glass fibres epoxy
 - (i) Full stitching of the part surface
 - (ii) Stitching on 30% of the part surface
4. RTM with SMA stitched glass fibres epoxy-PCL
 - (i) Full stitching of the part surface
 - (ii) Stitching on 30% of the part surface

Notice that when integrating SMA wires, stitching over part of the surface is also considered (30% of the surface in the present scenario) as it can be of interest for practical applications where the added costs must be minimized. The present calculation considers a model part geometry, which could be used as a structural part, for example protection of sensitive equipment in a remote area where autonomous healing can be of interest (see Figure 8.1). The thickness of this part is set to 2.5 mm (half of the thickness of the specimens produced within Chapter 5 and Chapter 6) and the fibre volume fraction is set to 50% (same as in Chapter 5 and Chapter 6). The area of the part is 1,000 x 700 mm².

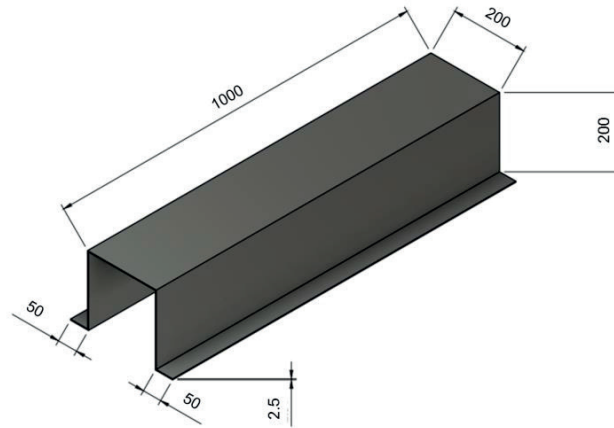


Figure 8.1: Reference part with 2.5 mm thickness.

8.1 Materials

In each of the scenarios considered, the glass fibre reinforcement is an E-glass weave 2x2 with an areal weight of 390 g/m², (as used in Chapter 5 and Chapter 6, see section 3.1.4 for material details) and its cost is set to 4 CHF/m². In each scenario, the epoxy resin (Epon 828) and hardener (DDS) are the same as in Chapter 4 to Chapter 6 (see section 3.1.4 for material details) and the overall cost is set to 10 CHF/kg (this cost is slightly larger than conventional epoxies (around 5 CHF/kg) due to the use of DDS as hardener). In the second scenario, PCL is added to the matrix at 25 vol% and the cost of PCL is set to 8 CHF/kg (source from *Perstorp*). Finally, the SMA wires are added in the third scenario, with a similar pattern as in Chapter 6 (4 x 4 mm) and the cost of the wires is set to 0.5 CHF/m (source from *Furakawa Techno Material*). Considering the part geometry (Figure 8.1), the quantity of material needed to produce one part for each scenario can be calculated (see Table 8.1).

Table 8.1: Material costs and weights according to the defined geometry (Figure 8.1). For scenarios with 30% of SMA, the cost of SMAs is simply multiplied by 30%.

	Scenario 1: RTM with glass fibres epoxy		Scenario 2: RTM with glass fibres epoxy-PCL		Scenario 3: RTM with SMA stitched glass fibres epoxy		Scenario 4: RTM with SMA stitched glass fibres epoxy-PCL	
	Weight in part [kg]	Price [CHF]	Weight in part [kg]	Price [CHF]	Weight in part [kg]	Price [CHF]	Weight in part [kg]	Price [CHF]
Glass fibres	2.18	22.40	2.18	22.40	2.18	22.40	2.18	22.40
Epoxy	1.17	11.73	0.88	8.79	1.17	11.73	0.88	8.79
PCL	-	-	0.25	2.00	-	-	0.25	2.00
SMA	-	-	-	-	0.21	231.22	0.21	231.22
Total weight [kg]	3.36		3.31		3.57		3.52	
Total price [CHF]	34.13		33.20		265.35		264.42	

8.2 Production line

The RTM production line considered is the same as the one of Verrey [327] (see Figure 8.2). It can be divided into 3 units: (i) the preforming cell; (ii) the RTM cell (with the injection unit containing 4 moulds to reach the production rate required) and (iii) the finishing cell. The costs associated with each machine as well as machine power and surface

area (important for factory costs) are assumed the same as Verrey [327] and are provided in Table 8.2. These costs are valid for *Scenario 1*, however for *Scenarios 2-3-4*, one or two additional cells must be added to this production line: (i) a mixing machine for epoxy and PCL to be blended prior to injection and (ii) a sewing (or embroidery) unit to stitch SMA wires through the dry preforms prior to infusion. The costs associated with those additional units are also shown in Table 8.2. Of importance as well is the cycle time needed to produce one part on each of the considered unit. These times, as well as the time increase for the two additional units considered, are shown in Table 8.2 and based again on [327]; however the times related to the RTM cell must be adapted considering the geometry of the part and the resin used. Considering Darcy's Law with an injection pressure of 10 bar, a reinforcement permeability as determined in [56] ($K = 5 \cdot 10^{-11} \text{ m}^2$), resin viscosity values at 140 °C of $\eta = 0.05 \text{ Pa}\cdot\text{s}$ in *Scenarios 1 and 3* and of $\eta = 0.5 \text{ Pa}\cdot\text{s}$ in *Scenarios 2 and 4* (measured by a plate rheometer AR 2000 from *TA Instrument*), and the time before demoulding corresponding to around 3 times the resin gel time (i.e. 3000s), the overall RTM cell cycle time is 3250s for *Scenarios 1 and 3* and 5500s for *Scenarios 2 and 4*. Those times are unrealistic for a large scale production and the resin cure kinetics would need to be adapted if such production is targeted. For convenience, the cycle time in the RTM cell is thus assumed the same as in [327] (around 600s) when using conventional epoxy (i.e. *Scenarios 1 and 3*). When using epoxy-PCL systems (i.e. *Scenarios 2 and 4*), the overall RTM cell cycle time increases to around 1400s as the resin viscosity increases by a factor of 10. For *Scenarios 3 and 4*, the machine considered to stitch SMA wires to the system can process 10 dry fibre stacks in parallel with a maximum speed of 1000 stitch per minute (source *ZSK Technical Embroidery Systems*). Considering the part geometry, as well as the stitching geometry, the cycle time for this additional unit is 694s.

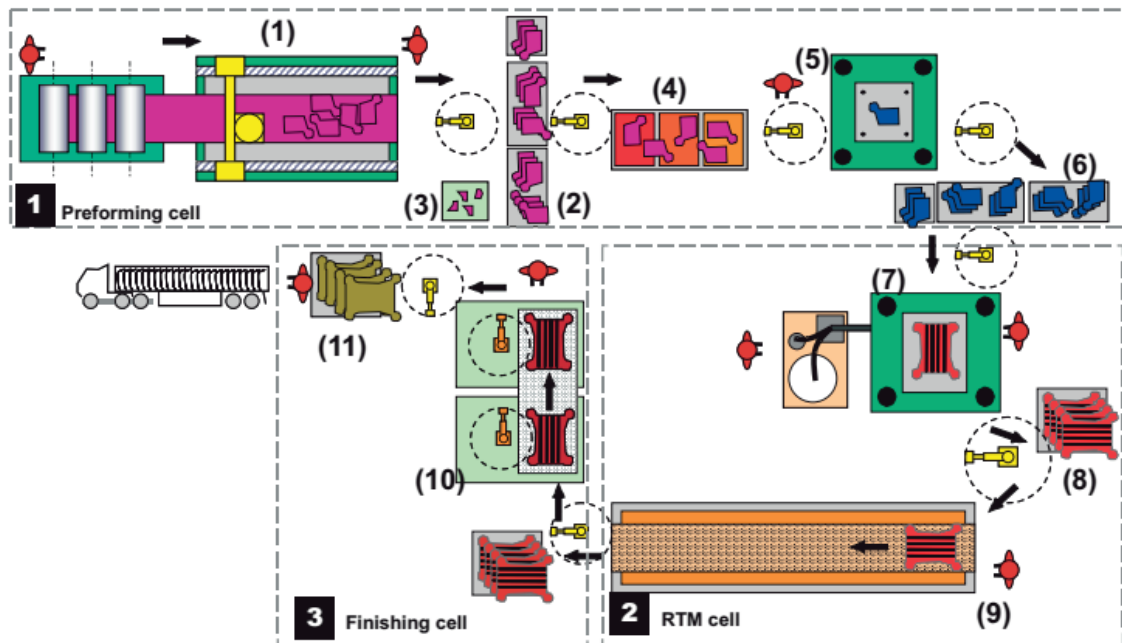


Figure 8.2: Plant diagram for production of 12,500 parts per year. (1) Ultrasonic cutting machine; (2) Buffer; (3) Waste buffer; (4) IR oven; (5) Preforming press; (6) Buffer; (7) RTM press with thermoset injection machine; (8) Buffer; (9) Post-cure oven; (10) Trimming cell; (11) shipping. Arrows indicate the flow of production. [328]

Cost modelling and industrial viability

Table 8.2: Price, power and surface for each machine of the three different units defined in Figure 8.2. These parameters are also defined for additional machines to produce parts for *Scenarios 2-3-4*. Cycle time needed for each unit is also given.

Unit	Machine	Price [CHF]	Puissance [kW]	Surface [m ²]	Cycle time [s]
Preforming Cell	NCF rolls unloading station	60,000	15	25	180
	Cutting machine	200,000	43	64	
	IR oven	68,000	150	15	
	Preforming press	413,000	150	110	
	Deburring	10,000	5	25	
	Robot	60,000	15	25	
	Robot	60,000	15	25	
	Sub-total	871,000	393	289	
RTM cell	RTM press	680,000	100	70	600
	RTM injection	170,000	20	15	
	Post cure oven	90,000	150	60	
	Robot	60,000	15	25	
	Robot	60,000	15	25	
	Sub-total	1,060,000	300	195	
Finishing cell	Trimming cell	300,000	40	20	60
Additional machines	Mixing machine/RTM injection	50,000	40	20	800
	Sewing machine	100,000	50	30	694

With the data provided in Table 8.1 and Table 8.2, the cost per produced part associated to materials and machines can be determined. However, the calculation needs also to take into account other parameters such as the factory cost, electricity, manpower, tools cost and consumables. These fixed parameters are listed in Table 8.3. Notice also that a dedicated-based scenario is considered here, but to reduce the costs, an utilisation-based scenario where machines are shared with others could be considered.

Table 8.3: Various fixed parameters for the overall cost calculation.

Production rate [part/year]	10,000 to 100,000
Depreciation period [year]	5
Working hours per shift [h/year]	7.5
Annual working days for workers [day/year]	250
Efficiency factor	85%
Reject rate	<ul style="list-style-type: none"> • 1% for injection • 5% for forming • 15% for cutting
Cost per injection mould [CHF]	30,000
Tool life [number of parts]	100,000
Factory cost per m ² [CHF]	120
Electricity cost [CHF/kWh]	0.1
Man power cost per hour [CHF]	25
Number of technicians on the line	<ul style="list-style-type: none"> • 1 for cutting • 1 for forming • 1 for SMA stitching • 2 for injection • 2 for finish
Consumable cost per hour per person [CHF]	1

8.3 Results

An overview of the production cost per part as a function of the number of parts produced per year is presented in Figure 8.3 for the different scenarios considered. Overall, the cost per part decreases rapidly as the number of parts produced per year increases due to the fixed costs that are rapidly absorbed. Three groups of curves can be highlighted and depend strongly on the cost associated with the use of SMA wires (see Table 8.1 for material price). The group with lower production cost is found for *Scenarios 1 and 2* (without SMA wires). *Scenario 1* is the reference case as it is made of standard materials for fibre-reinforced composites (pure epoxy and glass fibres). Adding the thermoplastic (PCL) to the system (*Scenario 2*) through blending before infusion is seen to slightly increase the cost because of two elements: (i) the blending process which requires an additional machine as well as additional time on the production line and (ii) the increase of viscosity as compared to pure epoxy (*Scenario 1*) which slows down the process. However, the associated cost increase from *Scenario 1* to *Scenario 2* is not higher than 13% and may be thus considered as acceptable commercially for the addition of a healing functionality to the system. When adding SMA wires to the system, an additional machine for sewing on the dry fibre fabric is needed. SMA wires are also relatively expensive (0.5 CHF/m). If SMA wires are integrated to the system on the entire part area, the cost per part increases considerably, up to 6 times, and thus the added crack closure functionality may not be relevant commercially, unless the cost to send someone to repair or change the part is higher than this cost (and that of a sensing device/heating device to trigger the SMA functionality). The scenarios with SMA stitched wires can also be considered if only a region of the part area is stitched with wires, as can be the case for practical applications. *Scenarios 3 and 4* named with *part SMA* consider such a case with 30% of the part area that is stitched with SMA wires. This operation diminishes considerably the cost as compared to a part entirely stitched with SMA wires, which may give to the system a commercial interest providing the crack closure functionality. Nevertheless, the cost of these systems with lower amount of SMA wires still increases by factors of 2.56 and 2.45 as compared to *Scenarios 1 and 2*. Notice that at 50,000 and 60,000 parts produced per year, one injection and one sewing machine must be respectively added in parallel to the initial ones in order to follow the targeted production volume. While the sewing machine does not highly influence the cost per part produced, the addition of an injection machine (much more expensive) creates the small bump on the curves seen at 50,000 parts produced per year.

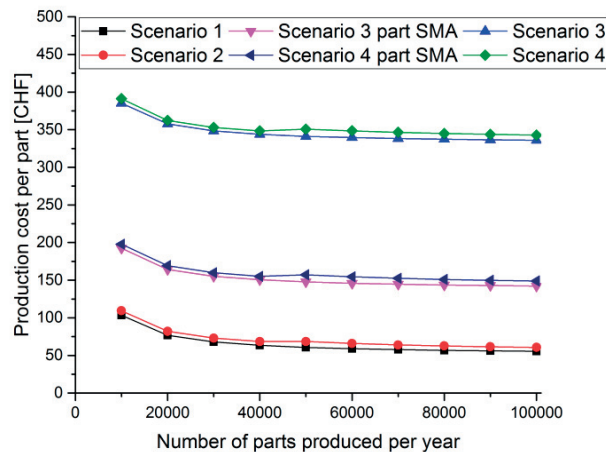


Figure 8.3: Production cost per part as a function of the number of parts produced per year: for *Scenarios 1 to 4*. *Scenarios 3 and 4* are also shown for stitching only on 30% of the part surface (named part SMA).

In depth analysis can be performed by inspecting the cost associated with the different cost positions of the production line. Figure 8.4 presents the cost per part for *Scenario 4 part SMA* and a production of 10,000 and 100,000 parts per year; the total cost is divided between the following cost positions of the production line: consumables,

manpower, electricity fixed costs, factory renting, tools (e.g. RTM moulds), machines and material costs (SMA, Epoxy-PCL and glass fibres). Material costs are fixed and cannot decrease when the number of part per year produced is increased. When adding SMA wires to the system, their high material cost thus increases considerably the cost associated with each produced part. Manpower as well as electricity are also fixed costs, thus the number of parts produced per year does not influence the cost associated with those elements of the production line. Increasing the number of parts produced per year however decreases considerably the cost associated to the machines, the tools and the factory running. Indeed, these are rapidly absorbed, which shows the interest of increasing the number of parts produced per year. Notice that the same behaviours are observed for the other scenarios considered.

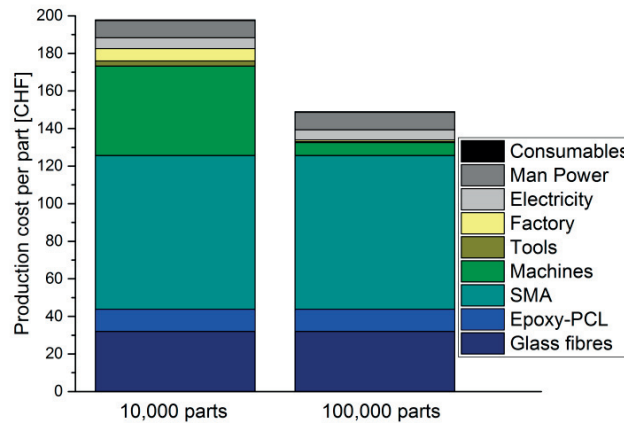


Figure 8.4: Cost per part for a production rate of 10,000 and 100,000 parts per year. For *Scenario 4* where only 30% of the part surface is stitched with SMA wires (i.e. *Scenario 4 part SMA*).

8.4 Conclusion and Industrial viability

Overall, this preliminary cost assessment for the different scenarios showed that producing composites with epoxy-PCL blends does not substantially increase the cost per part, thus adding a repair functionality to the composite can be of high commercial interest. Adding SMA wires to the system is also of interest for toughness, damage control and to increase the repair efficiency, however, their integration needs to be carefully studied as these are relatively expensive, which considerably increases the cost per produced part. It may thus be of relevance to integrate SMA wires only partially on the part area as this decreases almost linearly the cost associated to this functionality. At this stage, it is also worth mentioning that such smart systems may be of high interest for structural parts with difficult access (e.g. in a remote area) and thus costly to repair by the intervention of a human being. Therefore, if this intervention can be avoided by a fully autonomous system, the increased cost related to these added functionalities may lead to an overall lower cost associated to the part life time. In this concern, autonomous detection of the damage can be achieved by the use of sensors [2], [6], and autonomous repair of the damage can be remotely triggered by SMAs Joule heating [6], [210], but their use in FRPs would need to be addressed as they may interact with the healing system. Nevertheless, a proper market study would need to be performed to identify in which fields exactly such smart systems could be of interest.

Even though cost modelling of the studied smart composites has demonstrated a potential commercial interest, the scaling-up of manufacturing processes is another limiting factor for their integration into the industrial field. Indeed, processes that are viable on a lab-scale may not be viable on a larger scale, mainly considering the efficiency and achievable production rate of the desired part. For the manufacturing of composites with epoxy-PCL for healing and stitched SMA wires for crack closure, two processes may limit an industrial viability: (i) resin injection through the

reinforcement (i.e. RTM process) and (ii) stitching of the SMA wires into the fibre preform before resin injection. While (i) is much used by large composite manufacturers and should not pose cumbersome integration as it is close to the VARIM process used throughout the present study, (ii) is more limiting as fabric stitching is mostly performed with polymer wires in industries and not with metallic wires such as SMAs. To confirm the industrial viability of the stitching process demonstrated in the framework of the present work through the use of a commercial sewing machine (*Singer* model 632G), a company specialised in embroidery (*ZSK Technical Embroidery Systems*) of reinforcement fabrics has been approached to perform a proof of concept of the proposed SMA wires integration to composites. The principle of embroidery is slightly different than sewing (see Figure 8.5 (a)) and also much rougher. This implies that a material that can be sewn through a needle cannot be necessarily embroidered through a needle, the inverse being valid. Figure 8.5 (b) demonstrates that SMA wires can be embroidered into an E-glass reinforcement stack with appropriate reproducibility (pattern again of 4 x 4 mm between two needle point and notch), that could be achieved through setting of the adapted parameters on the embroidery system. Even though embroidery might lead to lower amount of crack closure capability as wires may be strained only over half of the part thickness (see Figure 8.5 (a)), this upscale demonstration shows promise for an industrial integration and could be shifted towards sewing systems in order for the SMAs to provide their maximum crack closure capacity.

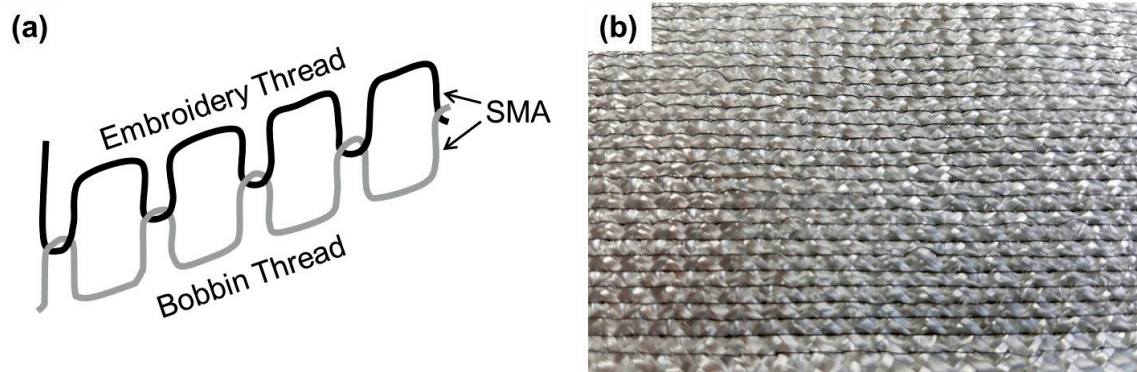


Figure 8.5: (a) schematic of the embroidery principle, both threads are SMAs in the present case; (b) dry E-glass preform after embroidery.

Chapter 9 Conclusions

The present work aimed to develop a Fibre-Reinforced Polymer (FRP), containing a fibre volume fraction of 50%, with added functionalities in order to provide efficient healing of damage, while preserving initial mechanical properties close to those of conventional FRP systems. To achieve such goals, three main directions were investigated: (i) the use of an intrinsic healing system consisting of an immiscible thermoset-thermoplastic blend to be used as a matrix for FRPs; (ii) the use of Shape Memory Alloy (SMA) wires as stitches in FRPs to reduce the crack size and improve the healing mechanism; (iii) the use of the healing thermoplastic phase under other forms to improve or at least maintain the resistance to crack propagation of the FRPs.

Blends of a commercial epoxy with different thermoplastics (PCL, PLA and PMMA) were first characterised in terms of thermal properties, strength, stiffness, fracture toughness as well as recovery in fracture toughness. The cured blends led to three general types of morphologies after polymerisation-induced phase separation: (i) an interconnected particulate epoxy phase and a co-continuous thermoplastic phase at high thermoplastic content (around 20-30 vol% of thermoplastic); (ii) a continuous epoxy phase containing thermoplastic inclusions at low thermoplastic content; (iii) a complex morphology with relatively coarse co-continuous thermoplastic and/or epoxy domains at intermediate thermoplastic content. Of particular interest for crack healing was morphology (i), which allows the molten polymer phase to flow and fill the crack during thermal mending at 150 °C for 30 minutes. Choosing the most appropriate system to be further integrated as a healing matrix in FRPs also required considering the matrix strength as well as its crack healing ability. Epoxy-PMMA blends were discarded due to the amorphous nature of the thermoplastic, hence its high viscosity, which prevented flow of the thermoplastic during the healing cycle. Epoxy-PLA blends could be of high interest for further integration into composites owing to their high strength combined with full crack recovery. However, due to the high PLA melting temperature and thus a healing temperature that is too close to the epoxy glass transition, structural integrity was lost during healing, which causes potential issues in structural applications. Moreover, its high viscosity made manufacturing difficult. PCL with a medium molecular weight (45,000 g/mol) was highlighted as most appropriate to be blended with epoxy and integrated to FRPs as this material presented a good compromise between suitable mechanical, processing and healing properties. These were further analysed over a large composition range with aim to understand morphology formation and healing. Overall, the observed phase-separated morphologies were consistent with simple model predictions, which suggested spinodal decomposition to be the dominant mode of phase separation over most of the assessed composition range. Increasing the PCL content reduced the dynamic and static tensile stiffness of the blends, which tended to a lower limit imposed by the presence of a continuous PCL phase at the highest PCL contents investigated. The stiffness nevertheless remained above 1 GPa, and the blends continued to behave as rigid elastic solids at the healing temperature of 150 °C, in spite of a sharp decrease in the Young's modulus at this temperature, owing to the interconnectivity of the epoxy-rich particulate phase. A four-fold decrease in strength and a two-fold decrease in fracture toughness were also observed for the blends containing a continuous PCL phase. These were attributed to both the high initial toughness of the baseline epoxy, and severe spatial confinement of the nominally ductile PCL. After a moderate healing treatment at 150 °C for 30 min, fracture toughness recovery increased strongly with PCL content, reaching over 70% efficiency for blends containing 25 vol% PCL. Because crack healing depends on the capacity of the PCL, which showed relatively high thermal expansion on melting, to expand, flow into newly formed cracks and bridge the crack faces, efficient healing was clearly contingent on the presence of a continuous PCL phase. It follows that blends with morphologies comprising interconnected epoxy particles embedded in a continuous PCL matrix were most suited to provide a part with crack healing properties, while maintaining adequate mechanical properties both in service and at the healing temperature of 150 °C.

Conclusions

Glass fibre-reinforced epoxy-PCL composites with fibre volume fractions around 50 vol% were then successfully processed through Vacuum Assisted Resin Infusion Moulding (VARIM) at elevated temperature when needed to accommodate viscosity increase of the matrix. The presence of PCL in the composites did not lead to a significant difference in room temperature storage modulus, flexural modulus and strength, as compared to pure epoxy composite systems, whereas a consequent decrease in interlaminar fracture toughness (35%) was found when PCL was added to the system. This decrease was attributed to the decrease in interfacial shear strength values and by the intrinsic fracture toughness of the blends, resulting from the phase-separated morphology and its scale. In these composites however, cracks could be healed. Higher efficiencies were observed for higher PCL contents as well as for a higher number of healing cycles due to the higher PCL coverage on the specimens fracture surface during healing. Even though phase separation was affected by the presence of fibres in composites and interlaminar fracture toughness was considerably decreased by the presence of PCL, 25 vol% of PCL within the matrix provided suitable healing efficiencies without any deterioration in modulus or strength of the composite. This combination was thus further investigated for its impact response at increasing levels of impact energies, analysing the resulting damage area recovery as well as the recovery of compressive residual strength after healing. As expected, the resistance to crack propagation was lower for epoxy-PCL composites as compared to pure epoxy composites. However, thermal mending demonstrated a damage area recovery from 40% up to 90% (for impact energies from 34 down to 8.5 J). Incomplete recovery was attributed to fibre damage and the formation of thick cracks. In addition, epoxy-PCL composites were able to recover between 22% and 96% of the compressive strength after the low-velocity impact damage events followed by healing. Although epoxy-PCL composites demonstrated lower compressive residual strength as compared to pure epoxy composites, the used woven reinforcement and the high fibre volume fraction provided strength values close to those encountered in other conventional FRPs. Phase-separated epoxy-PCL composites, providing their manufacturing feasibility through conventional industrial processes, their acceptable mechanical properties and their ability to fully heal low-velocity impact damage, can thus be of interest in composite structures that are subjected to moderate loads and not easily accessible to repair.

In order to repair composite structures that are subjected to higher loads and will thus experience larger damage volumes, the need to first reduce the crack thicknesses before (or during) healing was highlighted. Through the combination of stitched SMA wires with an epoxy-PCL healing matrix in FRPs, it has been demonstrated that such a smart structure, through heat treatment at moderate temperature, has the ability to first close a crack before sealing it. SMA stitched glass fibre-reinforced epoxy-PCL composites with fibre volume fractions around 50 vol% were successfully processed through semi-automatic sewing of the SMA wires on the dry fabric preforms followed by the VARIM process at elevated temperature. Pull-out testing results indicated that wires can debond in FRPs when placed perpendicular to the fibres whereas the wire deformation was completely blocked in the stitch bends, which is ideal to provide controlled debonding and thus the highest crack closure ability after a damage event. For a crack opening of 200 μm , SMA wires were overall able to bring the crack faces in close contact when activated through heat treatment and this over at least three cycles. The repair capacity of these smart systems was then demonstrated for low-velocity impacts at increasing energy levels. SMA stitched glass fibre-reinforced epoxy-PCL composites showed the ability to almost fully heal impact damage events from low energy up to 17 J, which has never been achieved before over this entire range. This achievement was possible through the combined effect of: (i) the epoxy-PCL healing matrix that could repeatedly expand and fill microcracks after multiple damage events; (ii) the stitched SMA wires, which autonomously closed cracks that were above a threshold thickness of PCL expansion. These smart materials can thus be of high interest in composite structures that are subjected to moderate loading events resulting in matrix microcracks as they can be produced with techniques close to conventional industrial processes, have acceptable damage resistance, improved energy absorption properties and are able to fully heal low-velocity impact damage events. Considering again Figure 2.35 in Chapter 2 from the review of Blaiszik *et al.* [4], which compared several systems in terms of healing efficiency for a defined damage volume, the materials proposed in the present work, highlighted in hashed green in Figure 9.1, are able to span damage volumes covering the range 0.01-100 mm^3 , making them closer to "real-life" application cases.

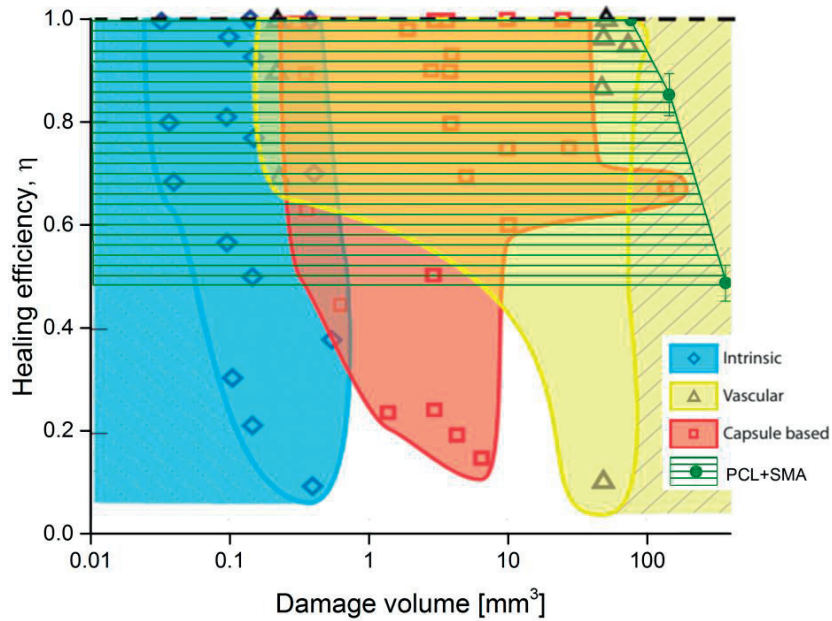


Figure 9.1: Performance map for self-healing materials. The data are organized according to the type of self-healing with shaded regions on the basis of data in the literature (plotted as discrete points). Each approach has demonstrated healing for different damage volume regimes. Intrinsic systems are relegated to small damage and can potentially heal at the molecular scale. Vascular systems have healed much larger damage volumes and can potentially extend the upper limit for self-healing systems. Capsule-based systems span the gap between intrinsic and vascular approaches. The use of epoxy-PCL blends in combination to stitched SMA wires in FRPs has the ability to cover the entire range of damage events that can be healed with most of the existing healing systems. Adapted from [4].

A major drawback of the proposed material combination, at least when no SMA wires are added, is the reduced toughness. Further investigations were thus carried out in order to improve this property and explore the combination of damage management (by healing) and damage prevention (by toughening). Damage prevention was first assessed by PCL microparticles integration into FRPs and the poor results highlighted both the need of a continuous PCL phase to provide enough material to flow and fill the crack, as well as the role of the molecular interactions taking place between PCL and epoxy (through phase separation or not). PCL interlayer films allowed increasing the continuity of the PCL phase, at least in plane, and as a result, demonstrated full crack healing capability, but still an extremely low interlaminar fracture toughness. As the characteristic morphology of the PCL phase, in particular the size of the PCL domains, was identified as a critical parameter, which could not be explored to submicron size through blends phase separation, another approach was followed, introducing PCL as nanofibres in combination to a phase separation process. Resin model samples first demonstrated that a combined microstructure could be achieved, consisting of phase-separated regions (epoxy particles surrounded by a PCL matrix) ideal for crack healing as well as of remaining intact nanofibres ideal for interlaminar toughening. FRPs interleaved with PCL nanofibres were produced by the VARIM process with a resulting slightly lower fibre volume fraction (40%) than previously as the nanofibre layers prevented compaction and nesting of the glass fibre reinforcement. Interlaminar toughness increase between 43 and 48% was demonstrated and attributed to interlaminar crack bridging by the nanofibres and the fine phase-separated microstructure. Indeed, due to the interplay between reaction kinetics and PCL diffusion with the resin, the epoxy particles were much smaller (1 μm diameter) than in the epoxy-PCL blends previously assessed (20 μm diameter). However, after thermal treatment of the damaged specimens, no healing could be obtained due to two limiting factors: (i) residual stresses in the nanofibres after electrospinning, which led to shrinkage during healing and thus limited the PCL expansion capacity; (ii) high PCL viscosity which prevented its flow in such a fine microstructure of

epoxy interconnected particles. Flow modelling demonstrated that the use of a lower PCL molecular weight, with lower viscosity, should allow crack healing while preserving high toughness. If such material could be electrospun, this would allow reaching the ultimate smart composite with both philosophies of damage prevention and damage management.

Finally, FRPs with a healing matrix (epoxy-PCL) and/or with stitched SMA wires have demonstrated their potential technical interest for damage prevention and repair. However, these functionalities come with an added cost, which may limit their integration into commercial markets. A preliminary cost modelling assessment concluded that producing composites with epoxy-PCL blends does not substantially increase the cost per part, so that adding a repair functionality to the composite can be of commercial relevance. However, adding SMA wires to the system considerably increases the cost per part; their integration therefore needs to be carefully evaluated if this added functionality is to be integrated in a commercial application. For example, it may be interesting to integrate SMA wires only locally on the part as this almost linearly decreases the cost associated to this functionality.

To summarize all the composite materials obtained in this work, a comparative map can be established for each combination, considering the crack healing efficiency in Mode I (after thermal mending at 150 °C for 30 minutes) and the corresponding interlaminar fracture toughness in the virgin state (Figure 9.2). On this map, the Epoxy/E-glass woven fabric baseline is also shown as a threshold for design requirements; obviously the crack healing efficiency of this system is null. When integrating PCL as an intact film within the FRP (Chapter 7), full crack recovery was found, however interlaminar fracture toughness was extremely low (bottom right of Figure 9.2). Using phase-separated blends of epoxy and PCL (Chapter 5) improved the interlaminar fracture toughness thanks to the load bearing capacity of the interconnected epoxy particle network; however the amount of PCL available to heal the crack was lower and thus incomplete crack filling in this testing mode occurred. PCL was also integrated as intact microparticles within the FRP (Chapter 7), which demonstrated further improvements in interlaminar fracture toughness but even lower healing efficiency due to the low ability of the PCL to flow and bridge the crack faces. To further improve interlaminar fracture toughness while keeping the healing ability through a phase-separated network, PCL under the form of nanofibrous veils was then integrated to FRPs prior to epoxy resin infusion (Chapter 7). This approach considerably increased the interlaminar fracture toughness; however crack healing could not occur due to a fine phase-separated structure, which prevented flow of PCL (top left of Figure 9.2). These four strategies, shown in Figure 9.2 form a typical material properties compromise diagram, where two properties of interest are interdependent and the improvement of one leads to the decrease of the other. The strategy followed in Chapter 6, where stitched SMA wires are integrated to FRPs made with a healing matrix provided points higher on both counts: high toughness as well as efficient crack healing thanks to the combined effect of (i) autonomous crack closure with SMAs; and (ii) expansion and filling of submicron cracks with PCL. In Figure 9.2 are also superimposed two values of healing efficiency (shown in red) measured after impact loading with two different energies (8.5 and 17 J) for Epoxy-PCL FRPs without and with stitched SMA wires. Impact loading conditions are more representative of what a real life structure can sustain during service; it was demonstrated that such conditions could be fully repaired thanks to the enhanced systems proposed in the present work. The advantages of using stitched SMA wires are demonstrated as higher damage amounts are repaired, albeit with a rather severe cost penalty.

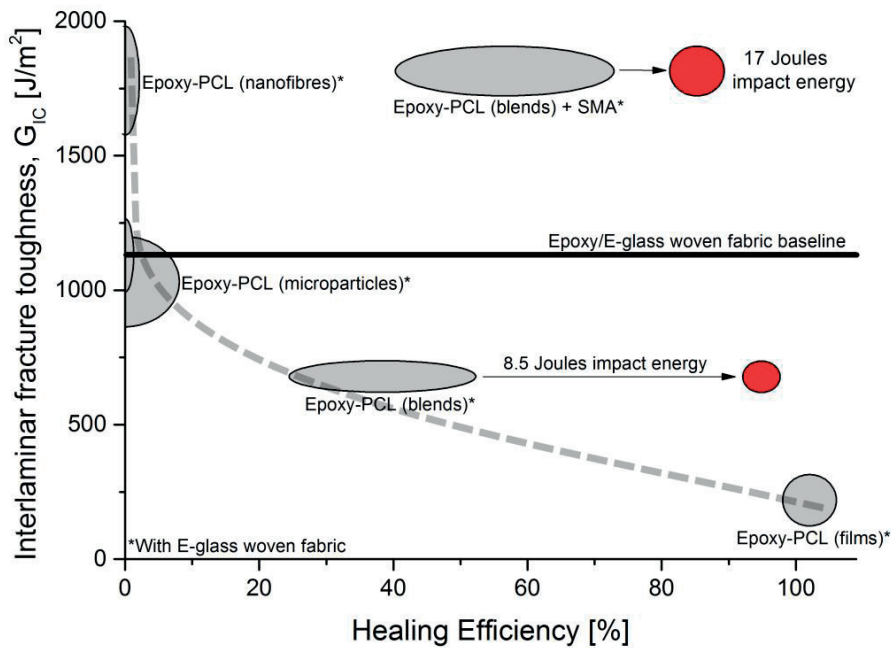


Figure 9.2: Interlaminar fracture toughness as a function of the corresponding healing efficiency in Mode I DCB testing (after thermal treatment at 150 °C for 30 minutes) for all the epoxy-PCL combination systems studied in the present work and integrated to FRPs (E-glass woven fabric). The two red regions show the healing efficiency for the corresponding system at the base of the arrow after impact loading of 8.5 or 17 J. The region shown for each system represents the standard deviation. Epoxy/E-glass woven fabric baseline is also shown as a threshold for design requirements, obviously the healing efficiency of this system is null.

9.1 Outlook

Several points have been raised and remain to be solved or addressed. This last section provides insights into next steps that would be worth exploring in order to confirm the interests of such smart systems.

Thermoplastic nanofibres provided a method to produce fine phase-separated microstructures into FRPs, in situ, during part curing; however crack healing could not take place because of the fine phase-separated microstructure preventing the viscous PCL to flow. Two solutions can be explored to obtain crack healing while preserving the energy dissipation during crack propagation. Flow modelling demonstrated that the use of a lower PCL viscosity should allow crack healing while keeping high toughness properties. This direction should be first explored in future studies even though the production of PCL nanofibres with a lower molecular weight is difficult as molecular entanglements may not be sufficient for a stable and continuous electrospinning process. If this works, the expected composite should combine both improved toughness and the ability to heal cracks as compared to conventional epoxy FRPs. An alternate solution would be to slow down the fast epoxy curing kinetics, which has been demonstrated to be the dominant parameter in the microstructure development, and may result in a coarser microstructure, thus allowing PCL flow and an efficient crack healing. A coarser microstructure would obviously provide a lower toughness to the resin; however it has been shown that a compromise may be obtained with microstructures of intermediate sizes as compared to the two extremes obtained within this work. Thermoplastic nanofibre layers with a different composition (for example PA) could also be inserted in specific locations, as in pure epoxy composites, only to provide toughening while the epoxy-PCL blend provides healing of the matrix. This approach is rather complex, and potential cross-interactions should be checked, but it may also form a further path towards a compromise in properties.

Conclusions

Thermoplastic nanofibrous veils were initially tested to provide a biphasic matrix containing phase-separated domains for healing as well as intact nanofibres for toughening. However, it has been demonstrated that toughness improvements were also obtained with the fine phase-separated microstructure, resulting from the fast epoxy curing kinetics, and thus PCL as nanofibres may not be necessary. In order to bypass the electrospinning process, but still provide an easy PCL integration (i.e. interleaving), the option to use thin PCL films that may be dissolved in epoxy (with slower curing kinetics) and further result in an intermediate size of phase-separated microstructure upon curing (thus providing healing as well as toughening) must be explored. This route may even result in a cheaper and easier method than epoxy-PCL blends as room temperature curing epoxy resins (without blending to the thermoplastic before the infusion process) could be used while providing the healing functionality. Based on the same principle, the composite industry increasingly considers interlayer stiffeners to stabilize composite structures, which consist of thermoplastic short fibre mats that are relatively light. These may thus be used to provide a phase-separated microstructure to the composite for healing purposes. Notice that with this process, using other thermoplastics also proven as efficient for healing (like PLA in the present work) could be proposed, as it would avoid the infusion of a viscous resin. It is also worth mentioning that the high temperature curing epoxy used in the present work could find applications for prepreg composites, which may be another potential route to explore for an industrial integration.

Even though the mechanical tests used throughout the present work are representative of loading cases that can be applied to real composite structures, practical loading cases are most often not static; fatigue loading tests thus need to be addressed to provide a coherent mechanical characterisation. In particular, while translaminar stitching demonstrated interlaminar fracture toughness improvements, the fatigue performance of the same systems may be reduced [329]; this may lead to serious complications in composite structures under complex loading cases. Translaminar stitching of SMA wires may however solve this issue by actuating the wires during fatigue loadings. This may also open a door to create adaptive structures that are of increasing interest for many applications.

Smart materials integrate new functionalities having the ability to detect damage, react to it and repair it if needed. Detecting damage has not been addressed in the present work. However, a fully smart system may integrate sensors (piezoelectric materials and/or optical fibres) to detect damage. Even though the integration of such sensors has been well demonstrated in composite materials to detect damage [2], [6], they may interact with the healing system and thus need to be tested in this context. Reacting to damage was achieved through the use of SMA wires and a thermal treatment to actuate them. It is worth to note that actuation may be performed by Joule heating [6], [210], which must be addressed as it may be more practical in real structures to trigger crack closure and repair.

Finally, PCL was concluded as the best thermoplastic to provide efficient crack healing when blended to epoxy thanks to its relatively high thermal expansion in the liquid state. However, for structural composite applications, its long-term stability would need to be assessed as PCL is a biodegradable polymer. This last property is nevertheless slower than for PLA for example (degradation in 2-4 year time [330]) and the manufacturer *Perstorp* has recently developed PCL grades (*CapaTM* series) that are hydrolytic resistant, which are currently applied to sports equipment.

Exploring these aspects further is believed to confirm the definite interest of smart FRPs containing epoxy-thermoplastic blends for crack healing in combination to stitched SMA wires for crack closure, toughness and crack healing efficiency improvement.

Bibliography

- [1] G. A. Schoeppner and S. Abrate, "Delamination threshold loads for low velocity impact on composite laminates," *Compos. Part A Appl. Sci. Manuf.*, vol. 31, no. 9, pp. 903–915, 2000.
- [2] L. P. Canal, M. Benavente, M. Hausmann, and V. Michaud, "Process-induced strains in RTM processing of polyurethane/carbon composites," *Compos. Part A Appl. Sci. Manuf.*, vol. 78, pp. 264–273, 2015.
- [3] V. Michaud, "Can shape memory alloy composites be smart?," *Scr. Mater.*, vol. 50, no. 2, pp. 249–253, Jan. 2004.
- [4] B. J. Blaiszik, S. L. B. Kramer, S. C. Olugebefola, J. S. Moore, N. R. Sottos, and S. R. White, "Self-Healing Polymers and Composites," *Annu. Rev. Mater. Res.*, vol. 40, no. 1, pp. 179–211, Jun. 2010.
- [5] S. van der Zwaag, *Self Healing Materials. An Alternative Approach to 20 Centuries of Materials Science*, Springer. 2007.
- [6] E. Kirkby, "Active Sensing and Repair Composites," *Thèse EPFL n°4409*, 2009.
- [7] X. Luo, R. Ou, D. E. Eberly, A. Singhal, W. Viratyaporn, and P. T. Mather, "A thermoplastic/thermoset blend exhibiting thermal mending and reversible adhesion," *ACS Appl. Mater. Interfaces*, vol. 1, no. 3, pp. 612–20, Mar. 2009.
- [8] S. Neuser, V. Michaud, and S. R. White, "Improving solvent-based self-healing materials through shape memory alloys," *Polymer (Guildf)*, vol. 53, no. 2, pp. 370–378, Jan. 2012.
- [9] E. L. Kirkby, J. D. Rule, V. J. Michaud, N. R. Sottos, S. R. White, and J.-A. E. Månson, "Embedded Shape-Memory Alloy Wires for Improved Performance of Self-Healing Polymers," *Adv. Funct. Mater.*, vol. 18, no. 15, pp. 2253–2260, Aug. 2008.
- [10] T. C. Bor, L. Warnet, R. Akkerman, and a. de Boer, "Modeling of Stress Development During Thermal Damage Healing in Fiber-reinforced Composite Materials Containing Embedded Shape Memory Alloy Wires," *J. Compos. Mater.*, vol. 44, no. 22, pp. 2547–2572, 2010.
- [11] L. Daelemans, S. Van Der Heijden, I. De Baere, H. Rahier, W. Van Paepegem, and K. De Clerck, "Damage-Resistant Composites Using Electrospun Nanofibers: A Multiscale Analysis of the Toughening Mechanisms," *ACS Appl. Mater. Interfaces*, vol. 8, no. 18, pp. 11806–11818, 2016.
- [12] L. Daelemans, S. van der Heijden, I. De Baere, H. Rahier, W. Van Paepegem, and K. De Clerck, "Improved fatigue delamination behaviour of composite laminates with electrospun thermoplastic nanofibrous interleaves using the Central Cut-Ply method," *Compos. Part A Appl. Sci. Manuf.*, vol. 94, pp. 10–20, 2017.
- [13] L. Daelemans, S. van der Heijden, I. De Baere, H. Rahier, W. Van Paepegem, and K. De Clerck, "Using aligned nanofibres for identifying the toughening micromechanisms in nanofibre interleaved laminates," *Compos. Sci. Technol.*, vol. 124, pp. 17–26, 2016.
- [14] B. Aïssa, D. Therriault, E. Haddad, and W. Jamroz, "Self-Healing Materials Systems: Overview of Major Approaches and Recent Developed Technologies," *Adv. Mater. Sci. Eng.*, vol. 2012, pp. 1–17, 2012.
- [15] S. D. Bergman and F. Wudl, "Mendable polymers," *J. Mater. Chem.*, vol. 18, no. 1, pp. 41–62, 2008.
- [16] I. P. Bond, R. S. Trask, and H. R. Williams, "Self-healing Fiber-Reinforced Polymer Composites," *MRS Bull.*, vol. 33, pp. 770–774, 2008.
- [17] M. M. Caruso, D. a Davis, Q. Shen, S. a Odom, N. R. Sottos, S. R. White, and J. S. Moore, "Mechanically-induced chemical changes in polymeric materials," *Chem. Rev.*, vol. 109, no. 11, pp. 5755–5798, Nov. 2009.
- [18] B. S. Hayes and J. C. Seferis, "Modification of thermosetting resins and composites through preformed polymer particles: A review," *Polym. Compos.*, vol. 22, no. 4, pp. 451–467, Aug. 2001.
- [19] M. D. Hager, P. Greil, C. Leyens, S. van der Zwaag, and U. S. Schubert, "Self-healing materials," *Adv. Mater.*,

Bibliography

- vol. 22, no. 47, pp. 5424–5430, Dec. 2010.
- [20] F. Herbst, D. Döhler, P. Michael, and W. H. Binder, "Self-healing polymers via supramolecular forces," *Macromol. Rapid Commun.*, vol. 34, no. 3, pp. 203–220, Feb. 2013.
- [21] M. R. Kessler, "Self-healing: a new paradigm in materials design," *Proc. Inst. Mech. Eng. Part G J. Aerosp. Eng.*, vol. 221, no. 4, pp. 479–495, Jan. 2007.
- [22] K. Takeda, M. Tanahashi, and H. Unno, "Self-repairing mechanism of plastics," *Sci. Technol. Adv. Mater.*, vol. 4, no. 5, pp. 435–444, Sep. 2003.
- [23] D. Y. Wu, S. Meure, and D. Solomon, "Self-healing polymeric materials: A review of recent developments," *Prog. Polym. Sci.*, vol. 33, no. 5, pp. 479–522, May 2008.
- [24] Y. C. Yuan, "Self healing in polymers and polymer composites. Concepts, realization and outlook: A review," *Express Polym. Lett.*, vol. 2, no. 4, pp. 238–250, Mar. 2008.
- [25] Y.-L. Liu and T.-W. Chuo, "Self-healing polymers based on thermally reversible Diels–Alder chemistry," *Polym. Chem.*, vol. 4, no. 7, pp. 2194–2205, 2013.
- [26] X. Yin, Z. Liu, D. Wang, X. Pei, B. Yu, and F. Zhou, "Bioinspired Self-Healing Organic Materials: Chemical Mechanisms and Fabrications," *J. Bionic Eng.*, vol. 12, no. 1, pp. 1–16, 2015.
- [27] Y. Yang, X. Ding, and M. W. Urban, "Chemical and physical aspects of self-healing materials," *Prog. Polym. Sci.*, vol. 49–50, pp. 34–59, 2015.
- [28] X. K. D. Hillewaere and F. E. Du Prez, "Fifteen Chemistries for Autonomous External Self-Healing Polymers and Composites," *Prog. Polym. Sci.*, vol. 49–50, pp. 121–153, 2015.
- [29] S. van der Zwaag, a. M. Grande, W. Post, S. J. Garcia, and T. C. Bor, "Review of current strategies to induce self-healing behaviour in fibre reinforced polymer based composites," *Mater. Sci. Technol.*, vol. 30, no. 13a, pp. 1633–1641, 2014.
- [30] R. P. Wool, "Self-healing materials: a review," *Soft Matter*, vol. 4, no. 3, pp. 400–418, 2008.
- [31] S. J. Garcia, "Effect of polymer architecture on the intrinsic self-healing character of polymers," *Eur. Polym. J.*, vol. 53, no. 1, pp. 118–125, 2014.
- [32] N. Zhong and W. Post, "Self-repair of structural and functional composites with intrinsically self-healing polymer matrices: A review," *Compos. Part A Appl. Sci. Manuf.*, vol. 69, pp. 226–239, 2015.
- [33] D. G. Bekas, K. Tsirka, D. Baltzis, and A. S. Paipetis, "Self-healing materials: A review of advances in materials, evaluation, characterization and monitoring techniques," *Compos. Part B Eng.*, vol. 87, pp. 92–119, 2016.
- [34] M. J. Laffan, S. T. Pinho, P. Robinson, and a. J. McMillan, "Translaminar fracture toughness testing of composites: A review," *Polym. Test.*, vol. 31, no. 3, pp. 481–489, May 2012.
- [35] ASTM D5528, "Standard Test Method for Mode I Interlaminar Fracture Toughness of Unidirectional Fiber-Reinforced Polymer Matrix Composites 1," *ASTM Stand.*, pp. 1–13, 2014.
- [36] JIS-K-7086, "Testing methods for interlaminar fracture toughness of carbon fibre reinforced plastics," 1993.
- [37] ASTM D6671, "Standard Test Method for Mixed Mode I-Mode II Interlaminar Fracture Toughness of," *ASTM Stand.*, pp. 1–15, 2014.
- [38] P. Davies, B. R. K. Blackman, and A. J. Brunner, "Standard Test Methods for Delamination Resistance of Composite Materials : Current Status," *Appl. Compos. Mater.*, vol. 5, pp. 345–364, 1998.
- [39] S. Jose, R. Ramesh Kumar, M. K. Jana, and G. Venkateswara Rao, "Intralaminar fracture toughness of a cross-ply laminate and its constituent sub-laminates," *Compos. Sci. Technol.*, vol. 61, no. 8, pp. 1115–1122, Jun. 2001.
- [40] T. K. O'Brien, "Interlaminar fracture toughness: the long and winding road to standardization," *Compos. Part B Eng.*, vol. 29, no. 1, pp. 57–62, Jan. 1998.
- [41] N. Sela and O. Ishai, "Interlaminar fracture toughness and toughening of laminated composite materials: a review," *Composites*, vol. 20, no. 5, pp. 423–435, Sep. 1989.
- [42] G. B. McKenna, "Polymer-Plastics Technology and Engineering Interlaminar Effects in Fiber- Reinforced Plastics-A Review," no. July 2012, pp. 37–41, 2006.

Bibliography

- [43] L. J. Broutman, "Measurement of the Fiber-Polymer Matrix Interfacial Strength," *ASTM STP 452*, vol. Interfaces, 1969.
- [44] J. C. Goan and S. P. Prosen, "Interfacial Bonding in Graphite Fiber-resin Composites," *ASTM STP 452*, vol. Interfaces, 1969.
- [45] K. Gutfreund, "Interfacial Relationships in Fiber-Reinforced Plastic Composites," *Mod. Compos. Mater.*, 1967.
- [46] J. T. Paul and J. B. Thompson, "The importance of Voids in the Filament Wound Structure," *SPI 20th Annu. Tech. Conf.*, 1965.
- [47] C. C. Chamis, M. P. Hanson, and T. T. Serafini, "Criteria for Selecting Resin Matrices for Improved Composite Strength," *Mod. Plast.*, 1973.
- [48] J. F. Mandell, S. s. Wang, and F. J. McGarry, "Fracture of Graphite Fiber Reinforced Composites," *AFML-TR-73-142*, 1973.
- [49] G. Frossard, J. Cugnoli, T. Gmür, and J. Botsis, "Mode I interlaminar fracture of carbon epoxy laminates: Effects of ply thickness," *Compos. Part A Appl. Sci. Manuf.*, vol. 91, pp. 1–8, 2016.
- [50] T. Tay, "Characterization and analysis of delamination fracture in composites: An overview of developments from 1990 to 2001," *Appl. Mech. Rev.*, vol. 56, no. 1, pp. 1–32, 2003.
- [51] R. Gutkin, M. L. Laffan, S. T. Pinho, P. Robinson, and P. T. Curtis, "Modelling the R-curve effect and its specimen-dependence," *Int. J. Solids Struct.*, vol. 48, no. 11–12, pp. 1767–1777, Jun. 2011.
- [52] S. T. Pinho, P. Robinson, and L. Iannucci, "Developing a four point bend specimen to measure the mode I intralaminar fracture toughness of unidirectional laminated composites," *Compos. Sci. Technol.*, vol. 69, no. 7–8, pp. 1303–1309, Jun. 2009.
- [53] W. A. Curtin, "Stochastic Damage Evolution and Failure in Fiber-Reinforced Composites," *Adv. Appl. Mech.*, vol. 36, pp. 163–253, 1999.
- [54] J. A. Nairn, "Matrix Microcracking in Composites," in *Comprehensive composite materials*, vol. 2, R. Areja and J.-A. E. Manson, Eds. Oxford: Elsevier Science, 2000, pp. 403–432.
- [55] A. C. Garg and Y.-W. Mai, "Failure Mechanisms in Toughened Epoxy Resins - A Review," *Compos. Sci. Technol.*, vol. 31, pp. 179–223, 1988.
- [56] E. Manfredi, "Assessment of solvent capsule-based healing for woven fibre-reinforced epoxies," *Thèse EPFL N° 6576*, 2015.
- [57] J. A. Nairn and S. Hu, "The formation and effects of outer-ply microcracks in cross-ply laminates: a variational approach," *Eng. Fract. Mecha*, vol. 41, no. 2, pp. 203–221, 1992.
- [58] E. J. Barbero, *Finite element analysis of composite materials using Abaqus*, Taylor & F. 2013.
- [59] P. R. Teagle, "The quality control and non-destructive evaluation of composite aerospace components," *Composites*, vol. 14, no. 2, pp. 115–128, 1983.
- [60] E. Tsangouri, D. Aggelis, and D. Van Hemelrijck, "Quantifying thermoset polymers healing efficiency: A systematic review of mechanical testing," *Prog. Polym. Sci.*, vol. 49–50, pp. 154–174, 2015.
- [61] W. Beres, A. Koul, and R. Thamburaj, "A Tapered Double-Cantilever-Beam Specimen Designed for Constant-K Testing at Elevated Temperatures," *J. Test. Eval.*, vol. 25, no. 6, pp. 536–542, 1997.
- [62] E. Brown, N. R. Sottos, and S. R. White, "Fracture Testing of a Self-Healing Polymer Composite," *Exp. Mech.*, vol. 42, no. 4, pp. 372–379, Dec. 2002.
- [63] M. R. Kessler, N. R. Sottos, and S. R. White, "Self-healing structural composite materials," *Compos. Part A Appl. Sci. Manuf.*, vol. 34, no. 8, pp. 743–753, Aug. 2003.
- [64] S. a. Hayes, F. R. Jones, K. Marshiya, and W. Zhang, "A self-healing thermosetting composite material," *Compos. Part A Appl. Sci. Manuf.*, vol. 38, no. 4, pp. 1116–1120, Apr. 2007.
- [65] M. R. Kessler and S. R. White, "Self-activated healing of delamination damage in woven composites," *Compos. Part A Appl. Sci. Manuf.*, vol. 32, no. 5, pp. 683–699, May 2001.
- [66] M. Heidari-Rarani, M. M. Shokrieh, and P. P. Camanho, "Finite element modeling of mode I delamination growth in laminated DCB specimens with R-curve effects," *Compos. Part B Eng.*, vol. 45, no. 1, pp. 897–903,

Bibliography

- 2013.
- [67] J. A. Nairn, "Analytical and numerical modeling of R curves for cracks with bridging zones," *Int. J. Fract.*, vol. 155, no. 2, pp. 167–181, 2009.
- [68] J. A. Nairn, "Fracture Mechanics of Composites With Residual Thermal Stresses," *J. Appl. Mech.*, vol. 64, no. 4, p. 804, 1997.
- [69] J. A. Nairn, "On the calculation of energy release rates for cracked laminates with residual stresses," *Int. J. Fract.*, vol. 139, no. 2, pp. 267–293, 2006.
- [70] J. A. Nairn, "Energy Release Rate Analysis for Adhesive and Laminate Double Cantilever Beam Specimens Emphasizing the Effect of Residual Stresses," *Int. J. Adhes. Adhes.*, vol. 20, pp. 1–15, 2000.
- [71] M. W. Keller, S. R. White, and N. R. Sottos, "An Elastomeric Self-Healing Material," pp. 2–5.
- [72] ASTM D7136, "Standard Test Method for Measuring the Damage Resistance of a Fiber-Reinforced Polymer Matrix Composite to a Drop-Weight Impact Event," *ASTM Stand.*, pp. 1–16, 2015.
- [73] J. Bayandor, R. S. Thomson, M. L. Scott, M. Q. Nguyen, and D. J. Elder, "Investigation of impact and damage tolerance in advanced aerospace composite structures," *Int. J. Crashworthiness*, vol. 8, no. 3, pp. 297–306, 2003.
- [74] M. O. W. Richardson and M. J. Wisheart, "Review of low-velocity impact properties of composite materials," *Compos. Part A Appl. Sci. Manuf.*, vol. 27, no. 12 PART A, pp. 1123–1133, 1996.
- [75] F. Sordo, L. Berret, B. Caglar, and V. Michaud, "Impact recovery of self-healing composites based on a supramolecular polymer matrix," *21st Int. Conf. Compos. Mater. Xi'an, China*, vol. 2216–3, 2017.
- [76] W. Post, A. Cohades, V. Michaud, S. van der Zwaag, and S. J. Garcia, "Healing of a glass fibre reinforced composite with a disulphide containing organic-inorganic epoxy matrix," *Compos. Sci. Technol.*, vol. 152, pp. 85–93, 2017.
- [77] F. Sordo, "Self-Healing Fiber-Reinforced Composites with Tailored Supramolecular Matrices," *Thèse EPFL N° 7032*, 2016.
- [78] A. J. Patel, N. R. Sottos, E. D. Wetzel, and S. R. White, "Autonomic healing of low-velocity impact damage in fiber-reinforced composites," *Compos. Part A Appl. Sci. Manuf.*, vol. 41, no. 3, pp. 360–368, Mar. 2010.
- [79] ASTM D7137, "Standard Test Method for Compressive Residual Strength Properties of Damaged Polymer Matrix Composite Plates," *ASTM Stand.*, pp. 1–16, 2012.
- [80] J. L. Moll, S. R. White, and N. R. Sottos, "A Self-sealing Fiber-reinforced Composite," *J. Compos. Mater.*, vol. 44, no. 22, pp. 2573–2585, Jan. 2010.
- [81] B. M. Bailey, Y. Leterrier, S. J. Garcia, S. van der Zwaag, and V. Michaud, "Electrically conductive self-healing polymer composite coatings," *Prog. Org. Coatings*, vol. 85, pp. 189–198, 2015.
- [82] S. Zhandarov and E. Mäder, "Characterization of fiber/matrix interface strength: applicability of different tests, approaches and parameters," *Compos. Sci. Technol.*, vol. 65, no. 1, pp. 149–160, Jan. 2005.
- [83] M. J. Pitkethly, J. Jakubowski, S. F. Mudrich, D. L. Caldwell, L. T. Drzal, L. D. Landro, A. Hampe, A. Armistead, M. Desaegeer, and I. Verpoest, "A round-robin programme on interfacial test methods," *Compos. Sci. Technol.*, vol. 48, pp. 205–214, 1993.
- [84] B. Golaz, "UV-cured Epoxy for Adhesion in Steel Reinforced Thermoplastic Composites," *Thèse EPFL N° 5466*, 2012.
- [85] B. Golaz, V. Michaud, and J. A. E. Månson, "Photo-polymerized epoxy primer for adhesion improvement at thermoplastics/metallic wires interfaces," *Compos. Part A Appl. Sci. Manuf.*, vol. 48, no. 1, pp. 171–180, 2013.
- [86] C.-H. Liu and J. A. Nairn, "Analytical and experimental methods for a fracture mechanics interpretation of the microbond test including the effects of friction and thermal stresses," *Int. J. Adhes. Adhes.*, vol. 19, no. 1, pp. 59–70, 1999.
- [87] L. B. Greszczuk, "Theoretical studies of the mechanics of the fiber-matrix interface in composites," *ASTM Int.*, 1969.
- [88] J. A. Nairn, "Analytical Fracture Mechanics Analysis of the Pull-Out Test Including the Effects of Friction and

Bibliography

- Thermal Stresses," *Adv. Compos. Lett.*, vol. 9, no. 6, pp. 373–383, 2000.
- [89] J. A. Nairn, C. Liu, D. A. Mendels, and S. Zhandarov, "Fracture Mechanics Analysis of the Single-Fiber Pull-Out Test and the Microbond Test Including The Effects of Friction and Thermal Stresses," *Proc. 16th Ann. Tech. Conf. Amer. Soc. Compos.*, pp. 9–12, 2001.
- [90] D. A. Mendels, Y. Leterrier, and J. A. E. Manson, "The influence of internal stresses on the microbond test - I: Theoretical analysis," *J. Compos. Mater.*, vol. 36, no. 3, pp. 347–363, 2002.
- [91] D. A. Mendels, "Coupling of physical aging and internal stresses in thermoset-based multimaterial systems," *Thèse EPFL N° 2358*, 2001.
- [92] D. A. Mendels, Y. Leterrier, and J. A. E. Manson, "Stress Transfer Model for Single Fibre and Platelet Composites," *J. Compos. Mater.*, vol. 33, no. 10, pp. 928–940, 1999.
- [93] G. M. Pax, "Aminosilanes and hyperbranched polymers for adhesion tailoring between metallic oxides and polyethylene," *Thèse EPFL N° 3339*, 2005.
- [94] U. Gaur and B. Miller, "Microbond method for determination of the shear strength of a fiber/resin interface: Evaluation of experimental parameters," *Compos. Sci. Technol.*, vol. 34, no. 1, pp. 35–51, 1989.
- [95] M. Kharrat, A. Chateauinois, L. Carpentier, and P. Kapsa, "On the interfacial behaviour of a glass/epoxy composite during a micro-indentation test: assessment of interfacial shear strength using reduced indentation curves," *Compos. Part A Appl. Sci. Manuf.*, vol. 28, no. 1, pp. 39–46, 1997.
- [96] M. Zidi, L. Carpentier, A. Chateauinois, and F. Sidoroff, "Quantitative analysis of the micro-indentation behaviour of fibre-reinforced composites: Development and validation of an analytical model," *Compos. Sci. Technol.*, vol. 60, pp. 429–437, 2000.
- [97] M. Desaeger and I. Verpoest, "On the use of the micro-indentation test technique to measure the interfacial shear strength of fibre-reinforced polymer composites," *Compos. Sci. Technol.*, vol. 48, pp. 215–226, 1993.
- [98] J. M. Molina-Aldareguía, M. Rodríguez, C. González, and J. Llorca, "An experimental and numerical study of the influence of local effects on the application of the fibre push-in test," *Philos. Mag.*, vol. 91, no. February 2015, pp. 1293–1307, 2011.
- [99] M. Rodríguez, J. M. Molina-Aldareguía, C. González, and J. Llorca, "A methodology to measure the interface shear strength by means of the fiber push-in test," *Compos. Sci. Technol.*, vol. 72, no. 15, pp. 1924–1932, 2012.
- [100] *Hexcel Composite repair manual*, Available from <http://www.hexcel.com/resources/technology-manuals>, accessed date: 15.06.2014, no. April. 1999, pp. 1–13.
- [101] S. H. Myhre and J. D. Labor, "Repair of advanced composite structures," *J. Aircr.*, vol. 18, no. 7, pp. 546–552, 1981.
- [102] K. Pingkarawat, C. H. Wang, R. J. Varley, and A. P. Mouritz, "Effect of mendable polymer stitch density on the toughening and healing of delamination cracks in carbon–epoxy laminates," *Compos. Part A Appl. Sci. Manuf.*, vol. 50, pp. 22–30, Jul. 2013.
- [103] K. Jud, H. H. Kausch, and G. Williams, "Fracture mechanics studies of crack healing and welding of polymers," *J. Mater. Sci.*, vol. 16, pp. 204–210, 1981.
- [104] K. Jud and H. H. Kausch, "Load Transfer Through Chain Molecules," *Polym. Bull.*, vol. 1, pp. 697–707, 1979.
- [105] R. P. Wool, "A theory of crack healing in polymers," *J. Appl. Phys.*, vol. 52, no. 10, pp. 5953–5963, 1981.
- [106] P. G. de Gennes, "Reptation of a Polymer Chain in the Presence of Fixed Obstacles," *J. Chem. Phys.*, vol. 55, no. 2, pp. 572–579, 1971.
- [107] S. Prager, "The healing process at polymer–polymer interfaces," *J. Chem. Phys.*, vol. 75, no. 10, pp. 5194–5198, 1981.
- [108] Y. H. Kim and R. P. Wool, "A theory of healing at a polymer-polymer interface," *Macromolecules*, vol. 16, no. 7, pp. 1115–1120, Jul. 1983.
- [109] F. Yang and R. Pitchumani, "Healing of Thermoplastic Polymers at an Interface under Nonisothermal Conditions," *Macromolecules*, vol. 35, no. 8, pp. 3213–3224, Apr. 2002.
- [110] R. P. Wool, *Polymer Interfaces: Structure and Strength*, Hanser/Gar. New-York, 1995.

Bibliography

- [111] J. Raghavan and R. P. Wool, "Interfaces in Repair , Recycling , Joining and Manufacturing," *J. Appl. Polym. Sci.*, vol. 71, pp. 775–785, 1999.
- [112] V. Sastri and G. C. Tesoro, "Reversible crosslinking in epoxy resins. II. New approaches," *J. Appl. Polym. Sci.*, vol. 39, no. 7, pp. 1439–1457, 1990.
- [113] G. C. Tesoro and V. Sastri, "Reversible crosslinking in epoxy resins. I. Feasibility studies," *J. Appl. Polym. Sci.*, vol. 39, no. 7, pp. 1425–1437, 1990.
- [114] J. Canadell, H. Goossens, and B. Klumperman, "Self-healing materials based on disulfide links," *Macromolecules*, vol. 44, no. 8, pp. 2536–2541, 2011.
- [115] S. Yang, J.-S. Chen, H. Korner, T. Breiner, and C. K. Ober, "Reworkable Epoxies : Thermosets with Thermally Cleavable Groups for Controlled Network Breakdown," *Chem. Mater.*, vol. 10, no. 6, 1998.
- [116] J.-S. Chen, C. K. Ober, and M. D. Poliks, "Characterization of thermally reworkable thermosets: materials for environmentally friendly processing and reuse," *Polymer (Guildf.)*, vol. 43, no. 1, pp. 131–139, Jan. 2002.
- [117] L. Wang and C. P. Wong, "Syntheses and characterizations of thermally reworkable epoxy resins. Part I," *J. Polym. Sci. Part A Polym. Chem.*, vol. 37, no. 15, pp. 2991–3001, Aug. 1999.
- [118] J.-S. Chen, C. K. Ober, M. D. Poliks, Y. Zhang, U. Wiesner, and C. Cohen, "Controlled degradation of epoxy networks: analysis of crosslink density and glass transition temperature changes in thermally reworkable thermosets," *Polymer (Guildf.)*, vol. 45, no. 6, pp. 1939–1950, Mar. 2004.
- [119] X. Chen, M. a Dam, K. Ono, A. Mal, H. Shen, S. R. Nutt, K. Sheran, and F. Wudl, "A thermally re-mendable cross-linked polymeric material," *Science (80-)*, vol. 295, no. 5560, pp. 1698–702, Mar. 2002.
- [120] X. Chen, F. Wudl, A. K. Mal, H. Shen, and S. R. Nutt, "New Thermally Remendable Highly Cross-Linked Polymeric Materials," *Macromolecules*, vol. 36, no. 6, pp. 1802–1807, Mar. 2003.
- [121] Q. Tian, Y. C. Yuan, M. Z. Rong, and M. Q. Zhang, "A thermally remendable epoxy resin," *J. Mater. Chem.*, vol. 19, no. 9, pp. 1289–1296, 2009.
- [122] K. M. Harris and M. Rajagopalan, "Self-healing polymers in sports equipment," United States Patent 2003/0032758 A1, 2003.
- [123] F. Wudl and X. Chen, "Thermally re-mendable cross-linked polymers," United States Patent 6,933,361 B2, 2005.
- [124] S. a Hayes, W. Zhang, M. Branthwaite, and F. R. Jones, "Self-healing of damage in fibre-reinforced polymer-matrix composites.," *J. R. Soc. Interface*, vol. 4, no. 13, pp. 381–387, Apr. 2007.
- [125] J. Zhang, Q. Guo, M. Huson, I. Slota, and B. Fox, "Interphase study of thermoplastic modified epoxy matrix composites: Phase behaviour around a single fibre influenced by heating rate and surface treatment," *Compos. Part A Appl. Sci. Manuf.*, vol. 41, no. 6, pp. 787–794, Jun. 2010.
- [126] X. Luo, K. E. Lauber, and P. T. Mather, "A thermally responsive, rigid, and reversible adhesive," *Polymer (Guildf.)*, vol. 51, no. 5, pp. 1169–1175, 2010.
- [127] X. Luo and P. T. Mather, "Shape Memory Assisted Self-Healing Coating," *ACS Macro Lett.*, vol. 2, no. 2, pp. 152–156, Feb. 2013.
- [128] E. D. Rodriguez, X. Luo, and P. T. Mather, "Linear/network poly(ϵ -caprolactone) blends exhibiting shape memory assisted self-healing (SMASH).," *ACS Appl. Mater. Interfaces*, vol. 3, no. 2, pp. 152–61, Feb. 2011.
- [129] E. D. Rodriguez, X. Luo, and P. T. Mather, "Shape memory miscible blends for thermal mending," *Proceeding SPIE*, vol. 7289, pp. 1–5, Mar. 2009.
- [130] Y. Yao, J. Wang, H. Lu, B. Xu, Y. Fu, Y. Liu, and J. Leng, "Thermosetting epoxy resin/thermoplastic system with combined shape memory and self-healing properties," *Smart Mater. Struct.*, vol. 25, no. 15021, pp. 1–8, 2016.
- [131] G. Li, H. Meng, and J. Hu, "Healable thermoset polymer composite embedded with stimuli-responsive fibres," *J. R. Soc. Interface*, vol. 9, no. 77, pp. 3279–3287, Dec. 2012.
- [132] G. Li and A. Shojaei, "A viscoplastic theory of shape memory polymer fibres with application to self-healing materials," *Proc. R. Soc. A Math. Phys. Eng. Sci.*, vol. 468, no. 2144, pp. 2319–2346, Apr. 2012.
- [133] A. Noshay and L. Robeson, "Epoxy/modifier block copolymers," *Polym. Chem.*, vol. 12, no. 3, pp. 689–705,

- 1974.
- [134] R. J. J. Williams, B. A. Rozenberg, and J. Pascault, "Reaction-Induced Phase Separation in Modified Thermosetting Polymers," *Adv. Polym. Sci.*, vol. 128, pp. 95–156, 1997.
- [135] J. Chen and F. Chang, "Temperature-dependent phase behavior in poly (ϵ -caprolactone)–epoxy blends," *Polymer (Guildf.)*, vol. 42, pp. 2193–2199, 2001.
- [136] J. Chen and F. Chang, "Phase Separation Process in Poly (ϵ -caprolactone) - Epoxy Blends," *Macromolecules*, vol. 32, pp. 5348–5356, 1999.
- [137] P. M. Remiro, M. M. Cortazar, M. E. Calahorra, and M. M. Calafel, "Miscibility and Crystallization of an Amine-Cured Epoxy Resin Modified with Crystalline Poly (ϵ -caprolactone)," *Macromol. Chem. Phys.*, vol. 202, no. 7, pp. 1077–1088, 2001.
- [138] Q. Guo, C. Harrats, G. Groeninckx, H. Reynaers, and M. H. J. Koch, "Miscibility, crystallization and real-time small-angle X-ray scattering investigation of the semicrystalline morphology in thermosetting polymer blends," *Polymer (Guildf.)*, vol. 42, no. 14, pp. 6031–6041, Jun. 2001.
- [139] Q. Guo and G. Groeninckx, "Crystallization kinetics of poly (ϵ -caprolactone) in miscible thermosetting polymer blends of epoxy resin and poly (ϵ -caprolactone)," *Polymer (Guildf.)*, vol. 42, no. 21, pp. 8647–8655, 2001.
- [140] Y. Ni and S. Zheng, "Influence of intramolecular specific interactions on phase behavior of epoxy resin and poly(ϵ -caprolactone) blends cured with aromatic amines," *Polymer (Guildf.)*, vol. 46, no. 15, pp. 5828–5839, Jul. 2005.
- [141] S. Zheng, H. Zheng, and Q. Guo, "Epoxy Resin / Poly (ϵ -caprolactone) Blends Cured with 2,2-Bis[4-(4-aminophenoxy)phenyl]propane. I. Miscibility and Crystallization Kinetics," *J. Polym. Sci. Part B Polym. Phys.*, vol. 41, pp. 1085–1098, 2003.
- [142] G. Vanden Poel, S. Goossens, B. Goderis, and G. Groeninckx, "Reaction induced phase separation in semicrystalline thermoplastic/epoxy resin blends," *Polymer (Guildf.)*, vol. 46, no. 24, pp. 10758–10771, Nov. 2005.
- [143] L. Barone, S. Carciotto, G. Cicala, and A. Recca, "Thermomechanical Properties of Epoxy / poly (ϵ -caprolactone) Blends," *Polym. Eng. Sci.*, 2006.
- [144] S. K. Siddhamalli, "Toughening of Epoxy / Polycaprolactone Composites via Reaction Induced Phase Separation," *Polym. Compos.*, vol. 21, no. 5, pp. 846–855, 2000.
- [145] H. Lützen and A. Hartwig, "Dynamics in Poly(ϵ -Caprolactone) Containing Phase Separated Epoxy Thermosets," *Macromol. Mater. Eng.*, vol. 298, no. 12, pp. 1275–1281, Dec. 2013.
- [146] Y. Liu, "Polymerization-induced phase separation and resulting thermomechanical properties of thermosetting/reactive nonlinear polymer blends: A review," *J. Appl. Polym. Sci.*, vol. 127, no. 5, pp. 3279–3292, 2013.
- [147] Y. Zhang, F. Chen, Z. Li, and C. C. Han, "Ubiquitous nature of the three-layered structure formation in the asymmetric phase separation of the epoxy/thermoplastic blends," *Polymer (Guildf.)*, vol. 53, no. 2, pp. 588–594, 2012.
- [148] B. S. Kim, T. Chiba, and T. Inoue, "A new time-temperature-transformation cure diagram for thermoset/thermoplastic blend: tetrafunctional epoxy/poly(ether sulfone)," *Polymer (Guildf.)*, vol. 34, no. 13, pp. 2809–2815, Jan. 1993.
- [149] B. S. Kim, T. Chiba, and T. Inoue, "Phase separation and apparent phase dissolution during cure process of thermoset/thermoplastic blend," *Polymer (Guildf.)*, vol. 36, no. 1, pp. 67–71, Jan. 1995.
- [150] K. Yamanaka and T. Inoue, "Structure development in epoxy resin modified with poly(ether sulphone)," *Polymer (Guildf.)*, vol. 30, no. 4, pp. 662–667, 1989.
- [151] D. Olmos and J. González-Benito, "Visualization of the morphology at the interphase of glass fibre reinforced epoxy-thermoplastic polymer composites," *Eur. Polym. J.*, vol. 43, no. 4, pp. 1487–1500, Apr. 2007.
- [152] D. Olmos, J. M. Arroyo, and J. González-Benito, "Interphase morphology in glass fiber/PMMA modified epoxy matrix composites. Effect of molecular weight of PMMA," *Polym. Test.*, vol. 31, no. 6, pp. 785–791, Sep. 2012.
- [153] R. J. Varley and J. H. Hodgkin, "Effect of reinforcing fibres on the morphology of a toughened epoxy/amine

Bibliography

- system," *Polymer (Guildf.)*, vol. 38, no. 5, pp. 1005–1009, Mar. 1997.
- [154] P. A. Oyanguren, M. J. Galante, K. Andromaque, P. M. Frontini, and R. J. J. Williams, "Development of bicontinuous morphologies in polysulfone–epoxy blends," *Polymer (Guildf.)*, vol. 40, no. 19, pp. 5249–5255, Sep. 1999.
- [155] J. Xu, M. Holst, M. Rüllmann, M. Wenzel, and I. Alig, "Reaction-induced Phase Separation in a Polysulfone-modified Epoxy-anhydride Thermoset," *J. Macromol. Sci. Part B*, vol. 46, no. 1, pp. 155–181, 2007.
- [156] I. Martinez, M. D. Martin, A. Eceiza, P. Oyanguren, and I. Mondragon, "Phase separation in polysulfone-modified epoxy mixtures. Relationships between curing conditions, morphology and ultimate behavior," *Polymer (Guildf.)*, vol. 41, no. 3, pp. 1027–1035, 2000.
- [157] D. J.-P. Turmel and I. K. Partridge, "Heterogeneous phase separation around fibres in epoxy/PEI blends and its effect on composite delamination resistance," *Compos. Sci. Technol.*, vol. 57, pp. 1001–1007, 1996.
- [158] E. Girard-reydet, H. Sautereau, J. P. Pascault, P. Keates, P. Navard, G. Thollet, and G. Vigier, "Reaction-induced phase separation mechanisms in modified thermosets," *Polymer (Guildf.)*, vol. 39, no. 11, pp. 2269–2279, 1998.
- [159] W. Gan, Y. Yu, M. Wang, Q. Tao, and S. Li, "Viscoelastic Effects on the Phase Separation in Thermoplastics-Modified Epoxy Resin," *Macromolecules*, vol. 36, no. 20, pp. 7746–7751, Oct. 2003.
- [160] M. Wang, Y. Yu, X. Wu, and S. Li, "Polymerization induced phase separation in poly(ether imide)-modified epoxy resin cured with imidazole," *Polymer (Guildf.)*, vol. 45, no. 4, pp. 1253–1259, Feb. 2004.
- [161] C. C. Su and E. M. Woo, "Cure kinetics and morphology of amine cured tetraglycidyl-4,4'-diaminodiphenylmethane epoxy blends with poly(ether imide)," *Polymer (Guildf.)*, vol. 36, no. 15, pp. 2883–2894, 1995.
- [162] L. Bonnaud, J. P. Pascault, H. Sautereau, J. Q. Zhao, and D. M. Jia, "Effect of reinforcing glass fibers on morphology and properties of thermoplastic modified epoxy-aromatic diamine matrix," *Polym. Compos.*, vol. 25, no. 4, pp. 368–374, Aug. 2004.
- [163] S. Ritzenthaler, E. Girard-Reydet, and J. P. Pascault, "Influence of epoxy hardener on miscibility of blends of poly(methyl methacrylate) and epoxy networks," *Polymer (Guildf.)*, vol. 41, no. 16, pp. 6375–6386, 2000.
- [164] M. J. Galante, P. A. Oyanguren, K. Andromaque, P. M. Frontini, and R. J. J. Williams, "Blends of epoxy/anhydride thermosets with a high-molar-mass poly (methyl methacrylate)," *Polym. Int.*, vol. 48, pp. 642–648, 1999.
- [165] H.-C. Kim, J. T. Kim, J. Kathi, and K.-Y. Rhee, "Phase Separation in Poly(Methyl Methacrylate)-Epoxy Blend," *J. Macromol. Sci. Part B*, vol. 48, no. 3, pp. 626–634, 2009.
- [166] J. C. Cabanelas, B. Serrano, and J. Baselga, "Development of Cocontinuous Morphologies in Initially Heterogeneous Thermosets Blended with Poly(methyl methacrylate)," *Macromolecules*, vol. 38, no. 3, pp. 961–970, Feb. 2005.
- [167] H. K. Hselh and E. M. Woo, "Preparation of Crosslinked Epoxy Microparticles via Phase Inversion," *J. Polym. Sci. Part B Polym. Phys.*, vol. 34, pp. 2591–2598, 1996.
- [168] S. Rastegar, N. Mohammadi, and R. Bagheri, "Development of co-continuous morphology in epoxy poly(methyl methacrylate) (PMMA) blends cured by mixtures of phase-separating and non-phase-separating curing agents," *Colloid Polym. Sci.*, vol. 283, no. 2, pp. 145–153, 2004.
- [169] B. B. Johnsen, A. J. Kinloch, and A. C. Taylor, "Toughness of syndiotactic polystyrene/epoxy polymer blends: microstructure and toughening mechanisms," *Polymer (Guildf.)*, vol. 46, no. 18, pp. 7352–7369, Aug. 2005.
- [170] L. Meynie, F. Fenouillot, and J.-P. Pascault, "Polymerization of a thermoset system into a thermoplastic matrix. Effect of the shear," *Polymer (Guildf.)*, vol. 45, no. 6, pp. 1867–1877, Mar. 2004.
- [171] Y. Ishii and A. J. Ryan, "Processing of Poly(2,6-dimethyl-1,4-phenylene ether) with Epoxy Resin. 1. Reaction-Induced Phase Separation," *Macromolecules*, vol. 33, no. 1, pp. 158–166, Jan. 2000.
- [172] R. W. Venderbosch, H. E. H. Meijer, and P. J. Lemstra, "Processing of intractable polymers using reactive solvents : 3 . Mechanical properties of poly(2,6-dimethyl-1,4-phenylene ether) processed by using various epoxy resin systems," *Polymer (Guildf.)*, vol. 36, no. 15, pp. 2903–2913, 1995.

Bibliography

- [173] S. J. Kalista and T. C. Ward, "Thermal characteristics of the self-healing response in poly(ethylene-co-methacrylic acid) copolymers," *J. R. Soc. Interface*, vol. 4, no. 13, pp. 405–411, Apr. 2007.
- [174] S. J. Kalista, T. C. Ward, and Z. Oyetunji, "Self-Healing of Poly(Ethylene-co-Methacrylic Acid) Copolymers Following Projectile Puncture," *Mech. Adv. Mater. Struct.*, vol. 14, no. 5, pp. 391–397, Jun. 2007.
- [175] R. J. Varley and S. van der Zwaag, "Towards an understanding of thermally activated self-healing of an ionomer system during ballistic penetration," *Acta Mater.*, vol. 56, no. 19, pp. 5737–5750, Nov. 2008.
- [176] R. J. Varley and S. van der Zwaag, "Development of a quasi-static test method to investigate the origin of self-healing in ionomers under ballistic conditions," *Polym. Test.*, vol. 27, no. 1, pp. 11–19, Feb. 2008.
- [177] S. Meure, D.-Y. Wu, and S. Furman, "FTIR study of bonding between a thermoplastic healing agent and a mendable epoxy resin," *Vib. Spectrosc.*, vol. 52, no. 1, pp. 10–15, Jan. 2010.
- [178] S. Meure, D. Y. Wu, and S. Furman, "Polyethylene-co-methacrylic acid healing agents for mendable epoxy resins," *Acta Mater.*, vol. 57, no. 14, pp. 4312–4320, Aug. 2009.
- [179] N. N. Muhamad and M. S. Jamil, "Homogeneous and Heterogeneous Solid State Self-Healing System," vol. 24, no. 9, pp. 815–825, 2016.
- [180] R. J. Varley, B. Dao, C. Pillsbury, S. J. Kalista, and F. R. Jones, "Low-molecular-weight thermoplastic modifiers as effective healing agents in mendable epoxy networks," *J. Intell. Mater. Syst. Struct.*, vol. 25, no. 1, pp. 107–117, 2014.
- [181] P. Cordier, F. Tournilhac, C. Soulié-Ziakovic, and L. Leibler, "Self-healing and thermoreversible rubber from supramolecular assembly," *Nature*, vol. 451, no. 7181, pp. 977–980, Feb. 2008.
- [182] F. Sordo, S. J. Mougner, N. Loureiro, F. Tournilhac, and V. Michaud, "Design of Self-Healing Supramolecular Rubbers with a Tunable Number of Chemical Cross-Links," *Macromolecules*, vol. 48, no. 13, pp. 4394–4402, 2015.
- [183] D. Montarnal, O. I. S. Tournilhac, M. Hidalgo, and L. Leibler, "Epoxy-Based Networks Combining Chemical and Supramolecular Hydrogen-Bonding Crosslinks," *J. Polym. Sci. Part A Polym. Chem.*, vol. 48, pp. 1133–1141, 2010.
- [184] J. S. Park, H. S. Kim, and H. Thomas Hahn, "Healing behavior of a matrix crack on a carbon fiber/mendomer composite," *Compos. Sci. Technol.*, vol. 69, no. 7–8, pp. 1082–1087, Jun. 2009.
- [185] F. Ghezzi, D. R. Smith, T. N. Starr, T. Perram, A. F. Starr, T. K. Darlington, R. K. Baldwin, and S. J. Oldenburg, "Development and Characterization of Healable Carbon Fiber Composites with a Reversibly Cross Linked Polymer," *J. Compos. Mater.*, vol. 44, no. 13, pp. 1587–1603, Mar. 2010.
- [186] Y. Heo and H. A. Sodano, "Thermally responsive self-healing composites with continuous carbon fiber reinforcement," *Compos. Sci. Technol.*, vol. 118, pp. 244–250, 2015.
- [187] E. H. Lim and K. Pickering, "Mechanical Properties of Self-Healing Carbon Fibre Fabric Reinforced Polymers (CFFRP)," *Adv. Mater. Res.*, vol. 700, pp. 107–110, 2013.
- [188] K. Pingkarawat, T. Bhat, D. A. Craze, C. H. Wang, R. J. Varley, and A. P. Mouritz, "Healing of carbon fibre–epoxy composites using thermoplastic additives," *Polym. Chem.*, vol. 4, no. 18, p. 5007, 2013.
- [189] K. Pingkarawat, C. H. Wang, R. J. Varley, and A. P. Mouritz, "Mechanical properties of mendable composites containing self-healing thermoplastic agents," *Compos. Part A Appl. Sci. Manuf.*, vol. 65, pp. 10–18, Jun. 2014.
- [190] C. H. Wang, K. Sidhu, T. Yang, J. Zhang, and R. Shanks, "Interlayer self-healing and toughening of carbon fibre/epoxy composites using copolymer films," *Compos. Part A Appl. Sci. Manuf.*, vol. 43, no. 3, pp. 512–518, Mar. 2012.
- [191] T. Yang, J. Zhang, A. P. Mouritz, and C. H. Wang, "Healing of carbon fibre–epoxy composite T-joints using mendable polymer fibre stitching," *Compos. Part B Eng.*, vol. 45, no. 1, pp. 1499–1507, Feb. 2013.
- [192] T. Yang, C. H. Wang, J. Zhang, S. He, and A. P. Mouritz, "Toughening and self-healing of epoxy matrix laminates using mendable polymer stitching," *Compos. Sci. Technol.*, vol. 72, no. 12, pp. 1396–1401, Jul. 2012.
- [193] S. Meure, S. Furman, and S. Khor, "Poly[ethylene-co-(methacrylic acid)] Healing Agents for Mendable Carbon Fiber Laminates," *Macromol. Mater. Eng.*, vol. 295, no. 5, pp. 420–424, May 2010.
- [194] F. Zhou, C. H. Wang, and A. P. Mouritz, "Computational Analysis of the Structural Integrity of Self-Healing

- Composites," *Mater. Sci. Forum*, vol. 654–656, pp. 2576–2578, 2010.
- [195] C. H. Wang, "Analysis of cracks in constrained layers," *Int. J. Fract.*, vol. 83, pp. 1–17, 1997.
- [196] C. H. Wang, "On the fracture of constrained layers," *Int. J. Fract.*, vol. 93, pp. 227–246, 1999.
- [197] K. Pingkarawat and A. P. Mouritz, "Stitched mendable composites: Balancing healing performance against mechanical performance," *Compos. Struct.*, vol. 123, pp. 54–64, 2015.
- [198] F. Sordo and V. Michaud, "Processing and damage recovery of intrinsic self-healing glass fiber reinforced composites," *Smart Mater. Struct.*, vol. 25, no. 8, pp. 1–9, 2016.
- [199] C. M. Dry and N. R. Sottos, "Passive smart self-repair in polymer matrix composite materials," *SPIE*, vol. 1916, pp. 438–444, Jul. 1993.
- [200] G. J. Williams, I. P. Bond, and R. S. Trask, "Compression after impact assessment of self-healing CFRP," *Compos. Part A Appl. Sci. Manuf.*, vol. 40, no. 9, pp. 1399–1406, 2009.
- [201] C. J. Norris, I. P. Bond, and R. S. Trask, "Healing of low-velocity impact damage in vascularised composites," *Compos. Part A Appl. Sci. Manuf.*, vol. 44, no. 1, pp. 78–85, 2013.
- [202] J. F. Patrick, K. R. Hart, B. P. Krull, C. E. Diesendruck, J. S. Moore, S. R. White, and N. R. Sottos, "Continuous Self-Healing Life Cycle in Vascularized Structural Composites," *Adv. Mater.*, pp. 1–7, Apr. 2014.
- [203] S. R. White, N. R. Sottos, P. H. Geubelle, J. S. Moore, M. R. Kessler, S. R. Sriram, E. N. Brown, and S. Viswanathan, "Autonomic healing of polymer composites," *Nature*, vol. 409, no. 6822, pp. 794–7, Feb. 2001.
- [204] M. W. Keller, S. R. White, and N. R. Sottos, "A self-healing poly(dimethyl siloxane) elastomer," *Adv. Funct. Mater.*, vol. 17, no. 14, pp. 2399–2404, 2007.
- [205] S. Neuser, P. W. Chen, A. R. Studart, and V. Michaud, "Fracture toughness healing in epoxy containing both epoxy and amine loaded capsules," *Adv. Eng. Mater.*, vol. 16, no. 5, pp. 581–587, 2014.
- [206] H. Jin, C. L. Mangun, D. S. Stradley, J. S. Moore, N. R. Sottos, and S. R. White, "Self-healing thermoset using encapsulated epoxy-amine healing chemistry," *Polymer (Guildf.)*, vol. 53, no. 2, pp. 581–587, 2012.
- [207] M. M. Caruso, D. A. Delafuente, V. Ho, N. R. Sottos, J. S. Moore, and S. R. White, "Solvent-Promoted Self-Healing Epoxy Materials," *Macromolecules*, vol. 40, no. 25, pp. 8830–8832, Dec. 2007.
- [208] S. Neuser and V. Michaud, "Effect of aging on the performance of solvent-based self-healing materials," *Polym. Chem.*, vol. 4, no. 18, pp. 4993–4999, 2013.
- [209] S. Neuser, E. Manfredi, and V. Michaud, "Characterization of solvent-filled polyurethane / urea - formaldehyde core - shell composites," *Mater. Chem. Phys.*, vol. 143, pp. 1018–1025, 2014.
- [210] S. Neuser, "Tailored Capsule Based Self-Healing for Epoxy Matrix Composites," *Thèse EPFL N° 5978*, 2013.
- [211] S. H. Cho, H. M. Andersson, S. R. White, N. R. Sottos, and P. V. Braun, "Polydimethylsiloxane-based self-healing materials," *Adv. Mater.*, vol. 18, no. 8, pp. 997–1000, 2006.
- [212] A. R. Jones, C. A. Watkins, S. R. White, and N. R. Sottos, "Self-healing Thermoplastic-toughened Epoxy," *Polymer (Guildf.)*, vol. 74, pp. 254–261, 2015.
- [213] J. D. Rule, E. N. Brown, N. R. Sottos, S. R. White, and J. S. Moore, "Wax-Protected Catalyst Microspheres for Efficient Self-Healing Materials," *Adv. Mater.*, vol. 17, no. 2, pp. 205–208, Jan. 2005.
- [214] T. S. Coope, U. F. J. Mayer, D. F. Wass, R. S. Trask, and I. P. Bond, "Self-Healing of an Epoxy Resin Using Scandium (III) Triflate as a Catalytic Curing Agent," vol. 21, pp. 4624–4631, 2011.
- [215] T. S. Coope, D. F. Wass, R. S. Trask, and I. P. Bond, "Metal triflates as catalytic curing agents in self-healing fibre reinforced polymer composite materials," *Macromol. Mater. Eng.*, vol. 299, no. 2, pp. 208–218, 2014.
- [216] E. Manfredi, A. Cohades, I. Richard, and V. Michaud, "Assessment of solvent capsule-based self-healing for woven E-glass fibre-reinforced polymers," *Smart Mater. Struct.*, vol. 24, pp. 1–11, 2015.
- [217] E. Manfredi and V. Michaud, "Packing and permeability properties of E-glass fibre reinforcements functionalised with capsules for self-healing applications," *Compos. Part A*, vol. 66, pp. 94–102, 2014.
- [218] T. Yin, M. Z. Rong, J. Wu, H. Chen, and M. Q. Zhang, "Healing of impact damage in woven glass fabric reinforced epoxy composites," *Compos. Part A Appl. Sci. Manuf.*, vol. 39, no. 9, pp. 1479–1487, 2008.

Bibliography

- [219] B. Caglar, L. Orgéas, S. Rolland du Roscoat, E. M. Sozer, and V. Michaud, "Permeability of textile fabrics with spherical inclusions," *Compos. Part A Appl. Sci. Manuf.*, vol. 99, pp. 1–14, 2017.
- [220] S. R. White, J. S. Moore, N. R. Sottos, B. P. Krull, W. A. Santa Cruz, and R. C. R. Gergely, "Restoration of large damage volumes in polymers.," *Science (80-.)*, vol. 344, no. 6184, pp. 620–623, May 2014.
- [221] E. L. Kirkby, J. O'Keane, R. de Oliveira, V. J. Michaud, and J. E. Månson, "Tailored processing of epoxy with embedded shape memory alloy wires," *Smart Mater. Struct.*, vol. 18, pp. 1–9, Sep. 2009.
- [222] S. Neuser and V. Michaud, "Fatigue Response of Solvent-Based Self-Healing Smart Materials," *Exp. Mech.*, vol. 54, no. 2, pp. 293–304, Aug. 2013.
- [223] D. C. Lagoudas, *Shape memory alloys: modeling and engineering applications*, Springer. New-York, 2008.
- [224] J. Mohd Jani, M. Leary, A. Subic, and M. A. Gibson, "A review of shape memory alloy research, applications and opportunities," *Mater. Des.*, vol. 56, pp. 1078–1113, Apr. 2014.
- [225] B. T. Lester, T. Baxevanis, Y. Chemisky, and D. C. Lagoudas, "Review and perspectives: shape memory alloy composite systems," *Acta Mech.*, vol. 226, no. 12, pp. 3907–3960, 2015.
- [226] Z. G. Wei, R. Sandström, and S. Miyazaki, "Review Shape-memory materials and hybrid composites for smart systems Part I Shape-memory materials," *J. Mater. Sci.*, vol. 33, pp. 3743–3762, 1998.
- [227] C. A. Rogers, C. Liang, and C. R. Fuller, "Modeling of shape memory alloy hybrid composites for structural," *J. Acoust. Soc. Am.*, vol. 89, pp. 210–220, 1991.
- [228] C. A. Rogers, "Active vibration and structural acoustic control of shape memory alloy hybrid composites : Experimental results," *J. Acoust. Soc. Am.*, vol. 88, pp. 2803–2811, 1990.
- [229] S. L. Angioni, M. Meo, and A. Foreman, "Impact damage resistance and damage suppression properties of shape memory alloys in hybrid composites—a review," *Smart Mater. Struct.*, vol. 20, no. 1, pp. 1–24, 2011.
- [230] J. A. Balta, V. Michaud, M. Parlinska, R. Gotthardt, and J. A. E. Manson, "Adaptive Composites with Embedded NiTiCu Wires," *Proc. SPIE*, vol. 4333, pp. 377–386, 2001.
- [231] J. E. Bidaux, L. Bataillard, J. A. E. Manson, and R. Gotthardt, "Phase transformation behavior of thin shape memory alloy wires embedded in a polymer matrix composite," *J. Phys. 4*, vol. 3, p. 561, 1993.
- [232] J. Schrooten, V. Michaud, J. Parthenios, G. C. Psarras, J. Van Humbeeck, C. Galiotis, R. Gotthardt, and J. A. E. Manson, "Progress on Composites with Embedded Shape Memory Alloy Wires," *Mater. Trans.*, vol. 43, no. 5, pp. 961–973, 2002.
- [233] L. C. Dickinson, G. L. Farley, and M. K. Hinders, "Translaminar Reinforced Composites : A Review," *J. Compos. Technol. Res.*, vol. 21, no. 1, pp. 3–15, 1999.
- [234] K. Lau, H. Ling, and L. Zhou, "Low velocity impact on shape memory alloy stitched composite plates," *Smart Mater. Struct.*, vol. 13, no. 2, pp. 364–370, Apr. 2004.
- [235] P.-L. Vachon, V. Brailovski, and P. Terriault, "Suppression of delamination propagation in carbon/epoxy laminates by the use of superelastic stitching wires: preliminary results," *Eight Jt. Canada-Japan Work. Compos.*, 2010.
- [236] S. Pappadà, R. Rametta, A. Largo, and A. Maffezzoli, "Low-Velocity Impact Response in Composite Plates Embedding Shape Memory Alloy Wires," *Polym. Compos.*, vol. 33, pp. 655–664, 2012.
- [237] Y. Xu, K. Otsuka, H. Yoshida, H. Nagai, R. Oishi, H. Horikawa, and T. Kishi, "A New Method for Fabricating SMA Smart Polymer Matrix Composites," *Adv. Eng. Mater.*, vol. 4, no. 9, pp. 683–686, Sep. 2002.
- [238] N. A. Smith, G. G. Antoun, A. B. Ellis, and W. C. Crone, "Improved adhesion between nickel–titanium shape memory alloy and a polymer matrix via silane coupling agents," *Compos. Part A Appl. Sci. Manuf.*, vol. 35, no. 11, pp. 1307–1312, Nov. 2004.
- [239] K. Jonnalagadda, G. E. Kline, and N. R. Sottos, "Local displacements and load transfer in shape memory alloy composites," *Exp. Mech.*, vol. 37, no. 1, pp. 78–86, Mar. 1997.
- [240] K. Lau, W. Tam, X. Meng, and L. Zhou, "Morphological study on twisted NiTi wires for smart composite systems," *Mater. Lett.*, vol. 57, no. December, pp. 364–368, 2002.
- [241] E. Sparnins, J. Andersons, V. Michaud, and Y. Leterrier, "Evaluation of the interfacial shear strength between

Bibliography

- pseudoplastic NiTi shape memory alloy wires and epoxy by the pull-out method," *Smart Mater. Struct.*, vol. 24, pp. 1–8, 2015.
- [242] P. Bettini, M. Riva, G. Sala, L. Landro, A. Airoidi, and J. Cucco, "Carbon Fiber Reinforced Smart Laminates with Embedded SMA Actuators—Part I: Embedding Techniques and Interface Analysis," *J. Mater. Eng. Perform.*, vol. 18, no. 5–6, pp. 664–671, Mar. 2009.
- [243] K. P. Unnikrishnan and E. T. Thachil, "Toughening of epoxy resins," *Des. Monomers Polym.*, vol. 9, no. 2, pp. 129–152, Mar. 2012.
- [244] V. Dikshit, S. Bhudolia, and S. Joshi, "Multiscale Polymer Composites: A Review of the Interlaminar Fracture Toughness Improvement," *Fibers*, vol. 5, no. 38, pp. 1–27, 2017.
- [245] W. J. Cantwell, J. W. Smith, H. H. Kausch, and T. Kaiser, "Examination of the processes of deformation and fracture in a silica-filled epoxy resin," *J. Mater. Sci.*, vol. 25, no. 1, pp. 633–648, 1990.
- [246] M. Bauer, O. Kahle, S. Landeck, C. Uhlig, and R. Wurzel, "High Performance Composites Using Nanotechnology," *Adv. Mater. Res.*, vol. 32, pp. 149–152, 2008.
- [247] T. H. Hsieh, A. J. Kinloch, K. Masania, J. S. Lee, A. C. Taylor, and S. Sprenger, "The toughness of epoxy polymers and fibre composites modified with rubber microparticles and silica nanoparticles," *J. Mater. Sci. (full set)*, pp. 1193–1210, 2010.
- [248] Z. Zhang, C. Breidt, L. Chang, F. Hauptert, and K. Friedrich, "Enhancement of the wear resistance of epoxy : short carbon fibre , graphite , PTFE and nano-TiO 2," *Matrix*, vol. 35, pp. 1385–1392, 2004.
- [249] N. Siddiqui, R. Woo, J. Kim, C. Leung, and A. Munir, "Mode I interlaminar fracture behavior and mechanical properties of CFRPs with nanoclay-filled epoxy matrix," *Compos. Part A Appl. Sci. Manuf.*, vol. 38, no. 2, pp. 449–460, Feb. 2007.
- [250] S. Roy, K. Vengadassalam, F. Hussain, and H. Lu, "Compressive strength enhancement of pultruded thermoplastic composites using nanoclay reinforcement," *49th Int. Symp. Exhib. Mater. Process. Technol. Years Progress, 2004, Long Beach, CA, United States*, pp. 2245–2259, 2004.
- [251] A. M. Díez-Pascual, B. Ashrafi, M. Naffakh, J. M. González-Domínguez, A. Johnston, B. Simard, M. T. Martínez, and M. A. Gómez-Fatou, "Influence of carbon nanotubes on the thermal, electrical and mechanical properties of poly(ether ether ketone)/glass fiber laminates," *Carbon N. Y.*, vol. 49, no. 8, pp. 2817–2833, Jul. 2011.
- [252] U. Rehan, E. Waggy, and A. C. Loos, "VARTM processing of glass fabric reinforcements coated with graphite nanoplatelets," in *Proceedings of the FPCM11, Auckland*, 2012.
- [253] M. Riccardis, D. Carbone, T. Makris, R. Giorgi, N. Lisi, and E. Salernitano, "Anchorage of carbon nanotubes grown on carbon fibres," *Carbon N. Y.*, vol. 44, no. 4, pp. 671–674, Apr. 2006.
- [254] V. P. Veedu, A. Cao, X. Li, K. Ma, C. Soldano, S. Kar, P. M. Ajayan, and M. N. Ghasemi-Nejhad, "Multifunctional composites using reinforced laminae with carbon-nanotube forests," *Nat. Mater.*, vol. 5, no. 6, pp. 457–462, Jun. 2006.
- [255] S. P. Sharma and S. C. Lakkad, "Effect of CNTs growth on carbon fibers on the tensile strength of CNTs grown carbon fiber-reinforced polymer matrix composites," *Compos. Part A Appl. Sci. Manuf.*, vol. 42, no. 1, pp. 8–15, Jan. 2011.
- [256] S. Kumar, T. D. Dang, F. E. Arnold, A. R. Bhattacharyya, B. G. Min, X. Zhang, R. A. Vaia, C. Park, W. W. Adams, R. H. Hauge, R. E. Smalley, S. Ramesh, and P. A. Willis, "Synthesis , Structure , and Properties of PBO / SWNT Composites," *Macromolecules*, vol. 35, pp. 9039–9043, 2002.
- [257] B. J. Blaiszik, M. Baginska, S. R. White, and N. R. Sottos, "Autonomic Recovery of Fiber/Matrix Interfacial Bond Strength in a Model Composite," *Adv. Funct. Mater.*, vol. 20, no. 20, pp. 3547–3554, Oct. 2010.
- [258] Z. Huang, "A review on polymer nanofibers by electrospinning and their applications in nanocomposites," *Compos. Sci. Technol.*, vol. 63, no. 15, pp. 2223–2253, Nov. 2003.
- [259] A. Zucchelli, M. L. Focarete, C. Gualandi, and S. Ramakrishna, "Electrospun nanofibers for enhancing structural performance of composite materials," *Polym. Adv. Technol.*, vol. 22, no. 3, pp. 339–349, Mar. 2011.
- [260] D. Li and Y. Xia, "Electrospinning of Nanofibers: Reinventing the Wheel?," *Adv. Mater.*, vol. 16, no. 14, pp. 1151–1170, Jul. 2004.

Bibliography

- [261] A. L. Yarin and E. Zussman, "Upward needleless electrospinning of multiple nanofibers," *Polymer (Guildf)*, vol. 45, no. 9, pp. 2977–2980, Apr. 2004.
- [262] Y. A. Dzenis and D. H. Reneker, "Delamination resistant composites prepared by small diameter fiber reinforcement at ply interfaces," United States Patent 6265333, 2001.
- [263] L. Liu, Z. Huang, C. He, and X. Han, "Mechanical performance of laminated composites incorporated with nanofibrous membranes," *Mater. Sci. Eng. A*, vol. 435–436, pp. 309–317, Nov. 2006.
- [264] S. Sihm, R. Y. Kim, W. Huh, K.-H. Lee, and A. K. Roy, "Improvement of damage resistance in laminated composites with electrospun nano-interlayers," *Compos. Sci. Technol.*, vol. 68, no. 3–4, pp. 673–683, Mar. 2008.
- [265] S. Hamer, H. Leibovich, A. Green, R. Intrater, and R. Avrahami, "Mode I Interlaminar Fracture Toughness of Nylon 66 Nanofibrilmat Interleaved Carbon/Epoxy Laminates," *Polym. Compos.*, vol. 32, no. 11, pp. 1781–1789, 2011.
- [266] H. Saghafi, A. Zucchelli, R. Palazzetti, and G. Minak, "The effect of interleaved composite nanofibrous mats on delamination behavior of polymeric composite materials," *Compos. Struct.*, vol. 109, pp. 41–47, 2014.
- [267] S. van der Heijden, L. Daelemans, B. De Schoenmaker, I. De Baere, H. Rahier, W. Van Paepegem, and K. De Clerck, "Interlaminar toughening of resin transfer moulded glass fibre epoxy laminates by polycaprolactone electrospun nanofibres," *Compos. Sci. Technol.*, vol. 104, pp. 66–73, Nov. 2014.
- [268] G. W. Beckermann and K. L. Pickering, "Mode I and Mode II interlaminar fracture toughness of composite laminates interleaved with electrospun nanofibre veils," *Compos. Part A Appl. Sci. Manuf.*, vol. 72, pp. 11–21, 2015.
- [269] A. D. Kelkar, R. Mohan, R. Bolick, and S. Shendokar, "Effect of nanoparticles and nanofibers on Mode I fracture toughness of fiber glass reinforced polymeric matrix composites," *Mater. Sci. Eng. B*, vol. 168, no. 1–3, pp. 85–89, Apr. 2010.
- [270] G. Li, P. Li, C. Zhang, Y. Yu, H. Liu, S. Zhang, X. Jia, X. Yang, Z. Xue, and S. Ryu, "Inhomogeneous toughening of carbon fiber/epoxy composite using electrospun polysulfone nanofibrous membranes by in situ phase separation," *Compos. Sci. Technol.*, vol. 68, no. 3–4, pp. 987–994, Mar. 2008.
- [271] K. Magniez, C. De Lavigne, and B. L. Fox, "The effects of molecular weight and polymorphism on the fracture and thermo-mechanical properties of a carbon-fibre composite modified by electrospun poly (vinylidene fluoride) membranes," *Polymer (Guildf)*, vol. 51, no. 12, pp. 2585–2596, May 2010.
- [272] K. Magniez, T. Chaffraix, and B. Fox, "Toughening of a Carbon-Fibre Composite Using Electrospun Poly(Hydroxyether of Bisphenol A) Nanofibrous Membranes Through Inverse Phase Separation and Inter-Domain Etherification," *Materials (Basel)*, vol. 4, no. 12, pp. 1967–1984, Nov. 2011.
- [273] J. A. VanderVennet, T. Duenas, Y. Dzenis, C. T. Peterson, C. E. Bakis, D. Carter, and J. K. Roberts, "Fracture toughness characterization of nanoreinforced carbon-fiber composite materials for damage mitigation," *Proceeding SPIE*, vol. 7978, pp. 797823-1–10, 2011.
- [274] J. Zhang, T. Lin, and X. Wang, "Electrospun nanofibre toughened carbon/epoxy composites: Effects of polyetherketone cardo (PEK-C) nanofibre diameter and interlayer thickness," *Compos. Sci. Technol.*, vol. 70, no. 11, pp. 1660–1666, Oct. 2010.
- [275] J. Zhang, T. Yang, T. Lin, and C. H. Wang, "Phase morphology of nanofibre interlayers: Critical factor for toughening carbon/epoxy composites," *Compos. Sci. Technol.*, vol. 72, no. 2, pp. 256–262, Jan. 2012.
- [276] J. Zhang, C. H. Wang, H. Niu, A. Gestos, T. Lin, and X. Wang, "Thermally mendable epoxy resin strengthened with carbon nanofibres," *Compos. Part A Appl. Sci. Manuf.*, vol. 55, pp. 45–52, Dec. 2013.
- [277] X.-F. Wu and A. L. Yarin, "Recent progress in interfacial toughening and damage self-healing of polymer composites based on electrospun and solution-blown nanofibers: An overview," *J. Appl. Polym. Sci.*, vol. 130, no. 4, pp. 2225–2237, Nov. 2013.
- [278] J. Seyyed Monfared Zanjani, B. Saner Okan, C. Yilmaz, Y. Menciloglu, and M. Yildiz, "Monitoring the interface and bulk self-healing capability of tri-axial electrospun fibers in glass fiber reinforced epoxy composites," *Compos. Part A Appl. Sci. Manuf.*, vol. 99, pp. 221–232, 2017.
- [279] L. Van der Schueren, B. De Schoenmaker, Ö. I. Kalaoglu, and K. De Clerck, "An alternative solvent system for

Bibliography

- the steady state electrospinning of polycaprolactone," *Eur. Polym. J.*, vol. 47, no. 6, pp. 1256–1263, Jun. 2011.
- [280] B. Carroll, "The accurate measurement of contact angle, phase contact areas, drop volume, and Laplace excess pressure in drop-on-fiber systems," *J. Colloid Interface Sci.*, vol. 57, no. 3, pp. 488–495, Dec. 1976.
- [281] ASTM D638-10, "Standard Test Method for Tensile Properties of Plastics 1," *ASTM Stand.*, pp. 1–16, 2012.
- [282] E. N. Brown, "Use of the tapered double-cantilever beam geometry for fracture toughness measurements and its application to the quantification of self-healing," *J. Strain Anal. Eng. Des.*, vol. 46, no. 3, pp. 167–186, 2011.
- [283] G. G. Trantina, "Fracture Mechanics Approach to Adhesive Joints," *J. Compos. Mater.*, vol. 6, pp. 192–207, 1972.
- [284] ASTM D790, "Standard Test Methods for Flexural Properties of Unreinforced and Reinforced Plastics and Electrical Insulating Materials," *ASTM Stand.*, pp. 1–12, 2002.
- [285] P. A. Rodgers, "Pressure-Volume-Temperature Relationships for Polymeric Liquids: A review of Equations of State and Their Characteristic Parameters for 56 Polymers," *J. Appl. Polym. Sci.*, vol. 48, no. 6, pp. 1031–1080, 1993.
- [286] "<http://matweb.com/>, accessed 06.01.2016." .
- [287] H. Cong, L. Li, and S. Zheng, "Formation of nanostructures in thermosets containing block copolymers: From self-assembly to reaction-induced microphase separation mechanism," *Polymer (Guildf.)*, vol. 55, pp. 1190–1201, 2014.
- [288] S. K. Siddhamalli, "Thermoset/(Thermoplastic Elastomer) Blends: Epoxy/EVA," *J. Vinyl Addit. Technol.*, vol. 6, no. 4, pp. 211–220, 2000.
- [289] Eastman, "Butvar. Polyvinyl butyral resin: Properties and uses," *Data sheet*, pp. 1–32, 2013.
- [290] S. Arayachukiat, V. A. Doan, T. Murakami, S. Nobukawa, and M. Yamaguchi, "Autonomic self-healing of poly(vinyl butyral)," *J. Appl. Polym. Sci.*, vol. 132, no. 22, pp. 42008–42014, 2015.
- [291] "<http://omnexus.specialchem.com/polymer-properties/properties/coefficient-of-linear-thermal-expansion>, accessed 06.01.2016." .
- [292] R. J. Lemmens, Q. Dai, and D. D. Meng, "Side-groove influenced parameters for determining fracture toughness of self-healing composites using a tapered double cantilever beam specimen," *Theor. Appl. Fract. Mech.*, vol. 74, pp. 23–29, 2014.
- [293] K. R. Hart, N. R. Sottos, and S. R. White, "Repeatable self-healing of an epoxy matrix using imidazole initiated polymerization," *Polymer (Guildf.)*, vol. 67, pp. 174–184, 2015.
- [294] S. Wong, A. Baji, S. Tripatanasuwan, T. Blackledge, and D. Reneker, "Mechanical Behavior and Toughness of Electrospun Polycaprolactone Nanofibers," *Proc. IMECE2007*, pp. 6–11, 2007.
- [295] A. Cohades, E. Manfredi, J.-C. Plummer, and V. Michaud, "Thermal mending in immiscible poly(ϵ -caprolactone)/epoxy blends," *Eur. Polym. J.*, vol. 81, pp. 114–128, 2016.
- [296] J. Rotrekl, L. Matějka, L. Kaprálková, A. Zhigunov, J. Hromádková, and I. Kelnar, "Epoxy/PCL nanocomposites: Effect of layered silicate on structure and behavior," *Express Polym. Lett.*, vol. 6, no. 12, pp. 975–986, 2012.
- [297] J. Lee, "Role of inherent matrix toughness on fracture of glass bead filled epoxies," *Polymer (Guildf.)*, vol. 41, no. 23, pp. 8375–8385, 2000.
- [298] W. J. Cantwell and H. H. Kausch, "Fracture behaviour of epoxy resins," in *Chemistry and Technology of Epoxy Resins*, 1993, pp. 144–174.
- [299] A. Cohades and V. Michaud, "Thermal mending in E-glass reinforced Poly(ϵ -caprolactone)/epoxy blends," *Compos. Part A Appl. Sci. Manuf.*, vol. 99, pp. 129–138, 2017.
- [300] ASTM D2734, "Standard Test Methods for Void Content of Reinforced Plastics," *ASTM Stand.*, pp. 1–4, 2003.
- [301] T. Ebeling, A. Hiltner, and E. Baer, "Delamination failure mechanisms in microlayers of polycarbonate and poly(styrene-co-acrylonitrile)," *J. Appl. Polym. Sci.*, vol. 68, no. 5, pp. 793–805, 1998.
- [302] A. Cohades and V. Michaud, "Damage recovery after impact in E-glass reinforced Poly(ϵ -caprolactone)/epoxy blends," *Compos. Struct.*, vol. 180, pp. 439–447, 2017.

- [303] *Military Handbook Mil-Hdbk-17 Rev. F. Composite Materials Handbook*, vol. 3. 2002.
- [304] T.-W. Shyr and Y.-H. Pan, "Impact resistance and damage characteristics of composite laminates," *Compos. Struct.*, vol. 62, no. 2, pp. 193–203, 2003.
- [305] M. Uyaner and M. Kara, "Dynamic Response of Laminated Composites Subjected to Low-velocity Impact," *J. Compos. Mater.*, vol. 41, no. 24, pp. 2877–2896, 2007.
- [306] M. V. Hosur, M. R. Karim, and S. Jeelani, "Experimental investigations on the response of stitched/unstitched woven S2-glass/SC15 epoxy composites under single and repeated low velocity impact loading," *Compos. Struct.*, vol. 61, no. 1–2, pp. 89–102, 2003.
- [307] C. Evcı and M. Gülgeç, "An experimental investigation on the impact response of composite materials," *Int. J. Impact Eng.*, vol. 43, pp. 40–51, 2012.
- [308] W. J. Cantwell and J. Morton, "The impact resistance of composite materials - a review," *Composites*, vol. 22, no. 5, pp. 347–362, 1991.
- [309] G. Belingardi and R. Vadori, "Influence of the laminate thickness in low velocity impact behavior of composite material plate," *Compos. Struct.*, vol. 61, no. 1–2, pp. 27–38, 2003.
- [310] M. Quaresimin, M. Ricotta, L. Martello, and S. Mian, "Energy absorption in composite laminates under impact loading," *Compos. Part B Eng.*, vol. 44, no. 1, pp. 133–140, 2013.
- [311] R. Reghunath, M. Lakshmanan, and K. M. Mini, "Low velocity impact analysis on glass fiber reinforced composites with varied volume fractions," *IOP Conf. Ser. Mater. Sci. Eng.*, vol. 73, pp. 1–8, 2015.
- [312] S. Abrate, *Impact on composite structures*. Cambridge: Cambridge University Press, 1998.
- [313] K. K. Namala, P. Mahajan, and N. Bhatnagar, "Digital Image Correlation of Low Velocity Impact on Glass/Epoxy Composite," *Int. J. Comput. Methods Eng. Sci. Mech.*, vol. 15, pp. 203–217, 2014.
- [314] W. Tan, B. G. Falzon, L. N. S. Chiu, and M. Price, "Predicting low velocity impact damage and Compression-After-Impact (CAI) behaviour of composite laminates," *Compos. Part A Appl. Sci. Manuf.*, vol. 71, pp. 212–226, 2015.
- [315] S. Rivallant, C. Bouvet, and N. Hongkarnjanakul, "Failure analysis of CFRP laminates subjected to compression after impact: FE simulation using discrete interface elements," *Compos. Part A Appl. Sci. Manuf.*, vol. 55, pp. 83–93, 2013.
- [316] B. Vieille, V. M. Casado, and C. Bouvet, "Influence of matrix toughness and ductility on the compression-after-impact behavior of woven-ply thermoplastic- and thermosetting-composites: A comparative study," *Compos. Struct.*, vol. 110, no. 1, pp. 207–218, 2014.
- [317] P. G. Slattery, C. T. McCarthy, and R. M. O'Higgins, "Assessment of residual strength of repaired solid laminate composite materials through mechanical testing," *Compos. Struct.*, vol. 147, pp. 122–130, 2016.
- [318] A. Cohades, N. Hostettler, M. Pauchard, J.-C. Plummer, and V. Michaud, "Stitched shape memory alloy wires enhance damage recovery in self-healing fiber-reinforced polymer composites- SUBMITTED," *Adv. Funct. Mater.*, 2017.
- [319] A. Cohades, M. Pauchard, and V. Michaud, "Impact resistance and recovery in SMA stitched E- glass reinforced Poly (ϵ - caprolactone)/ epoxy composites," *Proc. ICCM21*, 2017.
- [320] S. Pappadà, P. Gren, K. Tatar, T. Gustafson, R. Rametta, E. Rossini, and A. Maffezzoli, "Mechanical and Vibration Characteristics of Laminated Composite Plates Embedding Shape Memory Alloy Superelastic Wires," *J. Mater. Eng. Perform.*, vol. 18, no. 5–6, pp. 531–537, Mar. 2009.
- [321] R. A. Tuli, G. A. George, T. R. Dargaville, and N. Islam, "Studies on the Effect of the Size of Polycaprolactone Microspheres for the Dispersion of Salbutamol Sulfate from Dry Powder Inhaler Formulations," *Pharm. Res.*, vol. 29, pp. 2445–2455, 2012.
- [322] R. A. Tuli, T. I. M. R. Dargaville, G. A. George, and N. Islam, "Polycaprolactone Microspheres as Carriers for Dry Powder Inhalers : Effect of Surface Coating on Aerosolization of Salbutamol Sulfate," *Pharm. Technol.*, vol. 101, no. 2, pp. 733–745, 2012.
- [323] J. W. Smith, "Deformation induced failure mechanisms in particulate filled epoxy resins," *Thèse EPFL N° 792*, 1989.

Bibliography

- [324] N. Alif, L. A. Carlsson, and G. J. Gillespie, "Mode I mode II and mixed mode interlaminar fracture of woven fabric carbon/epoxy," in *Composites materials : testing and design*, Hooper, Ed. 1997, p. 20.
- [325] A. Cohades, L. Daelemans, C. Ward, T. Meireman, W. Van Paepegem, K. De Clerck, and V. Michaud, "Size limitations on achieving tough and healable fibre reinforced composites through the use of thermoplastic nanofibres-SUBMITTED," *Compos. Part A*, 2017.
- [326] E. Farmand-Ashtiani, J. Cugnoni, and J. Botsis, "Specimen thickness dependence of large scale fiber bridging in mode I interlaminar fracture of carbon epoxy composite," *Int. J. Solids Struct.*, vol. 55, pp. 58–65, 2014.
- [327] J. Verrey, "Resin Transfer Moulding of complex shaped composites using carbon fibre non-crimp fabrics," *Thèse EPFL n°3003*, 2004.
- [328] J. Verrey, M. D. Wakeman, V. Michaud, and J. A. E. Manson, "Manufacturing cost comparison of thermoplastic and thermoset RTM for an automotive floor pan," *Compos. Part A Appl. Sci. Manuf.*, vol. 37, no. 1, pp. 9–22, 2006.
- [329] M. Z. Shah Khan and A. P. Mouritz, "Fatigue behaviour of stitched GRP laminates," *Compos. Sci. Technol.*, vol. 56, no. 6, pp. 695–701, 1996.
- [330] M. A. Woodruff and D. W. Hutmacher, "The return of a forgotten polymer - Polycaprolactone in the 21st century," *Prog. Polym. Sci.*, vol. 35, no. 10, pp. 1217–1256, 2010.

Cohades Amaël E-mail: amael.cohades@alumni.epfl.ch
58, Rue de Rive 29 years old
1260 Nyon Single
Switzerland Swiss-French
Mobile: +41 79/780.06.15



Education

- PhD candidate, *Functional composites with damage control and repair*** 2014-now
Ecole Polytechnique Fédérale de Lausanne (EPFL), LPAC
- Master in Material Science and Engineering** 2010-2012
Ecole Polytechnique Fédérale de Lausanne (EPFL)
- **Field of courses:** processing, properties, structure, and application of materials
 - **Master Thesis:** University of Auckland (New Zealand), CACM
 - **Minor:** Management, Technology and Entrepreneurship
- Bachelor in Material Science and Engineering** 2007-2010
Ecole Polytechnique Fédérale de Lausanne (EPFL)
- High school degree, Biology and Chemistry option** 2003-2006
Gymnase Cantonal de Nyon, division Baccalauréat

Work experience

- EPFL, PhD, EPFL-LPAC** (Laboratory for Processing of Advanced Composites) 01.2014-now
EPFL, Scientific Assistant, EPFL- LMM (Laboratory of Mechanical Metallurgy) 12.2012-12.2013
EPFL, assistant in EPFL-LTC (Laboratory of composites and polymer technology) 02.2010-01.2012

Prizes and awards

- **PhD** : « Ma thèse en 180 secondes », EPFL 3rd place, Swiss 2nd place 2016-2017
- **Master studies** : Prize from the Commune de Chavannes-près-Renens (VD) 2012

Other activities

- Paléo Festival Nyon** 2012-now
- Area Manager-Bar-20 people for 6 days
- Enigma association** (Material students association) 2009-2010
PRESIDENT of the commission MX on Tour
- Organisation of a study trip to India (2 weeks, 25 participants)
- High school sport day association**
- Activities management for 700 students 2006

Computer skills

Word, Excel, LATEX, Matlab, Mathematica, Mathcad, Origin, Illustrator, Photoshop

Languages

French: mother tongue
English: Advanced level, C1
German: Elementary level, A2

Leisure activities

Table tennis, climbing, ski

Scientific projects

- **PhD Thesis, ongoing, EPFL-LPAC:**
 - Functional composites with damage control and repair
- **Projects as Scientific Assistant, EPFL-LMM:**
 - An analysis of the tensile elongation to failure of laminated metal composites in the presence of strain-rate hardening: simulation and experimental work
 - Microcasting of copper pieces in a ceramic mould
- **Projects as Student Assistant, EPFL-LTC:**
 - Out-of-autoclave processing of ribbed parts: technical assessment
 - Processing and characterisation of biocomposite foams
 - Processing and characterisation of polymer-ceramic films
- **Master Thesis:**
 - LCM Processing of Nanofibre Enhanced Textile Reinforcements

Conferences

- **ICCM 2017, August 2017, Xi'an (CN)**
 - **Oral presentation:** Impact resistance and recovery in SMA stitched E-glass Poly(ϵ -caprolactone)/epoxy composites
- **ICSHM 2017, June 2017, Friedrichshafen (DE)**
 - **Oral presentation:** Crack closure assessment through the use of SMA wires in thermally mended E-glass Poly(ϵ -caprolactone)/epoxy blends
- **My thesis in three minutes, French Version, "Les matériaux auto-réparables"**
 - International Final, September 2017, Liège (B)
 - Swiss-Final, May 2017, 2nd place, Geneva (CH)
 - EPFL-Final, October 2016, 3rd place, Lausanne (CH)
- **ECCM 2016, June 2016, Munich (DE)**
 - **Oral presentation:** Recovery after Mode I crack propagation and impact in E-glass reinforced Poly(ϵ -caprolactone)/epoxy blends
- **ICSHM 2015, June 2015, Raleigh (USA)**
 - **Oral presentation:** Thermal mending in E-glass Poly(ϵ -caprolactone)/epoxy blends
- **IOP Self-healing Materials Summer School, Vlieland (NL):** Participation only
- **Euromat, September 2013, Sevilla (ES)**
 - **Presentation Title:** Tensile instability in Unidirectional composites
- **34th SAMPE Europe Conference/JEC 2013, March 2013, Paris (FR)**
 - **Oral presentation:** LCM (Liquid Composite Moulding) Processing of Nanofibre Enhanced Textile Reinforcements
- **SAMPE Switzerland, January 2013, Zurich (CH)**
 - **Oral presentation:** LCM (Liquid Composite Moulding) Processing of Nanofibre Enhanced Textile Reinforcements
 - Selected during the student contest to go to SAMPE Europe in Paris
- **FPCM11, May 2012, Auckland (NZ)**
 - **Presentation title:** Out-of-autoclave processing of ribbed parts: technical, economic and environmental assessment

List of Publications

1. Cohades A, Daelemans L, Ward C, Meireman T, Van Paepegem W, De Clerck K, Michaud V. *Size limitations on achieving tough and healable fibre-reinforced composites through the use of thermoplastic nanofibres*. SUBMITTED, 2017
2. Cohades A, Hostettler N, Pauchard M, Plummer C J-G, Michaud V. *Stitched shape memory alloy wires enhance damage recovery in self-healing fiber-reinforced polymer composites*. SUBMITTED, 2017
3. Daelemans L, Cohades A, Meireman T, Beckx J, Spronk S, Kersemans M, De Baere Y, Rahier H, Michaud V, Van Paepegem W, De Clerck K. *Electrospun nanofibrous interleaves for improved low velocity impact resistance of glass fibre reinforced composite laminates*. Mater Des, In Press, Accepted Manuscript, 2017
4. Post W, Cohades A, Michaud V, van der Zwaag S, Garcia S J. *Healing of a glass fibre reinforced composite with a disulphide containing organic-inorganic epoxy matrix*. Compos Sci Technol, 2017; 152: 85–93.
5. Cohades A, Pauchard M, Michaud V. *Impact resistance and recovery in SMA stitched E- glass reinforced Poly(ϵ -caprolactone)/ epoxy composites*. Proc ICCM21, 2017.
6. Cohades A, Michaud V. *Damage recovery after impact in E-glass reinforced Poly(ϵ -caprolactone)/epoxy blends*. Compos Struct, 2017; 180:439-447
7. Cohades A, Michaud V. *Thermal mending in E-glass reinforced Poly(ϵ -caprolactone)/epoxy blends*. Compos Part A Appl Sci Manuf, 2017; 99:129–38.
8. Cohades A, Michaud V. *Recovery after Mode I crack propagation and impact in E-glass reinforced Poly(ϵ -caprolactone)/ epoxy blends*. Proc ECCM17, 2016; 1–8.
9. Cohades A, Manfredi E, Plummer J-C, Michaud V. *Thermal mending in immiscible poly(ϵ -caprolactone)/epoxy blends*. Eur Polym J, 2016; 81:114–28.
10. Manfredi E, Cohades A, Richard I, Michaud V. *Assessment of solvent capsule-based self-healing for woven E-glass fibre-reinforced polymers*. Smart Mater Struct, 2015; 24:1–11.
11. Cohades, A, Çetin, A, Mortensen, A. *Designing laminated metal composites for tensile ductility*. Mater Des, 2015; 66:412-420.
12. Cohades A, Mortensen A. *Tensile elongation of unidirectional or laminated composites combining a brittle reinforcement with a ductile strain and strain-rate hardening matrix*. Acta Mater, 2014; 71:31–43.